

*In Vivo* Remodeling of Settable, Cell-Degradable, and Application-Specific Poly(thioketal urethane) Tissue Engineering Composite Bone Grafts with Bone-Like Strength

By

Madison Ashli Pauline McGough

Dissertation

Submitted to the Faculty of the  
Graduate School of Vanderbilt University  
in partial fulfillment of the requirements

for the degree of

DOCTOR OF PHILOSOPHY

in

Biomedical Engineering

August 31, 2018

Nashville, Tennessee

Approved:

Scott A. Guelcher, Ph.D.

Mark D. Does, Ph.D.

Craig L. Duvall, Ph.D.

Ethan S. Lippmann, Ph.D.

Julie A. Sterling, Ph.D.

Dedicated to my husband Max, who has supported my dreams for so many years.

To my family who taught me to dream and pushed me to achieve my dreams from the beginning.

To my friends, new and old, who have made attaining my dreams so much fun.

## ACKNOWLEDGMENTS

Thank you to my research advisor, Dr. Scott Guelcher for guiding me through this research, supporting my ideas, and pushing me to achieve my goals. I am very thankful for all of the opportunities he afforded beyond research, including opportunities to work with many collaborators spanning the medical device industry and academia, attend national and international conferences, and participate in the patent approval process. I have gained invaluable experience that will provide a solid foundation for the next chapter of my career in research. I would also like to thank my PhD committee: Dr. Mark Does, Dr. Craig Duvall, Dr. Ethan Lippmann, and Dr. Julie Sterling for their guidance during my time at Vanderbilt University. I appreciate all of the insight and motivation you provided to make this project the best it can be and to help me learn all that I could.

I am extremely grateful for the members of the Biomaterials and Tissue Engineering Laboratory that were an integral part of my research from the beginning. The Guelcher Lab Manager, Katarzyna (Kasia) Zienkiewicz is vital to the smooth operation of the lab. Kasia, I am forever grateful for all that you have taught me, for your mentorship, and for supporting me and the projects that make up this dissertation. Thank you to Dr. Drew Harmata, Dr. Anne Talley, Dr. Ruijing Guo, Dr. Sichang Lu, Tom Spoonmore, Joe Vanderburgh, Lauren Boller, Dustin Groff, Greg Lowen, and David Florian for all of your support in and out of the lab and making my tenure at Vanderbilt so enjoyable. I would also like to acknowledge the undergraduate students I had the pleasure of working with: Cody Dykes, Gabrielle Betancourt, and Mollie Maples.

Our collaborations throughout Vanderbilt were essential to this work. Thank you to Dr. Mukesh Gupta and Dr. John Martin of the Duvall Lab for teaching me synthesis and

characterization techniques that kick-started this project. I would also like to thank Alyssa Merkel and Josh Johnson of the Julie Sterling Lab (Vanderbilt Center for Bone Biology) who taught me many histology procedures that were used throughout this work. Thank you to Sasi Uppuganti (Jeff Nyman Lab) for sharing his mechanical testing and  $\mu$ CT expertise and helping maintain the bone histology lab. Finally, I would like to thank Ryan Murray (Vanderbilt University Institute of Imaging Science) for his assistance with the  $\mu$ CT.

Collaborations with The United States Army Institute of Surgical Research (USAISR) and Medtronic Spinal and Biologics were imperative to this work. Thank you to Dr. Josh Wenke, Dr. Stefanie Shiels, and Dr. David Tennent for sharing your ideas and working with our lab to maximize the knowledge gained from the studies in this work. Thank you to Alicia Lofgren, Tina Sandoval, Kinton Armmer, and all of the other members of the Wenke group at USAISR for all of your hard work to ensure the *in vivo* studies went smoothly. I would also like to acknowledge Kerem Kalpakci, Dan Shimko, Cheyenne Rhodes, Bre Jacobs, and Roger Harrington at Medtronic for supporting this project and providing invaluable insight that helped maximize the potential of this work.

I am very fortunate to have strong female role models that have guided me through my scientific endeavors. Thank you to Lauren Gerardi, Dr. Rakhi Jain, Dr. Elizabeth Cosgriff-Hernandez, and Dr. Jenny Robinson. Your mentorship has truly been invaluable.

I am grateful for all of the funding sources that supported these studies. My tenure at Vanderbilt was supported by the National Science Foundation (NSF GRFP Grant No. 1445197). This dissertation research was supported in part by the National Institute of Health (R01AR064304, R01EB019409, R01AR064772), and Medtronic Spinal and Biologics. This work was also supported by an appointment to the Student Research

Participation Program administered by the Oak Ridge Institute for Science and Education.

Lastly, I am extremely grateful for the support of the Sid Richardson Memorial Fund who has provided financial support throughout my academic career.

## TABLE OF CONTENTS

DEDICATION .....	ii
ACKNOWLEDGMENTS.....	iii
LIST OF TABLES .....	ix
LIST OF FIGURES.....	x
Nomenclature .....	xvii
I. INTRODUCTION .....	1
1.1. Specific Aims .....	2
1.2. Approach .....	3
References .....	6
II. BACKGROUND.....	8
2.1. Bone Tissue Engineering.....	8
2.2. Biology of Bone Graft Remodeling.....	10
2.2. Bone Grafts.....	12
2.3. Polyurethanes in Bone Tissue Engineering.....	16
2.4. Oxidatively Degradable Biomaterial Scaffolds.....	20
2.5. Strategies to Confer Osteoinductivity .....	21
2.6. <i>In Vivo</i> Investigation of Bone Tissue Engineering Constructs.....	24
References .....	29
III. OXIDATIVELY DEGRADABLE POLY(THIOKETAL URETHANE) CERAMIC COMPOSITE BONE CEMENTS WITH BONE-LIKE STRENGTH.....	43
3.1 Abstract.....	43
3.2 Introduction .....	44
3.3 Methods .....	46
3.4 Results and Discussion .....	53
3.5 Conclusion.....	65
References .....	66
IV. REMODELING OF A SETTABLE, CELL-DEGRADABLE POLY(THIOKETAL- URETHANE) AUTOGRAFT EXTENDER FOR A MINIMALLY INVASIVE BONE GRAFT IN RABBITS.....	69
4.1 Abstract.....	69
4.2 Introduction .....	70
4.3 Materials and Methods .....	72
4.4 Results .....	79

4.5 Discussion.....	90
4.6 Conclusion.....	94
References .....	95
V. A COMPRESSION RESISTANT POLY(THIOKETAL URETHANE) AUTOGRAFT EXTENDER IN A RABBIT RADIUS MODEL.....	99
5.1 Abstract.....	99
5.2 Introduction .....	100
5.3 Materials and Methods .....	102
5.4 Results .....	105
5.5 Discussion.....	113
5.6 Conclusion.....	116
References .....	117
VI. LONG-TERM REMODELING OF A NANOCrystalline HYDROXYAPATITE- POLY(THIOKETAL URETHANE) BONE VOID FILLER IN A FEMORAL CONDYLE DEFECT.....	121
6.1 Abstract.....	121
6.2 Introduction .....	122
6.3 Materials and Methods .....	123
6.4 Preliminary Results .....	129
6.5 Discussion.....	140
6.6 Conclusion.....	144
References .....	145
VII. SUMMARY AND CONCLUSIONS .....	149
References .....	153
VIII. FUTURE DIRECTIONS.....	154
8.1 PTKUR Autograft Extender .....	154
<i>Enhancements to Current Approach</i> .....	154
<i>Alternative Approaches to Accelerate Cellular Infiltration and PTKUR AG Extender     Remodeling</i> .....	156
8.2 nHA-PUR Hybrid Nanocomposite.....	157
<i>Accelerated Remodeling of a Mechanically Robust nHA-PUR for Weight-Bearing     Applications</i> .....	157
<i>Condition-Based Remodeling Mechanisms of an nHA-PUR Bone Void Filler</i> .....	170
References .....	172
APPENDIX .....	175
EXPERIMENTAL PROTOCOLS .....	175

Thioketal Diol Synthesis .....	176
LTI-TK Quasi-Prepolymer.....	186
Quasi-Static Compressive Fatigue Testing .....	188
$\mu$ CT Analysis of Cylindrical Defects.....	197
Safranin O/Fast Green Staining of Ground Sections .....	200
Immunohistochemical Staining of Ground Sections.....	201



## LIST OF TABLES

<u>Table Caption</u>	<u>Page</u>
<b>Table 4.1.</b> Material properties of PTKUR AG extenders.....	80
<b>Table 5.1.</b> Mechanical properties of a PTKUR AG extender to be investigated in a rabbit radius defect model.....	106
<b>Table 8.1.</b> Sucrose sweep. Sucrose/CaP ratios and post-leach mechanical properties. Fatigue life is reported as average number of cycles until failure (number of specimen to runout/total number of specimens).....	165
<b>Table 8.2.</b> Porosity and mechanical properties of 10 wt% sucrose/45 wt% CaP materials explanted prior to the 16-week time point.....	166

## LIST OF FIGURES

<u>Figure Caption</u>	<u>Page</u>
<p><b>Figure 3.1.</b> Synthesis and characterization of low molecular weight thioketal diol. (A) Synthesis scheme. (B-C) Characterization by (B) NMR and (C) GPC indicate that the targeted molecular structure was obtained. (D) Viscosity of the TK diol is independent of sheer rate.....</p>	54
<p><b>Figure 3.2.</b> Synthesis of poly(thioketal urethane) (PTKUR)/ceramic composites. (A) Synthesis scheme for LTI-TK prepolymer. (B) Viscosity of the LTI-TK prepolymer is independent of shear rate. (C) Reaction of TK diol with LTI-TK prepolymer to form a crosslinked PTKUR network. (D) Fabrication of PTKUR/ceramic composites by mixing LTI-TK prepolymer, TK diol, and ceramic particles (MG or nHA). (E) The viscosity of uncatalyzed (non-reactive) LTI-TK/TK diol/ceramic mixtures decreases with increasing shear rate, providing evidence of shear-thinning behavior. (F-G) SEM images of (F) MG and (G) nHA composites show lack of porosity. Due to their relatively large size (100 – 300 <math>\mu\text{m}</math>), MG particles (light grey) can be distinguished from the PTKUR phase (dark grey).....</p>	55
<p><b>Figure 3.3.</b> Kinetics of the setting reaction. (A) The reaction rate constant (<math>k</math>) of a second order reaction is calculated from the slope of the line of <math>1/[\text{NCO}]</math> with time. The rate constant of the LTI-TK prepolymer-TK diol reaction (<math>\square</math>) is substantially greater than that measured for MG (<math>\Delta</math>), nHA (<math>\circ</math>), or water (<math>\diamond</math>). (B) Using the rate constant for the dominant reaction TK diol + LTI-TK prepolymer, the conversion of the NCO and OH functional groups was calculated versus time. (C) Storage (<math>G'</math>) and loss (<math>G''</math>) moduli of the reactive (catalyzed) LTI-TK/TK diol/MG mixture. The gel point (<i>i.e.</i>, working time) is identified as the <math>G'-G''</math> crossover point to be 6.7 min.....</p>	56
<p><b>Figure 3.4.</b> Mechanical properties of PTKUR/ceramic composites under static compressive loading. (A) Yield strength and (B) modulus of PTKUR/MG composites measured versus time for up to two weeks. (C) Yield strength and (D) modulus of PTKUR/nHA composites measured versus time for up to two weeks. Maximum compressive properties were achieved after 1-week cure time. The physical appearance of (E) MG and (F) nHA composites after compressive testing supports this finding.....</p>	59
<p><b>Figure 3.5.</b> Degradation of PCLUR and PTKUR films. (A) PTKUR films were hydrolytically stable in PBS despite their rapid degradation in oxidative media after only 4 days. (B) After 4 months, PCLUR and PTKUR substantially degraded in oxidative medium, while no degradation was observed in PBS. (C-E) SEM images show the effects of oxidative degradation on the architecture of the PTKUR films after (C) 24 h, (D) 48 h, and (E) 72 h.....</p>	60

<b>Figure 3.6.</b> MC3T3 cells (arrows) attached and spread on (A) MG and (B) nHA composites after 24 h incubation. Scale bar = 50 $\mu\text{m}$ . (C) Measurements of total protein versus time indicate that cells proliferated faster on nHA composites.....	61
<b>Figure 3.7.</b> Images of transverse $\mu\text{CT}$ sections of PTKUR/MG and PTKUR/nHA composite cements explanted at 6 and 12 weeks. Higher magnification images of the defect periphery show evidence of trabecular infiltration (single white arrows) and trabecular densification (double white arrows). Scale bar = 1 mm.....	62
<b>Figure 3.8.</b> Images of transverse histological sections of PTKUR/MG and PTKUR/nHA composite cements. Low-magnification (2X) images of cements at 12 weeks show appositional growth of dense trabecular bone near the host bone-cement interface. Higher magnification (20-40X) images of PTKUR/MG cements at 6 and 12 weeks reveal evidence of residual MG (dark grey) particles, resorption of PTKUR (P, light grey), cellular infiltration (blue), osteoid (arrows), and new bone (NB, red) formation. Similar observations were made for PTKUR/nHA cements, but the nHA particles could not be distinguished due to their small size. Resorption of the cement (CM) was evident in the histological sections.....	62
<b>Figure 3.9.</b> Resorption of PTKUR/MG and PTKUR/nHA cements mediated by osteoclast-like cells at 6 and 12 weeks. Osteoclasts are identified as large (>50 $\mu\text{m}$ ) multi-nucleated (nucleus stains dark blue) cells near the host bone-cement interface.....	64
<b>Figure 4.1.</b> SEM images of AG and AG/CaP extenders. (A) The AG extender indicates minimal porosity and an irregular architecture. (B) The AG/CaP extender has irregular pores and interconnects throughout the material. Arrows indicate CaP particles.....	81
<b>Figure 4.2.</b> Images of histological sections of femoral segmental defects in the rat at 4 weeks post-implantation showing areas of cellular activity (arrows) and new bone formation near edges of implanted AG. (A-B) AG extender at (A) 2X and (B) 40X magnification. (C-D) AG control at (C) 2X and (D) 40X magnification. (bone: red (“B”), cell nuclei: dark blue, PTKUR: teal (“P”)).....	82
<b>Figure 4.3.</b> (A) Anatomical representation of graft placement from L5 – L6. Materials were implanted bilaterally. (B) 3D <i>in vivo</i> CT images of L5 – L6 at time of surgery, 4 weeks post-implantation, and 8 weeks post-implantation. Dorsal views show an increase in mineralized tissue in all groups.....	84

**Figure 4.4.**  $\mu$ CT images of half of spines when cut down the spinal column. (A) Coronal sections of AG control, AG extender, and AG/CaP extender. Arrows show new bone formation. (Note: AG extender material is covering the superior lateral process.) (B) Serial sagittal sections taken from the end of the lateral processes (left) to the vertebral body (right) for the AG control, AG extender, and AG/CaP extender show ingrowth of new bone between the lateral processes. White arrows indicate new bone.....

85

**Figure 4.5.** Images of histological sections of AG control, AG extender, and AG/CaP extender implanted on the L5 - L6 lateral processes. (A) X-ray image detailing the histological sectioning procedure. Spines were cut in half along the spinal column. After embedding, sagittal serial sections were cut from the lateral most instance of the intertransverse process mass until the process was reached. (B-G) Histological sections of L5 – L6 in the sagittal plain showing the mass in the intertransverse process space. Sections are stained with Sanderson’s Rapid Bone Stain (B, D, F - bone: red, cell nuclei: dark blue, PTKUR: teal, CaP: black, cartilage-like tissue: purple) or unstained and imaged under a fluorescent microscope (C, E, G). Single arrows show areas of ongoing mineralization of soft tissue, double arrows indicate new bone. (C, E, G) Dynamic histomorphometry, where calcein green (green fluorescence) labeled actively mineralizing tissue at 2 weeks and xylenol orange (orange fluorescence) labeled actively mineralizing tissue at 6 weeks, shows remodeling was ongoing from 2 to 6 weeks as growth towards bridging continued.....

87

**Figure 4.6.** Magnified images (40X) of histological sections of the AG control (top row), AG extender (middle row), and AG/CaP extender (bottom row). (A) 20X images in the plane of the processes (yellow box in the 2X image) show collagen fibrils that are visible as bundles with their long axes aligned (single arrows), a pattern characteristic of lamellar bone structures. Evidence of new bone formation was also observed (\*). (B) Similar cellular activity was observed in the interior of the ITP space far from the processes (orange box in the 2X image). (C) 40X images of the AG extender in the plane of the processes (yellow box in the 2X image) show evidence of aligned collagen fibrils (single arrows), new bone formation (\*), residual polymer (P), and residual autograft (AG). (D) 40X images of the AG extender in the graft space far from the processes (orange box in the 2X image) also show evidence of new bone formation and residual polymer, indicating cells were able to infiltrate into the interior of AG extender (double arrows). Residual autograft particles (AG) embedded in polymer (P) are also observed. (E-F) 40X images of the AG/CaP extender (E) in the plane of the processes (yellow box) and (F) in the graft space (orange box) show evidence of aligned collagen fibrils, new bone, and residual polymer. (Arrows: aligned collagen fibrils, \*: new bone, P: residual polymer, AG: residual autograft).....

88

<b>Figure 4.7.</b> Quantification of bridging. (A) Method used to measure bridging. The green lines extend the front of the green fluorescence. These were added together for the length of bridging at 2 weeks and then normalized by the length of the ITP (black line). This was repeated for the orange fluorescence (6 weeks) and red staining (8 weeks). (B) Normalized bridging of the ITP space spanning the L5 – L6 transverse processes indicates progression from 2 to 8 weeks for all groups as assessed by histomorphometry. (Linear regression was calculated and included on the plot. Statistical symbols on the 8-week data represent a significant increase from the 2-week time point. *: $P \leq 0.05$ , **: $P \leq 0.01$ , ****: $P \leq 0.0001$ ).....	89
<b>Figure 5.1.</b> SEM image of PTKUR AG extender indicates minimal porosity and irregular micro-architecture.....	106
<b>Figure 5.2.</b> Photographs of (A) PTKUR AG extender and (B) AG control in the 20 mm defect prior to closure.....	107
<b>Figure 5.3.</b> CT images acquired immediately post-operatively, at 4, 8, and 12 weeks. Remodeling of the PTKUR AG extender progresses each time point (double arrows) and a perimeter of new bone is evident on the lateral surface of the control defect at 12 weeks (single arrow).....	108
<b>Figure 5.4.</b> $\mu$ CT reconstructions showing remodeling of (A) the AG extender and (B) the control 12 weeks post-operatively. (C) Bone area measurements by $\mu$ CT, from the proximal to distal interfaces of the defect (including the ulna) for the AG extender and AG control groups. Corresponding dotted lines are standard deviation.....	108
<b>Figure 5.5.</b> Dynamic (fluorescent) and 12-week (stained) histology for all specimen in the (A) AG extender group and (B) control group allude to the rate and patterns of bone regeneration and the variation in bone quality for each group.....	110
<b>Figure 5.6.</b> An area of interest (AOI) was selected to include new bone growth throughout the defect space (A). (B)Histomorphometrical area measurements indicated similar mineralization at 4 and 8 weeks for both groups and the difference between groups was not significant. The difference in the red-stained area (12 weeks) between the 2 groups was not significant indicating the AG extender performed similarly to the control.....	111

**Figure 5.7.** Magnified histology images show (A) the formation of Haversian canal-like structures (single arrow) forming at the interface of the AG extender and the calcified interosseous syndesmosis (20X). (B) Bone forming cells (double arrows) are actively remodeling the PTKUR AG extender at the polymer surface and intramembranous bone formation is ongoing towards the center of the AG extender. (C) Haversian canal-like structures are also evident in the AG control group (arrow) and (D) bone remodeling is evident. (Bone forming cells: double arrow, NB: new bone, AG: autograft, P: Polymer, scale bar=200µm)..... 112

**Figure 6.1.** Dewatered NanoStim™ nHA particles visualized with TEM..... 130

**Figure 6.2.** Qualitative analysis of three material groups tested *in vivo* as visualized by (A) µCT and (B) SEM..... 131

**Figure 6.3.** Mechanical analysis of material groups included in *in vivo* study revealed a statistically significant difference in modulus between the CaP and CaP/S group (A). nHA-PTKUR had a significantly higher (B) ultimate strength, (C) yield strength, and (D) yield strain compared to any of the putties. (#:  $P \leq 0.1$ , \*:  $P \leq 0.05$ , \*\*:  $P \leq 0.01$ )..... 132

**Figure 6.4.** (A) 2D µCT reconstructions were used to measure the length of the defects at 4, 12, and 18 months. (B) A schematic representation of the BV/TV µCT analysis procedure demonstrates the selection of concentric annular cylinders represented by the colored pipes. The dotted line and outer edge of the green circle represent the defect diameter. (B) Sample 2D images show the effects of thresholding on each of the different material groups. (D-G) The results of the BV/TV analysis are presented for the (D) glue, (E) CaP, (F) CaP/S, and (G) sucrose groups..... 133

**Figure 6.5.** Magnified histology images at 4 (A, C, E, G) and 12 (B, D, F, H) months demonstrate a combination of endochondral bone formation, indicated by the mineralization (\*\*) of cartilage-like nodules (#), and intramembranous bone formation, indicated by bone formation (single arrows) and osteoclast-like cells (double arrows) at the PTKUR interface. New bone (\*) is evident within the PTKUR bone grafts at 4 and 12 months. (\*: new bone, \*\*:mineralizing cartilage, #: cartilage-like nodules, single arrow: bone lining cells and osteoid, double arrows: osteoclast-like cells)..... 136

**Figure 6.6.** One slide from each material group was stained with Safranin O/Fast green to differentiate collagen. Collagen (pink stain, single arrows) was evident within the scaffold as early as 4 months and was generally surrounded by PTKUR material. Bone (teal, double arrows) was also easily distinguished using this stain..... 137

<b>Figure 6.7.</b> Preliminary histomorphometry quantifies (A) percent bone, (B) percent dark blue staining, (C) percent dark nodules that are hypothesized to represent areas undergoing endochondral bone formation, and (D) percent cartilage. (A-C: Stevenel’s Blue stain, D: Safranin O/Fast Green stain).....	138
<b>Figure 6.8.</b> Axial histology images of tibial slot defects. The PTKUR glue (no CaP or sucrose) persisted in the defect at (A) 4 and (B) 12 months. New bone was evident near the cortical perimeter at 4 months (A) and significant new bone could be seen within the graft at 12 months (arrows, *: bone ingrowth). The empty controls bridged by the 4-month time point (C) and this bone was replaced by trabecular bone by 12 months (D).....	139
<b>Figure 8.1.</b> Sagittal CT image demonstrating positioning and dimensions of the tibial plateau and femoral condyle defects.....	160
<b>Figure 8.2.</b> SEM images indicate the porosity of nHA-PEUR that resulted after performing a sucrose sweep from 0-55 wt% sucrose.....	162
<b>Figure 8.3.</b> Compressive mechanical properties resulting from sucrose sweep. (A) Representative stress-strain curves show a transition from plastic-like (0-20 wt% sucrose) to foam-like (45-55 wt% sucrose) mechanical properties. (B) Modulus and (C) yield strength decrease and (D) yield strain increases with increasing sucrose content, as anticipated by increased porosity. (E) Photographs of fatigue test specimens indicate a maximum of 10 wt% sucrose can be incorporated without losing weight-bearing potential. (*: $P \leq 0.05$ , **: $P \leq 0.01$ , ***: $P \leq 0.001$ , ****: $P \leq 0.0001$ ).....	164
<b>Figure 8.4.</b> $\mu$ CT images indicating tibial shelf fracture in sheep implanted with (A) nHA-PCLUR composite and (B) the nHA-PEUR composite materials. (arrows indicate location of host bone fracture).....	166
<b>Figure 8.5.</b> $\mu$ CT images of tibial plateau defects 16 weeks post-implantation show interruption of host bone at the defect site in all groups and a resorption gap in 1 nHA-PCLUR specimen and both nHA-PEUR specimens.....	168
<b>Figure 8.6.</b> $\mu$ CT images of femoral plug defects 16 weeks post-implantation for one femur specimen from the (A) nHA-PCLUR, (B) nHA-PEUR, and (C) Norian clinical control groups.....	168
<b>Figure 8.7.</b> Synthesis of a thioketal triol.....	169
<b>Figure 8.8.</b> Representative histology figures from study presented in Chapter 6 indicating environment surrounding endochondral bone formation (single arrow) versus that surrounding intramembranous bone formation (double arrow).....	170

<b>Figure A1.</b> MTS setup for fatigue testing.....	188
<b>Figure A2.</b> Tuning setup for fatigue testing.....	191
<b>Figure A3.</b> Desired defect orientation for $\mu$ CT analysis.....	197
<b>Figure A4.</b> Schematic of AOI using script 231. The green circle (dotted line) is the defect diameter, the blue circle is the circle drawn during contouring. Program outputs bone parameters for colored rings.....	198



## NOMENCLATURE

AG	autograft	NCO	isocyanate
AOI	area of interest	nHA	nanocrystalline hydroxyapatite
ATR-FTIR	attenuated total reflectance Fourier transform infrared spectroscopy	NS	Nanostim™
		OH	hydroxyl
BCP	biphasic calcium phosphate	PCLUR	poly(caprolactone urethane)
BG	bioactive glass	PEG	poly(ethylene glycol)
BMP	bone morphogenetic protein	PEUR	poly(ester urethane)
β-TCP	β-tricalcium phosphate	PLF	posterolateral fusion
BV/TV	bone volume/total volume	PLGA	poly(lactide-co-glycolide)
BVF	bone void filler	PMMA	poly(methyl methacrylate)
CaP	calcium phosphate	PTKUR	poly(thioketal urethane)
CPC	calcium phosphate cement	PUR	polyurethane
CT/μCT	computed tomography/micro- computed tomography	rhBMP-2	recombinant human bone morphogenetic protein-2
FDA	Food and Drug Administration	ROS	reactive oxygen species
FeAA	iron acetylacetonate	SEM	scanning electron microscopy
HA	hydroxyapatite	Tb. S.	trabecular spacing
IC/ICBG	iliac crest/iliac crest bone graft	Tb. Th.	trabecular thickness
IF	immunofluorescence	TFT	tack-free time
IHC	immunohistochemistry	TGF-β	transforming growth factor- beta
ITP	intertransverse process	TK	thioketal
LiAlH <sub>4</sub>	lithium aluminum hydride	VOI	volume of interest
LTI	lysine triisocyanate	WT	working time
MG	MASTERGRAFT		
MSC	mesenchymal stem cell		

## CHAPTER 1

### I. INTRODUCTION

Bone grafts are scaffold constructs required for the treatment of bone diseases and fracture when a defect is above a critical size to heal naturally.<sup>1</sup> Long bone non-unions, spinal fusion, tumor resection, dental and craniofacial applications, and screw augmentation are of the many conditions and treatment options that necessitate the 1.6 million bone grafting procedures performed annually in the United States.<sup>2,3</sup> Together these grafting procedures generate an estimated cost exceeding 2.5 billion US dollars per year.<sup>4</sup> Autograft (AG) bone is the gold standard in bone grafting since it is osteoinductive, osteoconductive, and osteogenic.<sup>5,6</sup> However, there are significant limitations in availability and donor site morbidity. Furthermore, the peri- and post-operative cost associated with autograft is greater than when graft substitutes are used.<sup>7</sup> Allograft bone graft is marketed as an alternative, but immune rejection and high failure rates preclude its use.<sup>8,9</sup> Synthetic bone grafts have evolved as a substitute for AG since they are relatively simple to manufacture, broadly available, and generally lower cost. The bone graft substitute market generates around 1 billion US dollars annually and the benefits associated with synthetic options, in particular, have led to an anticipated 15% annual growth rate.<sup>10</sup> Tissue engineering strategies aim to develop synthetic, biomaterial scaffolds to guide bone healing and achieve complete regeneration of the natural bone tissue. The ideal biomaterial for a regenerative bone graft will promote cellular proliferation and osteogenesis, degrade to non-toxic breakdown products at a rate that complements neotissue formation, and exhibit mechanical properties close to those of the innate bone tissue surrounding the implant. Ceramics, such as bioactive glasses,<sup>11</sup> calcium phosphate granules,<sup>12</sup> and injectable calcium phosphate cements,<sup>13</sup> have been used extensively for bone grafting due to their similarities in chemical composition to the mineral components in bone.

Polyurethanes (PURs) have been investigated as synthetic polymeric bone grafts. This family of materials can be formulated to be injectable and settable and have the advantages of tunable mechanical properties, controlled degradation into non-cytotoxic breakdown products, and local, diffusion-controlled release of biologics making them a promising candidate for bone tissue engineering scaffolds.<sup>14</sup> The Guelcher lab has successfully demonstrated lysine-based PURs promote osteogenesis and support remodeling *in vivo*.<sup>15-17</sup> Previous work has shown these lysine triisocyanate (LTI)-derived poly(ester urethane)s (PEURs) undergo autocatalytic hydrolytic degradation in which acidic breakdown products accelerate resorption.<sup>18,19</sup>

### 1.1. Specific Aims

The central goal of this work is to develop a lysine-based poly(thioketal urethane) (PTKUR) for a synthetic bone graft that degrades in the presence of reactive oxygen species (ROS) produced by the cells involved in healing but remains stable in hydrolytic conditions. This goal was achieved through the completion of the following aims:

**Aim I: *Fabricate a settable, cell-degradable poly(thioketal urethane) with cement-like properties.***

PTKURs have been shown to selectively degrade by ROS produced by cells involved in tissue healing. We propose a novel, low molecular weight thioketal (TK) crosslinker that can be used in the synthesis of a PTKUR that is mechanically robust and hydrolytically stable but degrades in the presence of ROS. We hypothesize that combining ceramic particles with the polymer will yield a moldable PTKUR composite that cures *in situ* with strengths exceeding those of trabecular bone. *To our knowledge, this will be the first ROS-degradable biomaterial for bone tissue engineering applications.*

**Aim II: *Develop poly(thioketal urethane) for application as a moldable, settable autograft extender.***

Autograft (AG) is the gold standard in bone grafting since it is osteogenic, osteoconductive, and

osteoinductive. The goal of this aim is to incorporate AG with cell-degradable PTKUR for an AG extender that can be molded in to the defect site to facilitate implantation and cure to a compression resistant AG extender. Furthermore, we hypothesize the AG necessary to maintain osteoinductivity may be minimized by the AG extender. *In vivo* studies will provide proof of concept that the PTKUR AG extender exhibits cellular infiltration and differentiation and maintains AG within the defect space. The AG extender will then be evaluated in the mechanically and biologically challenging environment of a spine model and the lead candidate will be implanted in a rabbit radius model.

**Aim III: Augment poly(thioketal urethane) for accelerated integration with the host bone and optimal mechanical properties for potential in weight-bearing applications.**

Previous work in our lab has proven the potential for lysine-based polyurethane/ceramic composites in weight-bearing defects; however, resorption gaps and biomaterial/host bone mechanical mismatch *in vivo* are major limitations of current formulations. The objective of Aim 3 is to synthesize a nanocrystalline hydroxyapatite (nHA)-PTKUR ceramic hybrid polymer. This material is hypothesized to have augmented mechanical properties to allow for incorporation of some porosity without sacrificing material mechanics. Porosity will be introduced to accelerate infiltration and peripheral remodeling. After selection of an appropriate porogen, effects of porogen loading on mechanical properties will be investigated. Lead candidate materials will be tested in a non-weight bearing rabbit femoral condyle plug defect model and remodeling investigated up to 18 months post-implantation. Conclusions from this aim will dictate implantation in a weight-bearing model in a large animal.

**1.2. Approach**

**Chapter 1** of this work gives a brief introduction to bone tissue engineering approaches and the potential for PURs. In this chapter, PTKURs are briefly introduced and the goal of the

dissertation described. **Chapter 2** provides background information necessary to justify the approach of developing a cell-degradable tissue engineering bone graft. An overview of bone tissue engineering, requirements for an ideal bone graft, and currently available technology are presented, followed by discussion of the science involved in the development of a PTKUR for bone tissue engineering.

**Chapter 3** of this work develops a lysine-based PTKUR for a synthetic bone graft that degrades in the presence of ROS produced by the cells involved in healing but remains stable in hydrolytic conditions. Combining osteoconductive ceramic particles with the polymer yields a moldable PTKUR composite that cures *in situ* with mechanical properties exceeding those of trabecular bone. Degradation mechanisms and remodeling of the resulting PTKUR composite were evaluated in a lateral condyle defect model in rabbits. This cell-degradable PTKUR addresses the demands of a tissue engineering bone graft with inherent properties that can be adapted for use in a multitude of orthopedic applications and became the foundation of this work. In this chapter, **Aim I** of this dissertation is addressed.

The development of a cell-degradable PTKUR led to its use as an AG extender. AG substitutes have been studied extensively, but synthetic grafts alone do not match the osteogenic nature of AG. AG extenders have been proposed to combine the benefits of synthetic bone grafts with the osteogenicity of AG.<sup>20-28</sup> In **Chapter 4**, an injectable, settable PTKUR AG extender is formulated and remodeling assessed in a biologically and mechanically rigorous *in vivo* model. Histological evidence of cellular infiltration and new bone formation led to implementation in a more relevant long bone segmental defect model in the rabbit radius in **Chapter 5**. *Chapters 4 & 5 describe the first demonstration of an injectable/moldable, settable polymeric AG extender and collectively comprise Aim II* of this dissertation.

**Chapters 6** addresses the overall goal of **Aim III** to enhance early integration of the grafts with the host-bone and optimize mechanical properties of lysine-based PTKUR bone grafts for potential use in a weight-bearing defect. Currently available ceramic bone cements are generally brittle and lack the resilience necessary for a self-sustaining, weight-bearing graft.<sup>29</sup> Polymer/ceramic composites have emerged as an alternative to combine the mechanical attributes of both materials.<sup>30</sup> In Chapter 6, conclusions from work outside the scope of this dissertation are amassed to investigate the addition of a porogen to a nHA-PTKUR ceramic hybrid polymer to identify the optimal material properties for a settable bone void filler. First, nHA is incorporated in the structure of PTKUR and the material properties characterized. The addition of a porogen was hypothesized to enhance cellular infiltration and increase the surface area of the cell-degradable material to accelerate resorption and remodeling. Furthermore, nHA was expected to enhance overall activity of the cells involved in remodeling. Lead candidate composites were implanted in a non-weight-bearing, femoral plug defect in rabbits to eliminate initial mechanical challenges. This study was taken out to 18 months to investigate long-term remodeling. Results from this study are anticipated to lead to implantation in a large animal model.

Finally, **Chapter 7** summarizes the overall findings of this work and suggestions for future directions based on these conclusions are discussed in **Chapter 8**.

***This research strategy addresses the limitations of currently available synthetic bone grafts from biomaterial, biological, and mechanical perspectives.*** *These chapters build upon one another to culminate in a degradable biomaterial that balances osteoconductivity and osteoinductivity with biomaterial properties for optimal bone graft remodeling for a given implantation site.*

## References

1. Hollinger JO, Kleinschmidt JC. The Critical Size Defect as an Experimental Model To Test Bone Repair Materials. *Journal of Craniofacial Surgery* 1990;1(1):60-68.
2. O'Keefe RJ, Mao J. Bone tissue engineering and regeneration: from discovery to the clinic—an overview. *Tissue Engineering Part B: Reviews* 2011;17(6):389-392.
3. Robinson JL, Moglia RS, Stuebben MC, McEnery MAP, Cosgriff-Hernandez E. Achieving Interconnected Pore Architecture in Injectable PolyHIPEs for Bone Tissue Engineering. *Tissue Engineering Part A* 2014;20(5-6):1103-12.
4. Amini AR, Laurencin CT, Nukavarapu SP. Bone Tissue Engineering: Recent Advances and Challenges. *Critical reviews in biomedical engineering* 2012;40(5):363-408.
5. Albrektsson T, Johansson C. Osteoinduction, osteoconduction and osseointegration. *European Spine Journal* 2001;10(2):S96-S101.
6. Shafiei Z, Bigham AS, Dehghani SN, Torabi Nezhad S. Fresh cortical autograft versus fresh cortical allograft effects on experimental bone healing in rabbits: radiological, Histopathological and Biomechanical evaluation. *Cell and Tissue Banking* 2009;10(1):19-26.
7. Glassman SD, Carreon LY, Campbell MJ, Johnson JR, Puno RM, Djurasovic M, Dimar JR. The perioperative cost of Infuse bone graft in posterolateral lumbar spine fusion. *The Spine Journal* 2008;8(3):443-448.
8. Aponte-Tinao L, Ayerza M, Muscolo D, Farfalli G. What are the risk factors and management options for infection after reconstruction with massive bone allografts? *Clinical orthopaedics and related research* 2016;474(3):669-73.
9. Yu X, Tang X, Gohil SV, Laurencin CT. Biomaterials for Bone Regenerative Engineering. *Advanced Healthcare Materials* 2015:n/a-n/a.
10. Bohner M. Resorbable biomaterials as bone graft substitutes. *Materials Today* 2010;13(1):24-30.
11. Jones JR. Review of bioactive glass: from Hench to hybrids. *Acta Biomater* 2013;9(1):4457-86.
12. Jarcho M. Calcium phosphate ceramics as hard tissue prosthetics. *Clin. Orthop. Rel. Res.* 1981;157:259-277.
13. Bohner M. Design of ceramic-based cements and putties for bone graft substitution. *Eur Cell Mater* 2010;20:1-12.
14. Fernando S, McEnery M, Guelcher S. Polyurethanes for bone tissue engineering. *Advances in Polyurethane Biomaterials* 2016:481.
15. Dumas JE, Davis T, Holt GE, Yoshii T, Perrien DS, Nyman JS, Boyce T, Guelcher SA. Synthesis, characterization, and remodeling of weight-bearing allograft bone/polyurethane composites in the rabbit. *Acta Biomaterialia* 2010;6(7):2394-2406.
16. Dumas JE, Zienkiewicz K, Tanner SA, Prieto EM, Bhattacharyya S, Guelcher SA. Synthesis and characterization of an injectable allograft bone/polymer composite bone void filler with tunable mechanical properties. *Tissue Engineering Part A* 2010;16(8):2505-2518.
17. Page JM, Prieto EM, Dumas JE, Zienkiewicz KJ, Wenke JC, Brown-Baer P, Guelcher SA. Biocompatibility and chemical reaction kinetics of injectable, settable polyurethane/allograft bone biocomposites. *Acta biomaterialia* 2012;8(12):4405-4416.
18. Dumas JE, BrownBaer PB, Prieto EM, Guda T, Hale RG, Wenke JC, Guelcher SA. Injectable reactive biocomposites for bone healing in critical-size rabbit calvarial defects.

- Biomedical Materials 2012;7(2):024112.
19. Hafeman AE, Zienkiewicz KJ, Zachman AL, Sung H-J, Nanney LB, Davidson JM, Guelcher SA. Characterization of the degradation mechanisms of lysine-derived aliphatic poly(ester urethane) scaffolds. *Biomaterials* 2011;32(2):419-429.
  20. Dai L-Y, Jiang L-S. Single-level instrumented posterolateral fusion of lumbar spine with  $\beta$ -tricalcium phosphate versus autograft: a prospective, randomized study with 3-year follow-up. *Spine* 2008;33(12):1299-1304.
  21. Hile DD, Kandziora F, Lewandrowski K-U, Doherty SA, Kowaleski MP, Trantolo DJ. A poly(propylene glycol-co-fumaric acid) based bone graft extender for lumbar spinal fusion: in vivo assessment in a rabbit model. *European spine journal : official publication of the European Spine Society, the European Spinal Deformity Society, and the European Section of the Cervical Spine Research Society* 2006;15(6):936-943.
  22. Lee JH, Chang B-S, Jeung U-O, Park K-W, Kim M-S, Lee C-K. The first clinical trial of beta-calcium pyrophosphate as a novel bone graft extender in instrumented posterolateral lumbar fusion. *Clinics in orthopedic surgery* 2011;3(3):238-244.
  23. Lee JH, Hwang CJ, Song BW, Koo KH, Chang BS, Lee CK. A prospective consecutive study of instrumented posterolateral lumbar fusion using synthetic hydroxyapatite (Bongros®-HA) as a bone graft extender. *Journal of Biomedical Materials Research Part A* 2009;90(3):804-810.
  24. Lerner T, Bullmann V, Schulte TL, Schneider M, Liljenqvist U. A level-1 pilot study to evaluate of ultraporous  $\beta$ -tricalcium phosphate as a graft extender in the posterior correction of adolescent idiopathic scoliosis. *European Spine Journal* 2009;18(2):170-179.
  25. Lewandrowski K-U, Hile DD, Thompson BM, Wise DL, Tomford WW, Trantolo DJ. Quantitative measures of osteoinductivity of a porous poly (propylene fumarate) bone graft extender. *Tissue engineering* 2003;9(1):85-93.
  26. Linovitz RJ, Peppers TA. Use of an advanced formulation of  $\beta$ -tricalcium phosphate as a bone extender in interbody lumbar fusion. *Orthopedics* 2002;25(5):S585-S589.
  27. Smucker JD, Petersen EB, Fredericks DC. Assessment of MASTERGRAFT PUTTY as a graft extender in a rabbit posterolateral fusion model. *Spine* 2012;37(12):1017-1021.
  28. Walsh WR, Oliver RA, Gage G, Yu Y, Bell D, Bellemore J, Adkisson HD. Application of resorbable poly (lactide-co-glycolide) with entangled hyaluronic acid as an autograft extender for posterolateral intertransverse lumbar fusion in rabbits. *Tissue Engineering Part A* 2010;17(1-2):213-220.
  29. Bohner M. Design of ceramic-based cements and putties for bone graft substitution. *Eur Cell Mater* 2010;20(1):3-10.
  30. Wagoner Johnson AJ, Herschler BA. A review of the mechanical behavior of CaP and CaP/polymer composites for applications in bone replacement and repair. *Acta Biomaterialia* 2011;7(1):16-30.



## CHAPTER 2

### II. BACKGROUND

#### **Adapted from:**

Fernando, S, **McEnery, M**, Guelcher, SA. "Polyurethanes for bone tissue engineering." *Advances in Polyurethane Biomaterials*, 2016, 481.

#### 2.1. Bone Tissue Engineering

Tissue engineering is the multidisciplinary science of combining natural and/or synthetic scaffolds with exogenous or local cells and biologics for the regeneration of native tissue.<sup>1,2</sup> Although the concept of regenerating a patient's natural tissue has been considered for centuries, the discipline of tissue engineering emerged in the late 1980s and transformed into the interpretation we now appreciate in the early 1990s.<sup>3,4</sup> More recently, from 2012 to 2014, nearly \$3 billion in federal funding was invested in the field of regenerative medicine which includes tissue engineering.<sup>5</sup> Tissue engineering strategies are currently being investigated for soft and hard tissue applications including vasculature,<sup>6</sup> skin,<sup>7-9</sup> muscle,<sup>10</sup> ligaments,<sup>11</sup> cartilage,<sup>12</sup> and bone.<sup>12-20</sup> Bone tissue engineering is of significant interest in the field of regenerative medicine given the numerous indications to which it can be applied. Bone is constantly remodeling through an infinite cycle of osteoclastic breakdown and osteoblastic bone formation. Given this dynamic state, small fractures can heal independently.<sup>21</sup> However, defects larger than a critical size and those that necessitate guidance to heal correctly require intervention to support bone ingrowth.<sup>22,23</sup> Examples of indications for bone grafts include trauma, non-union fractures, bone voids (ie. following tumor resection), implant fixation, craniomaxillofacial defects, dental implantation, sinus augmentation, and spinal fusion. Depending on the defect and patient conditions, autograft and allograft may be insufficient for complete healing. Synthetic bone substitutes have been introduced as an alternative. Non-resorbable poly(methyl methacrylate)

(PMMA)-based bone cements are the most commonly used synthetic bone grafts used in the clinic due to their high strength and desirable handling properties. While considered one of the “most enduring materials in orthopedic surgery,” the bioinert nature of the material and mechanical mismatch hinder bony ingrowth and can lead to stress shielding and subsequent tissue damage or implant loosening.<sup>24,25</sup> Titanium meshes and cages are used to provide structural support and maintain graft placement (ie. fractures, spinal fusion procedures, and autograft implantation following bone atrophy or preceding dental implantation).<sup>26-29</sup> However, these meshes do not remodel and may require an invasive follow-up procedure for removal after new bone has filled the void.<sup>30</sup>

The goal of bone tissue engineering is to replace these strategies with materials that match the physical, chemical, and mechanical properties of the host tissue to induce an osteogenic niche and biomimetic mechanical environment<sup>31</sup> that promotes natural healing and remodeling. An ideal tissue engineering bone graft material is both osteoinductive and osteoconductive and maintains space throughout the remodeling process. In general, tissue engineering grafts comprise a non-toxic, biodegradable scaffold that is replaced by natural tissue as it is resorbed. An orchestrated combination of cell populations use the graft as a scaffold to support proliferation and differentiation and guide tissue regeneration by providing a substrate onto which new matrix can be deposited. These substrates can be designed for controlled release of drugs,<sup>32-34</sup> biologics,<sup>9,27,35-38</sup> or particles containing such cargo<sup>7,39</sup> for local delivery applications.<sup>40,41</sup> Furthermore, these scaffolds can be seeded with a variety of cell populations to “prime” the scaffold to initiate differentiation and proliferation *in vitro* and accelerate regeneration once implanted.<sup>42</sup> Alternatively, cells can be encapsulated in the biomaterial to mimic natural regeneration without requiring endogenous osteoprogenitors.<sup>2,43</sup>

Scaffolds are ideally designed to recapitulate the physical and mechanical properties of the tissue being regenerated. An interconnected porous architecture mimics that of trabecular (spongy) bone and allows for cellular infiltration along with nutrient and waste transport throughout the graft. Literature suggests a range of pore sizes from 100-900  $\mu\text{m}$  for optimal osteogenesis *in vivo*, with 100  $\mu\text{m}$  being the minimum suggested for adequate cellular infiltration.<sup>44-46</sup> Similarly, the overall porosity affects the rate of regeneration and vascularization. Together, porosity and pore size can dictate the mechanism of regeneration. Research to circumvent porosity requirements is currently underway for weight-bearing bone tissue engineering applications.

## 2.2 Biology of Bone Graft Remodeling

Bone graft remodeling follows a similar cellular response to the bone fracture healing cascade. The most common form of fracture healing, secondary, is initiated by the formation of a hematoma and a subsequent immune response characterized by an influx of neutrophils, B cells, T cells, and macrophages.<sup>47-49</sup> Pro-inflammatory M1 macrophages are initially crucial to fracture healing to remove necrotic tissue and enhance leukocyte infiltration. Polarization to the anti-inflammatory M2 macrophage phenotype terminates the inflammatory stage. M2 macrophages eventually release factors to stimulate angiogenesis and tissue remodeling.<sup>47,48</sup> Local and systemic mesenchymal stem cells (MSCs) are then recruited. Differentiation to chondrocytes and the presence of fibroblasts leads to an unmineralized, cartilaginous soft callus.<sup>21</sup> Hypertrophic chondrocytes release cytokines to promote angiogenesis.<sup>24</sup> Vascularization brings oxygen to the fracture site promoting MSC differentiation to bone forming osteoblasts.<sup>47</sup> Simultaneous chondrocyte apoptosis, callus breakdown by osteoclasts, and osteoblastic bone formation replace the soft callus with a hard callus.<sup>21</sup> Finally, the hard callus is remodeled by osteoclasts and

osteoblasts and MSCs differentiate to osteocytes that are surrounded by an organic, mineralized matrix.<sup>21,50</sup>

Both intramembranous and endochondral ossification are involved in fracture healing and both forms have been noted in bone graft remodeling.<sup>24,51-53</sup> Endochondral bone formation most closely resembles secondary fracture healing. MSCs proceed down the chondrogenic pathway; a cartilaginous callus is formed and then remodeled to bone.<sup>54,55</sup> Intramembranous bone formation describes the direct differentiation of MSCs to osteoblasts and the subsequent deposition of bone.<sup>55,56</sup> Literature has shown that the mechanical environment surrounding a fracture or implant plays a significant role in determining which route of bone formation will ensue. In a stabilized fracture, little cartilaginous tissue was produced but a non-stabilized fracture produced a soft callus made up of cartilaginous tissue.<sup>57</sup> MSC differentiation to the chondrocyte lineage can also be promoted by the availability of oxygen to the remodeling site. Chondrogenesis thrives in hypoxic conditions whereas osteogenesis is more likely to occur in oxygenated tissue.<sup>51,58</sup> Growth factors surrounding the site of tissue healing also influence the route of osteogenesis.<sup>35,59</sup> These will be described in detail in section 2.5.

Creeping substitution describes a remodeling mechanism in which bone grafts are replaced by new bone (accompanied by vascularization) as they are resorbed by osteoclasts and remodeling progresses toward the interior of the graft. Osteoclastic breakdown and osteoblastic bone formation take place concurrently.<sup>60-62</sup> Alternatively, reverse creeping substitution refers to the osteoclastic breakdown of graft followed by subsequent bone formation. This process is generally the mechanism of dense, cortical autograft remodeling.<sup>63</sup> Both processes have been demonstrated in the remodeling of synthetic bone grafts.<sup>52,62,64-66</sup> Furthermore, literature has shown that remodeling of synthetic bone grafts involves the orchestration of many different cell

types and can incorporate one or many of the aforementioned remodeling mechanisms.<sup>67</sup>

## 2.2. Bone Grafts

When discussing materials used for regenerative bone grafts, it is important to describe the categories of materials that are generally used for bone tissue regeneration. These categories are briefly reviewed below.

*2.2.1 Bone void fillers.* Bone void fillers (BVs) are used to promote more reproducible healing of metaphyseal bone defects. BVs are designed to fill a large bone void and provide an osteoconductive scaffold for new bone formation, thereby preventing failure of fixation, supporting alignment of bone articulating surfaces, and preventing formation of fibrous tissue (scarring).<sup>68</sup> In contrast to bone cements, BVs do not require bone-like strength, and therefore are used in non-load-bearing metaphyseal bone defects. Materials used for BVs include autograft (AG) bone, allograft bone (including demineralized bone matrix), ceramics, natural and synthetic polymers, and composites of two or more of these materials.

AG is considered the gold standard since it is osteoconductive, osteoinductive, and mitigates the risk of immune rejection.<sup>69-72</sup> AG is generally harvested from the patients' iliac crest or local AG can be used depending on the indication.<sup>73-77</sup> Therefore, quantity is limited and AG harvesting is associated with donor site morbidity and prolonged surgery times.<sup>72,78</sup> Furthermore, AG lacks mechanical integrity and space maintenance capabilities.<sup>79</sup> AG extenders comprise a combination of AG and one or more of the other BVs listed above.<sup>18</sup> AG extenders will be discussed further in Section 2.5. Allograft bone harvested from a human cadaver can be used to avoid limitations in quantity and patient morbidity; however, immune rejection and high failure rates resulting from diminished osteogenicity limit its use as a BVF.<sup>58,80-82</sup>

Ceramic BVs are the most commonly used synthetic BVF and include calcium sulfate

(plaster of Paris), a family of calcium phosphates (CaPs), and bioactive glasses that can be used in particulate or in an injectable and settable form discussed in the following section. Ceramics are generally osteoconductive but associated with brittle mechanical properties and slow resorption.<sup>24,83</sup> Calcium sulfate is osteoconductive and low-cost, but accelerated resorption and a non-porous structure make it a less desirable option for a BVF.<sup>24</sup> CaP BVFs primarily include hydroxyapatite (HA,  $\text{Ca}_5(\text{PO}_4)_3\text{OH}$ ),  $\beta$ -tricalcium phosphate ( $\beta$ -TCP,  $\text{Ca}_3(\text{PO}_4)_2$ ), and biphasic calcium phosphate (BCP) that comprises a combination of HA and  $\beta$ -TCP.<sup>24</sup> HA makes up the majority of the mineral content of bone.<sup>84</sup> The similarity in chemical makeup to that of bone and high porosity make HA the most widely used CaP since it is osteoconductive and integrates well with the host-bone.<sup>85</sup> HA is often blended with a second phase for a composite BVF to address limitations of brittle and weak mechanical properties. HA has been added to natural and synthetic polymers to combine the osteogenic properties of HA with the ductile properties of polymeric materials such as PURs,<sup>33,86-91</sup> PLGA,<sup>92</sup> methacrylates,<sup>20,93</sup> and collagen<sup>92,94</sup> to name a few.<sup>95,96</sup> HA carbon nanotube composites have also been proposed to add strength to HA.<sup>24</sup> The development of nanocrystalline HA (nHA) BVFs has led to enhanced osteoclast differentiation and thus accelerated resorption and increased new bone formation.<sup>24,88,97</sup> Furthermore, the surface hydroxyl (OH) groups of HA potentiate surface grafting of organic molecules to enhance dispersion in organic polymers for enhanced mechanical and biological properties of hybrid polymer/ceramic composites.<sup>97-100</sup>  $\beta$ -TCP is similarly highly osteoconductive, but is generally more porous than HA and resorbs more rapidly.<sup>82,85,101</sup> Medtronic markets Food and Drug Administration (FDA) approved BVF, MASTERGRAFT (MG), a BCP available in granular and putty forms that consists of 85%  $\beta$ -TCP and 15% HA. MG has been shown to achieve balanced remodeling and new bone formation *in vivo* when used in its neat state or added to PUR for a

PUR/MG composite.<sup>27,62,102,103</sup>

Bioactive glass is a silica-based bone graft that has demonstrated strong bonding to the host-bone and actively remodels to form new bone. Dissolution of bioactive glass in physiological fluids releases soluble silica and calcium ions that initiate a cellular response for bone remodeling. A hydroxycarbonate apatite layer is formed on the glass surface which promotes integration with the host bone.<sup>24,104-106</sup> 45S5 bioactive glass is commercially available and one of the most commonly used formulations (composed of 46.1 mol% SiO<sub>2</sub>, 24.4 mol% Na<sub>2</sub>O, 26.9 mol% CaO, and 2.6 mol% P<sub>2</sub>O<sub>5</sub>). Like other ceramics, bioactive glass is often implanted as a composite.<sup>104,107-111</sup> Functionalization of the bioactive glass surface allows for surface grafting of proteins such as BMP-2 for additional bioactivity and controlled protein delivery<sup>112</sup> or organic molecules like  $\epsilon$ -caprolactone to improve the mechanical properties of bioactive glass/polymer hybrids.<sup>104</sup>

*2.2.2 Weight-bearing bone cements.* Bone cements are used for metaphyseal bone defects where the mechanical forces that the graft will be subjected to require bone-like strength. Intra-articular fractures generally involve a weight-bearing joint and require internal and external fixation to maintain articular congruence and mitigate the loss of reduction.<sup>113,114</sup> Furthermore, patient non-compliance during recovery has led to the failure of 25% of severe tibial plateau fractures.<sup>115</sup> Regions of the spine are also load bearing and special consideration must be taken when selecting a bone graft for various fusion applications.<sup>70</sup> Calcium phosphate cements (CPCs) have been reported to be superior to autograft for reconstruction of weight-bearing tibial plateau fractures and required minimal fixation.<sup>116,117</sup> However, the risk of micro-crack formation and resorption gaps have led to its contraindication as a weight-bearing bone graft.<sup>60,108,118</sup> Non-resorbable PMMA cements are frequently used in hip replacements and spine applications to

stabilize vertebral fractures by vertebroplasty.<sup>119,120</sup> The compressive strength of PMMA (70 – 90 MPa) serves as a baseline for mechanical properties required for weight-bearing bone grafts.<sup>97,118,121,122</sup> Tissue engineering approaches aim to replace these synthetic biomaterials with resorbable bone grafts that will stabilize the defect throughout remodeling and require minimal fixation. An ideal weight-bearing bone graft will allow for early load-bearing to reduce complications associated with patient non-compliance.<sup>115,118</sup> This will require a graft that rapidly achieves bone-like mechanical properties and resorbs as it is replaced by bone to maintain osseous integrity.<sup>108</sup>

*2.2.3 Settable tissue engineering bone grafts.* Injectable and settable bone grafts can space-fill irregularly shaped defects and enhance early integration with the native bone. Furthermore, implantation via a blunted syringe or by hand affords the potential for minimally invasive surgical techniques.<sup>123</sup> An injectable material ideally exhibits a viscosity that allows for controlled injection without filter-pressing or losing homogeneity (maximum of 100 N)<sup>83</sup> and shear thinning properties aid in delivery as well. Settable materials must exhibit clinically relevant working times (~10 minutes) and setting times of 10-15 minutes.<sup>52,83</sup> The heat of reaction through setting must be low enough to maintain viability of host cells. Many polymerization reactions are exothermic and contact with temperatures  $\geq 50$  °C for  $\geq 1$  minute can cause tissue necrosis.<sup>25,124</sup>

The graft design must consider cellular infiltration and the transport of nutrients and waste throughout the grafted site. Furthermore, a successful graft will degrade at a rate that complements the rate of cellular infiltration and new tissue generation.<sup>125</sup> Premature degradation may lead to the formation of scar tissue, and an over stable material may hinder cellular infiltration and prevent remodeling.<sup>126</sup> Requirements for mechanical properties are of significant



importance in orthopedic applications and must be tailored to match the defect site and the tissue being replaced.<sup>15</sup> For example, literature has reported a bulk modulus of 1 MPa as the lower limit for compression-resistance in the mandibular ridge.<sup>27</sup> Cancellous bone is reported to have a compressive strength of 5-10 MPa and modulus of 50-400 MPa, thus depending on the defect site, a settable bone graft should ideally cure to mechanical properties within this range.<sup>14,46,127</sup>

Currently available polymeric settable bone grafts, like PMMA provide the strength necessary for orthopedic applications;<sup>122</sup> however, these do not degrade and integration is limited. Injectable polyurethane (PUR) foams<sup>27,39,52,62,65,100,128-132</sup> and moldable PUR cements<sup>97,108,118,133</sup> have been studied extensively for bone tissue engineering applications. PURs will be discussed in detail in the following sections. Propylene fumarate dimethacrylate polymeric foams are also being investigated as settable bone grafts that promote osteogenic differentiation *in vitro*.<sup>20,134-136</sup> The majority of commercially available injectable bone grafts are ceramic in nature.<sup>60,83</sup> CaPs in particular are attractive since they are very osteoconductive but brittle mechanical properties and slow resorption limit the applications in which the material is favorable. Settable polymer/ceramic composites combine the ductility of polymers with the strength of ceramics;<sup>85</sup> however, balancing porosity and mechanical properties remains a challenge. *There is a clinical need for a resorbable, osteoconductive, settable bone cement that provides the mechanical properties necessary for weight-bearing orthopedic applications and remodels at a rate comparable to the gold standard.*

### 2.3. Polyurethanes in Bone Tissue Engineering

*2.3.1 Chemistry of polyurethane bone grafts.* The chemistry of polyurethane scaffolds for tissue regeneration has been reviewed.<sup>13,137</sup> PUR linkages are characterized by  $\text{-NHC=OOR-}$  and can be derived from a number of raw materials for a range of applications. In this section, PUR

chemistry relevant to orthopedic scaffolds will be presented.

*Polyisocyanates.* Polyisocyanates are characterized by multiple  $-N=C=O$  functionality and react with polyalcohols (polyols), polyamines, or water to form urethane or urea ( $-RNHC=ONHR'-$ ) linkages. Their chemistry has been extensively reviewed.<sup>138,139</sup> The reactions with polyols and polyamines are known as the gelling reaction, since the two liquid components react to form a solid crosslinked polymer. The water (blowing) reaction is important for the synthesis of PUR foams, where carbon dioxide gas functions as a biocompatible blowing agent. While carboxylic acids, ureas, urethanes, and amides also react with isocyanates, these reactions are generally much slower and not as important for the synthesis of PUR bone grafts. The choice of polyisocyanate can dramatically impact the degradation and mechanical properties of the resulting graft. PUR bone grafts are most frequently synthesized from either lysine- or hexamethylene-derived aliphatic polyisocyanates due to toxicity concerns associated with aromatic polyisocyanates.<sup>13,132,140,141</sup> Lysine triisocyanate (LTI)-derived PURs demonstrate higher mechanical properties and slower resorption compared to lysine diisocyanate (LDI)-derived, as anticipated for the different functionalities.<sup>142</sup> Hexamethylene diisocyanate (HDI) has also been used but slow to negligible resorption was reported.<sup>132,143</sup> Finally, diphenyl diisocyanate (MDI),<sup>144,145</sup> and butane-based isocyanates<sup>146</sup> have also been used in the synthesis of biodegradable PUR bone grafts.

*Polyols.* Polyols are multi-functional alcohols that generally comprise a polyether, polyester, or polycarbonate backbone. They are typically viscous liquids with molecular weights ranging from 200 – 5,000 g/mol. The polyol component of the polyurethane significantly affects the degradation rate of the final cured PUR. Typically, the rate of hydrolytic degradation of polyols observes the order polycarbonate < polyether < polyester. Furthermore, the molecular

weight and functionality can impact the mechanical properties of the resulting PUR. In general, high molecular weight polyols lead to a weaker PUR and higher functionality lends stronger mechanical properties.

*Prepolymers.* Prepolymers are frequently used in injectable two-component systems to improve handling properties and reduce toxicity. Isocyanate-terminated prepolymers are prepared by reacting an excess of a polyisocyanate with a polyol at 60 – 90 °C with or without a urethane catalyst, such as dibutyltin dilaurate. Although a prepolymer is defined as having an NCO:OH molar ratio of 2:1, quasi-prepolymers with a range of functionalities are often used. By varying the molar ratio of polyisocyanate:polyol, prepolymers with targeted free NCO content and average molecular weight, and desired handling properties can be prepared. The NCO content of prepolymers typically ranges from 5 – 25 wt-%, while less viscous quasi-prepolymers typically have NCO content exceeding 25%.<sup>139</sup>

*Reactive liquid molding.* Two-component PURs can be fabricated by reactive liquid molding, a process in which a polyisocyanate or isocyanate functional prepolymer is mixed with a polyol and either injected *in situ* or cast into a mold. The reactive liquid mixture cures after injection to form a solid scaffold. Water can be included as a blowing agent to generate carbon dioxide gas and consequently form pores.<sup>147,148</sup> To enhance the osteoconductivity and mechanical properties of the scaffolds, allograft bone,<sup>149-151</sup> bioactive glass,<sup>111,152</sup> or ceramic<sup>153</sup> particles can be added to the reactive PUR liquid. Segmented PUR elastomers, crosslinked cast elastomers, porous crosslinked foams, and crosslinked PUR/ceramic composites can be processed by reactive liquid molding. If the extent of chemical crosslinking is sufficiently high (functionality > 2), then the material is an insoluble thermoset. Triols and hexols, as well as low molecular weight triol and triamine crosslinkers, are commonly used to prepare chemically

crosslinked PURs.<sup>138</sup>

**2.3.2 Polyurethanes for orthopedic applications.** PURs are an attractive material for use in bone grafting applications such as BVFs, bone cements, and osteoconductive scaffolds due to their tunability.<sup>13</sup> These materials offer the necessary handling properties for injectability and moldability.<sup>123,154</sup> Furthermore, mechanical properties and degradation rates are easily altered to match the demands of the implantation site by altering the PUR chemistry. For example, PUR bone grafts have demonstrated strengths ranging from 40 kPa for foams<sup>155</sup> and up to 190 MPa for cements and moduli from the kPa to GPa range.<sup>123,132,140</sup> The isocyanate-water reaction produces carbon dioxide gas which has been utilized for the formation of porosity and modulation of mechanical properties in gas blown bone tissue engineering scaffolds that foam *in situ*.<sup>132,150,156</sup> The isocyanate-polyol reaction offers the flexibility of forming solid scaffolds or porous foams depending on the catalyst and water can be added to dictate scaffold porosity. Isocyanate functional prepolymers are also frequently used in the synthesis of PUR bone grafts to further optimize reactivity and handling properties.<sup>157</sup> By adjusting the functionality of the precursor materials, the extent of crosslinking (and therefore, the resulting polymer properties) can be tuned for the desired application. Recent work aimed to enhance the osteoconductivity of polyurethane scaffolds has focused on incorporating calcium phosphate ceramic particles<sup>123</sup>, bioactive glass<sup>104,111</sup>, and allograft<sup>65,158</sup> for PUR composites. Furthermore, mechanical properties and cellular activity are enhanced when nanocrystalline hydroxyapatite (nHA) is incorporated in the structure of the PUR.<sup>97,100,118</sup> While previous work has proven the benefits of using PURs in orthopedic applications, current strategies have yet to meet the desired balance of resorption and remodeling required for expanding their utility to more demanding implantation sites.

## 2.4. Oxidatively Degradable Biomaterial Scaffolds

As described in preceding sections, the endogenous bone healing cascade begins with hematoma formation that initiates an immune response and the release of pro-inflammatory factors<sup>47</sup>. The hematoma is replaced by a soft callus and the generation of woven, mineralized bone follows.<sup>49</sup> Cells involved in the inflammatory phase have been shown to produce free radicals referred to as reactive oxygen species (ROS).<sup>159,160</sup> Hydroxyl radicals (OH), hydrogen peroxides (H<sub>2</sub>O<sub>2</sub>), peroxynitrites (ONOO<sup>-</sup>), and superoxides (O<sub>2</sub><sup>-</sup>) are examples of cellularly produced ROS.<sup>161</sup> A subclass of environmentally responsive polymers has recently been under investigation to take advantage of the oxidative environment surrounding disease and tissue injuries. In the scope of bone grafting, oxidatively degradable biomaterials are anticipated to degrade in response to ROS produced by inflammatory cells and osteoclasts involved in the bone healing cascade.<sup>162</sup>

Thioketal (TK) bonds are cleaved by ROS leading to chain scission of TK-based polymers.<sup>162</sup> This degradation mechanism has compelled the development of polythioketals (PTKs) for targeted drug and biologic delivery and the chemistry has recently been implemented for scaffold based delivery.<sup>7,161,163,164</sup> Poly(ether-), poly(ester-), and poly(carbonate urethanes) have all been shown to be susceptible to oxidation to some extent.<sup>132,145</sup> Combining the material properties of TKs and PURs offers an appealing strategy for controlling degradation in tissue engineering applications. A PTKUR foam formulated with a 1000 g mol<sup>-1</sup> TK diol degraded in oxidative conditions and supported tissue regeneration in a subcutaneous wound.<sup>143</sup> However, the molecular weight of this TK diol limited mechanical properties of the resulting PTKUR and bone-like strength was not achieved. A low molecular weight TK diol crosslinker would allow for the synthesis of a mechanically robust PTKUR that exploits the benefits of an ROS-degradable biomaterial for bone tissue engineering applications.

## 2.5. Strategies to Confer Osteoinductivity

*2.5.1 Biologics.* Osteoconductive scaffolds provide a platform on which cells can proliferate and new bone can form but do not directly guide osteogenesis.<sup>82</sup> Some large defects or defects located in less biologically active sites may require osteoinductive factors to initiate bone formation and stimulate osteoblastic differentiation. Augmenting polymeric biomaterials with biologics like bone morphogenetic protein (BMP) has been heavily investigated to add osteoinductivity to bone tissue engineering grafts.<sup>27,39,165</sup> Urist is credited with the discovery of a morphogenetic growth factor that induced bone formation that was later determined a family of BMPs that belong to a superfamily – transforming growth factor-beta (TGF- $\beta$ ).<sup>166-168</sup> BMPs have been shown to promote osteoblast differentiation and proliferation during bone regeneration.<sup>169</sup> Of these, BMP-2 and BMP-7 (osteogenic protein-1, OP-1) have been shown to be most effective and are of greatest interest in bone tissue engineering.<sup>170-172</sup> These promising results led to the FDA approval of rhBMP-2 for posterolateral spinal fusion, tibial fractures, and sinus and alveolar ridge augmentation (INFUSE<sup>®</sup>, Medtronic Spinal and Biologics, Memphis, TN) and BMP-7 for revision posterolateral lumbar fusion. However, off-label use and side effects like swelling, ectopic bone formation, and carcinogenic risks have steered researchers to other options.<sup>36,173-178</sup> To circumvent risks associated with a bolus release of BMPs, literature has demonstrated release of BMP-2 from PUR grafts can be controlled by the incorporation of BMP containing microspheres<sup>39</sup> or by altering material properties like porosity or degradation rate.<sup>27,179</sup>

RGD peptide (arginine-glycine-aspartic acid) has been studied extensively as a biologic biomaterial surface modification to enhance cellular attachment and accelerate vascularization.<sup>82,180</sup> Increasing the concentration of RGD covalently incorporated in a

poly(ethylene glycol) diacrylate has been shown to significantly increase expression of bone-related markers<sup>181</sup> and PMMA with covalently bound RGD demonstrated binding of osteoblasts *in vitro* and accelerated integration with the host-bone *in vivo*.<sup>182</sup> RGD-functionalized PEG hydrogels stimulated osteoblastic bone formation<sup>183</sup> and an increase in cell spreading was observed for a propylene fumarate dimethacrylate polyHIPE bone grafts with RGD peptide at the pore surface *in vitro*.<sup>184,185</sup> Literature presents methods for covalently binding RGD peptide to the PUR backbone exploiting the potential to incorporate RGD in a PUR bone graft.<sup>186</sup> While lysine-based PURs alone have been shown to support cell attachment,<sup>142</sup> addition of RGD may accelerate differentiation.

**2.5.2 Cell-Based Strategies.** Encapsulation of cells within biomaterial bone scaffolds has been explored to accelerate integration and remodeling and to promote healing. Mesenchymal stem cells are an attractive cell-type for these materials since they are capable of maintaining pluripotency during proliferation and given their multilineage differentiation potential.<sup>2</sup> Alternatively, differentiated osteoblasts can be encapsulated to accelerate bone formation *in vivo*.<sup>183</sup> Maintaining cell viability is the biggest challenge for translation of cellularized scaffolds. The graft material must exhibit porosity and interconnectivity for transport of cell nutrients and waste. Cell delivery from hydrophobic materials, like PURs, is limited since aqueous nutrients are more readily transported through hydrophilic materials. Furthermore, reaction by-products like CO<sub>2</sub> and the heat of reaction must also be considered for bone grafts that cure *in situ*.<sup>43,158</sup> To address concerns of cell viability, a settable PUR was fabricated with cells encapsulated in cell-shielding, partially oxidized alginate beads that readily degrade *in vivo* after the PUR reaction takes place.<sup>43</sup> A similar approach was investigated for CPCs.<sup>187,188</sup> Poly(ethylene glycol) (PEG) offers another material attractive for use in cell delivery given the mild reaction conditions and

preferential biocompatibility; however, hydrogels do not exhibit the mechanical properties necessary for orthopedic applications.<sup>189</sup>

*2.5.3 Autograft.* To avoid the concerns associated with biologics, strategies to exploit the osteoinductivity of the gold standard are of significant interest to the field. Ceramic<sup>102,103,176,190-193</sup> and polymeric<sup>18,194,195</sup> materials have been investigated as AG extenders to address volume concerns and to prolong the presence of AG at the site of healing. The wide range of properties discussed above make PUR biomaterials a superior candidate for use as a settable AG extender that is moldable and resorbable. A cell-mediated oxidative polymer degradation mechanism may enhance the rate of remodeling and new bone quality even further by shielding AG from premature resorption until cells have migrated (by means of cell-mediated polymer degradation) to the biologically active AG.

AG extenders have gained particular interest for PLF applications for the treatment of various spinal disorders since the complicated biology surrounding the site necessitates the highly osteoinductive factors found in AG to achieve fusion.<sup>69</sup> This procedure requires a large volume of AG to be explanted from a second surgical site (usually the iliac crest) and requires an invasive cage or device to contain AG at the fusion site and resist compression from the surrounding musculature. We propose a settable PTKUR AG extender would address the challenges of this environment by conveying mechanical integrity to the osteoinductive characteristics of AG. Furthermore, supplementing AG volume with an osteoconductive PTKUR/ceramic composite yields the potential to minimize AG volume and determine the absolute minimum AG required to convey osteoinductivity. This strategy may also permit the use of osteoinductive AG in defects previously thought too large for the AG volume available (ie. long bone defects).



## 2.6. In Vivo Investigation of Bone Tissue Engineering Constructs

Preclinical *in vivo* studies are necessary to demonstrate efficacy, biocompatibility, safety, and dose response of tissue engineering constructs. Unlike *in vitro* characterization, *in vivo* studies show the comprehensive tissue response which comprises the interactions and signaling of all cell types involved in the remodeling process. The animal model used depends on the construct, intended applications, and the hypothesis being tested. In choosing a species, the bone microarchitecture and physiology, cost, and animal maintenance should all be considered.<sup>196-198</sup> Animal age should be chosen for the desired rate of bone turnover and strength as bone quality and remodeling rate may be lower in older animals.<sup>197</sup> Furthermore, the micro- and macro-mechanical load to which the implant will be subjected should be taken into consideration.<sup>199</sup>

The FDA requires proof of efficacy in a minimum of one small animal model and one larger animal model.<sup>200</sup> Pearce, et al. provide an overview of the most commonly used animals in bone research in terms of bone structure, composition, and remodeling in relation to that of humans.<sup>197</sup> Rodent models are primarily used for initial proof of concept studies and are useful for tracking cellular activity and differentiation, especially over time.<sup>197,199</sup> The low cost and ease of handling allow for studies involving many replicates, time points, and sample groups. However, clinical translation is limited. Aside from rats, rabbits are used the most in orthopedics due to ease of handling, size, and cost. Rabbit bone is the least similar to humans out of the non-rodent animal models; however, the bones have similar strength, elastic modulus, and fracture toughness compared to humans.<sup>197,199</sup> Bone turnover and remodeling is faster in rabbits than for some other species, but they are prime candidates for preliminary screening of tissue engineering constructs.<sup>197</sup>

Larger animals are best for clinical translation given their similarity in bone size and body mass. Canines (purpose-bred beagles and coon hounds being the most reproducible), sheep,

goats, and pigs are the most utilized due to similarities in bone composition and biology to that of humans.<sup>197,198</sup> Canine bone most closely matches the biochemical makeup and fracture stress of humans although the remodeling rate is generally faster.<sup>197-200</sup> They are the most commonly used animal model for spinal fusion and have utility in craniomaxillofacial models despite public criticism of the use of companion animals in research. Non-human primates may be the most predictive of the biological response and clinical performance in humans given their closeness in species. However, primates are generally expensive, difficult to maintain, and responses vary greatly between species.<sup>198</sup> Pigs have similar healing capacity to humans but are seldom used because they are difficult to handle and maintain. Sheep and goats are attractive animals for investigating bone graft remodeling since they demonstrate similar remodeling patterns in response to bony implants.<sup>197</sup>

There are a number of different defects that can be adapted based on the material or implant of interest. Critical-sized segmental defects are very useful to monitor and compare healing and effects of bioactive factors (ie. antibiotics, growth factors, cell seeding) in diaphyseal bone.<sup>1,32,201,202</sup> Critical-sized defects are those that will not heal on their own and are generally 1.5-2 times the diameter of the bone in which the defect is made. The femur and tibia are commonly used for segmental defects.<sup>40,59</sup> Other bones like the radius, ulna, and metatarsals are attractive alternatives since they do not require fixation.<sup>16,198,201,202</sup> Cylindrical defects are a good model for temporal studies and for detecting differences in remodeling between material groups. These defects are often created in the highly vascularized metaphysis of long bones to encourage cellular infiltration and revascularization.<sup>198</sup> Intertransverse posterolateral fusion (PLF) models provide a biologically and mechanically challenging environment in which to investigate remodeling. This defect is often used as an initial proof of concept model in rabbits since their

spinal anatomy is similar to that of humans and the iliac crests are large enough to harvest for a control.<sup>199</sup> Canines, goat, sheep, and pigs may also be used to model fusion; however, these generally require fixation and the mechanical challenge will differ in quadrupeds compared to humans.<sup>198</sup> Craniomaxillofacial defects are used to model common indications and applications such as sinus augmentation, alveolar ridge augmentation for dental implants, and mandibular defects.<sup>27</sup> Calvarial defects are also useful for modeling scaffold performance since defect creation is reproducible and the empty defect challenges bone regeneration.<sup>52,198</sup>

Power calculations should be used to determine the number of animals required to achieve the desired significance when analyzing the results of preclinical studies. These calculations should be taken into account when choosing a model. Analysis methods include *in vivo* computed tomography (CT) and x-ray which allow for monitoring healing over time in the same animal. Fluorochrome injections provide another, more precise dynamic method to monitor temporal mineralization. Tetracyclines, calcein green, alizarin red, and xylenol orange are examples of the most commonly used fluorochromes.<sup>60,123,203</sup> These are injected subcutaneously and bind selectively to actively mineralizing tissue during the time of circulation (around 24 hours).<sup>204</sup> Specimen are fixed, embedded, and sectioned using standard un-decalcified histology methods (decalcification will dissolve the fluorochrome label) and the fluorochrome labels are detectable using fluorescent microscopy.<sup>204</sup> By injecting fluorochromes with different emission wavelengths at various times, one can monitor the progression of mineralization within the same subject.

Micro-computed tomography ( $\mu$ CT) analysis allows for qualitative and quantitative evaluation of preclinical studies. 2D and 3D reconstructions of mineralized tissue within the defects allow for visualization of remodeling. BV/TV (bone volume/total volume), Tb. S.

(trabecular spacing), and Tb. Th. (trabecular thickness) are common outputs that can be calculated within a specified volume of interest (VOI) to quantify bone quantity and quality. It should be noted that if the implant contains a mineralized component (ie. HA, tricalcium phosphate, etc.), distinguishing bone from implant may be difficult.

Histology can be performed on decalcified, paraffin embedded sections or un-decalcified, plastic embedded, ground sections. Although generally much thicker, the latter may be more appropriate for implants containing a calcium-based component that may not demineralize using general methods. Osteoblasts and osteoclast may also be more distinguishable from the bone surface when samples are embedded in a methacrylate-based resin.<sup>205</sup> Histological stains used in studies for bone tissue engineering constructs include trichrome stains (ie. Masson-Goldners, Sanderson's Rapid Bone Stain, Stevenel's Blue) which differentiate bone, cartilage, muscle, cell nuclei, and collagen depending on the chosen stain.<sup>27,52,65,104,133,206-208</sup> Safranin O/Fast Green is commonly used to detect cartilage and may be useful for interpreting healing mechanisms.<sup>165,209</sup> Hematoxylin and eosin (H&E) is a commonly used histological dye that distinguishes various cell features and phenotypes and toluidine blue and acid fuchsin can be used together to identify new bone.<sup>210</sup>

Immunohistochemistry (IHC) and immunofluorescence (IF) techniques can also be employed to identify the different types of cells involved in remodeling and to elucidate tissue types. IHC utilizes labels to visualize specific binding of selected antibodies with an antigen of interest that identifies a cell genotype, phenotype, or event.<sup>211</sup> A counterstain like hematoxylin may be used to localize positive binding. IF follows the same principles as IHC with the incorporation of a fluorescent label visualized using a fluorescent microscope. IHC and IF are most commonly performed in paraffin sections since these are very thin. However, methods have

been adapted for use in thick, ground, plastic sections.<sup>118</sup>

## References

1. NIH: National Institute Biomedical Imaging and Bioengineering, Tissue Engineering and Regenerative Medicine. Science Education. Volume 2017: NIH: National Institute of Biomedical Imaging and Bioengineering.
2. Bruder SP, Fox BS. Tissue Engineering of Bone: Cell Based Strategies. Clinical orthopaedics and related research 1999;367:S68-S83.
3. Vacanti CA. History of tissue engineering and a glimpse into its future. Tissue engineering 2006;12(5):1137-1142.
4. Cima LG, Vacanti JP, Vacanti C, Ingber D, Mooney D, Langer R. Tissue Engineering by Cell Transplantation Using Degradable Polymer Substrates. Journal of Biomechanical Engineering 1991;113(2):143-151.
5. Regenerative medicine: Federal investment, informationsharing, and challenges in an evolving field: United States Government Accountability Office; 2015. Report nr GAO-15-553.
6. Nerem RM, Seliktar D. Vascular tissue engineering. Annual review of biomedical engineering 2001;3(1):225-243.
7. Martin JR, Nelson CE, Gupta MK, Yu F, Sarett SM, Hocking KM, Pollins AC, Nanney LB, Davidson JM, Guelcher SA. Local Delivery of PHD2 siRNA from ROS-Degradable Scaffolds to Promote Diabetic Wound Healing. Advanced Healthcare Materials 2016.
8. Adolph EJ, Guo R, Pollins AC, Zienkiewicz K, Cardwell N, Davidson JM, Guelcher SA, Nanney LB. Injected biodegradable polyurethane scaffolds support tissue infiltration and delay wound contraction in a porcine excisional model. Journal of Biomedical Materials Research Part B: Applied Biomaterials 2015.
9. Li B, Davidson JM, Guelcher SA. The effect of the local delivery of platelet-derived growth factor from reactive two-component polyurethane scaffolds on the healing in rat skin excisional wounds. Biomaterials 2009;30(20):3486-3494.
10. Qazi TH, Mooney DJ, Pumberger M, Geissler S, Duda GN. Biomaterials based strategies for skeletal muscle tissue engineering: existing technologies and future trends. Biomaterials 2015;53:502-521.
11. Samavedi S, Horton CO, Guelcher SA, Goldstein AS, Whittington AR. Fabrication of a model continuously graded co-electrospun mesh for regeneration of the ligament–bone interface. Acta biomaterialia 2011;7(12):4131-4138.
12. Hutmacher DW. Scaffolds in tissue engineering bone and cartilage. Biomaterials 2000;21(24):2529-2543.
13. Guelcher SA. Biodegradable polyurethanes: synthesis and applications in regenerative medicine. Tissue Engineering Part B: Reviews 2008;14(1):3-17.
14. Fernando S, McEnery M, Guelcher S. Polyurethanes for bone tissue engineering. Advances in Polyurethane Biomaterials 2016:481.
15. Giannoudis PV, Dinopoulos H, Tsiridis E. Bone substitutes: an update. Injury 2005;36(3):S20-S27.
16. Guda T, Walker JA, Singleton BM, Hernandez JW, Son J-S, Kim S-G, Oh DS, Appleford MR, Ong JL, Wenke JC. Guided bone regeneration in long-bone defects with a structural hydroxyapatite graft and collagen membrane. Tissue Engineering Part A 2012;19(17-18):1879-1888.
17. Khan Y, Yaszemski MJ, Mikos AG, Laurencin CT. Tissue Engineering of Bone: Material and Matrix Considerations; 2008. 36-42 p.

18. Lewandrowski K-U, Hile DD, Thompson BM, Wise DL, Tomford WW, Trantolo DJ. Quantitative measures of osteoinductivity of a porous poly (propylene fumarate) bone graft extender. *Tissue engineering* 2003;9(1):85-93.
19. O'Keefe RJ, Mao J. Bone tissue engineering and regeneration: from discovery to the clinic—an overview. *Tissue Engineering Part B: Reviews* 2011;17(6):389-392.
20. Robinson JL, McEnery MA, Pearce H, Whitely ME, Munoz-Pinto DJ, Hahn MS, Li H, Sears NA, Cosgriff-Hernandez E. Osteoinductive PolyHIPE Foams as Injectable Bone Grafts. *Tissue Engineering Part A* 2016;22(5-6):403-414.
21. Einhorn TA, Gerstenfeld LC. Fracture healing: mechanisms and interventions. *Nature Reviews Rheumatology* 2015;11(1):45-54.
22. Hollinger JO, Kleinschmidt JC. The Critical Size Defect as an Experimental Model To Test Bone Repair Materials. *Journal of Craniofacial Surgery* 1990;1(1):60-68.
23. Schmitz JP, Hollinger JO. The critical size defect as an experimental model for craniomaxillofacial nonunions: WALTER REED ARMY MEDICAL CENTER WASHINGTON DC; 1985.
24. Wang W, Yeung KWK. Bone grafts and biomaterials substitutes for bone defect repair: A review. *Bioactive Materials* 2017.
25. Webb J, Spencer R. The role of polymethylmethacrylate bone cement in modern orthopaedic surgery. *Bone & Joint Journal* 2007;89(7):851-857.
26. Daubs MD. Early Failures Following Cervical Corpectomy Reconstruction With Titanium Mesh Cages and Anterior Plating. *Spine* 2005;30(12):1402-1406.
27. Talley AD, Kalpakci KN, Shimko DA, Zienkiewicz K, Cochran D, Guelcher S. Effects of rhBMP-2 Dose and Ceramic Composition on New Bone Formation and Space Maintenance in a Canine Mandibular Ridge Saddle Defect Model. *Tissue Engineering* 2016(ja).
28. von Arx T, Kurt B. Implant placement and simultaneous ridge augmentation using autogenous bone and a micro titanium mesh: a prospective clinical study with 20 implants. *Clinical oral implants research* 1999;10(1):24-33.
29. Volgas D, Dreger TK. The Use of Mesh Plates for Difficult Fractures of the Patella. *The journal of knee surgery* 2017;30(03):200-203.
30. Rakhmatia YD, Ayukawa Y, Furuhashi A, Koyano K. Current barrier membranes: Titanium mesh and other membranes for guided bone regeneration in dental applications. *Journal of Prosthodontic Research* 2013;57(1):3-14.
31. Nerem RM, Sambanis A. Tissue engineering: from biology to biological substitutes. *Tissue engineering* 1995;1(1):3-13.
32. Li B, Brown KV, Wenke JC, Guelcher SA. Sustained release of vancomycin from polyurethane scaffolds inhibits infection of bone wounds in a rat femoral segmental defect model. *Journal of Controlled Release* 2010;145(3):221-230.
33. Liu H, Zhang L, Shi P, Zou Q, Zuo Y, Li Y. Hydroxyapatite/polyurethane scaffold incorporated with drug-loaded ethyl cellulose microspheres for bone regeneration. *Journal of Biomedical Materials Research Part B: Applied Biomaterials* 2010;95B(1):36-46.
34. Yoshii T, Hafeman AE, Nyman JS, Esparza JM, Shinomiya K, Spengler DM, Mundy GR, Gutierrez GE, Guelcher SA. A sustained release of lovastatin from biodegradable, elastomeric polyurethane scaffolds for enhanced bone regeneration. *Tissue Engineering, Part A: Tissue Engineering* 2010;16:2369+.

35. Boden SD. Bioactive factors for bone tissue engineering. *Clinical orthopaedics and related research* 1999;367:S84-S94.
36. McKay WF, Peckham SM, Badura JM. A comprehensive clinical review of recombinant human bone morphogenetic protein-2 (INFUSE® Bone Graft). *International orthopaedics* 2007;31(6):729-734.
37. Patel JJ, Flanagan CL, Hollister S. Bone Morphogenetic Protein-2 Adsorption onto Poly- $\epsilon$ -caprolactone Better Preserves Bioactivity in vitro and Produces More Bone in vivo than Conjugation under Clinically Relevant Loading Scenarios. *Tissue Engineering* 2014(ja).
38. Rodríguez-Évora M, Delgado A, Reyes R, Hernández-Daranas A, Soriano I, San Román J, Evora C. Osteogenic effect of local, long versus short term BMP-2 delivery from a novel SPU-PLGA- $\beta$ TCP concentric system in a critical size defect in rats. *European Journal of Pharmaceutical Sciences* 2013;49(5):873-884.
39. Li B, Yoshii T, Hafeman AE, Nyman JS, Wenke JC, Guelcher SA. The effects of rhBMP-2 released from biodegradable polyurethane/microsphere composite scaffolds on new bone formation in rat femora. *Biomaterials* 2009;30(35):6768-6779.
40. Guelcher SA, Brown KV, Li B, Guda T, Lee B-H, Wenke JC. Dual-purpose bone grafts improve healing and reduce infection. *Journal of orthopaedic trauma* 2011;25(8):477-482.
41. Wenke JC, Guelcher SA. Dual delivery of an antibiotic and a growth factor addresses both the microbiological and biological challenges of contaminated bone fractures. *Expert opinion on drug delivery* 2011;8(12):1555-1569.
42. Rathbone C, Guda T, Singleton B, Oh D, Appleford M, Ong J, Wenke J. Effect of cell-seeded hydroxyapatite scaffolds on rabbit radius bone regeneration. *Journal of Biomedical Materials Research Part A* 2014;102(5):1458-1466.
43. Guo R, Ward CL, Davidson JM, Duvall CL, Wenke JC, Guelcher SA. A transient cell-shielding method for viable MSC delivery within hydrophobic scaffolds polymerized in situ. *Biomaterials* 2015;54:21-33.
44. Guo R, Lu S, Page JM, Merkel AR, Basu S, Sterling JA, Guelcher SA. Fabrication of 3D scaffolds with precisely controlled substrate modulus and pore size by templated-fused deposition modeling to direct osteogenic differentiation. *Advanced healthcare materials* 2015;4(12):1826-1832.
45. Hulbert S, Young F, Mathews R, Klawitter J, Talbert C, Stelling F. Potential of ceramic materials as permanently implantable skeletal prostheses. *Journal of Biomedical Materials Research Part A* 1970;4(3):433-456.
46. Karageorgiou V, Kaplan D. Porosity of 3D biomaterial scaffolds and osteogenesis. *Biomaterials* 2005;26(27):5474-5491.
47. Loi F, Córdova LA, Pajarinen J, Lin T-h, Yao Z, Goodman SB. Inflammation, fracture and bone repair. *Bone* 2016;86:119-130.
48. Schmidt-Bleek K, Schell H, Schulz N, Hoff P, Perka C, Buttgerit F, Volk H-D, Lienau J, Duda GN. Inflammatory phase of bone healing initiates the regenerative healing cascade. *Cell and tissue research* 2012;347(3):567-573.
49. Schmidt-Bleek K, Kwee BJ, Mooney DJ, Duda GN. Boon and bane of inflammation in bone tissue regeneration and its link with angiogenesis. *Tissue Engineering Part B: Reviews* 2015;21(4):354-364.
50. Bonewald LF. The amazing osteocyte. *Journal of bone and mineral research* 2011;26(2):229-238.



51. Dennis SC, Berkland CJ, Bonewald LF, Detamore MS. Endochondral Ossification for Enhancing Bone Regeneration: Converging Native Extracellular Matrix Biomaterials and Developmental Engineering In Vivo. *Tissue Engineering Part B: Reviews* 2014.
52. Dumas JE, BrownBaer PB, Prieto EM, Guda T, Hale RG, Wenke JC, Guelcher SA. Injectable reactive biocomposites for bone healing in critical-size rabbit calvarial defects. *Biomedical Materials* 2012;7(2):024112.
53. Schindeler A, Mills RJ, Bobynd JD, Little DG. Preclinical Models for Orthopedic Research and Bone Tissue Engineering. *Journal of Orthopaedic Research* 2017.
54. Akter F, Ibanez J. Chapter 8 - Bone and Cartilage Tissue Engineering. *Tissue Engineering Made Easy: Academic Press; 2016.* p 77-97.
55. Gilbert S. Osteogenesis: the development of bones. *Developmental biology* 2000;6.
56. Stricker S, Mundlos S. Chapter seven - FGF and ROR2 Receptor Tyrosine Kinase Signaling in Human Skeletal Development. In: Birchmeier C, editor. *Current Topics in Developmental Biology: Academic Press; 2011.* p 179-206.
57. Thompson Z, Miclau T, Hu D, Helms JA. A model for intramembranous ossification during fracture healing. *Journal of Orthopaedic Research* 2002;20(5):1091-1098.
58. Bornes TD, Jomha NM, Mulet-Sierra A, Adesida AB. Hypoxic culture of bone marrow-derived mesenchymal stromal stem cells differentially enhances in vitro chondrogenesis within cell-seeded collagen and hyaluronic acid porous scaffolds. *Stem cell research & therapy* 2015;6(1):84.
59. Brown KV, Li B, Guda T, Perrien DS, Guelcher SA, Wenke JC. Improving bone formation in a rat femur segmental defect by controlling bone morphogenetic protein-2 release. *Tissue Engineering Part A* 2011;17(13-14):1735-1746.
60. Gisep A, Wieling R, Bohner M, Matter S, Schneider E, Rahn B. Resorption patterns of calcium-phosphate cements in bone. *Journal of Biomedical Materials Research Part A* 2003;66(3):532-540.
61. McAllister BS, Haghighat K. Bone augmentation techniques. *Journal of periodontology* 2007;78(3):377-396.
62. Talley AD, McEnery MA, Kalpakci KN, Zienkiewicz KJ, Shimko DA, Guelcher SA. Remodeling of injectable, low-viscosity polymer/ceramic bone grafts in a sheep femoral defect model. *Journal of Biomedical Materials Research Part B: Applied Biomaterials* 2016.
63. Burchardt H. The biology of bone graft repair. *Clinical orthopaedics and related research* 1983;174:28-34.
64. Khan SN, Cammisa FP, Sandhu HS, Diwan AD, Girardi FP, Lane JM. The Biology of Bone Grafting. *Journal of the American Academy of Orthopaedic Surgeons* 2005;13(1):77-86.
65. Dumas JE, Davis T, Holt GE, Yoshii T, Perrien DS, Nyman JS, Boyce T, Guelcher SA. Synthesis, characterization, and remodeling of weight-bearing allograft bone/polyurethane composites in the rabbit. *Acta Biomaterialia* 2010;6(7):2394-2406.
66. Yoshii T, Dumas JE, Okawa A, Spengler DM, Guelcher SA. Synthesis, characterization of calcium phosphates/polyurethane composites for weight-bearing implants. *Journal of Biomedical Materials Research Part B: Applied Biomaterials* 2012;100(1):32-40.
67. Prieto EM, Talley AD, Gould NR, Zienkiewicz KJ, Drapeau SJ, Kalpakci KN, Guelcher SA. Effects of particle size and porosity on in vivo remodeling of settable allograft bone/polymer composites. *Journal of Biomedical Materials Research Part B: Applied*

- Biomaterials 2015;103(8):1641-1651.
68. Tay BK, Patel VV, Bradford DS. Calcium sulfate- and calcium phosphate-based bone substitutes. Mimicry of the mineral phase of bone. *Orthop Clin North Am* 1999;30(4):615-23.
  69. Boden SD. Biology of lumbar spine fusion and use of bone graft substitutes: present, future, and next generation. *Tissue engineering* 2000;6(4):383-399.
  70. Boden SD. Overview of the biology of lumbar spine fusion and principles for selecting a bone graft substitute. *Spine* 2002;27(16S):S26-S31.
  71. Dumic-Cule I, Pecina M, Jelic M, Jankolija M, Popek I, Grgurevic L, Vukicevic S. Biological aspects of segmental bone defects management. *International Orthopaedics* 2015:1-7.
  72. Rogers GF, Greene AK. Autogenous Bone Graft: Basic Science and Clinical Implications. *Journal of Craniofacial Surgery* 2012;23(1):323-327.
  73. Brugnami F, Caiazzo A, Leone C. Local intraoral autologous bone harvesting for dental implant treatment: alternative sources and criteria of choice. *The Keio journal of medicine* 2009;58(1):24-28.
  74. Chen W-J, Tsai T-T, Chen L-H, Niu C-C, Lai P-L, Fu T-S, McCarthy K. The fusion rate of calcium sulfate with local autograft bone compared with autologous iliac bone graft for instrumented short-segment spinal fusion. *Spine* 2005;30(20):2293-2297.
  75. Couture DE, Branch Jr CL. Posterior lumbar interbody fusion with bioabsorbable spacers and local autograft in a series of 27 patients. *Neurosurgical focus* 2004;16(3):1-6.
  76. Johansson L-Å, Isaksson S, Lindh C, Becktor JP, Sennerby L. Maxillary sinus floor augmentation and simultaneous implant placement using locally harvested autogenous bone chips and bone debris: a prospective clinical study. *Journal of Oral and Maxillofacial Surgery* 2010;68(4):837-844.
  77. Kanayama M, Hashimoto T, Shigenobu K, Oha F, Ishida T, Yamane S. Pitfalls of anterior cervical fusion using titanium mesh and local autograft. *Clinical Spine Surgery* 2003;16(6):513-518.
  78. Arrington ED, Smith WJ, Chambers HG, Bucknell AL, Davino NA. Complications of iliac crest bone graft harvesting. *Clinical orthopaedics and related research* 1996;329:300-309.
  79. Burkus JK, Heim SE, Gornet MF, Zdeblick TA. Is INFUSE bone graft superior to autograft bone? An integrated analysis of clinical trials using the LT-CAGE lumbar tapered fusion device. *Clinical Spine Surgery* 2003;16(2):113-122.
  80. Aponte-Tinao L, Ayerza M, Muscolo D, Farfalli G. What are the risk factors and management options for infection after reconstruction with massive bone allografts? *Clinical orthopaedics and related research* 2016;474(3):669-73.
  81. Shafiei Z, Bigham AS, Dehghani SN, Torabi Nezhad S. Fresh cortical autograft versus fresh cortical allograft effects on experimental bone healing in rabbits: radiological, Histopathological and Biomechanical evaluation. *Cell and Tissue Banking* 2009;10(1):19-26.
  82. Yu X, Tang X, Gohil SV, Laurencin CT. Biomaterials for Bone Regenerative Engineering. *Advanced Healthcare Materials* 2015:n/a-n/a.
  83. Bohner M. Design of ceramic-based cements and putties for bone graft substitution. *Eur Cell Mater* 2010;20(1):3-10.
  84. Clarke B. Normal bone anatomy and physiology. *Clinical journal of the American*

- Society of Nephrology 2008;3(Supplement 3):S131-S139.
85. Wagoner Johnson AJ, Herschler BA. A review of the mechanical behavior of CaP and CaP/polymer composites for applications in bone replacement and repair. *Acta Biomaterialia* 2011;7(1):16-30.
  86. Dong Z, Li Y, Zou Q. Degradation and biocompatibility of porous nano-hydroxyapatite/polyurethane composite scaffold for bone tissue engineering. *Applied Surface Science* 2009;255(12):6087-6091.
  87. Laschke MW, Strohe A, Menger MD, Alini M, Eglin D. In vitro and in vivo evaluation of a novel nanosize hydroxyapatite particles/poly(ester-urethane) composite scaffold for bone tissue engineering. *Acta Biomaterialia* 2010;6(6):2020-2027.
  88. Mi HY, Palumbo S, Jing X, Turng LS, Li WJ, Peng XF. Thermoplastic polyurethane/hydroxyapatite electrospun scaffolds for bone tissue engineering: effects of polymer properties and particle size. *Journal of Biomedical Materials Research Part B: Applied Biomaterials* 2014;102(7):1434-1444.
  89. Mi H-Y, Jing X, Salick MR, Cordie TM, Peng X-F, Turng L-S. Morphology, mechanical properties, and mineralization of rigid thermoplastic polyurethane/hydroxyapatite scaffolds for bone tissue applications: effects of fabrication approaches and hydroxyapatite size. *Journal of Materials Science* 2014;49(5):2324-2337.
  90. Sheikh FA, Kanjwal MA, Macossay J, Barakat NAM, Kim HY. A simple approach for synthesis, characterization and bioactivity of bovine bones to fabricate the polyurethane nanofiber containing hydroxyapatite nanoparticle. *Express Polymer Letters* 2012;6(1):41-53.
  91. Yang W, Both SK, Zuo Y, Birgani ZT, Habibovic P, Li Y, Jansen JA, Yang F. Biological evaluation of porous aliphatic polyurethane/hydroxyapatite composite scaffolds for bone tissue engineering. *Journal of Biomedical Materials Research Part A* 2014.
  92. Ngiam M, Liao S, Patil AJ, Cheng Z, Chan CK, Ramakrishna S. The fabrication of nano-hydroxyapatite on PLGA and PLGA/collagen nanofibrous composite scaffolds and their effects in osteoblastic behavior for bone tissue engineering. *Bone* 2009;45(1):4-16.
  93. Sa Y, Yu N, Wolke JG, Chanchareonsook N, Goh BT, Wang Y, Yang F, Jansen JA. Bone Response to Porous Poly (methyl methacrylate) Cement Loaded with Hydroxyapatite Particles in a Rabbit Mandibular Model. *Tissue Engineering Part C: Methods* 2017.
  94. Kushioka J, Kaito T, Makino T, Fujiwara H, Tsukazaki H, Takenaka S, Sakai Y, Yoshikawa H. Difference in the fusion rate and bone formation between artificial bone and iliac autograft inside an inter-body fusion cage—A comparison between porous hydroxyapatite/type 1 collagen composite and autologous iliac bone. *Journal of Orthopaedic Science* 2018.
  95. Cisneros-Pineda OG, Herrera Kao W, Loría-Bastarrachea MI, Veranes-Pantoja Y, Cauch-Rodríguez JV, Cervantes-Uc JM. Towards optimization of the silanization process of hydroxyapatite for its use in bone cement formulations. *Materials Science and Engineering: C* 2014;40(0):157-163.
  96. Sun F, Zhou H, Lee J. Various preparation methods of highly porous hydroxyapatite/polymer nanoscale biocomposites for bone regeneration. *Acta Biomaterialia* 2011;7(11):3813-3828.
  97. Lu S, McGough M, Rogers B, Wenke J, Shimko D, Guelcher S. Resorbable nanocomposites with bone-like strength and enhanced cellular activity. *Journal of*

- Materials Chemistry B 2017;5(22):4198-4206.
98. Cetina-Diaz SM, Chan-Chan LH, Vargas-Coronado RF, Cervantes-Uc JM, Quintana-Owen P, Paakinaho K, Kellomaki M, Di Silvio L, Deb S, Cauich-Rodriguez JV. Physicochemical characterization of segmented polyurethanes prepared with glutamine or ascorbic acid as chain extenders and their hydroxyapatite composites. *Journal of Materials Chemistry B* 2014;2(14):1966-1976.
  99. Tetteh G, Khan AS, Delaine-Smith RM, Reilly GC, Rehman IU. Electrospun polyurethane/hydroxyapatite bioactive Scaffolds for bone tissue engineering: The role of solvent and hydroxyapatite particles. *Journal of the Mechanical Behavior of Biomedical Materials* 2014;39(0):95-110.
  100. Xie R, Hu J, Ng F, Tan L, Qin T, Zhang M, Guo X. High performance shape memory foams with isocyanate-modified hydroxyapatite nanoparticles for minimally invasive bone regeneration. *Ceramics International*.
  101. Campana V, Milano G, Pagano E, Barba M, Cicione C, Salonna G, Lattanzi W, Logroscino G. Bone substitutes in orthopaedic surgery: from basic science to clinical practice. *Journal of Materials Science: Materials in Medicine* 2014;25(10):2445-2461.
  102. Smucker JD, Petersen EB, Fredericks DC. Assessment of MASTERGRAFT PUTTY as a graft extender in a rabbit posterolateral fusion model. *Spine* 2012;37(12):1017-1021.
  103. Smucker JD, Petersen EB, Nepola JV, Fredericks DC. Assessment of MASTERGRAFT® STRIP with bone marrow aspirate as a graft extender in a rabbit posterolateral fusion model. *The Iowa orthopaedic journal* 2012;32:61.
  104. Harmata AJ, Ward CL, Zienkiewicz KJ, Wenke JC, Guelcher SA. Investigating the effects of surface-initiated polymerization of  $\epsilon$ -caprolactone to bioactive glass particles on the mechanical properties of settable polymer/ceramic composites. *Journal of Materials Research* 2014;29(20):2398-2407.
  105. Jones JR. Review of bioactive glass: From Hench to hybrids. *Acta Biomaterialia* 2013;9(1):4457-4486.
  106. Montazeri M, Karbasi S, Foroughi MR, Monshi A, Ebrahimi-Kahrizsangi R. Evaluation of mechanical property and bioactivity of nano-bioglass 45S5 scaffold coated with poly-3-hydroxybutyrate. *J Mater Sci Mater Med* 2015;26(2):5369.
  107. de Oliveira AAR, de Carvalho SM, de Fátima Leite M, Oréface RL, de Magalhães Pereira M. Development of biodegradable polyurethane and bioactive glass nanoparticles scaffolds for bone tissue engineering applications. *Journal of Biomedical Materials Research Part B: Applied Biomaterials* 2012;100B(5):1387-1396.
  108. Harmata AJ, Uppuganti S, Granke M, Guelcher SA, Nyman JS. Compressive fatigue and fracture toughness behavior of injectable, settable bone cements. *Journal of the mechanical behavior of biomedical materials* 2015;51:345-355.
  109. Khan A, Ahmed Z, Edirisinghe M, Wong F, Rehman I. Preparation and characterization of a novel bioactive restorative composite based on covalently coupled polyurethane–nanohydroxyapatite fibres. *Acta biomaterialia* 2008;4(5):1275-1287.
  110. Pugely AJ, Petersen EB, DeVries-Watson N, Fredericks DC. Influence of 45S5 Bioactive Glass in A Standard Calcium Phosphate Collagen Bone Graft Substitute on the Posterolateral Fusion of Rabbit Spine. *The Iowa orthopaedic journal* 2017;37:193.
  111. Ryszkowska JL, Auguścik M, Sheikh A, Boccaccini AR. Biodegradable polyurethane composite scaffolds containing Bioglass® for bone tissue engineering. *Composites Science and Technology* 2010;70(13):1894-1908.

112. Verné E, Vitale-Brovarone C, Bui E, Bianchi C, Boccaccini A. Surface functionalization of bioactive glasses. *Journal of biomedical materials research Part A* 2009;90(4):981-992.
113. Anderson DD, Van Hofwegen C, Marsh JL, Brown TD. Is elevated contact stress predictive of post-traumatic osteoarthritis for imprecisely reduced tibial plafond fractures? *Journal of Orthopaedic Research* 2011;29(1):33-39.
114. Goff T, Kanakaris NK, Giannoudis PV. Use of bone graft substitutes in the management of tibial plateau fractures. *Injury* 2013;44:S86-S94.
115. Ali AM, El-Shafie M, Willett K. Failure of fixation of tibial plateau fractures. *Journal of orthopaedic trauma* 2002;16(5):323-329.
116. Russell TA, Leighton RK. Comparison of autogenous bone graft and endothermic calcium phosphate cement for defect augmentation in tibial plateau fractures. A multicenter, prospective, randomized study. *J Bone Joint Surg Am* 2008;90(10):2057-61.
117. Simpson D, Keating J. Outcome of tibial plateau fractures managed with calcium phosphate cement. *Injury* 2004;35(9):913-918.
118. Lu S, McGough MA, Shiels SM, Zienkiewicz KJ, Merkel AR, Vanderburgh JP, Nyman JS, Sterling JA, Tennent DJ, Wenke JC. Settable polymer/ceramic composite bone grafts stabilize weight-bearing tibial plateau slot defects and integrate with host bone in an ovine model. *Biomaterials* 2018.
119. Verlaan JJ, Oner FC, Dhert WJ. Anterior spinal column augmentation with injectable bone cements. *Biomaterials* 2006;27(3):290-301.
120. Ramakrishna S, Mayer J, Wintermantel E, Leong KW. Biomedical applications of polymer-composite materials: a review. *Composites Science and Technology* 2001;61(9):1189-1224.
121. ISO. *Implants for Surgery—Acrylic Resin Cements*, 2002. International Standardization Organization Geneva; 2002.
122. Kühn K-D. *Bone cements: up-to-date comparison of physical and chemical properties of commercial materials*: Springer 2000.
123. Adhikari R, Gunatillake PA, Griffiths I, Tatai L, Wickramaratna M, Houshyar S, Moore T, Mayadunne RT, Field J, McGee M and others. Biodegradable injectable polyurethanes: synthesis and evaluation for orthopaedic applications. *Biomaterials* 2008;29(28):3762-3770.
124. Deramond H, Wright N, Belkoff S. Temperature elevation caused by bone cement polymerization during vertebroplasty. *Bone* 1999;25(2):17S-21S.
125. Langer R. Biodegradable polymer scaffolds for tissue engineering. *Nat Biotechnol* 1994.
126. Lorden ER, Miller KJ, Bashirov L, Ibrahim MM, Hammett E, Jung Y, Medina MA, Rastegarpour A, Selim MA, Leong KW. Mitigation of hypertrophic scar contraction via an elastomeric biodegradable scaffold. *Biomaterials* 2015;43:61-70.
127. Muggli DS, Burkoth AK, Anseth KS. Crosslinked polyanhydrides for use in orthopedic applications: degradation behavior and mechanics. *Journal of biomedical materials research* 1999;46(2):271-278.
128. Ashida K. *Polyurethane and related foams: chemistry and technology*: CRC press; 2006.
129. Elwell MJ, Ryan AJ, Grünbauer HJM, Van Lieshout HC. An FT i.r. study of reaction kinetics and structure development in model flexible polyurethane foam systems. *Polymer* 1996;37(8):1353-1361.
130. Guelcher SA, Patel V, Gallagher KM, Connolly S, Didier JE, Doctor JS, Hollinger JO. *Synthesis and In Vitro Biocompatibility of Injectable Polyurethane Foam Scaffolds*.

- Tissue Engineering 2006;12(5):1247-59.
131. Hafeman A, Li B, Yoshii T, Zienkiewicz K, Davidson J, Guelcher S. Injectable Biodegradable Polyurethane Scaffolds with Release of Platelet-derived Growth Factor for Tissue Repair and Regeneration. *Pharmaceutical Research* 2008;25(10):2387-2399.
  132. Hafeman AE, Zienkiewicz KJ, Zachman AL, Sung H-J, Nanney LB, Davidson JM, Guelcher SA. Characterization of the degradation mechanisms of lysine-derived aliphatic poly(ester urethane) scaffolds. *Biomaterials* 2011;32(2):419-429.
  133. McEnery MA, Lu S, Gupta MK, Zienkiewicz KJ, Wenke JC, Kalpakci KN, Shimko DA, Duvall CL, Guelcher SA. Oxidatively degradable poly (thioketal urethane)/ceramic composite bone cements with bone-like strength. *RSC advances* 2016;6(111):109414-109424.
  134. Moglia RS, Whitely M, Dhavalikar P, Robinson J, Pearce H, Brooks M, Stuebben M, Corder N, Cosgriff-Hernandez E. Injectable Polymerized High Internal Phase Emulsions with Rapid in Situ Curing. *Biomacromolecules* 2014;15(8):2870-2878.
  135. Robinson JL, Moglia RS, Stuebben MC, McEnery MAP, Cosgriff-Hernandez E. Achieving Interconnected Pore Architecture in Injectable PolyHIPEs for Bone Tissue Engineering. *Tissue Engineering Part A* 2014;20(5-6):1103-12.
  136. Whitely ME, Robinson JL, Stuebben MC, Pearce HA, McEnery MAP, Cosgriff-Hernandez E. Prevention of Oxygen Inhibition of PolyHIPE Radical Polymerization using a Thiol-based Crosslinker. *ACS Biomaterials Science & Engineering* 2017.
  137. Santerre J, Woodhouse K, Laroche G, Labow R. Understanding the biodegradation of polyurethanes: from classical implants to tissue engineering materials. *Biomaterials* 2005;26(35):7457-7470.
  138. Oertel G. *Polyurethane Handbook*. Berlin: Hanser Gardner Publications; 1994.
  139. Szycher M. *Szycher's Handbook of Polyurethanes*. Boca Raton: CRC Press; 1999.
  140. Bonzani IC, Adhikari R, Houshyar S, Mayadunne R, Gunatillake P, Stevens MM. Synthesis of two-component injectable polyurethanes for bone tissue engineering. *Biomaterials* 2007;28(3):423-433.
  141. Asplund JOB, Bowden T, Mathisen T, Hilborn J. Synthesis of highly elastic biodegradable poly(urethane urea). *Biomacromolecules* 2007;8(3):905-911.
  142. Guelcher SA, Srinivasan A, Dumas JE, Didier JE, McBride S, Hollinger JO. Synthesis, mechanical properties, biocompatibility, and biodegradation of polyurethane networks from lysine polyisocyanates. *Biomaterials* 2008;29(12):1762-1775.
  143. Martin JR, Gupta MK, Page JM, Yu F, Davidson JM, Guelcher SA, Duvall CL. A porous tissue engineering scaffold selectively degraded by cell-generated reactive oxygen species. *Biomaterials* 2014;35(12):3766-3776.
  144. Bertoldi S, Farè S, Denegri M, Rossi D, Haugen HJ, Parolini O, Tanzi MC. Ability of polyurethane foams to support placenta-derived cell adhesion and osteogenic differentiation: preliminary results. *Journal of Materials Science: Materials in Medicine* 2010;21(3):1005-1011.
  145. Christenson EM, Anderson JM, Hiltner A. Oxidative mechanisms of poly(carbonate urethane) and poly(ether urethane) biodegradation: In vivo and in vitro correlations. *Journal of Biomedical Materials Research Part A* 2004;70A(2):245-255.
  146. Kavlock KD, Pechar TW, Hollinger JO, Guelcher SA, Goldstein AS. Synthesis and characterization of segmented poly(esterurethane urea) elastomers for bone tissue engineering. *Acta Biomaterialia* 2007;3(4):475-484.

147. Zhang J, Doll BA, Beckman EJ, Hollinger JO. A biodegradable polyurethane-ascorbic acid scaffold for bone tissue engineering. *J Biomed Mater Res Pt A* 2003;67A:389-400.
148. Guelcher SA, Patel V, Gallagher KM, Connolly S, Didier JE, Doctor JS, Hollinger JO. Synthesis and in vitro biocompatibility of injectable polyurethane foam scaffolds. *Tissue Engineering* 2006;12(5):1247-1259.
149. Dumas JE, Zienkiewicz K, Tanner SA, Prieto EM, Bhattacharyya S, Guelcher S. Synthesis and Characterization of an Injectable Allograft Bone/polymer Composite Bone Void Filler with Tunable Mechanical Properties. *Tissue Eng Part A* 2010;16(8):2505-18.
150. Prieto EM, Talley AD, Gould NR, Zienkiewicz KJ, Drapeau SJ, Kalpakci KN, Guelcher SA. Effects of particle size and porosity on in vivo remodeling of settable allograft bone/polymer composites. *J Biomed Mater Res B Appl Biomater* 2015.
151. Bennett S, Connolly K, Lee DR, Jiang Y, Buck D, Hollinger JO, Gruskin EA. Initial biocompatibility studies of a novel degradable polymeric bone substitute that hardens in situ. *Bone* 1996;19(1, Supplement):101S-107S.
152. Harmata AJ, Ward CL, Zienkiewicz K, Wenke JC, Guelcher SA. Investigating the Effects of Surface-Initiated Polymerization of  $\epsilon$ -Caprolactone to Bioactive Glass Particles on the Mechanical Properties of Settable Polymer/Ceramic Composites. *J Mater Res* 2014;2014(29):20-30.
153. Adhikari R, Gunatillake PA, Griffiths I, Tatai L, Wickramaratna M, Houshyar S, Moore T, Mayadunne RT, Field J, McGee M and others. Biodegradable injectable polyurethanes: synthesis and evaluation for orthopaedic applications. *Biomaterials* 2008;29(28):3762-70.
154. Dumas JE, Zienkiewicz K, Tanner SA, Prieto EM, Bhattacharyya S, Guelcher SA. Synthesis and characterization of an injectable allograft bone/polymer composite bone void filler with tunable mechanical properties. *Tissue Engineering Part A* 2010;16(8):2505-2518.
155. Zanetta M, Quirici N, Demarosi F, Tanzi MC, Rimondini L, Farè S. Ability of polyurethane foams to support cell proliferation and the differentiation of MSCs into osteoblasts. *Acta Biomaterialia* 2009;5(4):1126-1136.
156. Guelcher S, Srinivasan A, Hafeman A, Gallagher K, Doctor J, Khetan S, McBride S, Hollinger J. Synthesis, in vitro degradation, and mechanical properties of two-component poly (ester urethane) urea scaffolds: effects of water and polyol composition. *Tissue engineering* 2007;13(9):2321-2333.
157. Dow polyurethanes - prepolymer definition. Volume 2016; 2014.
158. Page JM, Prieto EM, Dumas JE, Zienkiewicz KJ, Wenke JC, Brown-Baer P, Guelcher SA. Biocompatibility and chemical reaction kinetics of injectable, settable polyurethane/allograft bone biocomposites. *Acta biomaterialia* 2012;8(12):4405-4416.
159. Nukavarapu S, Freeman J, Laurencin C. *Regenerative Engineering of Musculoskeletal Tissues and Interfaces*: Woodhead Publishing; 2015.
160. Sheweita SA, Khoshhal KI, Baghdadi HH. Osteoporosis and Oxidative Stress—Role of Antioxidants. *Systems Biology of Free Radicals and Antioxidants*: Springer; 2014. p 2973-2995.
161. Lee SH, Gupta MK, Bang JB, Bae H, Sung H-J. Current Progress in Reactive Oxygen Species (ROS)-Responsive Materials for Biomedical Applications. *Advanced healthcare materials* 2013;2(6):908-915.
162. Xu Q, He C, Xiao C, Chen X. Reactive Oxygen Species (ROS) Responsive Polymers for

- Biomedical Applications. *Macromolecular bioscience* 2016.
163. Wilson DS, Dalmaso G, Wang L, Sitaraman SV, Merlin D, Murthy N. Orally delivered thioketal nanoparticles loaded with TNF- $\alpha$ -siRNA target inflammation and inhibit gene expression in the intestines. *Nat Mater* 2010;9(11):923-928.
  164. Shim MS, Xia Y. A reactive oxygen species (ROS)-responsive polymer for safe, efficient, and targeted gene delivery in cancer cells. *Angewandte Chemie* 2013;125(27):7064-7067.
  165. Krishnan L, Priddy LB, Esancy C, Li M-TA, Stevens HY, Jiang X, Tran L, Rowe DW, Guldberg RE. Hydrogel-based Delivery of rhBMP-2 Improves Healing of Large Bone Defects Compared With Autograft. *Clinical Orthopaedics and Related Research* 2015:1-13.
  166. Urist MR. Bone: formation by autoinduction. *Science* 1965;150(3698):893-899.
  167. Urist MR. The Classic: A Morphogenetic Matrix for Differentiation of Bone Tissue. *Clinical Orthopaedics and Related Research* 2009;467(12):3068.
  168. Wang EA, Rosen V, D'Alessandro JS, Bauduy M, Cordes P, Harada T, Israel DI, Hewick RM, Kerns KM, LaPan P. Recombinant human bone morphogenetic protein induces bone formation. *Proceedings of the National Academy of Sciences* 1990;87(6):2220-2224.
  169. Leach J, Bittar RG. BMP-7 (OP-1<sup>®</sup>) Safety in anterior cervical fusion surgery. *Journal of Clinical Neuroscience* 2009;16(11):1417-1420.
  170. Yilgor P, Tuzlakoglu K, Reis RL, Hasirci N, Hasirci V. Incorporation of a sequential BMP-2/BMP-7 delivery system into chitosan-based scaffolds for bone tissue engineering. *Biomaterials* 2009;30(21):3551-3559.
  171. Bessa PC, Casal M, Reis R. Bone morphogenetic proteins in tissue engineering: the road from the laboratory to the clinic, part I (basic concepts). *Journal of tissue engineering and regenerative medicine* 2008;2(1):1-13.
  172. White AP, Vaccaro AR, Hall JA, Whang PG, Friel BC, McKee MD. Clinical applications of BMP-7/OP-1 in fractures, nonunions and spinal fusion. *International orthopaedics* 2007;31(6):735-741.
  173. Perri B, Cooper M, Laurusyssen C, Anand N. Adverse swelling associated with use of rh-BMP-2 in anterior cervical discectomy and fusion: a case study. *The Spine Journal* 2007;7(2):235-239.
  174. Tannoury CA, An HS. Complications with the use of bone morphogenetic protein 2 (BMP-2) in spine surgery. *The Spine Journal* 2014;14(3):552-559.
  175. Wong DA, Kumar A, Jatana S, Ghiselli G, Wong K. Neurologic impairment from ectopic bone in the lumbar canal: a potential complication of off-label PLIF/TLIF use of bone morphogenetic protein-2 (BMP-2). *The Spine Journal* 2008;8(6):1011-1018.
  176. Smucker JD, Rhee JM, Singh K, Yoon ST, Heller JG. Increased swelling complications associated with off-label usage of rhBMP-2 in the anterior cervical spine. *Spine* 2006;31(24):2813-2819.
  177. Vavken J, Mameghani A, Vavken P, Schaeren S. Complications and cancer rates in spine fusion with recombinant human bone morphogenetic protein-2 (rhBMP-2). *European Spine Journal* 2015:1-11.
  178. McKay B, Sandhu HS. Use of recombinant human bone morphogenetic protein-2 in spinal fusion applications. *Spine* 2002;27(16S):S66-S85.
  179. Shiels SM, Talley AD, McGough MA, Zienkiewicz KJ, Kalpakci K, Shimko D, Guelcher SA, Wenke JC. Injectable and compression-resistant low-viscosity polymer/ceramic



- composite carriers for rhBMP-2 in a rabbit model of posterolateral fusion: a pilot study. *Journal of orthopaedic surgery and research* 2017;12(1):107.
180. Smith KE, Hyzy SL, Sunwoo M, Gall KA, Schwartz Z, Boyan BD. The dependence of MG63 osteoblast responses to (meth) acrylate-based networks on chemical structure and stiffness. *Biomaterials* 2010;31(24):6131-6141.
  181. Yang F, Williams CG, Wang D-a, Lee H, Manson PN, Elisseeff J. The effect of incorporating RGD adhesive peptide in polyethylene glycol diacrylate hydrogel on osteogenesis of bone marrow stromal cells. *Biomaterials* 2005;26(30):5991-5998.
  182. Kantlehner M, Schaffner P, Finsinger D, Meyer J, Jonczyk A, Diefenbach B, Nies B, Hölzemann G, Goodman SL, Kessler H. Surface coating with cyclic RGD peptides stimulates osteoblast adhesion and proliferation as well as bone formation. *Chembiochem* 2000;1(2):107-114.
  183. Burdick JA, Anseth KS. Photoencapsulation of osteoblasts in injectable RGD-modified PEG hydrogels for bone tissue engineering. *Biomaterials* 2002;23(22):4315-4323.
  184. Cosgriff-Hernandez EM, Moglia RS, Robinson JL, Sears NA. High porosity materials, scaffolds, and method of making. *Google Patents*; 2015.
  185. Robinson JL. Development of Osteoinductive, High Porosity PolyHIPEs as Injectable Bone Grafts; 2014.
  186. Lin HB, Sun W, Mosher DF, García-Echeverría C, Schaufelberger K, Lelkes PI, Cooper SL. Synthesis, surface, and cell-adhesion properties of polyurethanes containing covalently grafted RGD-peptides. *Journal of biomedical materials research* 1994;28(3):329-342.
  187. Chen W, Zhou H, Tang M, Weir MD, Bao C, Xu HH. Gas-foaming calcium phosphate cement scaffold encapsulating human umbilical cord stem cells. *Tissue Engineering Part A* 2011;18(7-8):816-827.
  188. Tang M, Chen W, Weir MD, Thein-Han W, Xu HH. Human embryonic stem cell encapsulation in alginate microbeads in macroporous calcium phosphate cement for bone tissue engineering. *Acta biomaterialia* 2012;8(9):3436-3445.
  189. Phelps EA, Enemchukwu NO, Fiore VF, Sy JC, Murthy N, Sulchek TA, Barker TH, García AJ. Maleimide cross-linked bioactive peg hydrogel exhibits improved reaction kinetics and cross-linking for cell encapsulation and in situ delivery. *Advanced materials* 2012;24(1):64-70.
  190. Gunzburg R, Szpalski M. Use of a novel  $\beta$ -tricalcium phosphate-based bone void filler as a graft extender in spinal fusion surgeries. *Orthopedics* 2002;25(5):S591-S595.
  191. Rantakokko J, Frantzén J, Heinänen J, Kajander S, Kotilainen E, Gullichsen E, Lindfors N. Posterolateral Spondylodesis Using Bioactive Glass S53P4 and Autogenous Bone in Instrumented Unstable Lumbar Spine Burst Fractures; a Prospective 10-Year Follow-Up Study. *Scandinavian Journal of Surgery* 2012;101(1):66-71.
  192. Lee JH, Hwang CJ, Song BW, Koo KH, Chang BS, Lee CK. A prospective consecutive study of instrumented posterolateral lumbar fusion using synthetic hydroxyapatite (Bongros®-HA) as a bone graft extender. *Journal of Biomedical Materials Research Part A* 2009;90(3):804-810.
  193. Lerner T, Bullmann V, Schulte TL, Schneider M, Liljenqvist U. A level-1 pilot study to evaluate of ultraporous  $\beta$ -tricalcium phosphate as a graft extender in the posterior correction of adolescent idiopathic scoliosis. *European Spine Journal* 2009;18(2):170-179.

194. Hile DD, Kandziora F, Lewandrowski K-U, Doherty SA, Kowaleski MP, Trantolo DJ. A poly(propylene glycol-co-fumaric acid) based bone graft extender for lumbar spinal fusion: in vivo assessment in a rabbit model. *European spine journal : official publication of the European Spine Society, the European Spinal Deformity Society, and the European Section of the Cervical Spine Research Society* 2006;15(6):936-943.
195. Walsh WR, Oliver RA, Gage G, Yu Y, Bell D, Bellemore J, Adkisson HD. Application of resorbable poly (lactide-co-glycolide) with entangled hyaluronic acid as an autograft extender for posterolateral intertransverse lumbar fusion in rabbits. *Tissue Engineering Part A* 2010;17(1-2):213-220.
196. Bagi CM, Berryman E, Moalli MR. Comparative bone anatomy of commonly used laboratory animals: implications for drug discovery. *Comparative medicine* 2011;61(1):76-85.
197. Pearce A, Richards R, Milz S, Schneider E, Pearce S. Animal models for implant biomaterial research in bone: a review. *Eur Cell Mater* 2007;13(1):1-10.
198. Muschler GF, Raut VP, Patterson TE, Wenke JC, Hollinger JO. The design and use of animal models for translational research in bone tissue engineering and regenerative medicine. *Tissue Engineering Part B: Reviews* 2010;16(1):123-145.
199. Liebschner MA. Biomechanical considerations of animal models used in tissue engineering of bone. *Biomaterials* 2004;25(9):1697-1714.
200. Aerssens J, Boonen S, Lowet G, Dequeker J. Interspecies differences in bone composition, density, and quality: potential implications for in vivo bone research. *Endocrinology* 1998;139(2):663-670.
201. McDaniel JS, Pilia M, Raut V, Ledford J, Shiels SM, Wenke JC, Barnes B, Rathbone CR. Alternatives to autograft evaluated in a rabbit segmental bone defect. *International orthopaedics* 2015:1-7.
202. Bodde EW, Spauwen PH, Mikos AG, Jansen JA. Closing capacity of segmental radius defects in rabbits. *Journal of Biomedical Materials Research Part A* 2008;85(1):206-217.
203. Wheeler DL, Stokes KE, Park HM, Hollinger JO. Evaluation of particulate Bioglass® in a rabbit radius osteotomy model. *Journal of Biomedical Materials Research* 1997;35(2):249-254.
204. van Gaalen SM, Kruyt MC, Geuze RE, de Bruijn JD, Alblas J, Dhert WJ. Use of fluorochrome labels in in vivo bone tissue engineering research. *Tissue engineering Part B: Reviews* 2010;16(2):209-217.
205. Gruber HE, Ingram JA. Basic staining and histochemical techniques and immunohistochemical localizations using bone sections. *Handbook of Histology Methods for Bone and Cartilage*: Springer; 2003. p 281-286.
206. Guo R, Merkel A, Sterling J, Davidson J, Guelcher S. Substrate modulus of 3D-printed scaffolds regulates the regenerative response in subcutaneous implants through the macrophage phenotype and Wnt signaling. *Biomaterials* 2015;73:85-95.
207. Dumas JE, Prieto EM, Zienkiewicz KJ, Guda T, Wenke JC, Bible J, Holt GE, Guelcher SA. Balancing the Rates of New Bone Formation and Polymer Degradation Enhances Healing of Weight-Bearing Allograft/Polyurethane Composites in Rabbit Femoral Defects. *Tissue Engineering Part A* 2014;20(1-2):115-129.
208. Del Cerro M, Cogen J, Del Cerro C. Stevenel's Blue, an excellent stain for optical microscopical study of plastic embedded tissues. *Microscopica acta* 1980;83(2):117-121.
209. Visser J, Gawlitta D, Benders KEM, Toma SMH, Pouran B, van Weeren PR, Dhert WJA,

- Malda J. Endochondral bone formation in gelatin methacrylamide hydrogel with embedded cartilage-derived matrix particles. *Biomaterials* 2015;37:174-182.
210. Scarano A, Petrone G, Piattelli A. Staining Techniques for Plastic-Embedded Specimens. *Handbook of histology methods for bone and cartilage*: Springer; 2003. p 315-319.
211. Ramos-Vara JA, Miller MA. When Tissue Antigens and Antibodies Get Along: Revisiting the Technical Aspects of Immunohistochemistry—The Red, Brown, and Blue Technique. *Veterinary Pathology* 2014;51(1):42-87.

## CHAPTER 3

### III. OXIDATIVELY DEGRADABLE POLY(THIOKETAL URETHANE) CERAMIC COMPOSITE BONE CEMENTS WITH BONE-LIKE STRENGTH

**Adapted with permission from The Royal Society of Chemistry:**

**McEnery, MAP, Lu, S, Gupta, MK, Zienkiewicz, KJ, Wenke, JC, Kalpakci, KN, Shimko, DA, Duvall, CL, Guelcher, SA.** “Oxidatively degradable poly(thioketal urethane)/ceramic composite bone cements with bone-like strength.” *RSC Advances*, 2016, **6**(111), 109414-109424.

#### 3.1 Abstract

Synthetic bone cements are commonly used in orthopaedic procedures to aid in bone regeneration following trauma or disease. Polymeric cements like PMMA provide the mechanical strength necessary for orthopaedic applications, but they are not resorbable and do not integrate with host bone. Ceramic cements have a chemical composition similar to that of bone, but their brittle mechanical properties limit their use in weight-bearing applications. In this study, we designed oxidatively degradable, polymeric bone cements with mechanical properties suitable for bone tissue engineering applications. We synthesized a novel thioketal (TK) diol, which was crosslinked with a lysine triisocyanate (LTI) prepolymer to create hydrolytically stable poly(thioketal urethane)s (PTKUR) that degrade in the oxidative environment associated with bone defects. PTKUR films were hydrolytically stable for up to 6 months but degraded rapidly (<1 week) under simulated oxidative conditions in vitro. When combined with ceramic micro- or nanoparticles, PTKUR cements exhibited working times comparable to calcium phosphate cements and strengths exceeding those of trabecular bone. PTKUR/ceramic composite cements supported appositional bone growth and integrated with host bone near the bone-cement

interface at 6 and 12 weeks post-implantation in rabbit femoral condyle plug defects. Histological evidence of osteoclast-mediated resorption of the cements was observed at 6 and 12 weeks. These findings demonstrate that a PTKUR bone cement with bone-like strength can be selectively resorbed by cells involved in bone remodeling, and thus represent an important initial step toward the development of resorbable bone cements for weight-bearing applications.

### 3.2 Introduction

Injectable and settable bone cements restore function to bone damaged by trauma or disease in a number of orthopaedic procedures, such as vertebroplasty, repair of tibial plateau fractures, and screw augmentation. Poly(methyl methacrylate) (PMMA) bone cements exhibit mechanical properties exceeding those of trabecular bone, and therefore provide mechanical stability to damaged bone.<sup>1</sup> However, PMMA cements are non-resorbable and do not integrate with host bone. Ceramic bone cements are osteoconductive and integrate with host bone, but their brittle mechanical properties preclude their use in weight-bearing applications.<sup>2</sup> Thus, composites of ceramics with resorbable polymers have emerged as an alternative approach that combines the ductile mechanical properties of polymers with the osteoconductivity of ceramics to provide mechanical stability and integration with host bone.<sup>3</sup>

Poly(ester urethane)s (PEUR) have been investigated as injectable bone grafts due to their injectability, settability, tunable mechanical properties, and resorption to breakdown products easily cleared from the body. PEUR grafts set within clinically relevant working times and attain strengths in the range of 10 – 80 MPa.<sup>4,5</sup> Lysine-derived PEUR composites incorporating ceramic particles or allograft bone set *in situ* with no surgical complications and support bone remodeling in sheep, rats, and rabbits.<sup>4-8</sup> Previous

work has shown LTI-derived PEURs undergo autocatalytic hydrolytic degradation in which the acidic breakdown products accelerate resorption.<sup>9,10</sup> A degradation mechanism that allows for a more controlled and predictable degradation rate is desired to ensure that the graft degrades at a rate complementary to bone formation and remodeling.

Bone remodeling is commonly achieved by creeping substitution, a process by which osteoclasts resorb residual graft and osteoblasts deposit new mineralized matrix near the graft-bone interface.<sup>11-13</sup> The normal endogenous bone healing cascade involves an initial hematoma formation that induces the immune response accompanied by a release of pro-inflammatory factors.<sup>14</sup> The inflammatory phase is followed by a soft callus formation that is rapidly replaced by woven mineralized bone.<sup>15</sup> As a result of the inflammatory response, reactive oxygen species (ROS) are generated by infiltrating cells at the defect site.<sup>16,17</sup> Mature osteoclasts at sites of active bone remodeling are also associated with an increase in ROS.<sup>17-19</sup> These findings suggest that hydrolytically stable biomaterials that degrade in response to cell-secreted ROS may be a useful new approach for the design of cell-degradable bone cements.

Thioketals (TKs), the sulfur analogs of ketals, degrade in response to cell-secreted ROS to thiol decomposition products with low cytotoxicity.<sup>20,21</sup> PTKUR foams synthesized from a TK macrodiol (1000 g mol<sup>-1</sup>) have been reported to support ROS-mediated degradation and healing in cutaneous wounds.<sup>20</sup> However, macrodiol-based PTKURs cannot achieve bone-like strength or the number of degradable units afforded by the new single TK-containing crosslinker. Furthermore, TK-based biomaterials have not been previously investigated in bone. In this study, a novel low molecular weight TK diol was synthesized and utilized to formulate PTKUR bone cements that are hydrolytically stable

but degradable by cell-secreted ROS. The TK diol was reacted with LTI to form a moldable and settable PTKUR cement with bone-like strength using a low-toxicity iron (III) acetylacetonate gelling catalyst. To enhance the osteoconductivity of the PTKUR, it was combined with two different types of ceramics: (1) 85%  $\beta$ -tricalcium phosphate ( $\beta$ -TCP)/15% hydroxyapatite (HA) ceramic mini-granules (MASTERGRAFT<sup>®</sup>, MG), or (2) nanocrystalline hydroxyapatite (nHA) particles.<sup>22,23</sup> The reactivity, rheological properties, mechanical properties, degradation rate, and cell proliferation response of the cements were assessed *in vitro*. The biocompatibility and remodeling of PTKUR/ceramic composite cements were investigated in a rabbit femoral condyle plug defect model to assess material resorption and integration with the host bone.

### 3.3 Methods

*Materials.* Thioglycolic acid, 2,2-dimethoxypropane, bismuth chloride, lithium aluminum hydride,  $\epsilon$ -caprolactone, nHA (<200 nm), and anhydrous solvents were purchased from Sigma-Aldrich (St. Louis, MO). The  $\epsilon$ -caprolactone was treated with magnesium sulfate, and nHA was dried under vacuum at 80°C for at least 24 hours prior to use. Acros Organics iron (III) acetylacetonate (FeAA) was purchased from Fisher Scientific and used as received. LTI was purchased from Jinan Haohua Industry Co., LTD (Jinan, China) and carbon-treated in methyl-tert-butyl ether 3 times for 24 hours at 70°C to remove impurities. MG particles supplied by Medtronic (Memphis, TN) were ground to 100-300  $\mu$ m diameter particles using a mortar and pestle and filtered between 100 and 300  $\mu$ m sieves. The resulting microparticles were washed in 95% acetone, triple rinsed with water, and dried under vacuum.

MC3T3 cells were supplied by ATCC (Manassas, VA). Gibco<sup>™</sup>  $\alpha$ -MEM medium,

penicillin/streptomycin (P/S) and a Pierce™ bicinchoninic (BCA) Protein Assay kit were purchased from Thermo Scientific™ (Waltham, MA). Sterile phosphate buffered saline (PBS) and 0.25% trypsin were purchased from Corning Cellgro (Manassas, VA) and fetal bovine serum (FBS) from HyClone (Pittsburgh, PA). Reagents for cell fixation including glutaraldehyde and osmium tetroxide were purchased from Fisher Scientific and Sigma Aldrich, respectively.

*Thioketal diol synthesis.* The schematic for thioketal diol synthesis is illustrated in **Figure 3.1A**. Bismuth (III) chloride was added to a dry boiling flask that was subsequently dried with a hot air gun under vacuum for about 5 minutes to ensure completely dry catalyst conditions. The flask was then purged with nitrogen and left under a positive pressure with nitrogen for the remainder of the reaction. Anhydrous acetonitrile was charged to the flask to dissolve the catalyst. 2,2-dimethoxypropane and thioglycolic acid were added to the flask, and the reaction was allowed to proceed for 24 hours while stirring at room temperature. The carboxyl-terminated intermediate was filtered with a Buchner funnel, rotary evaporated (Buchi Rotovap R-200, 35 °C), and dried under vacuum overnight. The carboxyl groups were then reduced to produce a hydroxyl-terminated TK. A 3-neck boiling flask was fitted to a 10 °C condenser capped with a 1-way glass stop-cock, a constant pressure dropping funnel, and a rubber stopper. The reactor was heated with a heat gun under vacuum for about 5 minutes to ensure completely dry reaction conditions. The reactor was then placed in an ice bath, purged with dry nitrogen, and maintained under positive pressure with nitrogen throughout the functionalization. Lithium aluminum hydride (LiAlH<sub>4</sub>) was added to the 3-neck boiling flask and dissolved in diethyl ether. Using anhydrous techniques, anhydrous tetrahydrofuran was added to the boiling flask



containing the carboxyl-terminated TK. The resulting solution was then transferred to the dropping funnel and added to the LiAlH<sub>4</sub> solution dropwise at 0 °C. After all of the TK solution was added, the ice bath was replaced with an oil bath and the reaction mixture was refluxed at 52 °C for 6-8 hours. Unreacted LiAlH<sub>4</sub> was quenched by adding DI water dropwise followed by 1M sodium hydroxide to aid in product extraction. By-products of the reaction were filtered using a Buchner funnel and filtration flask, and a separation funnel and diethyl ether were used to extract and isolate the TK diol product. The solvent was removed by rotary evaporation and the product dried under vacuum overnight for a completely dry, solvent-free TK diol. Nuclear magnetic resonance spectroscopy (<sup>1</sup>H NMR, Bruker 400 MHz NMR) in dimethylsulfoxide (DMSO) and attenuated total reflectance Fourier transform infrared spectroscopy (ATR-FTIR) verified the chemical structure of the TK diol. Titration of a sample reacted with excess *p*-toluenesulfonyl isocyanate with tetrabutylammonium hydroxide was used to determine the hydroxyl (OH) number of the TK diol according to ASTM E1899-08.<sup>24</sup> The molecular weight (M<sub>n</sub>) was calculated from the OH number using Eq (3.1):

$$M_n = \frac{56,100}{\text{OH Number}} \quad (3.1)$$

*Quasi-prepolymer synthesis and characterization.* A quasi-prepolymer was prepared according to methods previously described.<sup>25</sup> Briefly, a 2.5:1 molar ratio of LTI:TK (3.75:1 NCO:OH equivalent ratio) was charged to a 100-mL boiling flask and purged with nitrogen while stirring in an oil bath at 45°C. TK diol was added to LTI dropwise from a syringe through a 16G needle inserted through the rubber stopper. The reaction was allowed to proceed for 3 hours yielding an LTI-TK quasi-prepolymer. The NCO

number was determined by titration according to ASTM D2572-97.<sup>26</sup>

*Polyurethane/ceramic composite synthesis and characterization.* PTKUR/ceramic composites were fabricated by reactive liquid molding and catalyzed using a 5% FeAA solution in  $\epsilon$ -caprolactone. The isocyanate index (NCO:OH equivalent ratio \* 100) was 140 for all materials.<sup>8</sup> TK diol, LTI-TK prepolymer, and 55 wt% MG or 60 wt% nHA particles were hand-mixed to yield a reactive paste. These concentrations of the ceramic particles were selected as the maximum values that could be added while maintaining a cohesive reactive paste. Once homogeneous, 0.06 wt% FeAA (in solution) was added to catalyze the reaction between the LTI-TK prepolymer and the TK diol. The morphology of the composite was verified by scanning electron microscopy (Hitachi S4200 SEM) following gold sputter coating of thin sections of sample (Cressington Q108) for 45 seconds at 30 mA.

PTKUR films (without ceramic) synthesized using varying isocyanate indices were submerged in water for 2 weeks and water uptake measured periodically by weighing the samples. Swelling of films with indices of 110, 125, and 140 was calculated according to Eq (3.2), where  $M_s$  is the swollen mass and  $M_0$  is the initial mass. This information was used to determine effects of index on extent of crosslinking.

$$\% \text{ Swelling} = \frac{M_s - M_0}{M_0} \times 100\% \quad (3.2)$$

*Reaction kinetics and working time.* The reaction kinetics of the composite were assessed using methods described previously.<sup>8,27</sup> ATR-FTIR was used to evaluate the reaction rate of the isocyanate-terminated LTI-TK prepolymer with the other components of the composite individually by quantifying the disappearance of the isocyanate peak

(around  $2270\text{ cm}^{-1}$ ). The isocyanate peaks were calibrated to a standard curve of known NCO concentrations to find an initial rate constant for each reaction during the first 6 minutes. These rate constants along with the initial concentrations of each component were input into a Matlab program to calculate the number of isocyanate and hydroxyl equivalents versus time assuming second-order chemical kinetics. Isocyanate and hydroxyl conversion versus time were determined from the calculated numbers of equivalents.

The working time for the MG composites was defined using a rheometer with 25-mm plates. A gap size of 1.5 mm and constant strain (1%) and frequency (1 Hz) were applied to the composite and the working time defined by the time of the  $G' - G''$  crossover point. This time was compared to the tack-free time which was defined as when the material no longer stuck to a metal spatula.<sup>7</sup>

*Compressive mechanical properties.* Samples for compressive studies were prepared by injecting composites into 6 mm diameter tubes and compressing under a 0.96 kg weight to ensure cohesion throughout initial cure.<sup>28</sup> Samples were cut to a height equal to 2 times their diameter (12 mm) using a Buehler IsoMet Low Speed Saw (Lake Bluff, IL). Modulus and strength were measured at various time points over a 2-week period to determine when the composites were completely crosslinked. Specimens were preloaded to 12 N and compressed at a rate of  $25\text{ mm min}^{-1}$  using an MTS 858 Bionix Servohydraulic Test System (Eden Prairie, MN). The engineering stress was calculated by dividing the load by the platen-contacting surface area and the engineering strain determined by dividing the displacement by initial sample height. The slope of the linear-elastic portion of the resulting stress-strain curve was identified as the compressive modulus and the maximum stress as the compressive strength. When a maximum stress could not be

identified, the stress at 10% strain was reported.<sup>29</sup>

*Degradation.* The degradation characteristics of PTKUR were assessed in hydrolytic and oxidative conditions. An accelerated degradation medium comprising 20 wt% hydrogen peroxide in 0.1 M cobalt chloride in DI water simulated the environment produced by reactive oxygen species at the implant site.<sup>20,30,31</sup> PTKUR films (17 mg) were immersed in 350  $\mu$ L (1 mL/50 mg initial sample) degradation media and placed on a shaker table at 37°C. PTKUR degradation was compared to lysine-derived poly(caprolactone urethane) (PCLUR), which was expected to undergo minimal hydrolytic degradation. Oxidative media was changed every 72 hours when time points exceeded 3 days to ensure the presence of oxidizing radicals. Samples were washed 3X with 100 mL DI water, dried under vacuum for at least 48 hours, and weighed at various time points to determine the degradation rate. Samples were gold sputter-coated for 45 seconds and imaged using SEM to visualize the change in architecture with degradation.

*Rheology.* Viscosity was characterized using a TA Instruments AR 2000ex rheometer fitted with 25-mm parallel plates at 25 °C. For the starting materials (TK diol and LTI-TK prepolymer), a small sample was injected between the plates which were subsequently depressed to a gap size of 500  $\mu$ m. A frequency sweep was applied at a constant strain in the linear viscoelastic region (0.2 for the TK diol and 0.5 for the quasi prepolymer). A Cox-Merz transformation related the dynamic data to viscosity as a function of shear rate. The rheological properties of uncatalyzed (non-reactive) composites were found using a gap size of 1.5 mm. A constant strain of 1% was applied to the composite through a frequency sweep and a Cox-Merz transformation applied to characterize injectability.

*In vitro characterization.* The surface chemistry of PTKUR polymer films was observed by water contact angle using a Ramé-Hart Goniometer (Mountain Lakes, NJ) to predict cellular behavior at the material interface. Cellular attachment was verified using SEM and proliferation was observed using a BCA Protein Assay kit. MC3T3 cells were seeded ( $2 \times 10^4$  cells/mL) onto thin sections of MG and nHA composites that were conditioned in complete  $\alpha$ MEM medium with 10% FBS and 1% P/S overnight. Samples were submerged in 5% glutaraldehyde followed by 2% osmium tetroxide and an ethanol dehydration ladder to fix for SEM after 24 hours incubation. To measure proliferation, samples were taken from culture at 1, 4, and 7 days. Samples were transferred to a new well, washed with PBS, and the cells trypsinized. Cell pellets were lysed using RIPA buffer to extract the cellular protein. The BCA kit was used to quantify total protein at each time point.<sup>32</sup>

*Implantation of PTKUR/ceramic composite cements in rabbits.* PTKUR/ceramic composites were evaluated in cylindrical femoral condyle plug defects in eight New Zealand White rabbits weighing 4-5 kg. All surgical and care procedures were carried out at IBEX Preclinical Research, Inc. (Logan, UT) under aseptic conditions per the approved IACUC protocol. The reactive components (TK diol, FeAA catalyst, LTI-TK prepolymer, MasterGraft, and nHA) were gamma-irradiated using a dose of approximately 25 kGY prior to use. After administration of anesthesia, bilateral defects 6-8 mm deep x 5 mm diameter were drilled in the femoral condyle of the distal femurs of 8 rabbits. PTKUR/ceramic composites incorporating either MG or nHA (n=3) were mixed on site, injected into the defect, and allowed to cure for 10 minutes prior to closing the wound. Animals were euthanized and femurs harvested at 6 and 12 weeks to evaluate healing and

polymer degradation. Micro-computed tomography (Scanco  $\mu$ CT 50) was performed with a voxel size of 17.2  $\mu\text{m}$  and a threshold of 237 (386 mg HA/cm<sup>3</sup>) to match the intensity of the native trabecular bone surrounding the defect. Histology preparation was performed by Histon. Calcified samples were embedded in PMMA and sections taken from the center of the defect area; the sections were stained with Stevenel's Blue or hematoxylin and eosin (H&E) to identify new bone formation and cellular activity at the defect site.

*Statistical analysis.* Anova with post hoc comparisons using Tukey's multiple comparisons test was applied to compression testing data to compare statistical differences with cure time. The Holm-Sidak multiple comparison test was used to evaluate significance in total protein over time for each composite individually, and the plot shows standard error of the mean (SEM). All other data was plotted with standard deviation, and  $p < 0.05$  was considered statistically significant.

### 3.4 Results and Discussion

*Thioketal diol and quasi-prepolymer characterization.* The TK diol was synthesized following the two-step reaction scheme in **Figure 3.1A**. The characteristic NMR peak for the methyl (1.59 ppm) and hydroxyl (4.8 ppm) groups of the TK diol indicated that the targeted product was achieved (**Figure 3.1B**), and an ATR-FTIR absorbance peak around 3400  $\text{cm}^{-1}$  confirmed hydroxyl functionalization.<sup>20</sup> The OH number was found to be 574 mg KOH/g, which corresponds to a molecular weight of 196  $\text{g mol}^{-1}$  (Eq 3.1). These data combined with GPC elution data (**Figure 3.1C**) confirm that the desired product with a theoretical molecular weight of 196.3  $\text{g mol}^{-1}$  was achieved. This low-molecular weight TK diol had a viscosity of 0.11 Pa s at a shear rate of 5  $\text{s}^{-1}$  and exhibited near Newtonian behavior at shear rates below 100  $\text{s}^{-1}$  (**Figure 3.1D**).

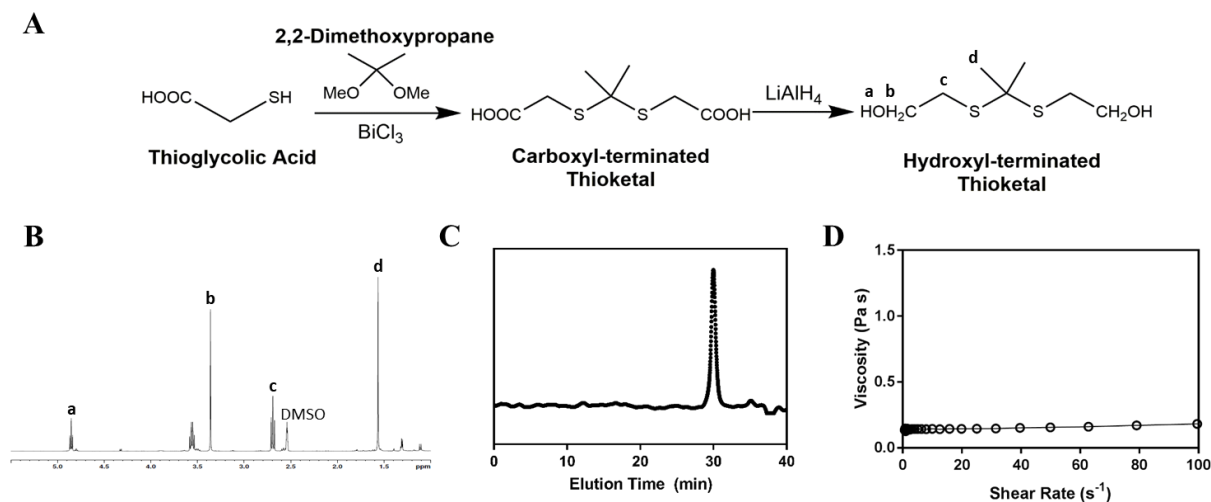


**Figure 3.1.** Synthesis and characterization of low molecular weight thioketal diol. (A) Synthesis scheme. (B-C) Characterization by (B) NMR and (C) GPC indicate that the targeted molecular structure was obtained. (D) Viscosity of the TK diol is independent of shear rate.

A quasi-prepolymer was synthesized to improve handling by increasing LTI viscosity, lowering the reaction exotherm, and minimizing phase separation during polymerization. TK diol was reacted with a 2.5 molar excess of LTI to form an LTI-TK prepolymer (**Figure 3.2A**). The excess of LTI greater than 2 renders this component a quasi-prepolymer, although it will be referred to as a prepolymer in this study.<sup>33</sup> The LTI-TK prepolymer exhibited Newtonian behavior, but the viscosity of 61 Pa s (measured at 5 s<sup>-1</sup>, **Figure 3.2B**) was considerably greater than that measured for TK diol or LTI (0.036 – 0.061 Pa s).<sup>25</sup> The %NCO number of the prepolymer determined by titration was 25.1%, which is slightly lower than the theoretical NCO number of 26.7% based on stoichiometry.

*Composite characterization.* Crosslinked PTKUR composites (**Figure 3.2C**) incorporating either MG or nHA particles were fabricated according to the schematic in **Figure 3.2D**. **Figure 3.2E** shows the initial (e.g., uncatalyzed) dynamic viscosities of both MG and nHA composites up to shear rates of 100 s<sup>-1</sup>. Both materials exhibit shear thinning

behavior that is more prominent at lower shear rates, which enhances injectability, and have viscosities of 20-25 Pa s at a shear rate of 100 s<sup>-1</sup>. SEM images of the composites showed minimal porosity was achieved using a low-toxicity, iron-based gelling catalyst (25:1 gel:blow, **Figure 3.2F-G**) compared to previously investigated amine-based catalysts with high blowing power (1:20 gel:blow).<sup>10,13,23,34</sup>

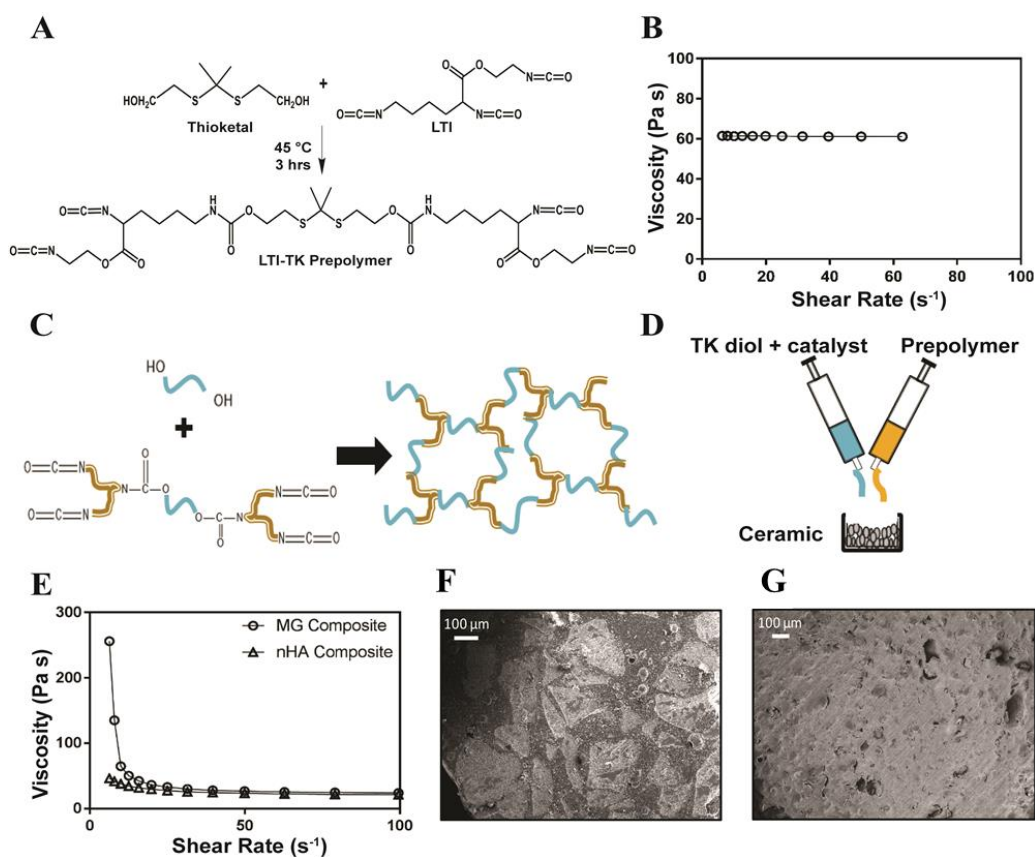


**Figure 3.2.** Synthesis of poly(thioketal urethane) (PTKUR)/ceramic composites. (A) Synthesis scheme for LTI-TK prepolymer. (B) Viscosity of the LTI-TK prepolymer is independent of shear rate. (C) Reaction of TK diol with LTI-TK prepolymer to form a crosslinked PTKUR network. (D) Fabrication of PTKUR/ceramic composites by mixing LTI-TK prepolymer, TK diol, and ceramic particles (MG or nHA). (E) The viscosity of uncatalyzed (non-reactive) LTI-TK/TK diol/ceramic mixtures decreases with increasing shear rate, providing evidence of shear-thinning behavior. (F-G) SEM images of (F) MG and (G) nHA composites show lack of porosity. Due to their relatively large size (100 – 300 μm), MG particles (light grey) can be distinguished from the PTKUR phase (dark grey).



PTKUR films were made by mixing TK and LTI-TK prepolymer with iron catalyst without incorporating ceramic particles. The polymer film exhibited a contact angle of 70.2° indicating a moderately hydrophobic surface. Films of indices 110, 125, and 140 all swelled less than 3.5% after soaking in water for 2 weeks and the differences between them were not significant. Since there was no difference in swelling and the swelling was less than 5% for all samples, all of the indices were considered suitable for use *in vivo*. An index of 140 was chosen for the studies in this work to ensure complete crosslinking and a more rigid composite as reported previously.<sup>8,28,35</sup>

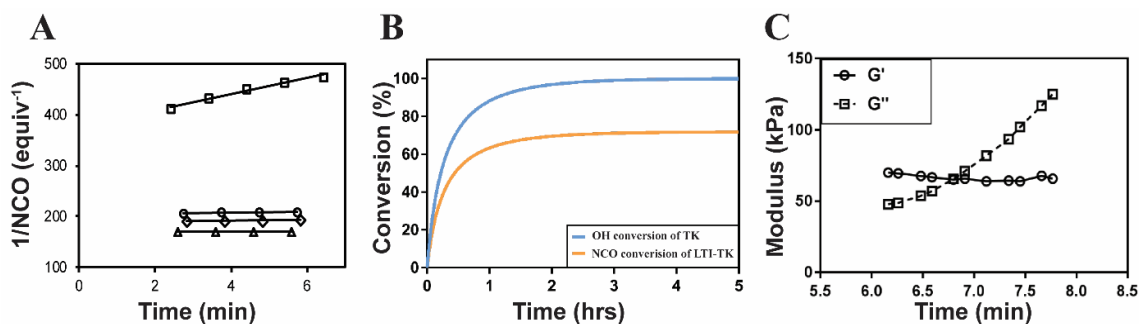


**Figure 3.3.** Kinetics of the setting reaction. (A) The reaction rate constant ( $k$ ) of a second order reaction is calculated from the slope of the line of  $1/[NCO]$  with time. The rate constant of the LTI-TK prepolymer-TK diol reaction ( $\square$ ) is substantially greater than that measured for MG ( $\Delta$ ), nHA ( $\circ$ ), or water ( $\diamond$ ). (B) Using the rate constant for the dominant reaction TK diol + LTI-TK prepolymer, the conversion of the NCO and OH functional groups was calculated versus time. (C) Storage ( $G'$ ) and loss ( $G''$ ) moduli of the reactive (catalyzed) LTI-TK/TK diol/MG mixture. The gel point (i.e., working time) is identified as the  $G'-G''$  crossover point to be 6.7 min.

The reactivity of the polymer was investigated using ATR-FTIR. The second-order rate constant ( $k_i$ , Eq (3.3)) of each component was calculated based on the initial isocyanate concentration ( $C_0$ ) and the disappearance of the isocyanate peak ( $C$ ).<sup>8,36</sup>

$$\frac{1}{C} = k_i t + \frac{1}{C_0} \quad (3.3)$$

The catalyst was reduced by half (compared to the *in vivo* studies) for the reactivity

experiments to slow the reaction, which was necessary to investigate the reaction mechanisms. **Figure 3.3A** shows the calculation of the initial rate constant ( $k_i$ ) for each reaction from the slope of the 2<sup>nd</sup> order rate plot, in which the inverse concentration of NCO equivalents (g / equiv NCO) is plotted versus time. The plot is linear for the first 6 minutes of the reaction, which confirms that the reactions are second order as anticipated.<sup>8,36</sup> Further, the very small slope for MG, nHA, and water with LTI-TK indicates these components have very low reactivity, and thus they were not included in the conversion calculations. The relatively high rate constant for the LTI-TK/TK gelling reaction compared to the LTI-TK/water blowing reaction (25:1 gel:blow ratio) confirms the preferential gelling activity of the iron acetylacetonate (FeAA) catalyst compared to the triethylene diamine (TEDA) catalyst investigated previously (1:20 gel:blow).<sup>8,35</sup> The concentration of LTI-TK prepolymer (I) and TK diol (D) were calculated as:

$$\frac{dC_D}{dt} = \frac{dC_I}{dt} = -k_D C_D C_I M \quad (3.4)$$

where  $C_j$  is the concentration of each component (I or D, g equiv<sup>-1</sup> min<sup>-1</sup>) and M is the mass of the composite (g). The conversions of LTI-TK prepolymer and TK diol were calculated from the second-order kinetic model as:

$$\xi_j = \frac{C_{j0} - C_j}{C_{j0}} \quad (3.5)$$

Conversion of NCO and OH groups are shown in **Figure 3.3B**. The hydroxyl groups in the TK diol are completely converted and an excess of isocyanate functional groups remain, as anticipated from the high isocyanate index of 140. The excess isocyanate is anticipated to slowly react with the ceramic and environmental water, as reported previously for allograft

bone composites<sup>9</sup>, due to the substantially lower reactivity of the LTI-TK prepolymer with these components. The tack-free time was determined by hand to be 6 minutes<sup>37</sup> after mixing, which agrees with the working time measured by rheometry (**Figure 3.3C**) and is comparable to the setting times for calcium phosphate cements.<sup>2</sup>

MG composites achieved a maximum compressive yield strength of  $40 \pm 7$  MPa and modulus of  $936 \pm 46$  MPa after 1 week of curing in air at RT (**Figure 3.4A-B**). These composites had an initial strength of 7.7 MPa and modulus of 36 MPa after 16 hours curing at RT. nHA composites exhibited initial strength and moduli much greater than MG composites as expected due to the increased surface area-to-volume ratio of the mechanically robust nanoparticles.<sup>38,39</sup> These cements had an initial compressive yield strength and modulus of  $31 \pm 3$  MPa and  $452 \pm 35$  MPa, respectively. The composites reached a yield strength of  $90 \pm 6$  MPa and modulus of  $1267 \pm 277$  MPa after 1 week (**Figure 3.4C-D**). The mechanical properties of both composites increased over the first week, indicating that complete crosslinking was achieved 1 week after fabrication. The physical appearance of the composites post-compression supports this finding. MG composites up to 48 hours cure time experience some elastic recovery to their original shape around 30 minutes post-compression, where plastic deformation is more evident in the 1- and 2-week samples (**Figure 3.4E**). These changes in resilience are less apparent in the stronger nHA samples (**Figure 3.4F**). Trabecular bone is reported to have a compressive strength of 5-10 MPa and modulus of 50-400 MPa.<sup>40-42</sup> Therefore, the initial compressive strength and modulus of MG composites are close to the properties of trabecular bone and nHA composites exceed these properties. Both composites are mechanically stronger than trabecular bone after 1 week.

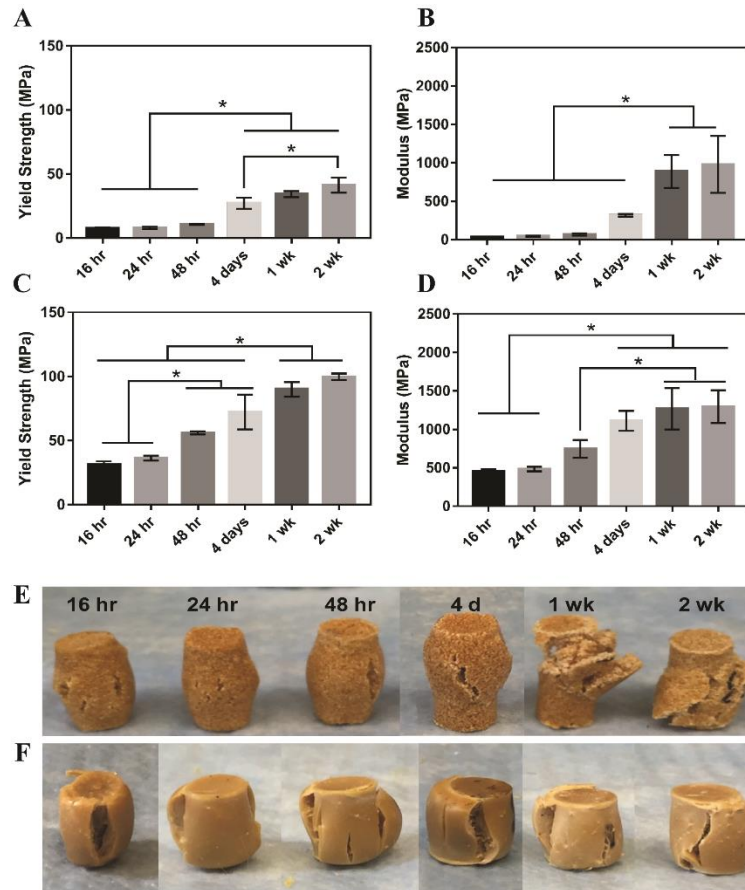


**Figure 3.4.** Mechanical properties of PTKUR/ceramic composites under static compressive loading. (A) Yield strength and (B) modulus of PTKUR/MG composites measured versus time for up to two weeks. (C) Yield strength and (D) modulus of PTKUR/nHA composites measured versus time for up to two weeks. Maximum compressive properties were achieved after 1-week cure time. The physical appearance of (E) MG and (F) nHA composites after compressive testing supports this finding.

The degradation rate of PTKUR films under hydrolytic and oxidative conditions was measured *in vitro*. PTKUR was compared to PCLUR as this material has been shown to degrade slowly *in vivo*.<sup>5</sup> PTKUR degraded completely after 4 days *in vitro* in oxidative media (**Figure 3.5A**) but experienced minimal hydrolytic degradation in PBS after 4 months (**Figure 3.5B**). SEM images of PTKUR after 24, 48, and 72 hours in oxidative media show morphological changes in the films in response to degradation, as evidenced by the formation of pores in the material (**Figure 3.5C-E**). PCLUR degraded minimally in

PBS as expected and did not completely degrade in oxidative media until about 5 months.

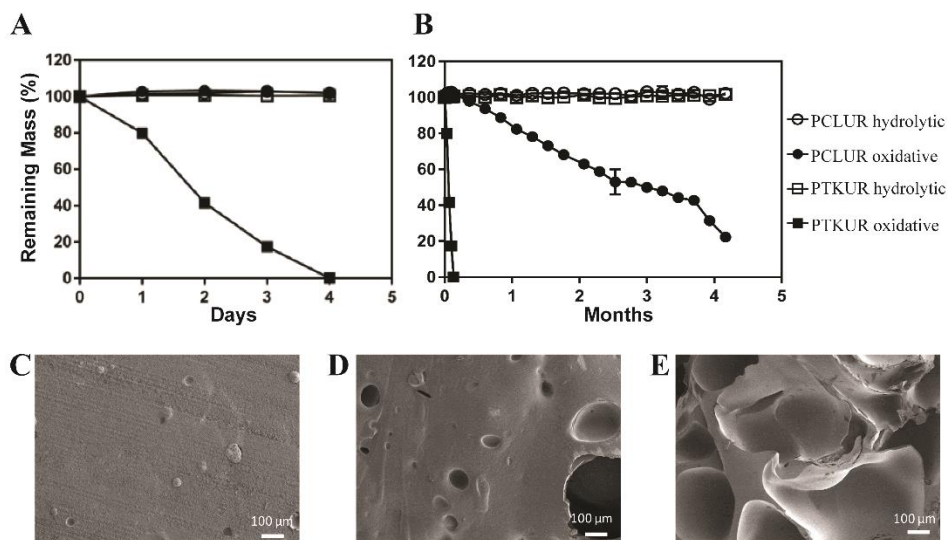


**Figure 3.5.** Degradation of PCLUR and PTKUR films. (A) PTKUR films were hydrolytically stable in PBS despite their rapid degradation in oxidative media after only 4 days. (B) After 4 months, PCLUR and PTKUR substantially degraded in oxidative medium, while no degradation was observed in PBS. (C-E) SEM images show the effects of oxidative degradation on the architecture of the PTKUR films after (C) 24 h, (D) 48 h, and (E) 72 h.

*In vitro characterization.* The osteoblast precursor MC3T3 cell line was used in all *in vitro* studies to assess cell attachment and proliferation. SEM images show that cells attached and spread on MG (**Figure 3.6A**) and nHA (**Figure 3.6B**) composites after 24 h culture. Cell proliferation on the films was assessed for up to 7 days post-seeding by measuring the change in total protein with time. **Figure 3.6C** shows that the cell population on MG composites increased with time, but the differences were not significant. Cells proliferated on nHA composites, as evidenced by the increase in total protein from day 1 to day 7. Hydroxyapatite is the primary mineral component in bone, and therefore MC3T3 cells were expected to adhere and proliferate on scaffolds comprising 60 wt% nHA.<sup>43</sup> While MG contains only 15% HA, the beta-tricalcium phosphate ( $\beta$ -TCP) component is also an osteoconductive ceramic.<sup>44,45</sup>



**Figure 3.6.** MC3T3 cells (arrows) attached and spread on (A) MG and (B) nHA composites after 24 h incubation. Scale bar = 50 µm. (C) Measurements of total protein versus time indicate that cells proliferated faster on nHA composites.

The slower proliferation rate of MC3T3 cells on MG composites could potentially be explained by the relatively large size (100 – 300 µm) of the MG microparticles, resulting in relatively large areas of polymer that are less osteoconductive than the ceramic. In contrast, phase-separation of the nHA and polymer components was not observed in the nHA composites, suggesting that the nHA is more uniformly distributed due to its smaller particle size.

*Tissue and cellular response in the femoral condyle defect model.* The composites were injected into femoral condyle plug defects in rabbits to assess bone healing and cement resorption. *In vivo* x-ray imaging immediately following the surgery indicated good placement and complete fill of the defect with the materials. µCT images of MG and nHA cements at 6 and 12 weeks are shown in **Figure 3.7**. Trabecular densification was evident at the periphery of the defects, indicating that the material was integrated with the host bone and initiating a healing response. Low-magnification (2X) images of histological sections stained with Stevenel’s Blue stain show appositional growth of dense trabecular bone near the host bone-cement interface at 12 weeks (**Figure 3.8**).

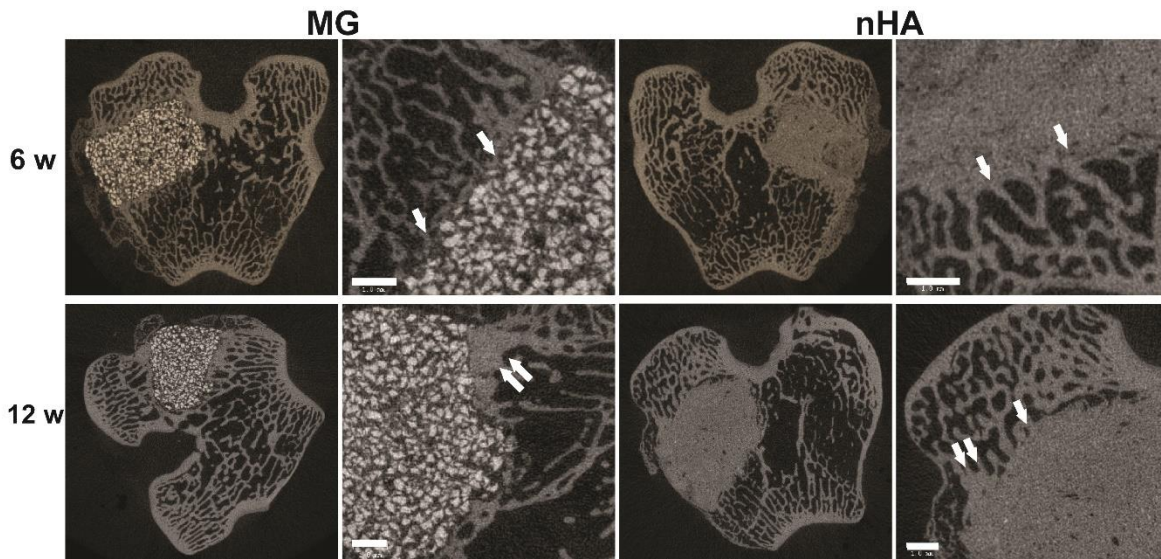


**Figure 3.7.** Images of transverse  $\mu$ CT sections of PTKUR/MG and PTKUR/nHA composite cements explanted at 6 and 12 weeks. Higher magnification images of the defect periphery show evidence of trabecular infiltration (single white arrows) and trabecular densification (double white arrows). Scale bar = 1 mm.

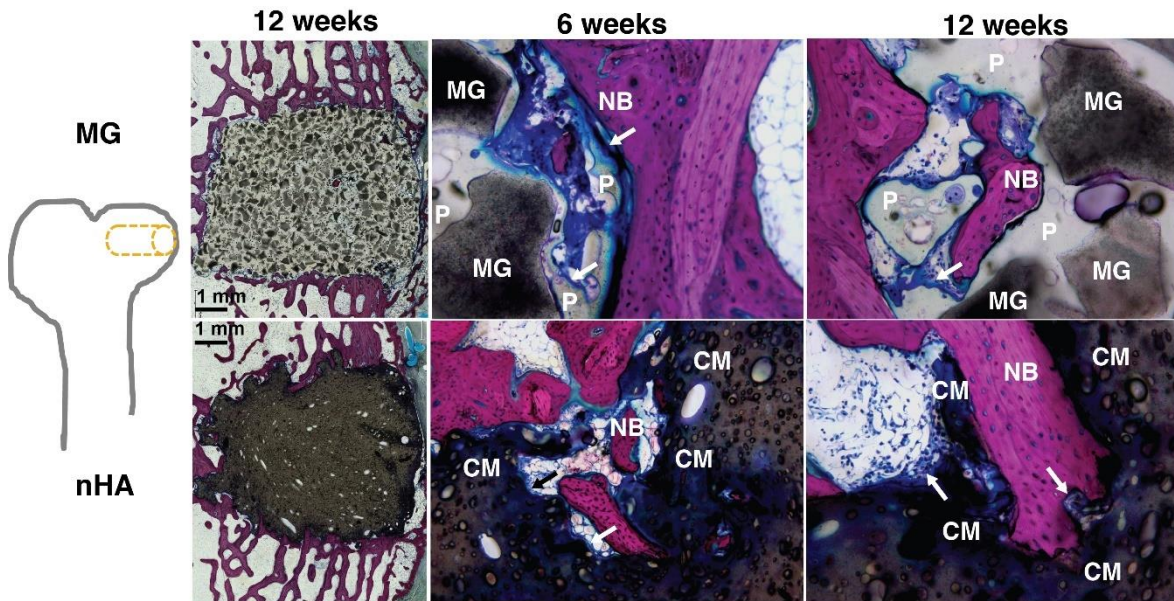


**Figure 3.8.** Images of transverse histological sections of PTKUR/MG and PTKUR/nHA composite cements. Low-magnification (2X) images of cements at 12 weeks show appositional growth of dense trabecular bone near the host bone-cement interface. Higher magnification (20-40X) images of PTKUR/MG cements at 6 and 12 weeks reveal evidence of residual MG (dark grey) particles, resorption of PTKUR (P, light grey), cellular infiltration (blue), osteoid (arrows), and new bone (NB, red) formation. Similar observations were made for PTKUR/nHA cements, but the nHA particles could not be distinguished due to their small size. Resorption of the cement (CM) was evident in the histological sections.

The materials were well-tolerated by the host tissue and no adverse reactions were evident. Higher magnification (20-40X) images show remodeling and integration of the cements with host bone near the surface of the cements at 6 and 12 weeks. Due to the relatively large size of MG particles (100 – 300  $\mu\text{m}$ ), the PKTUR (P) and MG particles (MG) could be distinguished in the histological sections. PTKUR resorption near the interface was observed, resulting in cellular infiltration and new bone (NB, red) formation. Osteoid (arrows) was observed near the surface of the residual PTKUR. While the nHA particles were too small to distinguish in the histological sections, similar phenomena were observed for nHA cements. Resorption of the cement (CM) near the host bone interface resulted in new bone formation and osteoid was evident near the surface of the cement.

Resorption appeared to be cell-mediated, as indicated by the irregular morphology of the cement (black arrows, **Figure 3.9**) and the presence of osteoclast-like cells, identified as large (>50  $\mu\text{m}$ ) multi-nucleated (nuclei stained dark blue, **Figure 3.9**) cells, near the bone-cement interface.



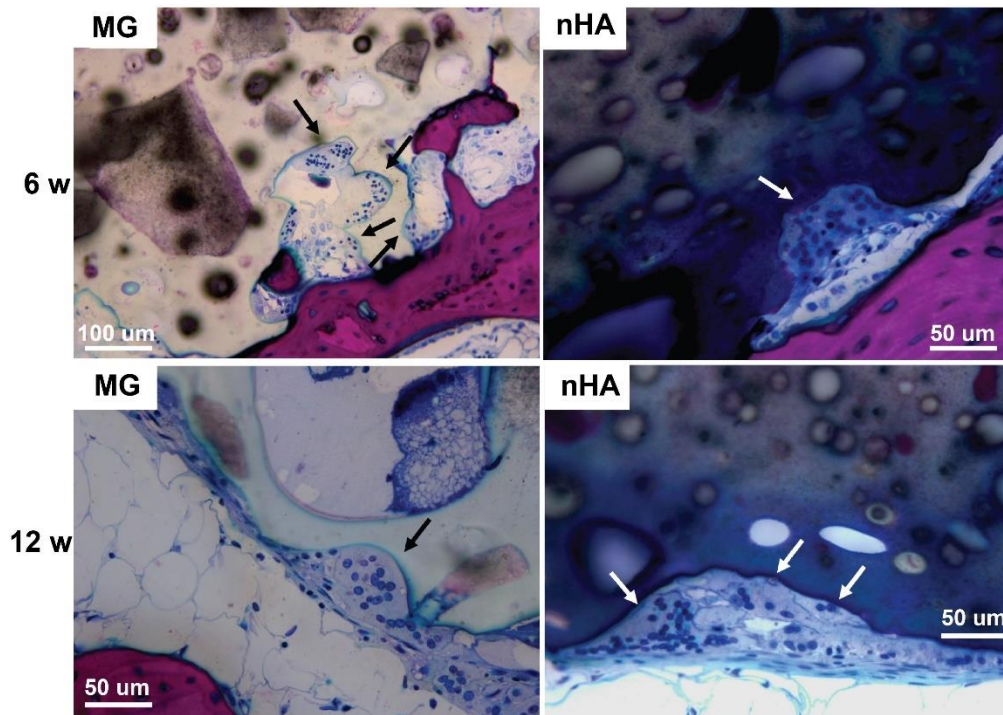


**Figure 3.9.** Resorption of PTKUR/MG and PTKUR/nHA cements mediated by osteoclast-like cells at 6 and 12 weeks. Osteoclasts are identified as large (>50  $\mu\text{m}$ ) multi-nucleated (nucleus stains dark blue) cells near the host bone-cement interface.

In contrast, negligible degradation was observed in the interior of the cement. These findings are consistent with the notion that resorption of the cements was surface-mediated by osteoclasts and/or macrophages through an ROS mechanism (**Figure 3.5**) as we have reported previously for PTKUR scaffolds implanted in cutaneous wounds.<sup>20</sup> Due to their relatively large size (100-300  $\mu\text{m}$ ), MG particles can be observed in the SEM images as a distinct phase (“MG”, **Figure 3.2F**). Since osteoclasts are smaller than MG particles, resorption of the MG and PTKUR phases is anticipated to proceed at different rates. In contrast, the smaller nHA particles (100 nm) cannot be distinguished from the PTKUR component (**Figure 3.2G**). At the length scale of an osteoclast, the nHA composites comprise a single phase and are anticipated to resorb at a rate averaged over the resorption rates of the individual nHA and PTKUR components. Thus, differences in MG and nHA

particle size may affect graft resorption. Due to the low (<10%) porosity of the cements, the rate of cellular infiltration and remodeling was slow. Increasing the porosity would be anticipated to accelerate infiltration of cells and consequent new bone formation.<sup>4</sup>

### 3.5 Conclusion

In this study, a novel low-molecular weight thioketal diol crosslinker was synthesized to prepare cell-degradable bone cements with initial bone-like strength. The cements exhibited initial compressive strength exceeding that of trabecular bone, working times comparable to commercial bone cements (5 – 10 min), and degradation in response to reactive oxygen species secreted by cells. When implanted into femoral condyle plug defects in rabbits, the cements supported appositional new bone growth, osteoclast-mediated resorption, and integration with host bone. These findings highlight the potential of poly(thioketal urethane)/ceramic composite bone cements for repair of bone damaged by trauma or disease.

## References

1. Kühn K-D. Bone cements: up-to-date comparison of physical and chemical properties of commercial materials: Springer 2000.
2. Bohner M. Design of ceramic-based cements and putties for bone graft substitution. *Eur Cell Mater* 2010;20(1):3-10.
3. Wagoner Johnson AJ, Herschler BA. A review of the mechanical behavior of CaP and CaP/polymer composites for applications in bone replacement and repair. *Acta Biomaterialia* 2011;7(1):16-30.
4. Adhikari R, Gunatillake PA, Griffiths I, Tatai L, Wickramaratna M, Houshyar S, Moore T, Mayadunne RT, Field J, McGee M and others. Biodegradable injectable polyurethanes: synthesis and evaluation for orthopaedic applications. *Biomaterials* 2008;29(28):3762-3770.
5. Dumas JE, Davis T, Holt GE, Yoshii T, Perrien DS, Nyman JS, Boyce T, Guelcher SA. Synthesis, characterization, and remodeling of weight-bearing allograft bone/polyurethane composites in the rabbit. *Acta Biomaterialia* 2010;6(7):2394-2406.
6. Bonzani IC, Adhikari R, Houshyar S, Mayadunne R, Gunatillake P, Stevens MM. Synthesis of two-component injectable polyurethanes for bone tissue engineering. *Biomaterials* 2007;28(3):423-433.
7. Dumas JE, Zienkiewicz K, Tanner SA, Prieto EM, Bhattacharyya S, Guelcher SA. Synthesis and characterization of an injectable allograft bone/polymer composite bone void filler with tunable mechanical properties. *Tissue Engineering Part A* 2010;16(8):2505-2518.
8. Page JM, Prieto EM, Dumas JE, Zienkiewicz KJ, Wenke JC, Brown-Baer P, Guelcher SA. Biocompatibility and chemical reaction kinetics of injectable, settable polyurethane/allograft bone biocomposites. *Acta biomaterialia* 2012;8(12):4405-4416.
9. Dumas JE, Prieto EM, Zienkiewicz KJ, Guda T, Wenke JC, Bible J, Holt GE, Guelcher SA. Balancing the Rates of New Bone Formation and Polymer Degradation Enhances Healing of Weight-Bearing Allograft/Polyurethane Composites in Rabbit Femoral Defects. *Tissue Engineering Part A* 2014;20(1-2):115-129.
10. Hafeman AE, Zienkiewicz KJ, Zachman AL, Sung H-J, Nanney LB, Davidson JM, Guelcher SA. Characterization of the degradation mechanisms of lysine-derived aliphatic poly(ester urethane) scaffolds. *Biomaterials* 2011;32(2):419-429.
11. de Bruyn PP, Kabisch WT. Bone formation by fresh and frozen, autogenous and homogenous transplants of bone, bone marrow and periosteum. *American Journal of Anatomy* 1955;96(3):375-417.
12. Dumas JE, BrownBaer PB, Prieto EM, Guda T, Hale RG, Wenke JC, Guelcher SA. Injectable reactive biocomposites for bone healing in critical-size rabbit calvarial defects. *Biomedical Materials* 2012;7(2):024112.
13. Prieto EM, Talley AD, Gould NR, Zienkiewicz KJ, Drapeau SJ, Kalpakci KN, Guelcher SA. Effects of particle size and porosity on in vivo remodeling of settable allograft bone/polymer composites. *J Biomed Mater Res B Appl Biomater* 2015.
14. Loi F, Córdova LA, Pajarinen J, Lin T-h, Yao Z, Goodman SB. Inflammation, fracture and bone repair. *Bone* 2016;86:119-130.

15. Schmidt-Bleek K, Kwee BJ, Mooney DJ, Duda GN. Boon and bane of inflammation in bone tissue regeneration and its link with angiogenesis. *Tissue Engineering Part B: Reviews* 2015;21(4):354-364.
16. Nukavarapu S, Freeman J, Laurencin C. *Regenerative Engineering of Musculoskeletal Tissues and Interfaces*: Woodhead Publishing; 2015.
17. Sheweita SA, Khoshhal KI, Baghdadi HH. Osteoporosis and Oxidative Stress—Role of Antioxidants. *Systems Biology of Free Radicals and Antioxidants*: Springer; 2014. p 2973-2995.
18. Garrett I, Boyce B, Oreffo R, Bonewald L, Poser J, Mundy G. Oxygen-derived free radicals stimulate osteoclastic bone resorption in rodent bone in vitro and in vivo. *Journal of Clinical Investigation* 1990;85(3):632.
19. Key LL, Wolf WC, Gundberg CM, Ries WL. Superoxide and bone resorption. *Bone* 1994;15(4):431-436.
20. Martin JR, Gupta MK, Page JM, Yu F, Davidson JM, Guelcher SA, Duvall CL. A porous tissue engineering scaffold selectively degraded by cell-generated reactive oxygen species. *Biomaterials* 2014;35(12):3766-3776.
21. Wilson DS, Dalmaso G, Wang L, Sitaraman SV, Merlin D, Murthy N. Orally delivered thioketal nanoparticles loaded with TNF- $\alpha$ -siRNA target inflammation and inhibit gene expression in the intestines. *Nat Mater* 2010;9(11):923-928.
22. LeGeros RZ. Properties of osteoconductive biomaterials: calcium phosphates. *Clinical orthopaedics and related research* 2002;395:81-98.
23. Talley AD, Mcenery MAP, Kalpakci KN, Zienkiewicz KJ, Shimko DA, Guelcher SA. Remodeling of injectable, low-viscosity polymer/ceramic bone grafts in a sheep femoral defect model. *Journal of Biomedical Materials Research Part B: Applied Biomaterials* 2016, in press.
24. International A. Standard test method for hydroxyl groups using reaction with p-toluenesulfonyl isocyanate (TSI) and potentiometric titration with tetrabutylammonium hydroxide. Volume E1899-16: ASTM International 2016.
25. Guelcher SA, Srinivasan A, Dumas JE, Didier JE, McBride S, Hollinger JO. Synthesis, mechanical properties, biocompatibility, and biodegradation of polyurethane networks from lysine polyisocyanates. *Biomaterials* 2008;29(12):1762-1775.
26. International A. Standard test method for isocyanate groups in urethane materials or prepolymers. ASTM International; 2010.
27. Guo R, Ward CL, Davidson JM, Duvall CL, Wenke JC, Guelcher SA. A transient cell-shielding method for viable MSC delivery within hydrophobic scaffolds polymerized in situ. *Biomaterials* 2015;54:21-33.
28. Harmata AJ, Uppuganti S, Granke M, Guelcher SA, Nyman JS. Compressive fatigue and fracture toughness behavior of injectable, settable bone cements. *Journal of the mechanical behavior of biomedical materials* 2015;51:345-355.
29. International A. Standard test method for compressive properties of rigid cellular plastics. ASTM International; 2016.
30. Schubert MA, Wiggins MJ, Anderson JM, Hiltner A. Role of oxygen in biodegradation of poly(etherurethane urea) elastomers. *Journal of Biomedical Materials Research* 1997;34(4):519-530.
31. Christenson EM, Anderson JM, Hiltner A. Oxidative mechanisms of

- poly(carbonate urethane) and poly(ether urethane) biodegradation: In vivo and in vitro correlations. *Journal of Biomedical Materials Research Part A* 2004;70A(2):245-255.
32. Guo R, Lu S, Page JM, Merkel AR, Basu S, Sterling JA, Guelcher SA. Fabrication of 3D scaffolds with precisely controlled substrate modulus and pore size by templated-fused deposition modeling to direct osteogenic differentiation. *Advanced healthcare materials* 2015;4(12):1826-1832.
  33. Dow polyurethanes - prepolymer definition. Volume 2016; 2014.
  34. Guelcher SA, Patel V, Gallagher KM, Connolly S, Didier JE, Doctor JS, Hollinger JO. Synthesis and In Vitro Biocompatibility of Injectable Polyurethane Foam Scaffolds. *Tissue Engineering* 2006;12(5):1247-59.
  35. Harmata AJ, Ward CL, Zienkiewicz KJ, Wenke JC, Guelcher SA. Investigating the effects of surface-initiated polymerization of  $\epsilon$ -caprolactone to bioactive glass particles on the mechanical properties of settable polymer/ceramic composites. *Journal of Materials Research* 2014;29(20):2398-2407.
  36. Parnell S, Min K, Cakmak M. Kinetic studies of polyurethane polymerization with Raman spectroscopy. *Polymer* 2003;44(18):5137-5144.
  37. Ashida K. *Polyurethane and related foams: chemistry and technology*: CRC press; 2006.
  38. Mi H-Y, Jing X, Salick MR, Cordie TM, Peng X-F, Turng L-S. Morphology, mechanical properties, and mineralization of rigid thermoplastic polyurethane/hydroxyapatite scaffolds for bone tissue applications: effects of fabrication approaches and hydroxyapatite size. *Journal of Materials Science* 2014;49(5):2324-2337.
  39. Rezwani K, Chen Q, Blaker J, Boccaccini AR. Biodegradable and bioactive porous polymer/inorganic composite scaffolds for bone tissue engineering. *Biomaterials* 2006;27(18):3413-3431.
  40. Fernando S, McEnery M, Guelcher S. Polyurethanes for bone tissue engineering. *Advances in Polyurethane Biomaterials* 2016:481.
  41. Karageorgiou V, Kaplan D. Porosity of 3D biomaterial scaffolds and osteogenesis. *Biomaterials* 2005;26(27):5474-5491.
  42. Muggli DS, Burkoth AK, Anseth KS. Crosslinked polyanhydrides for use in orthopedic applications: degradation behavior and mechanics. *Journal of biomedical materials research* 1999;46(2):271-278.
  43. Buckwalter J, Glimcher M, Cooper R, Recker R. Bone biology. *J Bone Joint Surg Am* 1995;77(8):1256-1275.
  44. Gaasbeek RDA, Toonen HG, van Heerwaarden RJ, Buma P. Mechanism of bone incorporation of  $\beta$ -TCP bone substitute in open wedge tibial osteotomy in patients. *Biomaterials* 2005;26(33):6713-6719.
  45. Giannoudis PV, Dinopoulos H, Tsiridis E. Bone substitutes: an update. *Injury* 2005;36(3):S20-S27.

## CHAPTER 4

### IV. REMODELING OF A SETTABLE, CELL-DEGRADABLE POLY(THIOKETAL-URETHANE) AUTOGRAFT EXTENDER FOR A MINIMALLY INVASIVE BONE GRAFT IN RABBITS

#### **Adapted from:**

McGough, MAP, Shiels, SM, Zienkiewicz, KJ, Wenke, JC, Guelcher, SA. “Remodeling of a settable, cell degradable poly(thioketal urethane) autograft extender for a minimally invasive bone graft in rabbits.”

#### 4.1 Abstract

Iliac crest autograft (AG) is the gold standard for bone grafting. Due to the limited supply of AG, calcium phosphate ceramics have been proposed as AG extenders to minimize the volume of AG required to maintain osteoinductivity. Current strategies aim to improve handling and afford mechanical integrity to the graft for a minimally invasive procedure. In this study, a moldable, settable poly(thioketal urethane) (PTKUR) AG extender with a setting time of 20-30 minutes was developed to expand the use of AG and provide mechanical stability to the defect throughout remodeling. The cell-mediated degradation mechanism of PTKUR makes the material a promising candidate for use as an AG extender. AG was anticipated to enhance infiltration of cells into the defect, thereby initiating oxidative degradation of PTKUR and accelerating remodeling. Histological analysis of a preliminary study in a rat model showed that cells were able to infiltrate the PTKUR AG extender and osteogenesis was ongoing at 4 weeks. Subsequent implantation in a biologically stringent spine model showed ample remodeling from the superior and inferior transverse processes. Histological analysis combining data from stains and fluorochrome injections showed lamellar bone formation ongoing near the base of the transverse processes after 8 weeks. Similar findings in a second group incorporating

calcium phosphate particles with the PTKUR AG extender provided evidence that AG may be extended further. These findings show that PTKUR AG extenders resorb at a rate complementary to bone regeneration and highlight the potential to further minimize the volume of AG needed while enhancing bone regeneration.

#### 4.2 Introduction

The American Academy of Orthopaedic Surgeons reports that over half a million bone grafting procedures are performed every year in the United States.<sup>1</sup> Iliac crest autograft (AG) is the gold standard for bone grafting of open fractures and has utility in extremity, spine, and craniomaxillofacial bone regeneration.<sup>2-5</sup> However, aside from the well-known limitations of available quantity and donor site morbidity, AG lacks mechanical integrity and generally requires the additional implantation of a retainer to maintain graft placement throughout healing.<sup>6</sup> Local delivery of growth factors, such as recombinant human bone morphogenetic protein-2 (rhBMP-2), from synthetic scaffolds is used clinically and new carriers are being investigated<sup>6-9</sup>, but the risks of adverse events associated with these growth factors have been reported to be higher than those associated with iliac crest AG.<sup>10,11</sup> AG extenders have been proposed to combine the osteoinductivity of AG with the osteoconductivity and mechanical integrity of established bone graft substitutes.<sup>12</sup> Additionally, AG extenders may allow the use of AG in large defects that require more graft than can be harvested or conserve AG for revision or future use. Furthermore, use of an extender may eliminate the need for multiple surgical sites, thereby reducing patient morbidity.

Ceramics such as hydroxyapatite,  $\beta$ -tricalcium phosphate ( $\beta$ -TCP), and calcium sulfate have been proposed as porous AG extenders to minimize the volume of AG required and enhance osteoconductivity.<sup>13-19</sup> Clinical studies have shown that blending AG

bone with ceramic particles at ratios up to 1:1 leads to comparable or improved new bone formation than achieved with AG alone.<sup>13,14,19,20</sup> While these extenders enhance osteogenesis and reduce the amount of AG needed, their particulate form yields unfavorable handling properties that could lead to implantation and fixation challenges that may limit their application.<sup>21-24</sup> A ceramic/collagen putty AG extender has been reported to improve new bone formation in rabbits at ratios of 1:1 AG:extender.<sup>18</sup> However, a settable AG extender with mechanical properties comparable to those of trabecular bone has not been previously reported.

While polymeric AG extenders have also shown promise in small animal models<sup>12,25,26</sup>, injectable and settable polymers have not been previously investigated in this application. In Chapter 3, injectable and settable poly(thioketal urethane)s (PTKURs) set to yield bone cements with mechanical properties matching those of trabecular bone.<sup>27</sup> Furthermore, PTKUR degrades in the oxidative microenvironment generated by osteoclasts and macrophages present during wound healing and bone remodeling.<sup>27-29</sup> Thus, the favorable handling, mechanical, and resorptive properties of PTKUR render it a promising candidate for use as a settable AG extender that can be molded to conform to the geometry of the defect where it cures *in situ*.

An AG extender exhibiting handling and mechanical properties comparable to bone cements while maintaining sufficient osteoinductivity to promote bone healing could potentially improve outcomes for a number of orthopedic procedures, but these materials are currently not available. In this study, we report injectable and settable PTKUR AG extenders designed to exploit the osteoinductive properties of AG while providing injectability using minimally invasive surgical techniques, rapid cure (e.g. tack-free time



10-20 min), and bone-like mechanical properties. We hypothesized that cells would infiltrate the PTKUR AG extender through cell-mediated resorption of the polymer, resulting in remodeling of the AG particles and consequent new bone formation. Handling properties were measured by direct measurement of tack-free and setting times, and mechanical properties were assessed by compression testing. Remodeling of PTKUR AG extenders was evaluated in two stringent models of bone regeneration: a femoral segmental defect model in rats and a posterolateral intertransverse process bone formation model in rabbits. To our knowledge, this is the first report of a settable, compression-resistant autograft extender investigated in this challenging, non-instrumented model in rabbits.

#### 4.3 Materials and Methods

*Experimental design.* A moldable PTKUR AG extender was formulated to cure to a compression-resistant solid *in situ* at a clinically relevant rate. The potential of this approach was first investigated in a critical sized defect in rat femurs. After observing successful implantation, space maintenance, and cellular infiltration, the remodeling potential was evaluated in a commonly-used and stringent rabbit spine model.

*Materials.* Materials for thioketal diol (TK) synthesis, including solvents, were purchased from Sigma-Aldrich. Lysine triisocyanate-poly(ethylene glycol) prepolymer (LTI-PEG) was acquired from Ricerca Biosciences LLC and used as received. Iron (III) acetylacetonate (FeAA) catalyst was purchased from Fisher Scientific. Calcium phosphate ceramic particles (CaP, MASTERGRAFT®: 85%  $\beta$ -TCP/15% hydroxyapatite) were acquired from Medtronic and ground to 100-300  $\mu$ m diameter particles using a mortar and pestle.

*Synthesis of thioketal diol.* A TK diol (MW = 196 g/mol) was synthesized as described previously.<sup>27</sup> Briefly, thioglycolic acid and 2,2-dimethoxypropane were reacted

in the presence of bismuth (III) chloride for 24 hours at room temperature. The intermediate product was filtered and dried for 24 hours under vacuum. The intermediate was then dissolved in 100 mL of tetrahydrofuran (THF) and slowly added to lithium aluminum hydride (LiAlH<sub>4</sub>) in diethyl ether at 0°C. After all of the intermediate was added, the reaction was refluxed at 52°C overnight. Excess LiAlH<sub>4</sub> was quenched by adding water dropwise. The product was then filtered from the by-products and extracted using aqueous NaOH and diethyl ether. The aqueous layer was removed using a separation funnel and sodium sulfate. After filtering, solvent was removed from the product using rotary evaporation and the product dried under vacuum at least 24 hours. FeAA catalyst was dissolved directly in the dry TK diol (0.5% FeAA in TK) by stirring in a closed vial overnight.

*Autograft extender fabrication and characterization.* Settable PTKUR AG and AG/CaP extenders were prepared by adapting a reactive liquid molding technique. Two volume fractions of AG were investigated, and the volume fraction PTKUR was selected as the minimal amount required to provide desirable handling properties. The AG extender incorporated 69 vol% AG, which was the highest concentration that could be achieved to maintain a cohesive paste when mixed with the reactive PTKUR (31 vol%). The AG/CaP extender incorporated 44 vol% AG, which is at the low end of the range that has been previously reported to be effective for bone regeneration.<sup>13,14,19,20,26</sup> CaP particles (17 vol%) were added to enhance the osteoconductivity while maintaining a cohesive paste when mixed with the reactive PTKUR (39 vol%). AG was weighed and (when appropriate) mixed with CaP prior to reacting with the polymer components. Separately, TK diol (with catalyst) and LTI-PEG prepolymer (NCO=21%) were hand mixed together for 45 seconds.

An NCO:OH index of 140 was used for all extenders. AG or AG/CaP was then added to the reactive polymer mixture and mixed vigorously until homogeneous. Tack-free time was reported as the time when a metal spatula no longer stuck to the composite material. Setting time was measured by hand as the time after which the material was no longer moldable. The morphology of the PTKUR AG extenders was visualized by scanning electron microscopy (SEM, Ziess Merlin) of gold coated specimens.

The degradation characteristics of PTKUR were investigated in accelerated oxidative conditions to estimate degradation *in vivo*.<sup>27,28</sup> PTKUR films, without AG or CaP, were cast in cylindrical tubes and cured overnight. The material was cut into small discs (50 mg) using an IsoMet Low Speed Saw. The initial mass of each sample was recorded before immersing the samples in oxidative media (20 wt% hydrogen peroxide in 0.1 M cobalt chloride) or PBS (hydrolytic control). Samples were incubated at 37 °C on a shaker table for 72 hours. They were then washed 3X in 1 mL of deionized water and dried under vacuum for 48 hours. The mass of the dry sample was compared to the initial mass to determine extent of degradation in oxidative and hydrolytic conditions. The degradation characteristics of the PTKUR films were compared to those of a polyester/LTI-PEG polyurethane (PEUR) that has been shown to degrade hydrolytically.<sup>30,31</sup>

Bulk compressive properties were tested to understand the mechanical limits of the material. AG and AG/CaP extenders were synthesized as described above and molded into cylindrical tubes with a diameter of 6 mm (n=3). The specimens were compressed under a weight (0.96 kg) for 2 hours to ensure cohesion and mimic forces of surrounding musculature *in vivo*.<sup>27,32</sup> After 24 hours, completely cured materials were removed from the molds and hydrated over night with wet gauze at 37 °C. Hydrated samples were cut to a

height of 12 mm (2X diameter) prior to mechanical testing. Prepared specimens were compressed between flat platens to a preload of 5 N and then to failure at a rate of 25 mm min<sup>-1</sup> (MTS 858 Bionix Servohydraulic Test System). The strain and load were recorded throughout the test and used to calculate engineering stress and engineering strain based on the specimen geometry. The compressive modulus, strength, and yield strain were calculated from the resulting stress-strain curve.

*In vivo analysis.* All animal procedures were approved by the Institutional Animal Care and Use Committee of the US Army Institute of Surgical Research, Fort Sam Houston, TX, and were conducted in compliance with the Animal Welfare Act, implementing Animal Welfare Regulations, and the principles of the Guide for the Care and Use of Laboratory Animals.

*PTKUR AG extender in a rodent model.* A critical-size segmental defect in athymic nude rat femurs was used to assess cellular infiltration of the PTKUR AG extender at an early time point (4 weeks). Fresh iliac crest bone graft (ICBG) was harvested from donated New Zealand White (NZW) rabbit cadavers and used in place of “autograft” for the rat study. For purposes of clarity, we refer to the xenograft ICBG as autograft in this study and the use of athymic rats prevents the immune rejection.<sup>33-35</sup> AG from the same animals and syngeneic grafts were not used because of the lack of cancellous bone in rats.<sup>36</sup> Following humane euthanization, the NZW rabbit ICs were exposed and AG aseptically removed using an oscillating saw. The AG was scraped of soft tissue and processed using a bone mill (R. Quetin) to yield particulated bone, approximately 3 mm in diameter. Bone was patted dry with sterile gauze and set aside until use.

Immediately following AG harvesting, a 6-mm segmental defect was created in the

right femurs of six anesthetized athymic nude rats (Harlan Laboratories, Houston TX; 341±8.5 g). Animals were premedicated with SR Buprenorphine (1.2 mg/kg SC) and anesthetized with 1-3% isoflurane in oxygen. The right hindlimb was shaved and prepped for sterile surgery with alternating 70% ethanol and betadine scrubs. The right femur was exposed, a stabilizing polyacetyl plate affixed with 4 threaded K-wires, and a 6 mm mid-diaphyseal segment of the bone removed.<sup>37,38</sup> Animals received one of two treatment groups: AG only (n=3) or PTKUR AG extender (n=3). The PTKUR AG extenders were mixed as described above with the composition of 69 vol% AG/31 vol% PTKUR (60 wt% AG/40 wt% PTKUR) described above. The PTKUR AG extender was loaded into a blunted 1 cc syringe five minutes prior to use. The AG extender was then injected into the defect space and positioned using a small surgical elevator to ensure contact with the bone on each side. The materials cured for 10 minutes *in situ* prior to wound approximation and closure. High resolution x-ray images (Faxitron X20) were acquired and the animal recovered. Similar volumes of AG only (no PTKUR) were used as clinical controls. Four weeks post-operative, animals were sedated, euthanized, and the femurs harvested and placed in 10% neutral buffered formalin for  $\mu$ CT and histology. Bone regeneration and material degradation were assessed via  $\mu$ CT (Scanco  $\mu$ CT 50) and non-decalcified histology. Formalin fixed femurs were dehydrated in ethanol and embedded in PMMA for histological analysis. Sagittal sections were taken from the center of the defect and stained with Sanderson's Rapid Bone Stain and Van Gieson to qualitatively assess cellular infiltration, bone regeneration, and polymer degradation.

*Autograft extender in challenging in vivo spine model.* After confirming cellular infiltration at early time points in the rat model, remodeling of PTKUR AG extenders was

evaluated in a stringent posterolateral intertransverse process bone formation model in 13 New Zealand White rabbits ( $4.0 \pm 0.06$  kg). The same groups from the rodent model study were used in this *in vivo* study with the addition of an AG + CaP extender (AG/CaP) hypothesized to reduce the AG content even further. This additional group comprised 44 vol% AG blended with 17 vol% CaP and 39 vol% PTKUR (65 wt% total solids in 35 wt% PTKUR). All graft components were gamma irradiated at approximately 25 kGY prior to surgery.

Animals were premedicated with SR Buprenorphine (0.5 mg/kg SC). Anesthesia was induced with ketamine/xylazine (25/5 mg/kg IM, respectively) and maintained with 1-3% isoflurane via a laryngeal mask airway. Animal dorsums were shaved and prepped for sterile harvest and surgery with alternating 70% ethanol and betadine scrubs. The IC harvest and placement of bone graft procedures were accessed from a single cutaneous midline incision from L4 to L7. First, 3 cc of IC was harvested from each IC. Briefly, sharp dissection was used to access the IC through the posterior musculature and blunt dissection used to elevate the muscle off the IC. Using an oscillating saw, the dorsal third of each IC was removed followed by closure of the musculature over the remaining IC. ICBG was morselized as described above using a bone mill and set aside until implantation of the bone grafts. Following ICBG harvest, two paramedian incisions were made through the fascia and musculature over the L5-L6 transverse processes. Using blunt dissection, the plane between the multifundus and longissimus muscles was developed to expose the transverse processes as well as the intertransverse membrane. The dorsolateral two-thirds of the transverse processes were decorticated using an electric burr to enhance cellular activity at the tissue/implant interface.

Materials were prepared as described above. For the AG/CaP extender, AG and CaP were mixed by hand until homogeneous before adding to the polymer mixture. Materials were loaded into a blunted 5 cc syringe and delivered on the paraspinal bed, between the decorticated transverse processes. A surgical elevator was used to adjust positioning and ensure contact between the material and the transverse processes. Once the material was placed, the surrounding musculature was sutured and the wound closed. *In vivo* CT scans (Prime Aquilon TSX-303A, Toshiba) were acquired immediately and at 4 and 8 weeks post-operatively to investigate the progression of mineralization. Aqueous fluorochromes were injected subcutaneously at two (calcein green, 10 mg/kg) and six (xylenol orange, 90 mg/kg) weeks as a complementary tool to investigate this mineralization progression.<sup>39</sup>

Eight weeks post-implantation, the animals were anesthetized and euthanized with sodium pentobarbital (Fatal Plus®), the spinal segments (L4-L7) were harvested, and the soft tissue removed. Spinal segments were cut in half longitudinally then immersed in 10% formalin for  $\mu$ CT and non-decalcified histology.  $\mu$ CT was acquired at a voxel size of 24.2  $\mu$ m and evaluated from both coronal and sagittal views through the entirety of the implant followed by dehydration and embedding in PMMA for histological analysis. Longitudinal histology sections were made to assess bone formation between the L5 and L6 transverse processes. Serial sagittal sections (30-70  $\mu$ m), with both L5 and L6 in view, were cut from the lateral most incidence of the implant, until the spinal column was reached. Every other section was stained with Sanderson's Rapid Bone Stain/Van Gieson to visualize cellular activity and neotissue formation. The remaining sections were used for fluorochrome analysis. An Olympus BX60 microscope equipped with a Luminera Infinity 2 camera and

an Olympus Reflected Light Fluorescence attachment was used to image sections at 2X magnification. 2X images were stitched together to visualize the continuity of new bone and fluorescence throughout the entire section. Magnified images were also acquired for cellular detail. Stained and fluorescent images were overlaid to provide an understanding of the mechanism of bone regeneration from the transverse processes and implanted AG. For each specimen, the section with the largest area of new bone without reaching the vertebral column was selected for further analysis. Image J was used to quantify the front of new bone growth and intertransverse process (ITP) space dimensions at each time point (2 weeks-green, 6 weeks-orange, 8 weeks-red (Sanderson's Rapid Bone stain)). In order to make consistent measurements between groups, the transverse processes were included when measuring distances in both the fluorescent and brightfield images. The measurements were then normalized by the entire process-to-process distance for each sample (**Figure 4.7A**).

*Statistical methods.* Unpaired t-tests were used to compare the handling and mechanical properties of the extenders and the data is reported with standard deviation. Progression of bridging between the processes was calculated as the slope of the linear regression of normalized bridging with time. The data is reported with standard error of the mean (SEM). A two-way ANOVA (GraphPad Prism) was used to compare the statistical significance between groups and time points. A post-hoc Tukey's multiple comparison test compared the difference in bridging between the AG extender, AG/CaP extender, and AG control at each individual time point. A second post-hoc Tukey's test compared the increase in bridging over time for each individual group.

#### 4.4 Results

*Synthesis of PTKUR AG extenders.* The FeAA catalyst has a high selectivity for



the gelling reaction (gelling reaction rate constant / blowing reaction rate constant = 6.4).<sup>27,40</sup> However, the AG particles contained a significant amount of moisture. PTKUR AG and AG/CaP extenders were prepared by manipulating the fabrication technique to initiate the polymerization reaction prior to introducing the AG component. The “pre-reaction” time of 45 seconds allowed the TK diol/LTI-PEG reaction to dominate over the water/LTI-PEG reaction when AG was added. After pre-reacting about 1 minute, the material was too crosslinked to homogeneously mix the AG or AG/CaP components into the polymer phase.

**Table 4.1.** Material properties of PTKUR AG extenders.

Material	Tack-Free Time (min:sec)	Setting Time (min:sec)	Modulus (MPa)	Ultimate Yield Strength (MPa)	Yield Strain (%)
AG Extender	18:29 ± 0:42	29:04 ± 2:25	5.91 ± 0.789	1.17 ± 0.0950	18.4 ± 2.87
AG/CaP Extender	11:27 ± 2:23**	23:02 ± 2:17*	12.5 ± 0.868***	2.05 ± 0.126***	17.6 ± 1.00

(\*: P ≤ 0.05, \*\*: P ≤ 0.01, \*\*\*: P ≤ 0.001)

Tack-free and setting times are reported in **Table 4.1**. Thus, the AG/CaP extender set faster (23:02 ± 2:17 min) than the AG extender (29:04 ± 2:25), but both cured in less than 30 min. Representative SEM images of the AG (**Figure 4.1A**) and AG/CaP (**Figure 4.1B**) extenders indicate minimal porosity and an irregular pore architecture. The AG particles are not readily detectable likely due to the small size of the particulated AG and its cohesive integration within the PTKUR. The CaP particles (arrows, **Figure 4.1B**) can be observed in the AG/CaP extender, which also showed evidence of spherical pores associated with gas blowing due to the water reaction.<sup>41</sup>

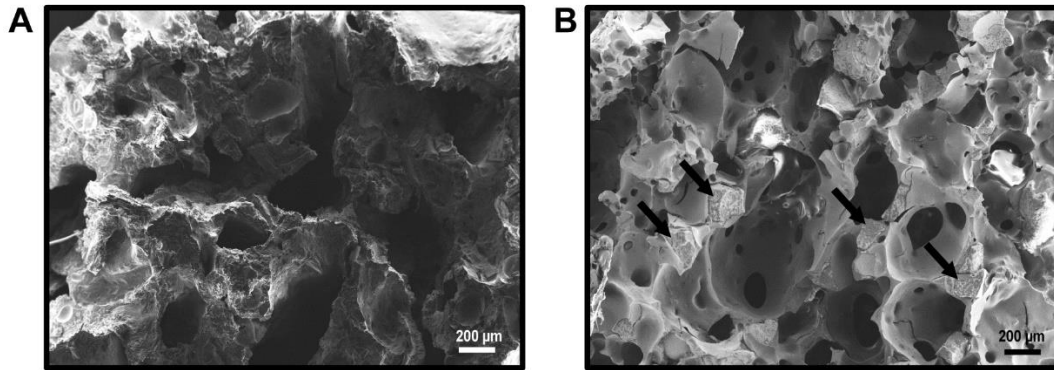


**Figure 4.1.** SEM images of AG and AG/CaP extenders. (A) The AG extender indicates minimal porosity and an irregular architecture. (B) The AG/CaP extender has irregular pores and interconnects throughout the material. Arrows indicate CaP particles.

PTKUR films were immersed in oxidative media to evaluate degradation in oxidative conditions simulating the wound healing microenvironment. Degradation of the PTKUR was compared to that of a degradable PEUR composed of a 300 g/mol polyester triol (poly( $\epsilon$ -caprolactone-*co*-glycolide-*co*-DL-lactide) and LTI-PEG prepolymer.<sup>31,42</sup> While the PTKUR film had completely degraded after 72 h in oxidative media, it showed no measurable degradation when immersed in PBS. In contrast, PEUR films showed a mass loss of 8.0% in oxidative conditions and 5.7% in PBS, which indicates a combination of degradation mechanisms when the polyester triol is used in PUR synthesis. These data suggest that PTKUR selectively degrades in response to ROS secreted by infiltrating cells. Mechanical properties were assessed after 24 h of cure time followed by hydration at 37°C overnight. The compressive modulus and strength of the AG/CaP extenders ( $12.5 \pm 0.9$  MPa and  $2.05 \pm 0.1$  MPa, respectively) were significantly higher than the AG extenders ( $5.91 \pm 0.8$  MPa and  $1.17 \pm 0.1$  MPa, respectively, **Table 4.1**). This difference can be attributed to the higher modulus and strength of the CaP particles compared to particulated bone. Despite the difference in yield strength, the yield strain for both extenders was 18%.

*Cellular infiltration in a rat model.* *In vivo* cellular infiltration of the low-porosity

PTKUR AG extender was first assessed in a segmental defect in rats. This study employed athymic rats and rabbit ICs to eliminate graft volume limitations. Histological sections of the AG extender group showed evidence of new bone formation throughout the implant after 4 weeks (**Figure 4.2A, B**). Bone forming cells were identified at the center of the defect area in both the AG extender (**Figure 4.2A, B**, arrows) and AG control (**Figure 4.2C, D**, arrows) groups and ongoing bone formation was indicated by the red staining in **Figures 4.2B, D**. These proof-of-concept experiments showed that low-porosity PTKUR AG extenders support cellular infiltration at 4 weeks, thereby justifying evaluation in the more challenging rabbit spine model.

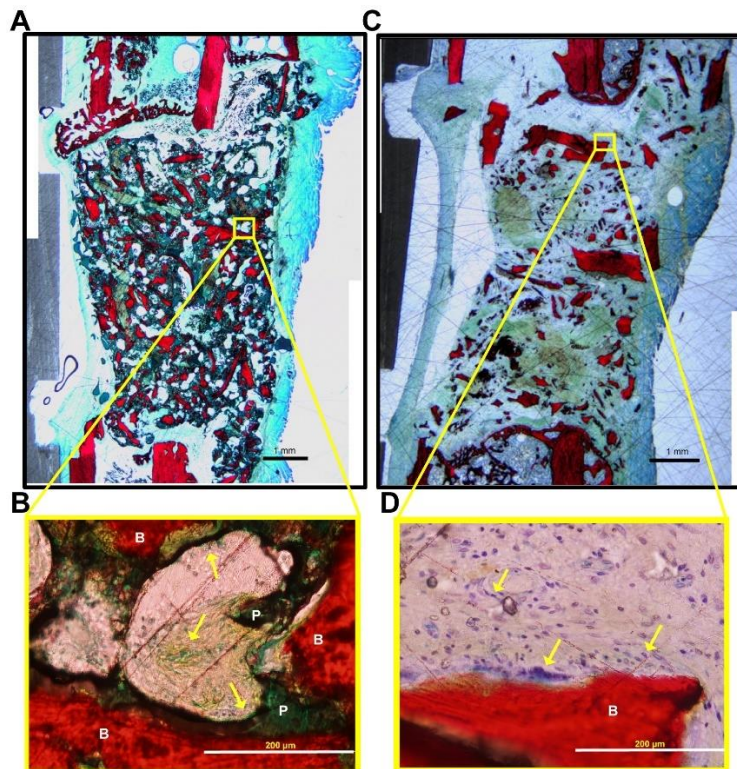


**Figure 4.2.** Images of histological sections of femoral segmental defects in the rat at 4 weeks post-implantation showing areas of cellular activity (arrows) and new bone formation near edges of implanted AG. (A-B) AG extender at (A) 2X and (B) 40X magnification. (C-D) AG control at (C) 2X and (D) 40X magnification. (bone: red (“B”), cell nuclei: dark blue, PTKUR: teal (“P”))

*AG extender remodeling in rabbits.* The rabbit spine model requires 2 cc graft to bridge L5 and L6 (**Figure 4.3A**) on each side of the vertebral column (4 cc total/animal). The PTKUR AG and AG/CaP extenders received 1.4 cc and 0.88 cc AG, respectively. Although *in vivo* CT images cannot provide sufficient resolution to image trabeculae, they showed correct placement of the implants at the time of surgery and provided qualitative data for temporal ossification. These images show a denser ITP space for the AG control than the experimental groups initially (**Figure 4.3B**) since more AG was implanted for this group. This trend is reversed at weeks 4 and 8, where the radiodensity is greatest for the area surrounding the AG/CaP extender and lowest for the AG control. All groups appear to have similarly sized intertransverse process masses at 4 and 8 weeks.

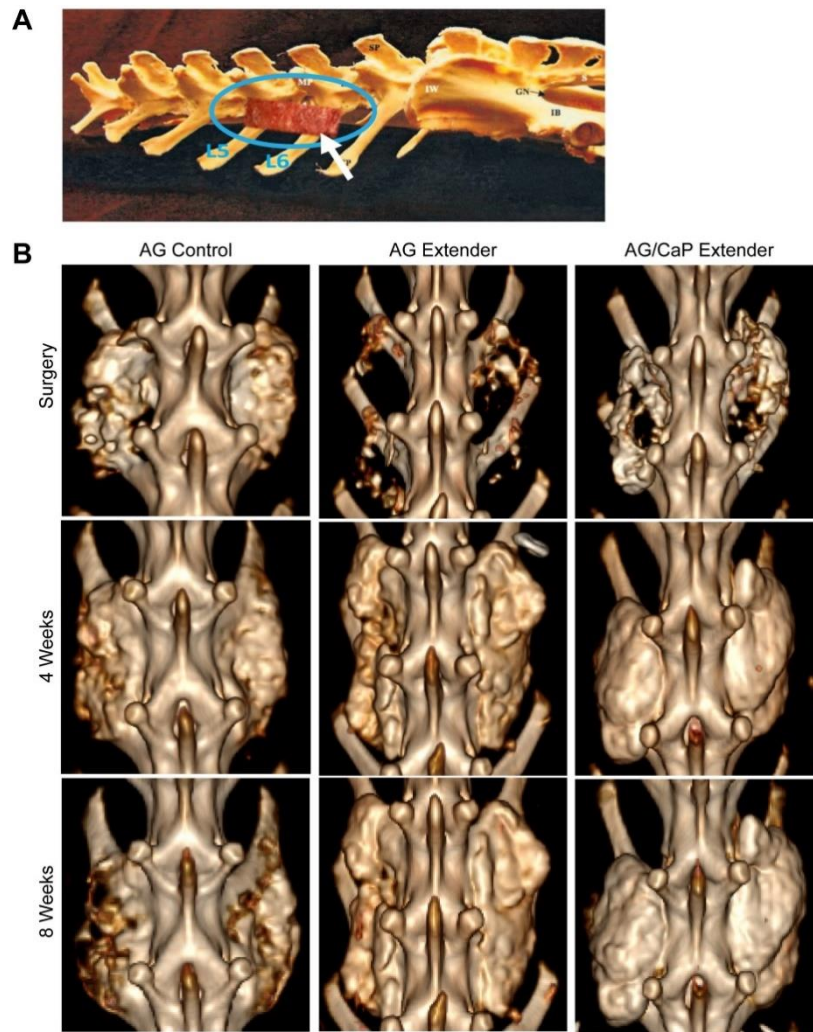


**Figure 4.3.** (A) Anatomical representation of graft placement from L5 – L6. Materials were implanted bilaterally. (B) 3D in vivo CT images of L5 – L6 at time of surgery, 4 weeks post-implantation, and 8 weeks post-implantation. Dorsal views show an increase in mineralized tissue in all groups.

Coronal sections of  $\mu$ CT images showed trabecular bone formation in the ITP space from the transverse processes for all groups (**Figure 4.4A**). Serial 2D sagittal sections exemplified the healing pattern throughout the graft. The AG control groups showed new bone growth on the transverse processes, but radiographical bridging of the processes did not occur before reaching the vertebral body (**Figure 4.4B**). Both the AG extender and AG/CaP extender showed similar growth patterns as the vertebral body was approached

(Figure 4.4B). Bone appeared to grow from both processes towards the center of the ITP space in the plane of the transverse processes, with superior and inferior growths approaching complete bridging near the vertebral body.

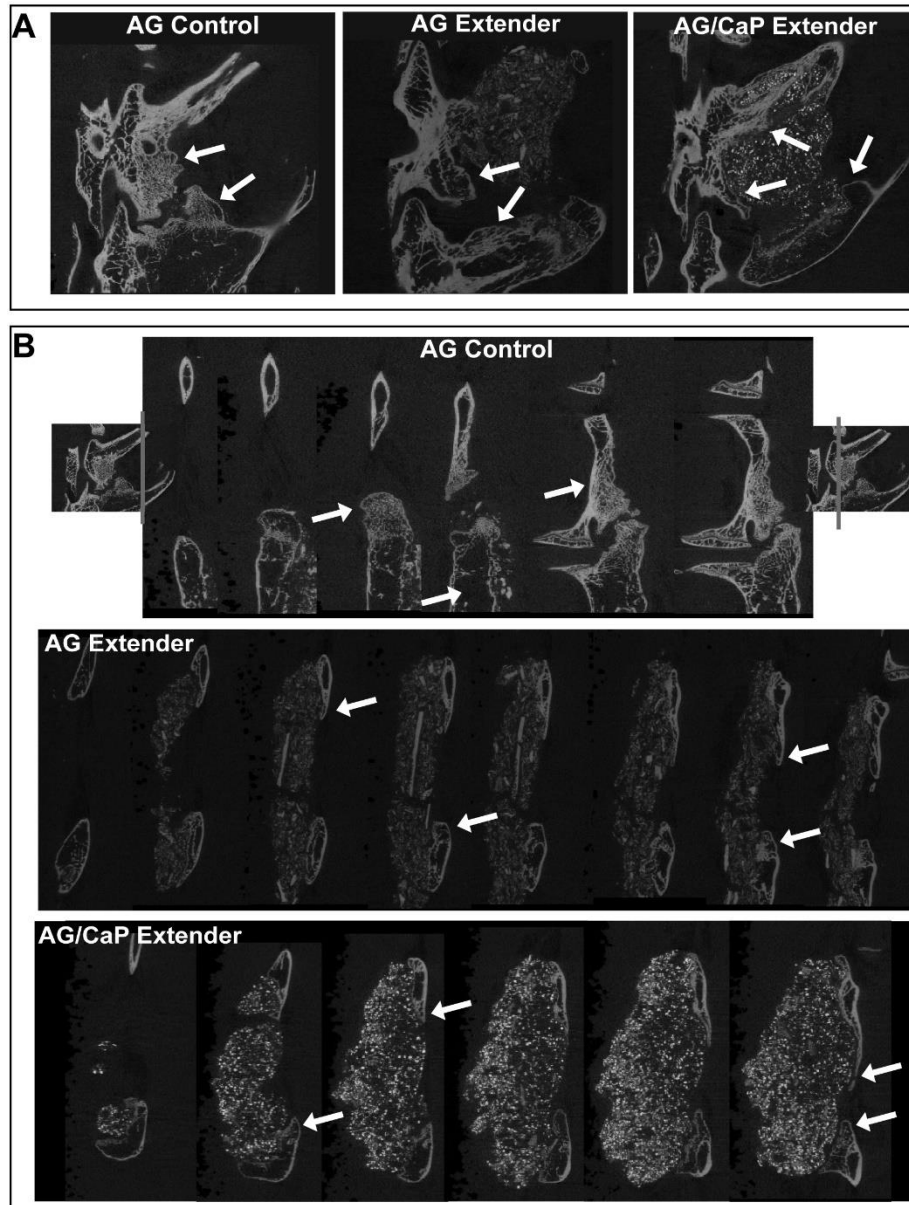


**Figure 4.4.**  $\mu$ CT images of half of spines when cut down the spinal column. (A) Coronal sections of AG control, AG extender, and AG/CaP extender. Arrows show new bone formation. (Note: AG extender material is covering the superior lateral process.) (B) Serial sagittal sections taken from the end of the lateral processes (left) to the vertebral body (right) for the AG control, AG extender, and AG/CaP extender show ingrowth of new bone between the lateral processes. White arrows indicate new bone.

Serial sagittal sections were cut throughout the defect to assess bone growth patterns histologically. Stained histology sections indicated small gaps of connective tissue where specimens were close to bridging of the processes with new bone (**Figure 4.5B, D, F** - single arrows: ongoing lamellar bone formation, double arrows: new bone). Fluorescent images of unstained sections demonstrated the chronological patterns of osteogenesis for each graft type. The AG control showed mineralization throughout the graft at 2 weeks post-implantation (**Figure 4.5C**, green). There was some continuation of growth at 6 weeks (orange fluorescence) within the graft; however, the perimeter of bone evident in the stained section was produced between 6 and 8 (red, stained histology) weeks. Bright-field and fluorescent images of adjacent slides were compared side-by-side in an effort to differentiate implanted AG from new bone. Fluorescent images of the AG extender and AG/CaP extender revealed autofluorescence of the polymer; therefore, it was not possible to quantify mineralization far from the processes and this area was excluded from the fluorescent images for analysis. The fluorescent images of the PTKUR AG extender group showed initial bone growth near the processes at 2 weeks (green) followed by a semi-linear continuation along the base of the ITP space from process to process at 6 weeks (orange, **Figure 4.5E**). Orange and green fluorescence within the graft may indicate mineralization from the presence of osteoblasts throughout the ITP space, originating from either the implanted AG or migrating from the transverse processes. To eliminate discrimination between auto-fluorescent polymer and mineralization within the graft, analysis was focused on the area of interest spanning the base of the processes. The AG/CaP extender showed a similar growth pattern from process to process (**Figure 4.5G**).

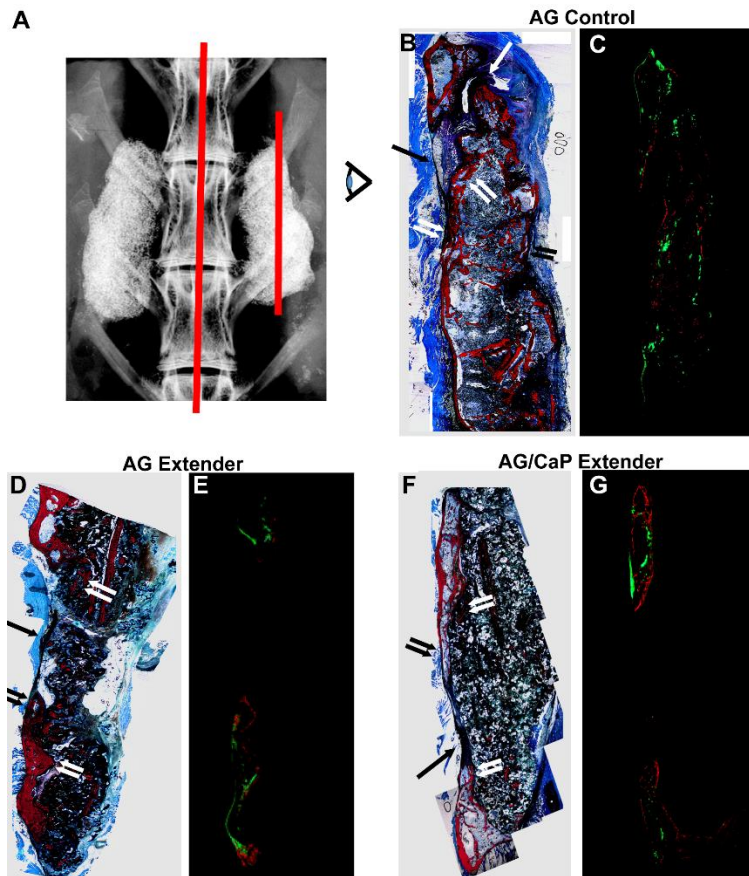


**Figure 4.5.** Images of histological sections of AG control, AG extender, and AG/CaP extender implanted on the L5 - L6 lateral processes. (A) X-ray image detailing the histological sectioning procedure. Spines were cut in half along the spinal column. After embedding, sagittal serial sections were cut from the lateral most instance of the intertransverse process mass until the process was reached. (B-G) Histological sections of L5 - L6 in the sagittal plain showing the mass in the intertransverse process space. Sections are stained with Sanderson's Rapid Bone Stain (B, D, F - bone: red, cell nuclei: dark blue, PTKUR: teal, CaP: black, cartilage-like tissue: purple) or unstained and imaged under a fluorescent microscope (C, E, G). Single arrows show areas of ongoing mineralization of soft tissue, double arrows indicate new bone. (C, E, G) Dynamic histomorphometry, where calcein green (green fluorescence) labeled actively mineralizing tissue at 2 weeks and xylenol orange (orange fluorescence) labeled actively mineralizing tissue at 6 weeks, shows remodeling was ongoing from 2 to 6 weeks as growth towards bridging continued.



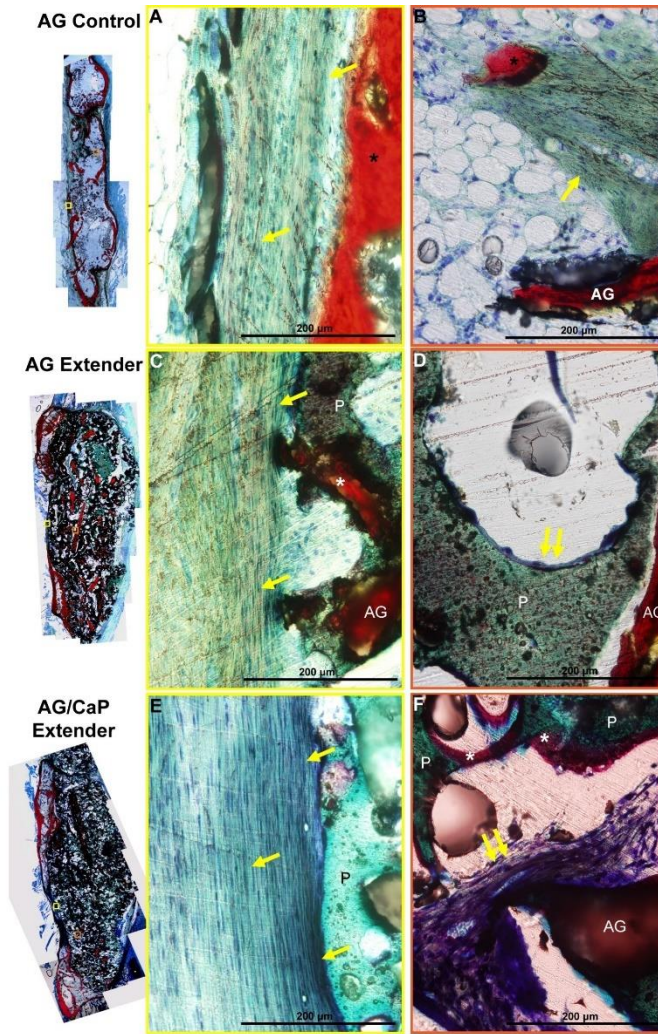


**Figure 4.6.** Magnified images (40X) of histological sections of the AG control (top row), AG extender (middle row), and AG/CaP extender (bottom row). (A) 40X images in the plane of the processes (yellow box in the 2X image) show collagen fibrils that are visible as bundles with their long axes aligned (single arrows), a pattern characteristic of lamellar bone structures. Evidence of new bone formation was also observed (\*). (B) Similar cellular activity was observed in the interior of the ITP space far from the processes (orange box in the 2X image). (C) 40X images of the AG extender in the plane of the processes (yellow box in the 2X image) show evidence of aligned collagen fibrils (single arrows), new bone formation (\*), residual polymer (P), and residual autograft (AG). (D) 40X images of the AG extender in the graft space far from the processes (orange box in the 2X image) also show evidence of new bone formation and residual polymer, indicating cells were able to infiltrate into the interior of AG extender (double arrows). Residual autograft particles (AG) embedded in polymer (P) are also observed. (E-F) 40X images of the AG/CaP extender (E) in the plane of the processes (yellow box) and (F) in the graft space (orange box) show evidence of aligned collagen fibrils, new bone, and residual polymer. Arrows: aligned collagen fibrils, \*: new bone, P: residual polymer, AG: residual autograft.

Magnified histology images taken from the center of stained sections indicate that cells (double arrows) infiltrated the AG extender (**Figure 4.6D**) and AG/CaP extender (**Figure 4.6F**), resulting in new bone formation (indicated by \* in **Figure 4.6**). Cells were also identified within the remodeled graft space of the AG control (**Figure 4.6A**) despite large voids where no implanted AG and little new bone remained. The striated cellular patterns at the base of the ITP space, from process to process, suggest that lamellar bone formation is ongoing between the processes (**Figure 4.6A, C, E**, single arrows) in all groups.

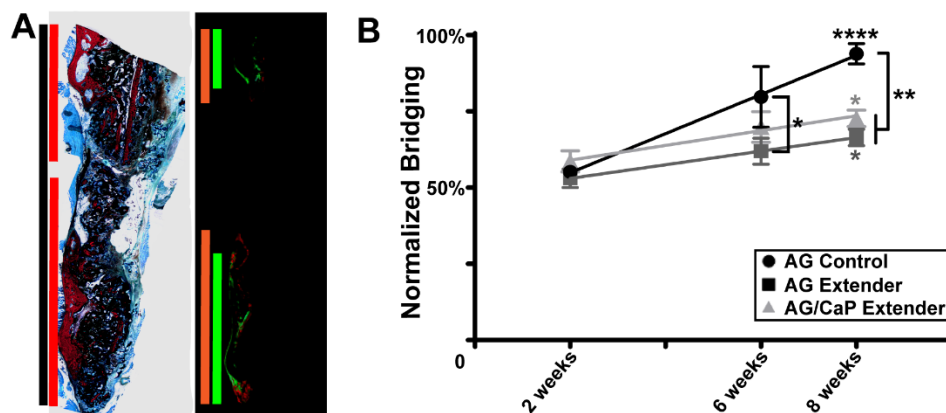


**Figure 4.7.** Quantification of bridging. (A) Method used to measure bridging. The green lines extend the front of the green fluorescence. These were added together for the length of bridging at 2 weeks and then normalized by the length of the ITP (black line). This was repeated for the orange fluorescence (6 weeks) and red staining (8 weeks). (B) Normalized bridging of the ITP space spanning the L5 – L6 transverse processes indicates progression from 2 to 8 weeks for all groups as assessed by histomorphometry. (Linear regression was calculated and included on the plot. Statistical symbols on the 8-week data represent a significant increase from the 2-week time point. \*:  $P \leq 0.05$ , \*\*:  $P \leq 0.01$ , \*\*\*\*:  $P \leq 0.0001$ ).

Combining data from the fluorescent dyes and histological stain and focusing on the plane of the processes allowed for temporal investigation of the mechanisms of neo-osteogenesis. Because osteogenesis generally started at the processes, the processes were included in quantification of the osteogenesis front (bridging) to eliminate bias associated

with process size (**Figure 4.7A**). **Figure 4.7B** shows that osteogenesis was ongoing at the base of the ITP space from 2 to 8 weeks in all groups, indicated by a significant increase in bridging. At 2 weeks, the extender groups performed similarly to the control. At the time of sacrifice, bridging for both extenders was greater than at 6 weeks, although these differences were not significant. The rate of bridging was calculated from the plot in **Figure 4.7B**. Both extenders had an average bridging rate of 2% per week (AG extender:  $2.2 \pm 0.0076\%$ , AG/CaP extender:  $2.4 \pm 0.35\%$ ) while the AG control had an average bridging rate 2.7 - 3 times that of the extenders ( $6.4 \pm 0.23\%$ ). These data suggest that although slower than the AG control, osteogenesis in the PTKUR extender groups is ongoing ( $R^2 > 0.98$  for all groups).

#### 4.5 Discussion

It is widely accepted that AG is the gold standard in bone grafting. AG processed using a bone mill retains its osteoinductivity and growth factors that aid in bone regeneration.<sup>43,44</sup> The importance of osteocytes in orchestrating bone regeneration has recently been highlighted<sup>45,46</sup>, and a recent study has shown that milled AG releases the signaling molecules involved in directing the activity of osteoblasts and osteoclasts.<sup>46</sup> The finite availability, invasive harvesting methods, and unpredictable resorption have stimulated interest in synthetic materials to extend the osteoinductive capacity of AG.<sup>6,12</sup> In this work, a PTKUR was formulated to incorporate milled AG and cure *in vivo* to yield a compression-resistant, oxidatively degradable AG extender.

An athymic rat model allowed for the use of rabbit xenograft, which has higher graft volume available for implantation. A PTKUR extender was used since these materials have previously been reported to degrade selectively by osteoclast-like cells in rabbits.<sup>27</sup> The xenograft was well tolerated by the rats and there was no evidence of graft rejection.

Histological analysis revealed the presence of cells at the center of the defect, suggesting that cells were able to degrade and infiltrate the PTKUR AG extender. Enhanced cellular activity near the AG was observed, which revealed evidence of osteoclastic resorption and osteoblastic bone formation (**Figure 4.2B, D**). These qualitative observations representative of cellular infiltration and graft remodeling supported more extensive testing in the rabbit spine model.

The posterolateral intertransverse process bone formation model has been used to investigate osteogenesis in a biologically stringent environment. Synthetic and natural autograft extenders in preclinical and clinical lumbar spine applications have been reviewed.<sup>47,48</sup> In this model, host cells migrate into the graft from the transverse processes. The space maintenance aspect of the graft is also critical as demonstrated by insufficient bone induction when clinically relevant rhBMP-2 doses were delivered via a mechanically compliant collagen sponge in nonhuman primates.<sup>49</sup> Gravitational compression, tension, torsion from rotational movement, and compression from the muscles posterior to the lumbar spine all exert forces on the graft in this challenging model.<sup>50</sup> Various particulated ceramic AG extenders, including  $\beta$ -TCP<sup>13,16,20</sup>, hydroxyapatite<sup>15</sup>, and  $\beta$ -calcium pyrophosphate<sup>14</sup>, have been used in clinical trials with successful outcomes comparable to an AG control demonstrated 1-3 years postoperatively. These formulations all involved mixing granular ceramic particles with autograft (local and/or ICBG) and lacked mechanical integrity. The PTKUR AG extender is injectable and moldable initially and cures to form a rigid graft that adheres to the bone surface upon implantation. These curing characteristics facilitate the minimally invasive implantation of the material, which has the potential to decrease post-operative pain and morbidity and minimize the length of hospital

stay and recovery.<sup>51</sup>

Fluorochromes allowed for the differentiation of implanted AG and new bone growth and also provided insight into the regeneration patterns of the PTKUR AG extenders compared to the control. The distance of the osteogenesis front for each fluorochrome and the final stain were compared to investigate phases of remodeling. Areas of fluorescence within the graft were co-localized with more darkly stained areas of stained sections. There was evidence of endochondral bone formation in these areas where a cartilaginous phase (stains dark blue-purple) was actively being calcified into bone (**Figure 4.5**). Stained histology slides showed evidence of possible pseudarthrosis in specimens from all groups (**Figure 4.5**, single arrows). This “false joint” of cartilaginous tissue centrally located between the 2 processes may have had enough mechanical stability to simulate bridging of the processes. This has been described as the “reparative phase” characteristic of weeks 4-6 post implantation when there is a lag between cartilage formation and ossification.<sup>3,52</sup> This reparative phase was delayed for the PTKUR AG extenders, which could be due to the lower concentration of osteoinductive AG particles near the vertebral bodies compared to the AG control. Bone grew around the entire implanted graft in the AG controls whereas a planar growth from process to process was ongoing in both AG extender groups (**Figure 4.5**).

Enhanced new bone formation compared to an autograft control has been reported for a ceramic extender (25 or 75% MASTERGRAFT granules) in the same rabbit model used in the present study.<sup>18</sup> When a MASTERGRAFT strip was used, the 50% MASTERGRAFT AG extender group exhibited new bone formation superior to the autograft control while the 75% MASTERGRAFT group generated less bone than the AG

control.<sup>53</sup> However, neither of these AG extenders was formulated to cure to a compression resistant solid *in vivo*. In the present study, new bone formation was observed in the AG and AG/CaP extender groups, but complete bony bridging of the processes was not observed (**Figure 4.7B**). These findings suggest that while the settable polymer enhanced the handling and mechanical properties of the AG extender, the presence of the cell-degradable polymer slowed cellular infiltration into the graft since the polymer must be degraded by infiltrating cells.

When implanted alone, AG undergoes rapid and unpredictable resorption compared to some synthetic grafts.<sup>5,54</sup> Premature graft resorption could result in incomplete healing and the formation of fibrous tissue.<sup>55</sup> A non-settable polymeric AG extender comprising poly(lactide-co-glycolide) (PLGA)/hyaluronic acid (50 vol% AG) has been investigated in the same rabbit model used in this study.<sup>26</sup> Progression was noted from 3 to 6 months and a radiographic bone fill score of 4.5 (0-5 scale, 5=81-100% bone fill) reported for the AG extender 6 months post-implantation. The AG extender group exhibited a score of 4.0 at 3 months compared to 4.75 for the control animals. The authors also noted PLGA extender material remaining at the implantation site at 3 months. These observations are consistent with our findings that implementation of a degradable polymeric AG extender protects against premature AG resorption and maintains a persistent and osteoinductive scaffold at the defect site throughout the remodeling phases. Furthermore, the persistence of resorbable, polymeric AG extenders may support more extensive bridging of the transverse processes at later time points. Future studies will investigate remodeling of the PTKUR AG extender at longer time points and aim to find the minimum amount of AG required to maintain osteoinductivity of the AG extender.

#### 4.6 Conclusion

In this study, injectable, settable, cell-degradable PTKUR AG extenders were formulated and tested in 2 *in vivo* models. Bone regeneration and cellular infiltration were evident in a rat femoral segmental defect model. This initial study was followed by investigation in a stringent bone formation model in rabbits. The ease of implantation of the moldable AG extenders compared to the particulated AG control was particularly important for a minimally invasive procedure. This model further demonstrated that cells were present throughout the graft space and actively degrading the PTKUR. The inclusion of an AG/CaP group established that AG content can be reduced further without significantly compromising bone healing. Bone growth along the posterior plane of the processes was consistent from 2 to 6 weeks for the AG and AG/CaP extenders and bone regeneration was evident within the ITP space away from the processes. This work provides evidence for the potential of a PTKUR AG extender to expand the utility of AG and allow for its use in larger, more demanding defects.

## References

1. Greenwald AS, Boden SD, Goldberg VM, Khan Y, Laurencin CT, Rosier RN. Bone-graft substitutes: facts, fictions, and applications. *The Journal of Bone & Joint Surgery* 2001;83(2 suppl 2):S98-103.
2. Boden SD. Biology of lumbar spine fusion and use of bone graft substitutes: present, future, and next generation. *Tissue engineering* 2000;6(4):383-399.
3. Boden SD. Overview of the biology of lumbar spine fusion and principles for selecting a bone graft substitute. *Spine* 2002;27(16S):S26-S31.
4. Domic-Cule I, Pecina M, Jelic M, Jankolija M, Popek I, Grgurevic L, Vukicevic S. Biological aspects of segmental bone defects management. *International Orthopaedics* 2015:1-7.
5. Rogers GF, Greene AK. Autogenous Bone Graft: Basic Science and Clinical Implications. *Journal of Craniofacial Surgery* 2012;23(1):323-327.
6. Burkus JK, Heim SE, Gornet MF, Zdeblick TA. Is INFUSE bone graft superior to autograft bone? An integrated analysis of clinical trials using the LT-CAGE lumbar tapered fusion device. *Clinical Spine Surgery* 2003;16(2):113-122.
7. Kraiwattanapong C, Boden SD, Louis-Ugbo J, Attallah E, Barnes B, Hutton WC. Comparison of Healos/bone marrow to INFUSE (rhBMP-2/ACS) with a collagen-ceramic sponge bulking agent as graft substitutes for lumbar spine fusion. *Spine* 2005;30(9):1001-1007.
8. McKay WF, Peckham SM, Badura JM. A comprehensive clinical review of recombinant human bone morphogenetic protein-2 (INFUSE® Bone Graft). *International orthopaedics* 2007;31(6):729-734.
9. Talley AD, Kalpakci KN, Shimko DA, Zienkiewicz K, Cochran D, Guelcher S. Effects of rhBMP-2 Dose and Ceramic Composition on New Bone Formation and Space Maintenance in a Canine Mandibular Ridge Saddle Defect Model. *Tissue Engineering* 2016(ja).
10. Carragee EJ, Ghanayem AJ, Weiner BK, Rothman DJ, Bono CM. A challenge to integrity in spine publications: years of living dangerously with the promotion of bone growth factors. *The Spine Journal*;11(6):463-468.
11. Carragee EJ, Hurwitz EL, Weiner BK. A critical review of recombinant human bone morphogenetic protein-2 trials in spinal surgery: emerging safety concerns and lessons learned. *The Spine Journal*;11(6):471-491.
12. Lewandrowski K-U, Hile DD, Thompson BM, Wise DL, Tomford WW, Trantolo DJ. Quantitative measures of osteoinductivity of a porous poly (propylene fumarate) bone graft extender. *Tissue engineering* 2003;9(1):85-93.
13. Dai L-Y, Jiang L-S. Single-level instrumented posterolateral fusion of lumbar spine with  $\beta$ -tricalcium phosphate versus autograft: a prospective, randomized study with 3-year follow-up. *Spine* 2008;33(12):1299-1304.
14. Lee JH, Chang B-S, Jeung U-O, Park K-W, Kim M-S, Lee C-K. The first clinical trial of beta-calcium pyrophosphate as a novel bone graft extender in instrumented posterolateral lumbar fusion. *Clinics in orthopedic surgery* 2011;3(3):238-244.
15. Lee JH, Hwang CJ, Song BW, Koo KH, Chang BS, Lee CK. A prospective consecutive study of instrumented posterolateral lumbar fusion using synthetic hydroxyapatite (Bongros®-HA) as a bone graft extender. *Journal of Biomedical Materials Research Part A* 2009;90(3):804-810.



16. Lerner T, Bullmann V, Schulte TL, Schneider M, Liljenqvist U. A level-1 pilot study to evaluate of ultraporous  $\beta$ -tricalcium phosphate as a graft extender in the posterior correction of adolescent idiopathic scoliosis. *European Spine Journal* 2009;18(2):170-179.
17. Linovitz RJ, Peppers TA. Use of an advanced formulation of  $\beta$ -tricalcium phosphate as a bone extender in interbody lumbar fusion. *Orthopedics* 2002;25(5):S585-S589.
18. Smucker JD, Petersen EB, Fredericks DC. Assessment of MASTERGRAFT PUTTY as a graft extender in a rabbit posterolateral fusion model. *Spine* 2012;37(12):1017-1021.
19. Chen W-J, Tsai T-T, Chen L-H, Niu C-C, Lai P-L, Fu T-S, McCarthy K. The fusion rate of calcium sulfate with local autograft bone compared with autologous iliac bone graft for instrumented short-segment spinal fusion. *Spine* 2005;30(20):2293-2297.
20. Gunzburg R, Szpalski M. Use of a novel  $\beta$ -tricalcium phosphate-based bone void filler as a graft extender in spinal fusion surgeries. *Orthopedics* 2002;25(5):S591-S595.
21. Kanayama M, Hashimoto T, Shigenobu K, Oha F, Ishida T, Yamane S. Pitfalls of anterior cervical fusion using titanium mesh and local autograft. *Clinical Spine Surgery* 2003;16(6):513-518.
22. von Arx T, Kurt B. Implant placement and simultaneous ridge augmentation using autogenous bone and a micro titanium mesh: a prospective clinical study with 20 implants. *Clinical oral implants research* 1999;10(1):24-33.
23. Von Arx T, Schenk RK, Buser D, Cochran DL, Hermann JS. Lateral ridge augmentation using different bone fillers and barrier membrane application. *Clinical oral implants research* 2001;12(3):260-269.
24. McAllister BS, Haghighat K. Bone augmentation techniques. *Journal of periodontology* 2007;78(3):377-396.
25. Hile DD, Kandziora F, Lewandrowski K-U, Doherty SA, Kowaleski MP, Trantolo DJ. A poly(propylene glycol-co-fumaric acid) based bone graft extender for lumbar spinal fusion: in vivo assessment in a rabbit model. *European spine journal : official publication of the European Spine Society, the European Spinal Deformity Society, and the European Section of the Cervical Spine Research Society* 2006;15(6):936-943.
26. Walsh WR, Oliver RA, Gage G, Yu Y, Bell D, Bellemore J, Adkisson HD. Application of resorbable poly (lactide-co-glycolide) with entangled hyaluronic acid as an autograft extender for posterolateral intertransverse lumbar fusion in rabbits. *Tissue Engineering Part A* 2010;17(1-2):213-220.
27. McEnery MA, Lu S, Gupta MK, Zienkiewicz KJ, Wenke JC, Kalpakci KN, Shimko DA, Duvall CL, Guelcher SA. Oxidatively degradable poly (thioketal urethane)/ceramic composite bone cements with bone-like strength. *RSC advances* 2016;6(111):109414-109424.
28. Martin JR, Gupta MK, Page JM, Yu F, Davidson JM, Guelcher SA, Duvall CL. A porous tissue engineering scaffold selectively degraded by cell-generated reactive oxygen species. *Biomaterials* 2014;35(12):3766-3776.
29. Martin JR, Nelson CE, Gupta MK, Yu F, Sarett SM, Hocking KM, Pollins AC,

- Nanney LB, Davidson JM, Guelcher SA. Local Delivery of PHD2 siRNA from ROS-Degradable Scaffolds to Promote Diabetic Wound Healing. *Advanced Healthcare Materials* 2016.
30. Guelcher SA, Srinivasan A, Dumas JE, Didier JE, McBride S, Hollinger JO. Synthesis, mechanical properties, biocompatibility, and biodegradation of polyurethane networks from lysine polyisocyanates. *Biomaterials* 2008;29(12):1762-1775.
  31. Hafeman AE, Zienkiewicz KJ, Zachman AL, Sung H-J, Nanney LB, Davidson JM, Guelcher SA. Characterization of the degradation mechanisms of lysine-derived aliphatic poly(ester urethane) scaffolds. *Biomaterials* 2011;32(2):419-429.
  32. Harmata AJ, Uppuganti S, Granke M, Guelcher SA, Nyman JS. Compressive fatigue and fracture toughness behavior of injectable, settable bone cements. *Journal of the mechanical behavior of biomedical materials* 2015;51:345-355.
  33. Kirkeby OJ, Nordsletten L, Skjeldal S. Healing of cortical bone grafts in athymic rats. *Acta Orthopaedica Scandinavica* 1992;63(3):318-322.
  34. Chesmel KD, Branger J, Wertheim H, Scarborough N. Healing response to various forms of human demineralized bone matrix in athymic rat cranial defects. *Journal of oral and maxillofacial surgery* 1998;56(7):857-863.
  35. Festing MF. Athymic Nude Rats. In: Gershwin ME, Merchant B, editors. *Immunologic Defects in Laboratory Animals 1*. Boston, MA: Springer US; 1981. p 267-283.
  36. Pearce A, Richards R, Milz S, Schneider E, Pearce S. Animal models for implant biomaterial research in bone: a review. *Eur Cell Mater* 2007;13(1):1-10.
  37. Guelcher SA, Brown KV, Li B, Guda T, Lee B-H, Wenke JC. Dual-purpose bone grafts improve healing and reduce infection. *Journal of orthopaedic trauma* 2011;25(8):477-482.
  38. Brown KV, Li B, Guda T, Perrien DS, Guelcher SA, Wenke JC. Improving bone formation in a rat femur segmental defect by controlling bone morphogenetic protein-2 release. *Tissue Engineering Part A* 2011;17(13-14):1735-1746.
  39. Rathbone C, Guda T, Singleton B, Oh D, Appleford M, Ong J, Wenke J. Effect of cell-seeded hydroxyapatite scaffolds on rabbit radius bone regeneration. *Journal of Biomedical Materials Research Part A* 2014;102(5):1458-1466.
  40. Guo R, Ward CL, Davidson JM, Duvall CL, Wenke JC, Guelcher SA. A transient cell-shielding method for viable MSC delivery within hydrophobic scaffolds polymerized in situ. *Biomaterials* 2015;54:21-33.
  41. Talley AD, McEnery MA, Kalpakci KN, Zienkiewicz KJ, Shimko DA, Guelcher SA. Remodeling of injectable, low-viscosity polymer/ceramic bone grafts in a sheep femoral defect model. *Journal of Biomedical Materials Research Part B: Applied Biomaterials* 2016.
  42. Guelcher SA, Patel V, Gallagher KM, Connolly S, Didier JE, Doctor JS, Hollinger JO. Synthesis and In Vitro Biocompatibility of Injectable Polyurethane Foam Scaffolds. *Tissue Engineering* 2006;12(5):1247-59.
  43. Fulzele K, Krause DS, Panaroni C, Saini V, Barry KJ, Liu X, Lotinun S, Baron R, Bonewald L, Feng JQ. Myelopoiesis is regulated by osteocytes through Gs $\alpha$ -dependent signaling. *Blood* 2013;121(6):930-939.
  44. Miron RJ, Gruber R, Hedbom E, Saulacic N, Zhang Y, Sculean A, Bosshardt DD,

- Buser D. Impact of Bone Harvesting Techniques on Cell Viability and the Release of Growth Factors of Autografts. *Clinical Implant Dentistry and Related Research* 2013;15(4):481-489.
45. Bonewald LF. The amazing osteocyte. *Journal of bone and mineral research* 2011;26(2):229-238.
  46. Brolese E, Buser D, Kuchler U, Schaller B, Gruber R. Human bone chips release of sclerostin and FGF-23 into the culture medium: an in vitro pilot study. *Clinical Oral Implants Research* 2015;26(10):1211-1214.
  47. Epstein NE. Efficacy of different bone volume expanders for augmenting lumbar fusions. *Surgical neurology* 2008;69(1):16-19.
  48. Kaiser MG, Groff MW, Watters III WC, Ghogawala Z, Mummaneni PV, Dailey AT, Choudhri TF, Eck JC, Sharan A, Wang JC. Guideline update for the performance of fusion procedures for degenerative disease of the lumbar spine. Part 16: bone graft extenders and substitutes as an adjunct for lumbar fusion. *Journal of Neurosurgery: Spine* 2014;21(1):106-132.
  49. Martin JG, Boden SD, Marone M, Moskovitz PA. Posterolateral intertransverse process spinal arthrodesis with rhBMP-2 in a nonhuman primate: important lessons learned regarding dose, carrier, and safety. *Journal of spinal disorders* 1999;12(3):179-186.
  50. Reid JJ, Johnson JS, Wang JC. Challenges to bone formation in spinal fusion. *Journal of biomechanics* 2011;44(2):213-220.
  51. Skovrlj B, Gilligan J, Cutler HS, Qureshi SA. Minimally invasive procedures on the lumbar spine. *World Journal of Clinical Cases: WJCC* 2015;3(1):1.
  52. Boden SD, Schimandle JH, Hutton WC, Chen MI. The Use of an Osteoinductive Growth Factor for Lumbar Spinal Fusion: Part I: Biolog of Spinal Fusion. *Spine* 1995;20(24):2626-2632.
  53. Smucker JD, Petersen EB, Nepola JV, Fredericks DC. Assessment of MASTERGRAFT® STRIP with bone marrow aspirate as a graft extender in a rabbit posterolateral fusion model. *The Iowa orthopaedic journal* 2012;32:61.
  54. Sanz M, Vignoletti F. Key aspects on the use of bone substitutes for bone regeneration of edentulous ridges. *Dental Materials* 2015;31(6):640-647.
  55. Dumas JE, Prieto EM, Zienkiewicz KJ, Guda T, Wenke JC, Bible J, Holt GE, Guelcher SA. Balancing the Rates of New Bone Formation and Polymer Degradation Enhances Healing of Weight-Bearing Allograft/Polyurethane Composites in Rabbit Femoral Defects. *Tissue Engineering Part A* 2014;20(1-2):115-129.

## CHAPTER 5

### V. A COMPRESSION RESISTANT POLY(THIOKETAL URETHANE) AUTOGRAFT EXTENDER IN A RABBIT RADIUS MODEL

#### 5.1 Abstract

Iliac crest autograft (AG) is the standard for bone grafts, but patient pain and morbidity limit the amount of bone available for harvesting, prompting a search for alternatives. Bone graft substitutes have been studied extensively but designing a synthetic graft to match the osteogenic properties of autologous bone is challenging. Synthetic AG extenders have recently been proposed to minimize the volume of AG required to maintain osteoinductivity, alleviating the repercussions associated with AG harvest. In this work, a moldable, settable, and cell-degradable poly(thioketal urethane) (PTKUR) AG extender was developed to afford mechanical integrity to ease implantation and improve fixation for a minimally invasive procedure. The PTKUR was formulated to yield an AG extender that incorporated 70 wt% morselized AG without sacrificing handling properties. The PTKUR AG extender exhibited a clinically relevant working time of 35 minutes and set in less than one hour to a compression resistant bone graft with a final modulus of 4.5-5 MPa when completely cured. The PTKUR AG extender was implanted in a stringent 20 mm rabbit radius model for 12 weeks to investigate cellular infiltration and graft remodeling. Packed, morselized AG was included as a control. X-ray and  $\mu$ CT indicated bone growth from the defect interfaces in both groups. Positive fluorochrome binding within the PTKUR AG extender at 4 and 8 weeks suggests implanted AG may have acted as nucleation sites for mineralization and cells were identified at the center of the defect in 12-week histology sections. The defect space was bridged to some extent in all specimens from the control group; however, bone quality was inconsistent and implanted AG was completely

resorbed. The PTKUR AG extender persisted in the defect, maintained implanted AG, and remodeling was ongoing 12 weeks post-implantation. These findings highlight the potential to combine the compression resistance and desirable handling properties of a cell-degradable PTKUR with osteoinductive AG and suggest consistent osteogenesis and improved new bone quality over the gold standard.

## 5.2 Introduction

Autograft (AG) bone is the gold standard in bone grafting since it is osteoinductive, osteoconductive, and osteogenic.<sup>1,2</sup> Cancellous bone specifically undergoes rapid revascularization and remodeling by inherent cells from both the donor and host tissue upon implantation.<sup>3</sup> Autogenous cortical bone can also be used; however, the density of this bone causes slower revascularization and limited initial cellular infiltration prompting surgeons to use cancellous bone when possible.<sup>3-5</sup> AG is most commonly harvested from the iliac crest (IC) which is associated with significant limitations in availability and donor site morbidity that limit its use in larger defects.<sup>5,6</sup> Local AG is sometimes taken from the implant site in cases like spinal fusion and some maxillofacial procedures; however, availability is a hindrance limiting the applications for which this technique can be applied.<sup>7-11</sup> Furthermore, AG chips cannot conform to irregularly shaped defects and morselized AG lacks mechanical properties. Retainers and surgical meshes marketed to maintain AG space and placement generally require a second operation for removal or remain in place for the duration of the patient's life.<sup>12-14</sup>

Allograft is marketed as an alternative, but immune rejection and high failure rates preclude its use.<sup>2,15,16</sup> Synthetic bone grafts have evolved as a substitute for AG, but none have been shown to match all of the benefits provided by AG without the use of potentially harmful biologics like rhBMP-2.<sup>17-21</sup> Tissue engineering approaches to combine AG with

synthetic, resorbable AG extenders have recently been suggested to maintain the osteogenic properties of AG while overcoming the limited availability. Various forms of ceramics such as  $\beta$ -tricalcium phosphate ( $\beta$ -TCP) and hydroxyapatite, along with bioactive glass particles, have been investigated as bone graft extenders in spinal, long bone non-union, and maxillofacial applications.<sup>22-29</sup> Poly(propylene fumarate)- and poly(lactide-co-glycolide) (PLGA)-based polymers have also been proposed in morselized and paste forms.<sup>30-33</sup> This concept of blending AG with synthetic extenders has the potential to minimize AG necessary for osteoinductivity, expanding the applications for which AG can be used to include larger bone injuries and defects. Furthermore, adapting these techniques to a settable formulation may afford space maintenance and compression resistance to the biological benefits of AG to maximize its utility.

In Chapter 3, we showed that a lysine-based poly(thioketal urethane) (PTKUR) degrades selectively in the oxidative environment surrounding bone healing.<sup>34</sup> In Chapter 4, this PTKUR was combined with AG for a moldable AG extender that cured to a rigid bone graft *in situ*. The extender was shown to generate new bone in a challenging spinal application when combined with AG and the presence of cells was evident throughout the AG extender indicating cellular infiltration and polymer resorption.

In this study, a settable and compression resistant, resorbable PTKUR AG extender is compared to an AG control in an aggressive 20 mm segmental defect model in the rabbit radius to investigate remodeling capabilities in a clinically relevant application. The presence of the ulna allows for a minimally invasive procedure that does not require fixation of the defect for comparison against an AG control.<sup>35-37</sup> In this work, catalyzed PTKUR is blended with fresh IC AG and molded for implantation into the defect where it

cures *in situ*. AG extender remodeling is investigated 12 weeks post-operatively and x-ray images and fluorochrome injections are employed to visualize osteogenesis temporally.

### 5.3 Materials and Methods

*Materials.* Materials for TK diol synthesis including thioglycolic acid, 2,2-dimethoxypropane, bismuth (III) chloride, lithium aluminum hydride, acetonitrile, and tetrahydrofuran (THF) were purchased from Sigma-Aldrich. Anhydrous diethyl ether from Fisher Scientific was also used in the TK diol synthesis. Iron (III) acetylacetonate (FeAA) catalyst was purchased from Sigma-Aldrich and lysine triisocyanate-polyethylene glycol (LTI-PEG) prepolymer (NCO=21.7%) from Ricerca Biosciences LLC.

*Thioketal diol synthesis.* TK diol was synthesized as discussed in Chapter 3.<sup>34</sup> An excess of 2,2-dimethoxypropane was reacted with thioglycolic acid in the presence of bismuth(III) chloride at room temperature. After 24 hours, the product was filtered and the solvent removed. Lithium aluminum hydride ( $\text{LiAlH}_4$ ) was charged to a flask containing ether which was then chilled in an ice bath. The intermediate was dissolved in THF and added to  $\text{LiAlH}_4$  dropwise under anhydrous conditions. The reaction was refluxed at  $52^\circ\text{C}$  for 18 hours and excess  $\text{LiAlH}_4$  quenched with water. The product was filtered, extracted with NaOH and ether, and dried for 48 hours under vacuum. 0.5% (w/w) FeAA catalyst was dissolved in the dry TK diol by stirring overnight under inert conditions.

*Autograft extender fabrication and characterization.* PTKUR AG extenders were fabricated via reactive liquid molding adapting methods described previously in Chapter 4. Briefly, TK/FeAA was mixed with LTI-PEG prepolymer at an index of 200. Morselized AG was added to the mixture (70 wt%) and stirred by hand until homogeneous. The AG extender was then molded or loaded into a syringe for delivery into the defect where it cured *in situ*. The handling properties were defined by the tack-free time (TFT) and the

working time (WT). TFT was determined as the time when a metal spatula no longer stuck to the material and the working time was measured by hand as the time after which the material lost cohesiveness from continued hand molding. The architecture of cured AG extenders was visualized using scanning electron microscopy (SEM, Zeiss Merlin) after sputter coating the specimen with gold.

The compressive mechanical properties were measured to define the compression resistance limits of the PTKUR AG extender. Specimens were fabricated as described above (n=4). After a final mix time of 5 minutes, the materials were molded into cylindrical tubes (6 mm diameter). They were compressed and cured under a weight (0.96 kg) for at least 1 hour to simulate the compressive forces of surrounding musculature and other soft tissue *in vivo*. Approximately 24 hours post-fabrication, the cylindrical specimens were wrapped in PBS soaked gauze and sealed in glass vials. The vials were kept at 37 °C for 24 hours. The PTKUR AG extenders were cut to a height of 12 mm (2:1 length:diameter) prior to testing.<sup>38</sup> Hydrated specimens were preloaded between flat platens (1.5 N), then compressed at a rate of 25 mm min<sup>-1</sup> to failure (MTS 858 Bionix Servohydraulic System). The compressive force and displacement were recorded throughout testing and used to calculate engineering stress and engineering strain. The modulus was calculated as the slope of the linear elastic portion of the stress-strain curve. Yield strength and strain were reported using the 2.0 % offset method and ultimate strength defined as the maximum stress before failure.

*Autograft extender in rabbit radius defect.* This animal procedure was approved by the Institutional Animal Care and Use Committee of the US Army Institute of Surgical Research, Fort Sam Houston, TX. Procedures were performed in compliance with the



Animal Welfare Act, Animal Welfare Regulations, and the Guide for the Care and Use of Laboratory Animals.

Remodeling of a PTKUR AG extender was compared to an AG control in a unilateral segmental defect in the radii of 8 New Zealand White rabbits.<sup>35-37</sup> The animals were anesthetized with isoflurane (1-3% in oxygen). AG was harvested from the left IC using an oscillating saw (0.4-0.5 g). Excess soft tissue was removed and the harvested bone chip morselized using a bonemill (R. Quetin). Following closure of the IC harvest site, the right radius was exposed and a 20 mm segmental diaphyseal defect created using an oscillating saw. PTKUR AG extenders were prepared as described above and shaped using a rectangular polyacetyl mold (2 mm x 20 mm). The material was then placed in the defect using a surgical elevator to ensure correct placement and contact with the host bone. Morselized AG (without PTKUR) was used as a clinical control. The AG was packed into the mold and carefully formed to the defect. The wound was closed in layers and post-operative x-ray images (Faxitron X20) taken prior to recovery. Fluorochromes were injected and x-ray images acquired at 4 (calcein green) and 8 (xylenol orange) weeks post-operatively. Animals were anesthetized and euthanized at 12 weeks followed by a final x-ray prior to tissue harvesting. Micro computed tomography (Scanco  $\mu$ CT 50) and histology were used to assess bone graft remodeling after 12 weeks.

*$\mu$ CT analysis.*  $\mu$ CT data was attained at a voxel size of 17.2  $\mu$ m and two-dimensional and three-dimensional images analyzed for induced bone formation through the defect. Bone regeneration patterns were analyzed quantitatively following methods previously described.<sup>36,39</sup> Bone area was calculated for each reconstructed 2D, axial section (every 17.2  $\mu$ m) starting from the proximal onset of the defect extending the total 20 mm

defect length. The area of interest (AOI) was chosen to include the defect and the ulna since there was significant bone growth in the interosseous syndesmosis, interfacing the ulna. Bone area was plotted for the defect length where 0 mm corresponds to the proximal interface of the defect and 20 mm is the distal end.

*Histological evaluation.* After fixing in 10% formalin, calcified samples were dehydrated and embedded in PMMA for histological analysis. Two serial coronal sections were taken from the center of the defect. One section was stained with Sanderson's Rapid Bone Stain and magnified images (Olympus BX60 microscope) assessed for osteogenesis and cellular infiltration. The other section was left unstained and fluorochrome binding analyzed using a fluorescent microscope (Olympus Reflected Light Fluorescence attachment). Fluorescent (4 and 8 weeks) and stained (total) areas were quantified to compare bone growth in the experimental versus control group at the various time points. An inclusive 20 x 5 mm AOI was selected from the fluorescent image to include any area of fluorescence (**Figure 5.6A**). The ulna rarely exhibited fluorescence, but the boundary was set to exclude the ulna if this did occur. The AOI on the stained image was chosen to match that of the fluorescent section. Fluorescent images of the sections were analyzed adjacent to the stained sections to describe the regeneration patterns qualitatively.

*Statistical analysis.* All data including WT/TFT (n=3), mechanical analyses (n=4), and  $\mu$ CT evaluation were reported with standard deviation. GraphPad Prism software was used to compute a two-way ANOVA and Bonferroni's multiple comparison test to compare  $\mu$ CT densities of the two groups along the length of the defect.

#### 5.4 Results

*PTKUR AG extender characterization.* Settable PTKUR AG extenders incorporated 70 wt% AG derived from the iliac crest of New Zealand White rabbits. An

NCO:OH ratio of 2.0 and the addition of solid AG lent handling properties of a moldable material that could be formed to a desired shape by hand or using a mold. The materials exhibited a TFT of  $8:37 \pm 0:33$  (min:seconds) and a WT of  $34:28 \pm 2:11$ . The materials were incompressible by hand  $48 \pm 6$  minutes after the start of fabrication. A representative SEM image revealed a dense microarchitecture with intermittent pores of various sizes (**Figure 5.1**). The AG is indistinguishable among the polymer indicating the AG was well integrated within the PTKUR. Compressive mechanical properties were measured for hydrated, cylindrical specimens approximately 48 hours post-fabrication to mimic *in vivo* conditions and ensure the PTKUR AG extender was completely cured. The mechanical characteristics are summarized in **Table 5.1**.

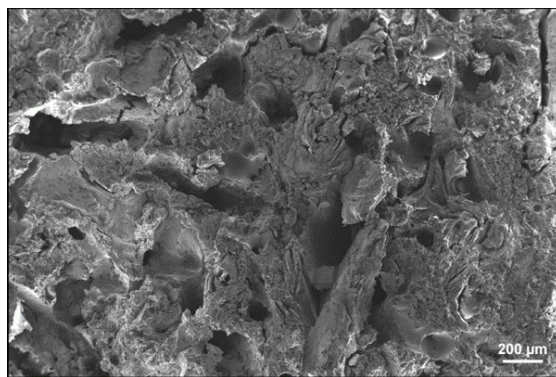


**Figure 5.1.** SEM image of PTKUR AG extender indicates minimal porosity and irregular micro-architecture.

**Table 5.1.** Mechanical properties of a PTKUR AG extender to be investigated in a rabbit radius defect model.

Modulus (MPa)	Yield Strength (kPa)	Yield Strain (%)	Strain to Failure (%)
$4.71 \pm 0.36$	$903 \pm 70$	$16.5 \pm 1.3$	$22.6 \pm 2.3$

*PTKUR AG extender in rabbit radius defect model.* PTKUR AG extenders were placed in the defect site approximately 10 minutes after the start of fabrication at which point the material was no longer tacky, but still workable to adhere to the host bone. The PTKUR AG extender was cohesive throughout placement (**Figure 5.2A**). The AG control formed to the mold given the inherent moisture of bone marrow and soft tissue remnants; however, the lack of a cohesive binder sometimes made implantation and shape maintenance throughout the procedure problematic (**Figure 5.2B**).

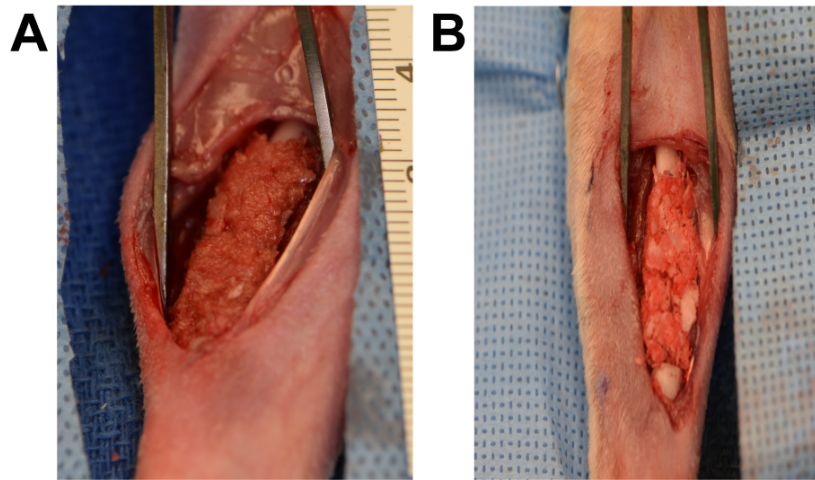


**Figure 5.2.** Photographs of (A) PTKUR AG extender and (B) AG control in the 20 mm defect prior to closure.

Radiographs demonstrate healing progression from 0 to 12 weeks (**Figure 5.3**). New bone formation is ongoing for both groups from 0 to 12 weeks and the defect interfaces are still distinct. The AG extender is maintained at the defect for 12 weeks and new bone growth is evident from the defect interfaces (**Figure 5.3**, double arrows). Complete bridging of the AG control is evident on the medial side, opposite the ulna (**Figure 5.3**, single arrow). However, the low radiodensity at the center of the defect indicates the bone quality may be lacking away from this edge.

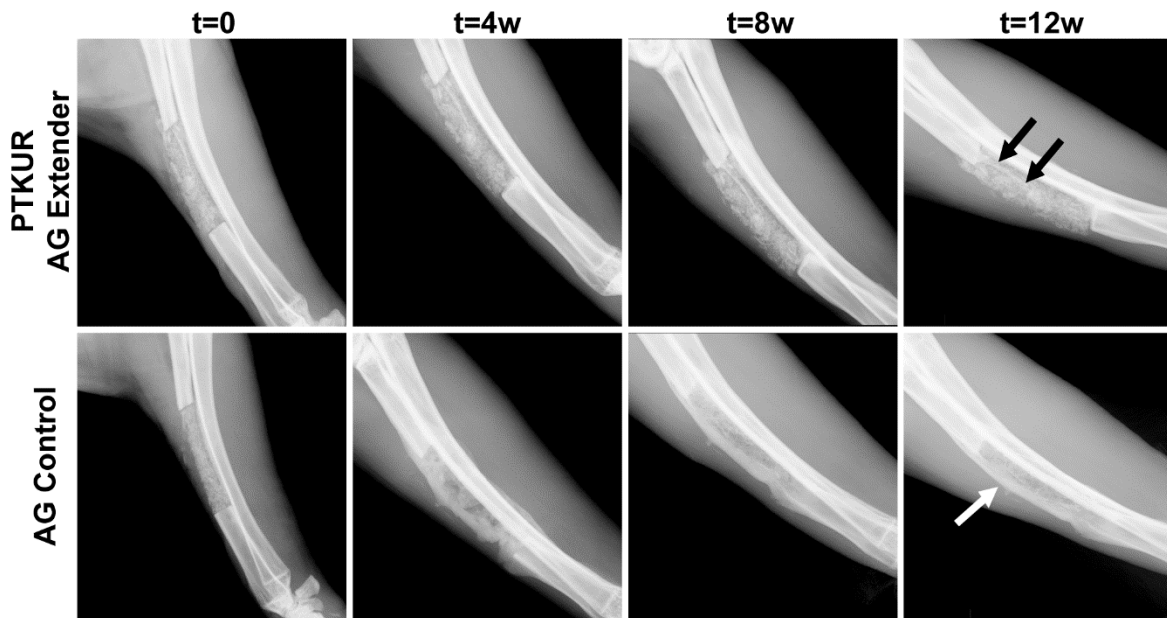


**Figure 5.3.** CT images acquired immediately post-operatively, at 4, 8, and 12 weeks. Remodeling of the PTKUR AG extender progresses each time point (double arrows) and a perimeter of new bone is evident on the lateral surface of the control defect at 12 weeks (single arrow).

Two-dimensional representative  $\mu$ CT reconstructions of the AG extender (**Figure 5.4A**) and the AG control (**Figure 5.4B**) at 12 weeks provide more detail of the extent of graft remodeling and bone quality.

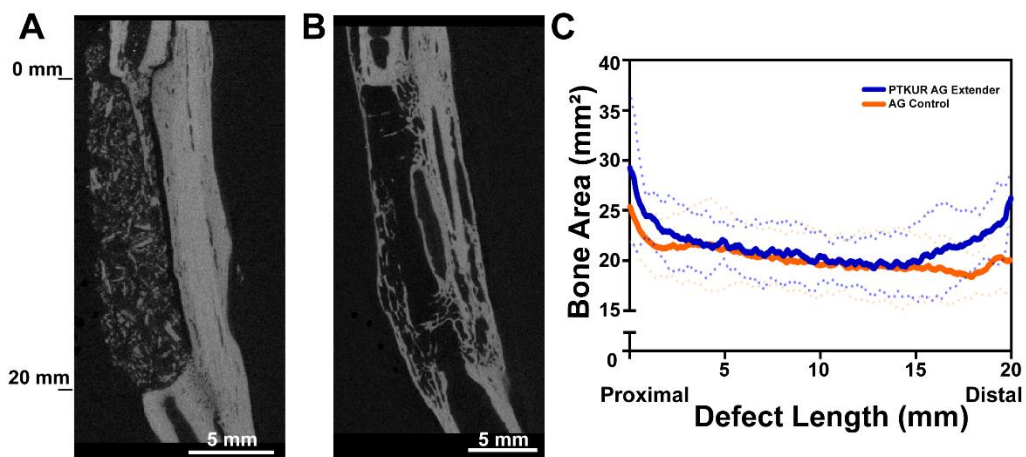


**Figure 5.4.**  $\mu$ CT reconstructions showing remodeling of (A) the AG extender and (B) the control 12 weeks post-operatively. (C) Bone area measurements by  $\mu$ CT, from the proximal to distal interfaces of the defect (including the ulna) for the AG extender and AG control groups. Corresponding dotted lines are standard deviation.

Although implanted AG and new bone are indistinguishable using  $\mu$ CT, reconstructions confirm that the AG extender maintains implanted AG throughout the defect after 12 weeks. Furthermore, new bone from the proximal interface along the medial perimeter of the defect is evident. The high density of the interosseous syndesmosis in all experimental specimens confirms significant new bone growth occurred in this space and along the ulna. Half of the specimens from the experimental group show complete bridging of the defect interfaces through the calcified interosseous syndesmosis and the other half are bridged at one interface and close to bridging at the other. The AG control is completely bridged at the lateral perimeter of the defect; however, calcified tissue is minimal and sporadic throughout the defect space. The AG control exhibited a calcified interosseous syndesmosis and also showed significant new bone growth along the surface of the ulna.

$\mu$ CT was used to quantify the difference in bone formation between the AG extender and AG control groups along the length of the defect. The boundaries of the ulna were indistinguishable at 12 weeks post-implantation, so the entire forearm, from the proximal to distal defect interface, was included in the analysis. Increased axial bone areas were reported for each group toward the interfaces with a gradual decrease as the center was approached (**Figure 5.4C**). This trend indicates a bone growth front from the interfaces, as anticipated. The bone area was higher for the experimental group at the defect interfaces, but very similar toward the center. Given the small sample size, these differences were not significant.

Histological analysis echoed  $\mu$ CT data. Sections from the PTKUR AG extender group stained 12 weeks post-implantation verify that the AG extender (PTKUR stains dark teal/black) was maintained in the defect space and implanted AG persists within the

extender (**Figure 5.5A**, stained). Furthermore, these sections exhibited new bone (red) from the defect interfaces along the medial perimeter of the AG extender and into the interosseous syndesmosis space. Stained sections from the control group demonstrated inconsistent remodeling 12 weeks post-implantation. (**Figure 5.5B**). Two of the four defects treated with AG were filled with trabecular bone. However, the other two formed a sporadic perimeter of bone with little trabecula evident within the defect space. AG control sections imaged under fluorescence indicate mineralization extending the length of the defect as early as 4 weeks. Eight-week fluorochrome binding (orange) extends from the 4-week fluorescence.

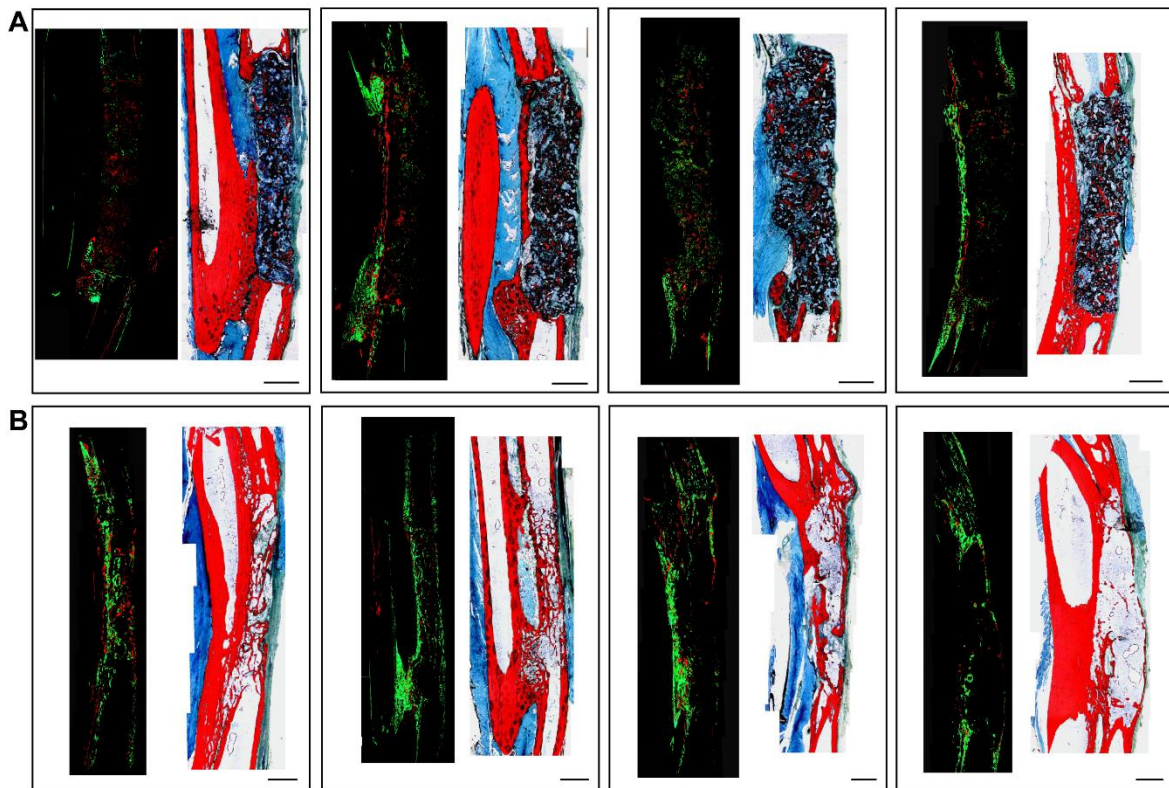


**Figure 5.5.** Dynamic (fluorescent) and 12-week (stained) histology for all specimen in the (A) AG extender group and (B) control group allude to the rate and patterns of bone regeneration and the variation in bone quality for each group.

Fluorochrome injections bind to tissue that is actively mineralizing within 24-36 hours of injection.<sup>40,41</sup> Unstained sections from the PTKUR AG extender group imaged under a fluorescent microscope show temporal regeneration patterns. These validate that bone grew from the defect interfaces at 4 weeks (green) and growth continued towards defect bridging at 8 weeks (orange). Mineralization is evident within the PTKUR AG extender at 4 and 8 weeks which is indicative of mineralization nucleating from implanted AG particles within the extender. The PTKUR AG extender exhibited slightly less mineralization than the AG control at 4 weeks, but this difference is not significant (**Figure 5.6B**).

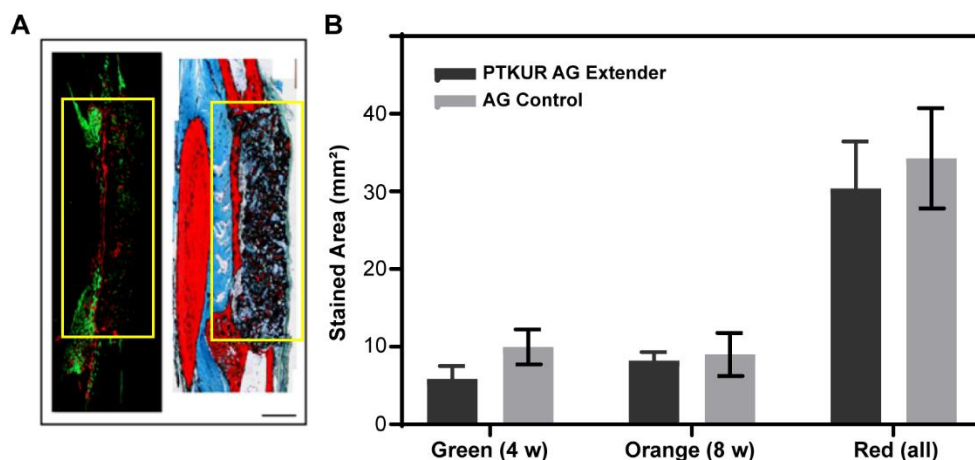


**Figure 5.6.** An area of interest (AOI) was selected to include new bone growth throughout the defect space (A). (B) Histomorphometrical area measurements indicated similar mineralization at 4 and 8 weeks for both groups and the difference between groups was not significant. The difference in the red-stained area (12 weeks) between the 2 groups was not significant indicating the AG extender performed similarly to the control.

A similar amount of mineralization activity from 4 to 8 weeks indicates a linear mineralization rate in the 20 mm defect. Statistically comparable staining between the experimental and control groups at 12 weeks shows that together, new bone and implanted AG maintained within the PTKUR AG extender equated to a similar amount of bone generated in the control group histologically. Magnified images of stained histological



sections show the formation of haversian canal-like structures, the functional units of cortical bone identified by concentric lamellae,<sup>42</sup> in new bone at medial edge of the defect (**Figure 5.7A**, single arrow). A magnified image from within the PTKUR AG extender exhibits bone lining cells at the PTKUR interface (**Figure 5.7B**, double arrows) and the light green staining of the small void suggests the presence of collagen indicating intramembranous bone formation is ongoing. Haversian canal-like structures are also evident in the AG control (**Figure 5.7C**, single arrow) and cellular activity is evident near the bone surface (**Figure 5.7D**).

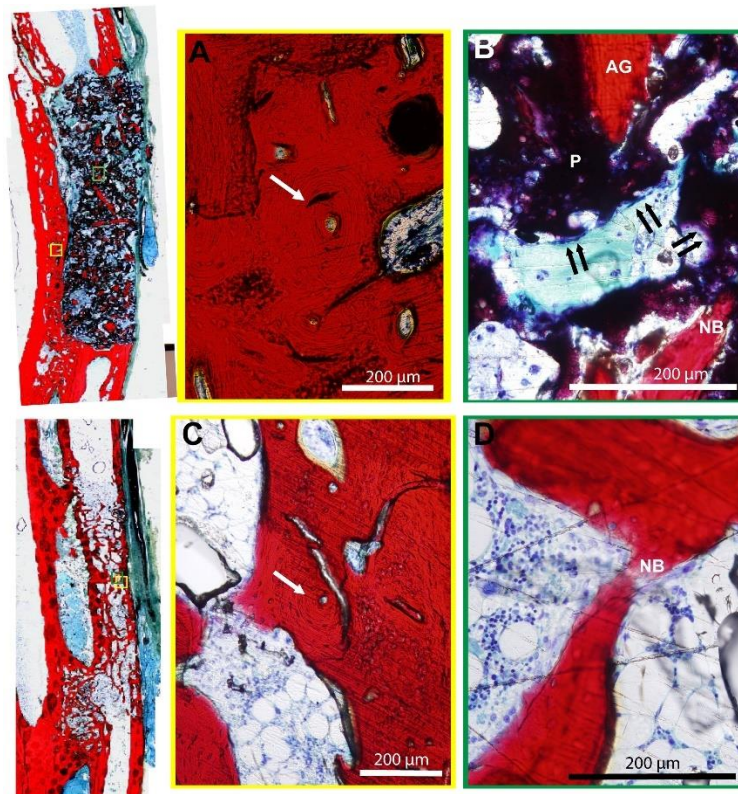


**Figure 5.7.** Magnified histology images show (A) the formation of Haversian canal-like structures (single arrow) forming at the interface of the AG extender and the calcified interosseous syndesmosis (20X). (B) Bone forming cells (double arrows) are actively remodeling the PTKUR AG extender at the polymer surface and intramembranous bone formation is ongoing towards the center of the AG extender. (C) Haversian canal-like structures are also evident in the AG control group (arrow) and (D) bone remodeling is evident. (Bone forming cells: double arrow, NB: new bone, AG: autograft, P: Polymer, scale bar=200μm)

## 5.5 Discussion

In this work, the formulation of PTKUR was modified for application as an AG extender to expand the utility of AG in bone tissue engineering. This PTKUR AG extender exhibited compression resistance, prevented premature AG resorption and graft displacement, and supported cellular infiltration, differentiation, and new bone growth. By increasing the NCO:OH index to 200, a maximum of 70 wt% AG was incorporated in this PTKUR AG extender without sacrificing mechanical properties. At this index, a TFT under 10 minutes was achieved compared to 18 minutes in the previous study presented in Chapter 4. Despite the increase in index, the mechanical properties were slightly reduced given the simultaneous increase in mechanically weak AG. Previous work in the mandible and spine have shown a modulus greater than 1 MPa lends compression resistant properties, so the PTKUR AG extender is anticipated to maintain the defect space in most applications.<sup>21,43</sup>

This material was implanted in a challenging 20 mm defect in the rabbit radius to investigate remodeling *in vivo*. While some have reported non-union of an untreated 10 mm segmental defect in the radius after 8 weeks,<sup>36,39</sup> this model has been shown to heal to some degree without intervention for both 15- and 20 mm defect lengths after 12 weeks and is therefore not considered critical size.<sup>35,44</sup> However, given that the ulna does not eliminate all micromotion at the defect interfaces and the inconsistent regeneration patterns in empty defects, this non-union model is considered stringent for investigating bone graft remodeling.<sup>45</sup> Polymeric AG extenders consisting of 25-75% autograft have shown enhanced or equivalent remodeling compared to AG alone in various *in vivo* models.<sup>32,46</sup> In this work, the maximum AG content that maintained handling, cure rate, and mechanical

properties was incorporated in the PTKUR AG extender.

Subcutaneous injections of fluorochromes with distinguishable emission spectra were implemented to bind calcium ions to detect active tissue mineralization throughout the study.<sup>37,40</sup> This technique was especially valuable in this study to differentiate implanted AG from new bone growth since the AG extender preserved implanted AG at the defect site up to 12 weeks. Qualitatively, mineralization was detected at 4 and 8 weeks at the center of the AG extender. Highly porous, cell-seeded hydroxyapatite implants in radius defects of only 10 mm did not exhibit positive fluorochrome binding throughout the defect until the sixth week post-implantation which suggests enhanced bioactivity of encapsulated AG compared to undifferentiated stem cells (BMSCs).<sup>37</sup> Implanted AG maintains some cell viability and releases paracrine factors that may have drawn cells in to the center of the defect and initiated this turnover within the AG extender.<sup>3,47</sup> Similarly, grafts containing demineralized bone matrix (DBM), which has been shown to retain osteoinductive bone morphogenetic protein (BMP), exhibited greater bone formation in a 15 mm radius defect compared to a collagen/beta-tricalcium phosphate ( $\beta$ -TCP).<sup>48</sup> Histological analysis indicated comparable performance between the AG extender and the control since there was no significant difference in fluorescent/stained bone area between the AG extender and AG control at any time point. Furthermore, the statistically equivalent fluorescent area at 4 and 8 weeks shows a consistent healing rate through 8 weeks. Bodde, et al. suggests healing between 8 and 12 weeks may be critical.<sup>35</sup> Future work should incorporate a distinguishable fluorochrome marker prior to the final time point to quantify bone growth in the final week.

Multiple studies performed in the rabbit radius have reported bone growth from the

proximal, distal, and medial (interosseous membrane) directions with and without a scaffold.<sup>35-37,39,48</sup> The interosseous syndesmosis is a fibrous joint that contains a membrane connecting the ulna and the radius. Significant ossification of the interosseous membrane and fusion of the ulna and radius validated the consideration of the two bones as a unit for  $\mu$ CT analysis.<sup>35,36,49</sup> Despite the ossification of the ulna,  $\mu$ CT quantification showed more bone towards the proximal and distal ends of the defects as anticipated for a creeping substitution mechanism from the defect interfaces. Histology showed, and  $\mu$ CT verified, slightly less bone generation at the distal end of the defect for both groups (**Figure 5.4-5.5**).

A settable poly(propylene fumarate) (PPF) extender showed enhanced bone formation when combined with either 50% AG or 50% allograft in metaphyseal and cortical defects when compared to an AG control.<sup>32</sup> The AG extender had a significantly higher remodeling index, validating the use of AG over allograft.<sup>2</sup> Hydroxylapatite was added to the PPF material to enhance the osteoconductivity of the extender. AG was minimized to 25% in this formulation without sacrificing new bone volume.<sup>46</sup> These studies advocate the use of settable, polymeric AG extenders to expand the application of AG. Furthermore, a PTKUR AG extender with an additional calcium phosphate filler may minimize the AG needed for osteogenesis even further. In the aforementioned study, the extender porosity and small defect sizes allowed for early infiltration. Remodeling of these PPF-based polymeric AG extenders should be evaluated in larger defects at later time points to compare graft resorption and bone formation in critical sized defects.

While the handling properties of a particulate AG extender may not be sufficient for some applications, bioactive glass has been investigated as a bone graft extender given

its osteogenic properties.<sup>44</sup> Bioactive glass AG extenders with as little as 40 wt% AG showed increased new bone formation in cranial defects.<sup>50</sup> The same study showed 20 wt% AG was insufficient to improve osteogenesis. Another study concluded a 1:1 blend of AG and bioactive glass particles may not be adequate after implantation in a mechanically loaded, 16 mm segmental defect in the canine femur.<sup>29</sup> This study included torsional testing as an output parameter. Although these anatomical environments are very different, these contradictions allude to mechanical testing as an important assessment for bone quality when investigating bone graft remodeling in segmental defects.

Future work will identify the minimum AG content that will preserve osteoinductivity of the PTKUR AG extender. These studies will go beyond 12 weeks to investigate the complete remodeling rate. Additional post-harvest mechanical analysis will also be included to investigate bone quality at these late time points.

## 5.6 Conclusion

This work describes the formulation of a moldable and settable PTKUR AG extender that affords handling properties to AG, the gold standard bone graft material. The AG extender incorporated 70 wt% AG and cured to a compression resistant, cell-degradable tissue engineering bone graft. When implanted in a large rabbit radius segmental defect model, bone-forming cells were identified at the center of the AG extender after 12 weeks. AG was maintained in the defect and remodeling was ongoing. The results described herein demonstrate a minimally invasive PTKUR AG extender that incorporates the osteoinductive properties of AG and the potential for consistent and improved bone quality.

## References

1. Albrektsson T, Johansson C. Osteoinduction, osteoconduction and osseointegration. *European Spine Journal* 2001;10(2):S96-S101.
2. Shafiei Z, Bigham AS, Dehghani SN, Torabi Nezhad S. Fresh cortical autograft versus fresh cortical allograft effects on experimental bone healing in rabbits: radiological, Histopathological and Biomechanical evaluation. *Cell and Tissue Banking* 2009;10(1):19-26.
3. Khan SN, Cammisa FP, Sandhu HS, Diwan AD, Girardi FP, Lane JM. The Biology of Bone Grafting. *Journal of the American Academy of Orthopaedic Surgeons* 2005;13(1):77-86.
4. Burchardt H. The biology of bone graft repair. *Clinical orthopaedics and related research* 1983;174:28-34.
5. Rogers GF, Greene AK. Autogenous Bone Graft: Basic Science and Clinical Implications. *Journal of Craniofacial Surgery* 2012;23(1):323-327.
6. Arrington ED, Smith WJ, Chambers HG, Bucknell AL, Davino NA. Complications of iliac crest bone graft harvesting. *Clinical orthopaedics and related research* 1996;329:300-309.
7. Kanayama M, Hashimoto T, Shigenobu K, Oha F, Ishida T, Yamane S. Pitfalls of anterior cervical fusion using titanium mesh and local autograft. *Clinical Spine Surgery* 2003;16(6):513-518.
8. Couture DE, Branch Jr CL. Posterior lumbar interbody fusion with bioabsorbable spacers and local autograft in a series of 27 patients. *Neurosurgical focus* 2004;16(3):1-6.
9. Chen W-J, Tsai T-T, Chen L-H, Niu C-C, Lai P-L, Fu T-S, McCarthy K. The fusion rate of calcium sulfate with local autograft bone compared with autologous iliac bone graft for instrumented short-segment spinal fusion. *Spine* 2005;30(20):2293-2297.
10. Brugnami F, Caiazzo A, Leone C. Local intraoral autologous bone harvesting for dental implant treatment: alternative sources and criteria of choice. *The Keio journal of medicine* 2009;58(1):24-28.
11. Johansson L-Å, Isaksson S, Lindh C, Becktor JP, Sennerby L. Maxillary sinus floor augmentation and simultaneous implant placement using locally harvested autogenous bone chips and bone debris: a prospective clinical study. *Journal of Oral and Maxillofacial Surgery* 2010;68(4):837-844.
12. Daubs MD. Early Failures Following Cervical Corpectomy Reconstruction With Titanium Mesh Cages and Anterior Plating. *Spine* 2005;30(12):1402-1406.
13. von Arx T, Kurt B. Implant placement and simultaneous ridge augmentation using autogenous bone and a micro titanium mesh: a prospective clinical study with 20 implants. *Clinical oral implants research* 1999;10(1):24-33.
14. Rosenberg WS, Mummaneni PV. Transforaminal lumbar interbody fusion: technique, complications, and early results. *Neurosurgery* 2001;48(3):569-575.
15. Aponte-Tinao L, Ayerza M, Muscolo D, Farfalli G. What are the risk factors and management options for infection after reconstruction with massive bone allografts? *Clinical orthopaedics and related research* 2016;474(3):669-73.
16. Yu X, Tang X, Gohil SV, Laurencin CT. Biomaterials for Bone Regenerative Engineering. *Advanced Healthcare Materials* 2015;n/a-n/a.

17. Brown KV, Li B, Guda T, Perrien DS, Guelcher SA, Wenke JC. Improving bone formation in a rat femur segmental defect by controlling bone morphogenetic protein-2 release. *Tissue Engineering Part A* 2011;17(13-14):1735-1746.
18. James AW, LaChaud G, Shen J, Asatrian G, Nguyen V, Zhang X, Ting K, Soo C. A Review of the Clinical Side Effects of Bone Morphogenetic Protein-2. *Tissue Engineering* 2016(ja).
19. Li B, Yoshii T, Hafeman AE, Nyman JS, Wenke JC, Guelcher SA. The effects of rhBMP-2 released from biodegradable polyurethane/microsphere composite scaffolds on new bone formation in rat femora. *Biomaterials* 2009;30(35):6768-6779.
20. McKay WF, Peckham SM, Badura JM. A comprehensive clinical review of recombinant human bone morphogenetic protein-2 (INFUSE® Bone Graft). *International orthopaedics* 2007;31(6):729-734.
21. Talley AD, Kalpakci KN, Shimko DA, Zienkiewicz K, Cochran D, Guelcher S. Effects of rhBMP-2 Dose and Ceramic Composition on New Bone Formation and Space Maintenance in a Canine Mandibular Ridge Saddle Defect Model. *Tissue Engineering* 2016(ja).
22. Lee JH, Hwang CJ, Song BW, Koo KH, Chang BS, Lee CK. A prospective consecutive study of instrumented posterolateral lumbar fusion using synthetic hydroxyapatite (Bongros®-HA) as a bone graft extender. *Journal of Biomedical Materials Research Part A* 2009;90(3):804-810.
23. Lee JH, Chang B-S, Jeung U-O, Park K-W, Kim M-S, Lee C-K. The first clinical trial of beta-calcium pyrophosphate as a novel bone graft extender in instrumented posterolateral lumbar fusion. *Clinics in orthopedic surgery* 2011;3(3):238-244.
24. Dai L-Y, Jiang L-S. Single-level instrumented posterolateral fusion of lumbar spine with  $\beta$ -tricalcium phosphate versus autograft: a prospective, randomized study with 3-year follow-up. *Spine* 2008;33(12):1299-1304.
25. Lerner T, Bullmann V, Schulte TL, Schneider M, Liljenqvist U. A level-1 pilot study to evaluate of ultraporous  $\beta$ -tricalcium phosphate as a graft extender in the posterior correction of adolescent idiopathic scoliosis. *European Spine Journal* 2009;18(2):170-179.
26. Linovitz RJ, Peppers TA. Use of an advanced formulation of  $\beta$ -tricalcium phosphate as a bone extender in interbody lumbar fusion. *Orthopedics* 2002;25(5):S585-S589.
27. Smucker JD, Petersen EB, Fredericks DC. Assessment of MASTERGRAFT PUTTY as a graft extender in a rabbit posterolateral fusion model. *Spine* 2012;37(12):1017-1021.
28. Smucker JD, Petersen EB, Nepola JV, Fredericks DC. Assessment of MASTERGRAFT® STRIP with bone marrow aspirate as a graft extender in a rabbit posterolateral fusion model. *The Iowa orthopaedic journal* 2012;32:61.
29. Keränen P, Itälä A, Koort J, Kohonen I, Dalstra M, Kommonen B, Aro HT. Bioactive Glass Granules as Extender of Autogenous Bone Grafting in Cementless Intercalary Implant of the Canine Femur. *Scandinavian Journal of Surgery* 2007;96(3):243-251.
30. Chedid MK, Tundo KM, Block JE, Muir JM. Hybrid Biosynthetic Autograft Extender for Use in Posterior Lumbar Interbody Fusion: Safety and Clinical

- Effectiveness. *The open orthopaedics journal* 2015;9:218.
31. Hile DD, Kandziora F, Lewandrowski K-U, Doherty SA, Kowaleski MP, Trantolo DJ. A poly(propylene glycol-co-fumaric acid) based bone graft extender for lumbar spinal fusion: in vivo assessment in a rabbit model. *European spine journal : official publication of the European Spine Society, the European Spinal Deformity Society, and the European Section of the Cervical Spine Research Society* 2006;15(6):936-943.
  32. Lewandrowski KU, Bondre S, Gresser JD, Silva AE, Wise DL, Trantolo DJ. Augmentation of osteoinduction with a biodegradable poly (propylene glycol-co-fumaric acid) bone graft extender. *Bio-medical materials and engineering* 1999;9(5, 6):325-334.
  33. Walsh WR, Oliver RA, Gage G, Yu Y, Bell D, Bellemore J, Adkisson HD. Application of resorbable poly (lactide-co-glycolide) with entangled hyaluronic acid as an autograft extender for posterolateral intertransverse lumbar fusion in rabbits. *Tissue Engineering Part A* 2010;17(1-2):213-220.
  34. McEnery MA, Lu S, Gupta MK, Zienkiewicz KJ, Wenke JC, Kalpakci KN, Shimko DA, Duvall CL, Guelcher SA. Oxidatively degradable poly (thioketal urethane)/ceramic composite bone cements with bone-like strength. *RSC advances* 2016;6(111):109414-109424.
  35. Bodde EW, Spauwen PH, Mikos AG, Jansen JA. Closing capacity of segmental radius defects in rabbits. *Journal of Biomedical Materials Research Part A* 2008;85(1):206-217.
  36. Guda T, Walker JA, Pollot BE, Appleford MR, Oh S, Ong JL, Wenke JC. In vivo performance of bilayer hydroxyapatite scaffolds for bone tissue regeneration in the rabbit radius. *Journal of Materials Science: Materials in Medicine* 2011;22(3):647-656.
  37. Rathbone C, Guda T, Singleton B, Oh D, Appleford M, Ong J, Wenke J. Effect of cell-seeded hydroxyapatite scaffolds on rabbit radius bone regeneration. *Journal of Biomedical Materials Research Part A* 2014;102(5):1458-1466.
  38. International A. ASTM F451-16, Standard specification for acrylic bone cement. West Conshohocken, PA; 2016.
  39. Guda T, Walker JA, Singleton BM, Hernandez JW, Son J-S, Kim S-G, Oh DS, Appleford MR, Ong JL, Wenke JC. Guided bone regeneration in long-bone defects with a structural hydroxyapatite graft and collagen membrane. *Tissue Engineering Part A* 2012;19(17-18):1879-1888.
  40. van Gaalen SM, Kruyt MC, Geuze RE, de Bruijn JD, Alblas J, Dhert WJ. Use of fluorochrome labels in in vivo bone tissue engineering research. *Tissue engineering Part B: Reviews* 2010;16(2):209-217.
  41. Lu S, McGough MA, Shiels SM, Zienkiewicz KJ, Merkel AR, Vanderburgh JP, Nyman JS, Sterling JA, Tennent DJ, Wenke JC. Settable polymer/ceramic composite bone grafts stabilize weight-bearing tibial plateau slot defects and integrate with host bone in an ovine model. *Biomaterials* 2018.
  42. Frankenburg EP, Goldstein SA, Bauer TW, Harris SA, Poser RD. Biomechanical and histological evaluation of a calcium phosphate cement. *J Bone Joint Surg Am* 1998;80(8):1112-24.
  43. Shiels SM, Talley AD, McGough MA, Zienkiewicz KJ, Kalpakci K, Shimko D,



- Guelcher SA, Wenke JC. Injectable and compression-resistant low-viscosity polymer/ceramic composite carriers for rhBMP-2 in a rabbit model of posterolateral fusion: a pilot study. *Journal of orthopaedic surgery and research* 2017;12(1):107.
44. Wheeler DL, Stokes KE, Park HM, Hollinger JO. Evaluation of particulate Bioglass® in a rabbit radius osteotomy model. *Journal of Biomedical Materials Research* 1997;35(2):249-254.
45. Rodriguez-Merchan EC, Forriol F. Nonunion: General Principles and Experimental Data. *Clinical Orthopaedics and Related Research* 2004;419:4-12.
46. Lewandrowski K-U, Hile DD, Thompson BM, Wise DL, Tomford WW, Trantolo DJ. Quantitative measures of osteoinductivity of a porous poly (propylene fumarate) bone graft extender. *Tissue engineering* 2003;9(1):85-93.
47. Miron RJ, Gruber R, Hedbom E, Saulacic N, Zhang Y, Sculean A, Bosshardt DD, Buser D. Impact of Bone Harvesting Techniques on Cell Viability and the Release of Growth Factors of Autografts. *Clinical Implant Dentistry and Related Research* 2013;15(4):481-489.
48. McDaniel JS, Pilia M, Raut V, Ledford J, Shiels SM, Wenke JC, Barnes B, Rathbone CR. Alternatives to autograft evaluated in a rabbit segmental bone defect. *International orthopaedics* 2015:1-7.
49. Meinig RP, Rahn B, Perren SM, Gogolewski S. Bone regeneration with resorbable polymeric membranes: treatment of diaphyseal bone defects in the rabbit radius with poly (L-lactide) membrane. A pilot study. *Journal of orthopaedic trauma* 1996;10(3):178-190.
50. Conejero JA, Lee JA, Ascherman JA. Cranial Defect Reconstruction in an Experimental Model Using Different Mixtures of Bioglass and Autologous Bone. *Journal of Craniofacial Surgery* 2007;18(6):1290-1295.

## CHAPTER 6

### VI. LONG-TERM REMODELING OF A NANOCRYSTALLINE HYDROXYAPATITE-POLY(THIOKETAL URETHANE) BONE VOID FILLER IN A FEMORAL CONDYLE DEFECT

#### 6.1 Abstract

Polyurethanes (PURs) are an attractive material for tissue engineering bone graft substitutes since they can be formulated to be injectable, settable, and biocompatible, and their mechanical properties and degradation rates can be tuned for specific orthopedic applications. Recently, a novel poly(thioketal urethane) (PTKUR) bone graft was developed to address unpredictable resorption associated with hydrolytic degradation of ester groups in poly(ester urethane) bone grafts *in vivo*. In the present study, nanocrystalline hydroxyapatite (nHA) was incorporated with PTKUR to exploit the osteogenic and mechanical benefits of nHA in a polymeric nHA-PTKUR bone graft. nHA was grafted with lysine triisocyanate to enhance nHA dispersion in a lysine-based nHA-PTKUR hybrid polymer that exhibits a complementary combination of cell-mediated resorption mechanisms as PTKUR degrades by ROS and nHA is resorbed by osteoclasts that release ROS. nHA-PTKUR “glue,” without inorganic filler particles, incorporated 25 vol% nHA, degraded rapidly in oxidative conditions, and remained stable at 4 wt% mass loss after 10 days in hydrolytic conditions. Mechanical analysis revealed a modulus of 370 MPa and ultimate strength of 53 MPa. HA-PTKUR “putties” (14 vol% nHA) contained 45 wt% calcium phosphate particles (CaP), 10 wt% CaP/35 wt% sucrose porogen, or 45 wt% sucrose to explore the addition of slowly-degrading, mechanically robust, and osteoconductive CaP particles and porosity on mechanical properties and remodeling *in vivo*. nHA-PTKUR glue and putties demonstrated cellular infiltration, a combination of endochondral and intramembranous bone formation, and new calcified bone within

femoral condyle defects as early as four months. This work presents a critical step towards the development of a nHA-PTKUR bone graft with potential application in weight-bearing defects.

## 6.2 Introduction

Previous work has demonstrated the advantages of lysine-based poly(ester urethane) (PEUR) as a settable, tissue engineering bone graft.<sup>1-10</sup> As discussed in the preceding chapters, these PEURs undergo autocatalytic degradation in hydrolytic environments leading to unpredictable resorption that may not match patient biology.<sup>8,11</sup> In Chapter 3, a poly(thioketal urethane) (PTKUR) was introduced to overcome the shortcomings of PEURs. A novel thioketal (TK) diol was synthesized for fabrication of a hydrolytically stable PTKUR that undergoes oxidation of the lysine and TK residues in the presence of cell-generated reactive oxygen species (ROS).<sup>12</sup> PTKURs demonstrated bone-like strength and histological analysis showed evidence of osteoclast-mediated resorption of the cements at 6 and 12 weeks *in vivo*.

Hydroxyapatite (HA) makes up 50-70% of native bone making it another attractive bone graft substitute.<sup>13-18</sup> Nanocrystalline hydroxyapatite (nHA) in particular has been shown to stimulate new bone formation by enhancing osteoblastic differentiation compared to micron-scale hydroxyapatite.<sup>19,20</sup> Polyurethane/nHA composite bone grafts have been proposed to take advantage of the properties of the two components.<sup>21-23</sup> However, despite the inherent strength of HA, limited HA-polymer bonding and HA aggregation generally decrease the mechanical properties of these composites.<sup>13</sup> To overcome this, the surface hydroxyl (OH) groups of nHA can be grafted with isocyanate (NCO) for NCO-grafted nHA prepolymer and synthesis of nHA-PUR hybrid polymers.<sup>19,22,24-26</sup> Previously, we presented enhanced dispersion of lysine triisocyanate grafted nHA (nHA-LTI) in nHA-

LTI-PEUR nanocomposites synthesized from nHA-LTI/LTI prepolymer and PCL triol (MW=300). LTI grafting yielded compressive properties and bending strengths suitable for weight-bearing applications and *in vitro* studies demonstrated enhanced mineralization compared with nHA-PEUR nanocomposites in which the nHA was not grafted in a prepolymer step.<sup>19</sup> Furthermore, nHA-LTI-PEUR nanocomposites incorporating 55 wt% CaP particles mechanically stabilized un-instrumented tibial plateau defects in sheep and supported remodeling and osteogenesis at 16 weeks.<sup>25</sup>

In this study, the osteogenic properties of nHA were combined with the bulk material properties of PTKURs in a new class of settable nHA-PTKUR hybrid polymer synthesized by the reaction of nHA-LTI/LTI prepolymer and TK diol. A complementary combination of cell-mediated resorption mechanisms was anticipated as PTKUR degrades by ROS and nHA is resorbed by osteoclasts that release ROS.<sup>12,27-29</sup> The bulk material properties were characterized prior to implantation in a rabbit femoral condyle defect model. The material was also tested in a small notch defect in the tibial diaphysis to investigate persistence of the nHA-PTKUR bone graft in a non-critical defect. These studies were carried out 18 months to explore cellular infiltration, differentiation of osteoprogenitor cells, and nHA-PTKUR resorption long-term. The addition of CaP particles and two ranges of sucrose porogen is also investigated to determine the effects of slowly-degrading CaP and porosity on mechanical properties and remodeling *in vivo*.

### 6.3 Materials and Methods

*Materials.* All reagents for thioketal (TK) diol synthesis, iron (III) acetylacetonate (FeAA) catalyst,  $\epsilon$ -caprolactone, and sucrose were purchased from Sigma Aldrich. FeAA was dissolved in dry  $\epsilon$ -caprolactone (5 % w/w) prior to use for a flowable, low concentration catalyst solution. Lysine triisocyanate (LTI) was purchased from Jinan

Haohua Industry Co., LTD (Jinan, China) and carbon treated in tert-butyl-methyl ether (TBME, Acros Organics) prior to use.<sup>12,19,25</sup> Nanostim<sup>TM</sup> Synthetic Bone Paste (NS) and ceramic calcium phosphate (CaP) particles were provided by Medtronic (Memphis, TN). Upon receipt, particles were ground to 100-300  $\mu\text{m}$ , washed with acetone and water, and dried under vacuum (100  $^{\circ}\text{C}$ ).<sup>12</sup>

*Hydroxyapatite dewatering.* Nano-scale hydroxyapatite (nHA) was isolated from the NS suspension for use in nHA-PTKUR synthesis. Approximately 5 cc NS was dispensed into a 50 mL centrifuge tube. The centrifuge tube was filled with 40 mL 2-propanol and the mixture vortexed until the NS suspension was dispersed in the solvent. The nHA was separated using centrifugation and the process repeated 3 times. The isolated nHA pellet was dried under vacuum overnight and then under vacuum at 80  $^{\circ}\text{C}$  for at least 24 hours. The dry pellet was morselized to nano-scaled particles using a mortar and pestle. Transmission electron microscopy (TEM) was used to visualize the geometry of the resulting nHA particles and Image J to measure particle diameter from SEM images. The nHA was re-dried for at least 48 hours at 80  $^{\circ}\text{C}$  immediately prior to use. Dry material was sent to Micromeritics Analytical Services for analysis. The density and surface area were evaluated by gas displacement (helium) and the BET method according to ISO 9277, respectively.<sup>30</sup>

*Hydroxyapatite surface modification.* nHA was grafted with polycaprolactone (PCL-g-nHA) or LTI (LTI-g-nHA) for addition to the diol and isocyanate phases, respectively, adapting methods described previously.<sup>19,25,31</sup> Dry  $\epsilon$ -caprolactone was charged to a three-neck boiling flask containing dry nHA particles (3.7:1) and equipped with a condenser. The reaction was stirred for 24 hours at 150  $^{\circ}\text{C}$ . Grafted particles were

recovered from excess  $\epsilon$ -caprolactone by sonicating with chloroform four times. PCL grafted nHA was dried under vacuum at 80 °C overnight. LTI was grafted to the surface of nHA by combining dry nHA particles with LTI (1:1) and mixing for 1 minute (FlackTek SpeedMixer, DAC 150 FVZ-K). FeAA catalyst solution (0.5 % w/w) was added and the suspension mixed at maximum speed for a total of 10 minutes. Surface modified particles were washed from excess LTI and catalyst with TBME. Clean LTI-g-NS was dried under vacuum.

*Nano-scale hydroxyapatite thioketal synthesis.* A TK diol was synthesized as described in the previous chapters.<sup>12</sup> 2,2-dimethoxypropane was reacted with thioglycolic acid in acetonitrile for 24 hours at room temperature. The intermediate was filtered and the solvent removed. Dry intermediate was dissolved in tetrahydrofuran and added to lithium aluminum hydride in diethyl ether dropwise in an ice bath. The reaction was refluxed at 52 °C overnight and the product extracted. The product was dried under vacuum for at least 48 hours to ensure all solvents were removed. FeAA catalyst was dissolved in the TK diol (for total of 0.125 wt% FeAA in nHA-PTKUR material for composite putties or 0.0625% for nHA-PTKUR glue) on a stir plate overnight. The catalyzed TK was then blended 1:1 with dry PCL-g-NS and mixed until homogeneous (about 5 minutes) using a speed mixer. The nHA-TK was stored at 4 °C.

*nHA-LTI prepolymer synthesis.* The prepolymer was synthesized according to methods published previously.<sup>19,25</sup> Dry, LTI-g-NS was ground with a mortar and pestle to ensure nano-scale powder. Then, HA was added to a mixing cup followed by the addition of LTI for 40 wt% LTI-g-NS in LTI. The mixture was mixed in 1-minute intervals using a speed mixer until homogeneous (about 5 minutes). The NCO number was verified by NCO

titration.<sup>32</sup>

*nHA-PTKUR fabrication and characterization.* Remodeling of a settable nHA-PTKUR hybrid polymer bone graft was investigated with and without porogen and CaP. All formulations were fabricated by first blending catalyzed nHA-PTKUR and nHA-LTI prepolymer at an NCO:OH index of 140 for composites and 120 for nHA-PTKUR glue. The lower index of the glue was chosen to achieve approximately equal volumes of nHA-LTI and nHA-PTKUR. The solids (CaP ± sucrose) were then added and mixed by hand until homogeneous, about 30 seconds. The material was molded or loaded into a syringe for the desired delivery method. The materials were cured overnight in cylindrical tubes (6 mm diameter) for characterization. Cured samples were then leached in water at 37 °C for 5 days to ensure all sucrose was removed. Samples without solids were  $\gamma$ -irradiated at a dose of 25 kGY and sent NAMSA<sup>®</sup> for cytotoxicity testing to ensure nHA-PTKUR biocompatibility. There, *in vitro* cytotoxicity testing was performed according to ISO 10993-5 under an ISO 13485 certified Quality System with the test method accredited to ISO 17025.

*Topographical characterization.* The HA content in the polymer allowed for the use of micro computed tomography ( $\mu$ CT) to quantify porosity. Cured, leached samples were imaged via  $\mu$ CT. BV/TV analysis was performed on the center of the sample and the complement taken as the porosity. The appropriate threshold for analysis was determined for each group. Scanning electron microscopy (SEM, Zeiss Merlin) was performed on gold coated samples to expand on the findings from  $\mu$ CT.

*Degradation mechanism.* Samples without filler were incubated in both accelerated oxidative and hydrolytic conditions to explore the degradation mechanisms of nHA-

PTKUR. Oxidative media was made as described in the preceding chapters.<sup>12,27,33</sup> 20 wt% hydrogen peroxide was added to 0.1 M cobalt chloride and stirred to form solution. The media was stored at 4 °C protected from light. Cylindrical samples were cut to 30-40 mg samples and dried under vacuum. The initial mass was recorded before submerging samples in oxidative media or PBS. Samples were removed from the solutions periodically, washed 3 times with deionized water, and dried under vacuum for 48 hours. Dry samples were massed and re-introduced to fresh media. The mass was compared to the initial mass to approximate a degradation rate.

*Mechanical characterization.* Quasi-static compression testing was performed on all groups to quantify the mechanical characteristics and investigate the mechanical consequences of sucrose addition.<sup>12,34,35</sup> Leached cylindrical samples were cut to a height of 12 mm (2X diameter) using an IsoMet Low Speed Saw to ensure flat, parallel edges. The samples were compressed between circular platens at a rate of 25 mm/min and the force and displacement recorded (MTS 858 Bionix Servohydraulic Test System). Engineering stress and strain were calculated and used to determine the modulus, maximum stress, and yield point for each material.

*nHA-PTKUR in rabbits.* All surgical and care procedures were carried out at IBEX Preclinical Research, Inc. (Logan, UT) under aseptic conditions per the approved IACUC protocol. nHA-PTKUR putties containing 45 wt% CaP (CaP group), 35 wt% sucrose plus 10 wt% CaP (CaP/S group), or 45 wt% sucrose (S group), and an nHA-PTKUR “glue” without solids were implanted in bilateral cylindrical defects (5 mm Ø x 8 mm) in the distal femoral condyles of rabbits. Unilateral slot defects (10 mm length x 2 mm) were also created in the right tibia and filled with the glue material or left empty as a control. Each



rabbit received a different graft in each femur for n=3 for each group at each time point. Animals were sacrificed at 4, 12 and 18 months. The femurs and tibias were harvested and fixed in 10% formalin for two weeks.

*In vivo analysis.* While in formalin, the bones were scanned with a voxel size of 17.2  $\mu\text{m}$  using a  $\mu\text{CT}$  50 (Scanco). 2D images were taken at the center of the defect and the defect length measured using ImageJ. The length of the graft was measured at three different points on the graft for each 2D image and an average reported for each specimen. Bone volume percent (BV/TV) was quantified for three concentric, annular cylinders (“rings”) with a width of 0.8 mm and a central core cylinder with a radius of 1.6 mm (**Figure 6.4B**). Theoretically, the inner bound of Pipe 1 is at the interface of the defect and the host-bone and consists of mostly host bone. The cylinders were morphed to a length encompassing the center 5 mm of the defect. A constant analysis threshold was maintained for all groups (**Figure 6.4C**).

Calcified specimens were processed and plastic-embedded by Histon for histology. Sections were taken from the center of the defect, ground to 30-70  $\mu\text{m}$ , and stained with Stevenel’s Blue for histological analysis. Methods described previously were adapted for quantitative histomorphometry. A 2 mm x 8 mm rectangle was created 2 mm from the insertion point of the cylindrical defect. The rectangle was divided into 8 smaller rectangles that were 1 mm x 2 mm to compare staining at various regions from the host-bone, host-bone/defect interface and within the defect at 4, 12, and 18 months (**Figure 6.7**). The distal 4 regions were included in analysis since the marrow space (included in the most proximal regions) will introduce significant error. One section from each group was stained with Safranin O and Fast Green which better distinguishes cartilage and bone. A similar

histomorphometric analysis was performed for these sections, although these sections may not have been taken directly from the center of the defect.

*Statistical methods.* All data is reported as the average  $\pm$  standard deviation unless otherwise specified. A one-way ANOVA (GraphPad Prism) with a post-hoc Tukey Test was used to test for significance of mechanical properties. A Student's t-Test was performed to detect differences in defect length with time for a given material group. A two-way ANOVA with a post-hoc Tukey Test was used to investigate differences in BV/TV for each pipe at the various time points for each material. Because the common threshold may have included more or less graft depending on the group, BV/TV could not be compared between the different materials. A two-way ANOVA was also performed on histomorphometry data with a post-hoc Sidak's multiple comparisons test. Histomorphometry is plotted with standard error of the mean (SEM).

#### 6.4 Preliminary Results

*nHA-PTKUR characterization.* NS nHA was used to synthesize nHA-PTKUR. After de-watering, NS particles were short fibers with a width of 20 nm (**Figure 6.1**). This shape yielded a high surface area of 58 m<sup>2</sup>/g and a density of 2.9 g/cm<sup>3</sup>. Surface grafting did not affect the shape of the fibers.

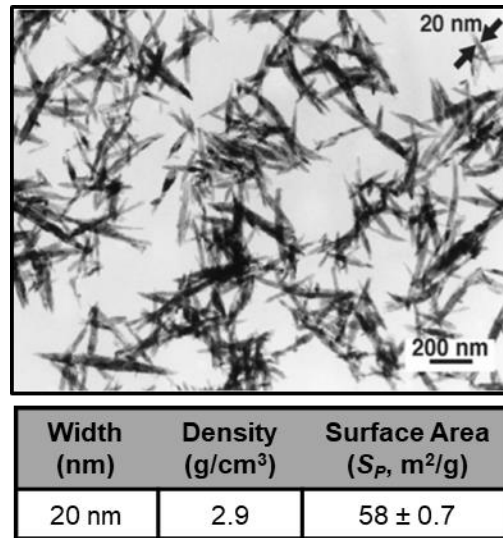


**Figure 6.1.** Dewatered NanoStim™ nHA particles visualized with TEM.

nHA-TK, nHA-LTI, CaP, and sucrose were sterilized using radiation and composites fabricated under sterile conditions for cytotoxicity testing. Both the glue and the CaP/S putty showed no signs of causing cell lysis or toxicity. The nHA-PTKUR glue was subjected to an accelerated oxidative environment to investigate degradation mechanisms of the polymer. Specimens exhibited a mass loss of 41% after 24 hours in oxidative media and were mostly degraded after 48 hours. Conversely, in hydrolytic conditions, nHA-PTKUR had a mass loss of 4 wt% after 10 days and remained stable for 90 days when the experiment was ended.

The putties incorporated a total of 14 vol% nHA and nHA-PTKUR glue contained 25 vol%. This high HA content allowed for visualization of the nHA-PTKUR polymer using  $\mu$ CT. 2D  $\mu$ CT reconstructions of leached samples revealed minimal porosity for the 45 wt% CaP group and an increase in porosity with increasing sucrose, as anticipated (**Figure 6.2A**). SEM images paralleled these findings (**Figure 6.2B**). All samples were leached in water for 5 days prior to mechanical testing. nHA-PTKUR glue exhibited a

significantly higher ultimate strength, yield strength, and yield strain than any of the putties and the addition of sucrose porogen did not have a significant effect on these parameters (Figure 6.3B-D). The moduli of the glue and CaP putty were similar (370 MPa), but there was a significant difference between the modulus of the CaP putty and the CaP/S putty that incorporated porogen (Figure 6.3A).

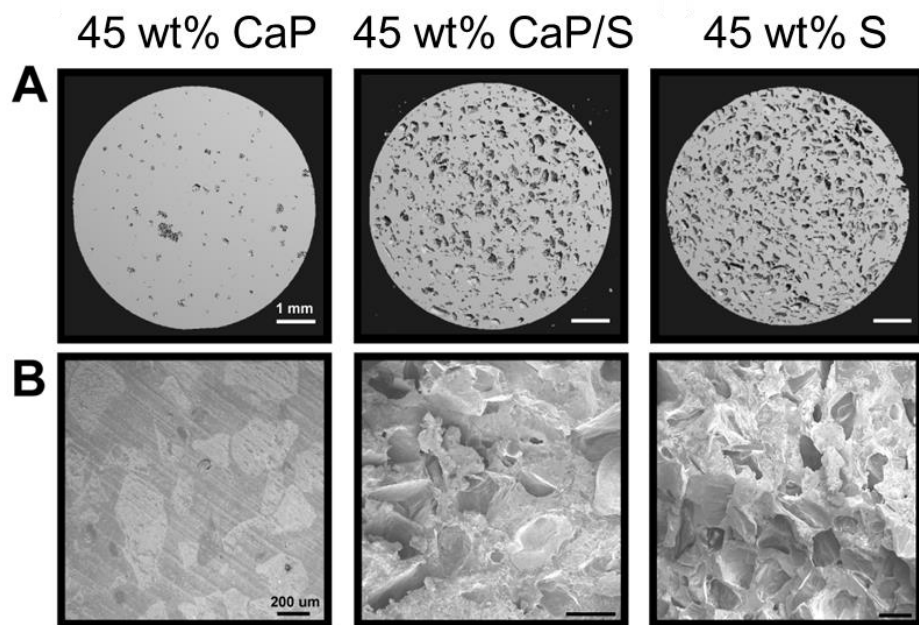


**Figure 6.2.** Qualitative analysis of three material groups tested *in vivo* as visualized by (A)  $\mu$ CT and (B) SEM.

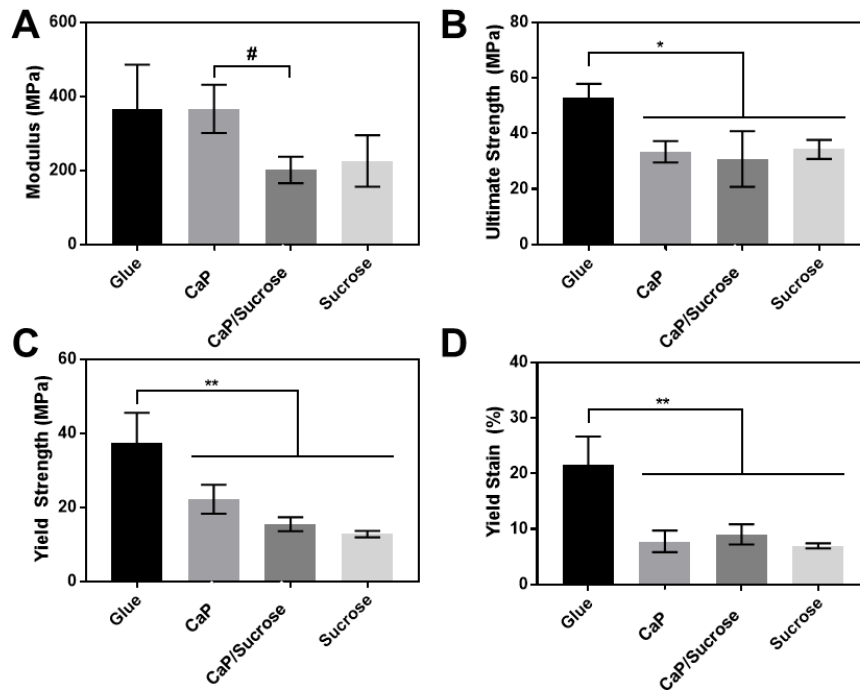


**Figure 6.3.** Mechanical analysis of material groups included in the *in vivo* study revealed a statistically significant difference in modulus between the CaP and CaP/S group (A). nHA-PTKUR had a significantly higher (B) ultimate strength, (C) yield strength, and (D) yield strain compared to any of the putties. (#:  $P \leq 0.1$ , \*:  $P \leq 0.05$ , \*\*:  $P \leq 0.01$ ).

*In vivo analysis of nHA-PTKUR in rabbit hind-limb defects.* Remodeling of nHA-PTKUR (“glue”) and putties with three different solid and porogen loading ratios were investigated in femoral condyle plug defects in rabbits.  $\mu$ CT analysis revealed a statistically significant decrease in defect length from 4 to 18 months in all groups and all groups trended shorter for each timepoint (**Figure 6.4A**). BV/TV analysis revealed temporal and spatial changes in bone volume (**Figure 6.4D-G**).

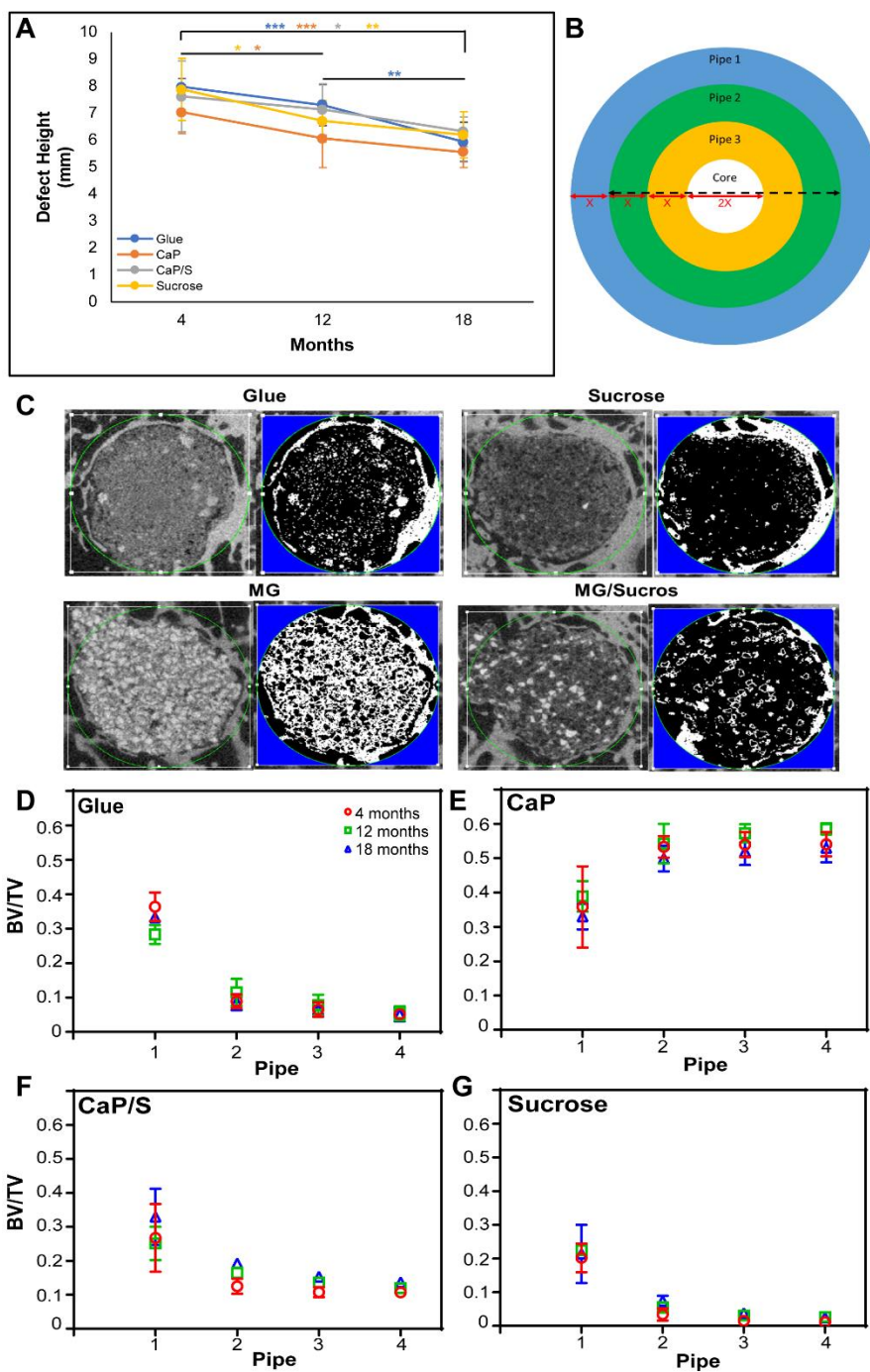


**Figure 6.4.** (A) 2D  $\mu$ CT reconstructions were used to measure the length of the defects at 4, 12, and 18 months. (B) A schematic representation of the BV/TV  $\mu$ CT analysis procedure demonstrates the selection of concentric annular cylinders represented by the colored pipes. The dotted line and outer edge of the green circle represent the defect diameter. (C) Sample 2D images show the effects of thresholding on each of the different material groups. (D-G) The results of the BV/TV analysis are presented for the (D) glue, (E) CaP, (F) CaP/S, and (G) sucrose groups.

A constant threshold that included bone but eliminated nHA-PTKUR and CaP particles was maintained for all groups at all time points (**Figure 6.4C**). However, the high radiodensity of CaP particles caused the surrounding nHA-PTKUR to appear denser than in other groups and consequently an increasing BV/TV as the core of the defect was approached was observed (**Figure 6.4E**). Therefore, BV/TV could only be compared within each material group. Changes in BV/TV as revealed by  $\mu$ CT were negligible in most cases with the most changes occurring in Pipe 1, at the outer perimeter of the defect. The CaP/S group trended as anticipated with a slightly higher BV/TV at each time point for all Pipes (**Figure 6.4F**).

New bone, cellular activity, and material degradation can be distinguished using Stevenel's Blue histological stain. A combination of endochondral and intramembranous ossification was evident for all groups at 4 and 12 months. Histological analysis of implants 18 months post-implantation is ongoing. The glue material demonstrated significant cellular infiltrate at the periphery of the graft at four months (**Figure 6.5A**). New bone (\*) was evident within the graft space, multi-nucleated osteoclast-like cells (double arrow) were seen at the interface of the nHA-PTKUR glue, and bone-forming cells were depositing osteoid (single arrow) at the interfaces of new bone and nHA-PTKUR. Cartilage-like, dark nodules were abundant near the perimeter of the graft (#) and cartilage mineralization (\*\*\*) was ongoing. A similar response is evident at 12 months and cartilage mineralization progressed (**Figure 6.5B**). The CaP group had less cellular infiltration at four months than other groups (**Figure 6.5C**), but a greater response of macrophages and giant cells was evident at the graft perimeter. Cartilage nodules were dispersed throughout the polymer towards the center of the graft and cartilage mineralization was ongoing at 12

months (**Figure 6.5D**, \*\*). The CaP/S group demonstrated new bone (\*), endochondral bone formation (\*\*), and intramembranous bone formation (arrow) at four months (**Figure 6.5E**), and a similar combination bone formation pattern was seen closer to the center of the graft at 12 months (**Figure 6.5F**). The response to the sucrose group was similar to the CaP/S group with new bone evident further within the implant at just four months (**Figure 6.5G-H**). Positive staining of Safarnin O/Fast Green verified the presence of cartilage nodules within the grafts (pink stain) and better demonstrated mineralization (turquoise stain) of cartilage (**Figure 6.6**).



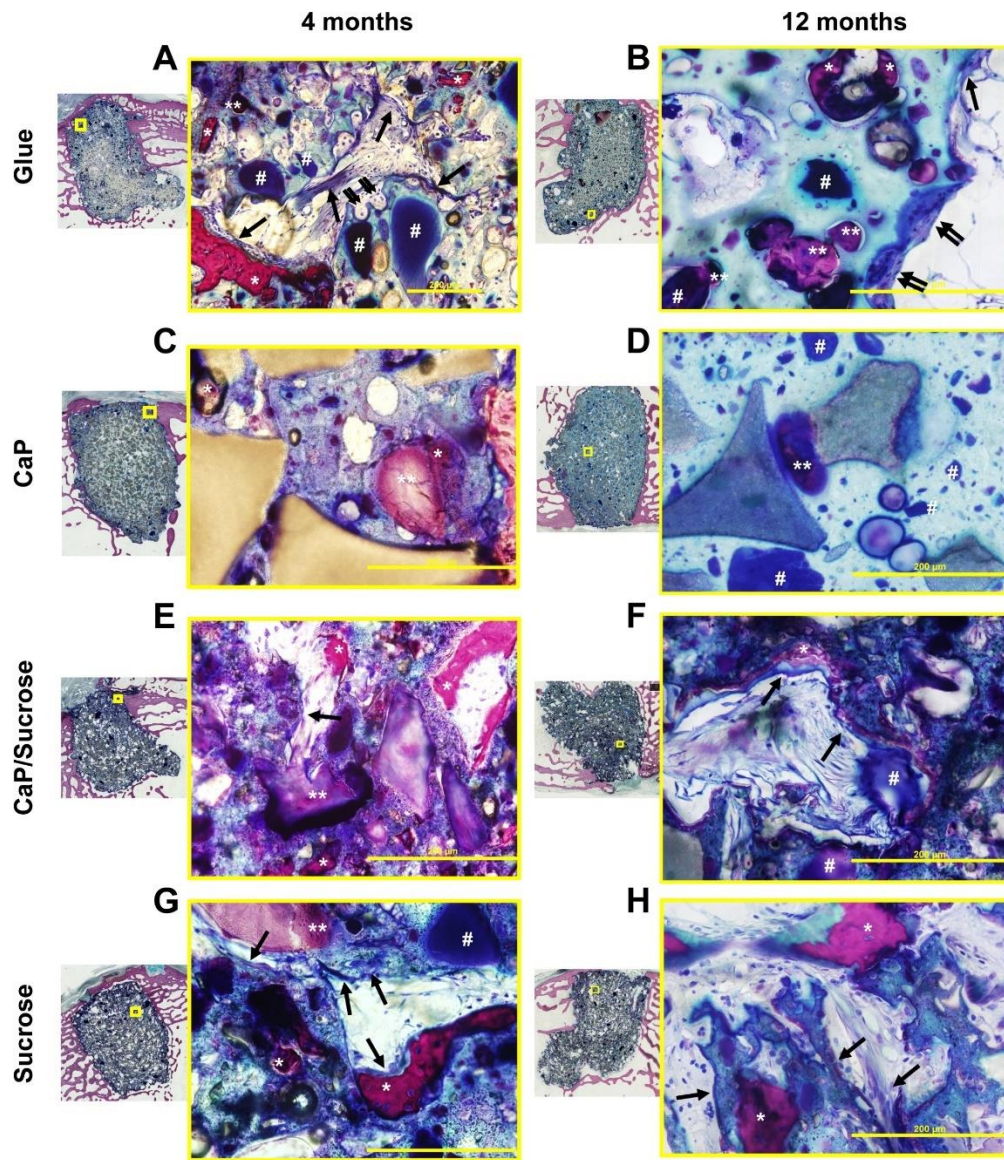


**Figure 6.5.** Magnified histology images at 4 (A, C, E, G) and 12 (B, D, F, H) months demonstrate a combination of endochondral bone formation, indicated by the mineralization (\*\*\*) of cartilage-like nodules (#), and intramembranous bone formation, indicated by bone formation (single arrows) and osteoclast-like cells (double arrows) at the PTKUR interface. New bone (\*) is evident within the PTKUR bone grafts at 4 and 12 months. (scale bar = 200  $\mu$ m, \*: new bone, \*\*:mineralizing cartilage, #: cartilage-like nodules, single arrow: bone lining cells and osteoid, double arrows: osteoclast-like cells)

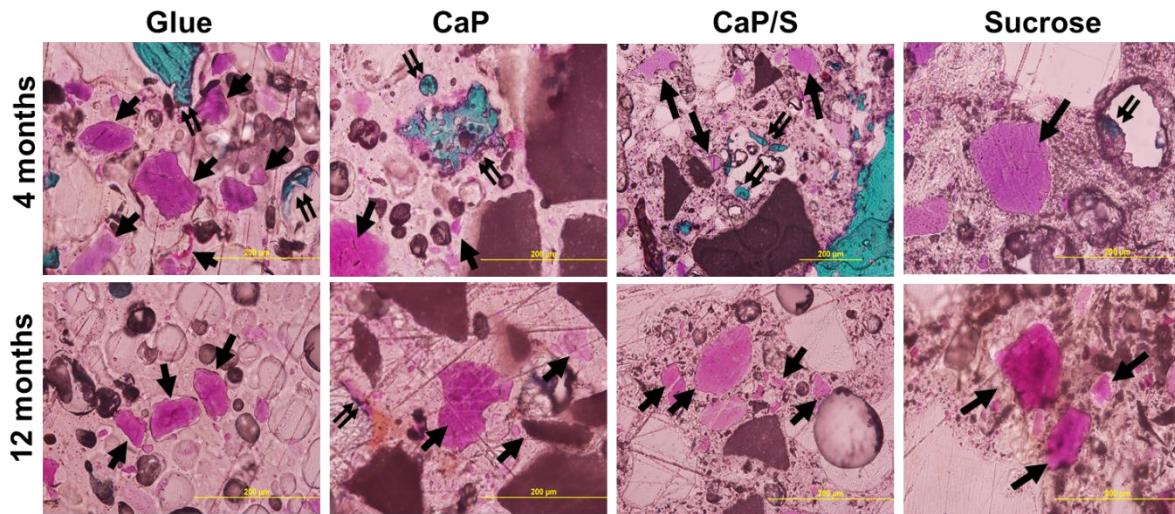


**Figure 6.6.** One slide from each material group was stained with Safranin O/Fast Green to differentiate collagen. Collagen (pink stain, single arrows) was evident within the scaffold as early as 4 months and was generally surrounded by PTKUR material. Bone (turquoise, double arrows) was also easily distinguished using this stain.

Histomorphometry was performed on the distal half of the defects to quantify differences in bone (**Figure 6.7A**), cartilage-like dark nodules (**Figure 6.7C**), and darker blue stained areas of polymer (**Figure 6.7B**). Bone percent trended down as the center of the grafts were approached, as expected, and only small changes were evident from 4 to 12 months (**Figure 6.7A**). The sucrose group demonstrated the most change from 4 to 12 months in region two, at the host-bone/defect interface, and region three which indicates bone ingrowth. Dark-stained nodules were evident in all groups (**Figure 6.7C**). Histomorphometry plots show an upward trend as the center of the graft is approached for all groups containing solids, and especially for the groups containing sucrose (CaP/S, Sucrose). A significant decrease in staining was seen from 4 to 12 months in region four of the sucrose group. Fewer nodules were evident in the glue group. For regions within the graft (2-4), a downward trend was apparent as the center was approached. The same analysis method was used for one slide per group for each time point stained with Safranin

O/Fast Green to compare what appeared as dark nodules using Stevenel’s Blue stain with positive staining with Safranin O/Fast Green (**Figure 6.7D**). Similar trends were seen between the two stains. Staining spiked in region two of the glue group, very low cartilage staining was evident for the CaP group, and the highest staining was seen in the central region, four, of the groups containing sucrose. A larger sample size of Safranin O/Fast Green stained sections would allow for a better comparison and indications of trends for chondrogenesis and endochondral ossification.

A distinct, darker blue staining of the nHA-PTKUR polymer was apparent in areas of all groups possibly indicating a change in material chemistry or a cellular response affecting staining in these areas. As demonstrated in the sample section (**Figure 6.7B**), the glue group exhibited a perimeter (associated with region two) of the darker stain that trended downward as the center of the graft was approached. The CaP group plateaued for all regions within the graft and groups containing sucrose trended up as the center of the graft was approached.

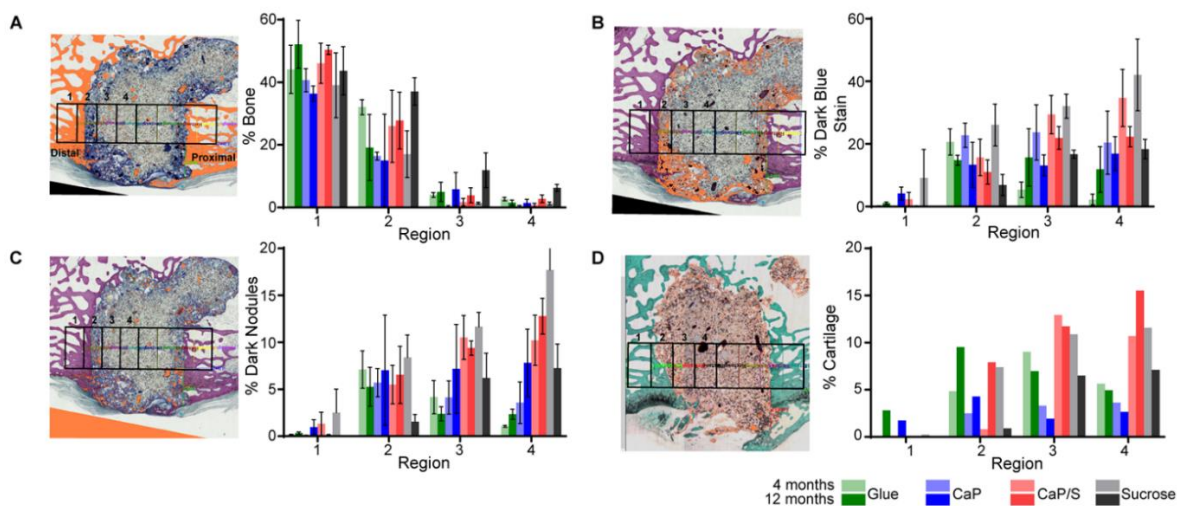


**Figure 6.7.** Preliminary histomorphometry quantifies (A) percent bone, (B) percent dark blue staining, (C) percent dark nodules that are hypothesized to represent areas undergoing endochondral bone formation, and (D) percent cartilage. (A-C: Stevenel’s Blue stain, D: Safranin O/Fast Green stain)

Tibial slot defects were created to investigate remodeling in non-critical defects and the potential for the nHA-PTKUR to act as a “bone glue”. Axial sections from the center of the tibial defects were stained with Stevenel’s Blue. Islands of new bone were evident as early as four months (**Figure 6.8A**, white arrow). These islands were more abundant and more infiltrated at 12 months (**Figure 6.8B**, white arrows). The experimental group exhibited significant ingrowth of new bone from the defect edges at 12 months (\*) and a perimeter of new bone was close to bridging at the nHA-PTKUR edges. Dark-stained nodules seen in grafts in the femoral condyle were also present in the tibial slots and darker blue staining on the nHA-PTKUR was evident at 4 and 12 months. Unfilled tibial slot defects bridged by the four-month time period (**Figure 6.8C**) and dense, cortical-like bone was replaced by trabecular bone by 12 months (**Figure 6.8D**).

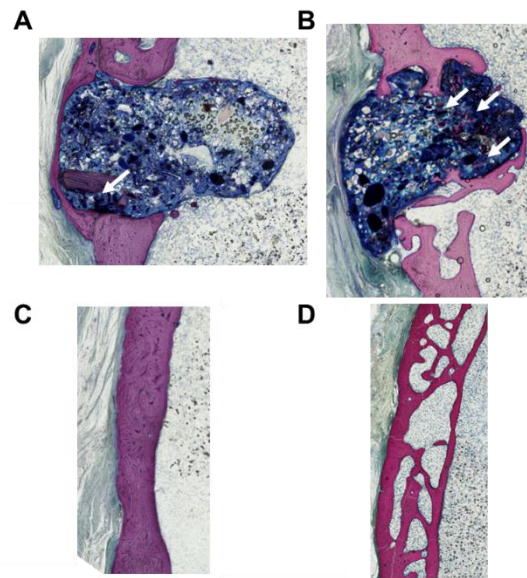


**Figure 6.8.** Axial histology images of tibial slot defects. The PTKUR glue (no CaP or sucrose) persisted in the defect at (A) 4 and (B) 12 months. New bone was evident near the cortical perimeter at 4 months (A) and significant new bone could be seen within the graft at 12 months (arrows, \*: bone ingrowth). The empty controls bridged by the 4-month time point (C). This bone was replaced by trabecular bone by 12 months (D).

## 6.5 Discussion

In this study, a nHA-PTKUR material that incorporated 20 nm nHA in both phases of the PUR precursor materials was developed. By adding 50 wt% nHA in the TK diol phase and 40 wt% nHA in the nHA-LTI prepolymer, similar handling properties were achieved. The similar phases were anticipated to improve mixing and minimize phase separation for maximum mechanical properties.<sup>7</sup> Previous work incorporated 65 wt% nHA in an nHA-LTI prepolymer; however, this method necessitated the addition of catalyst to maintain flowability and a reactive prepolymer may decrease storage time.<sup>19,25</sup> Furthermore, FeAA catalyst was included in the TK phase which decreased fabrication steps necessary in the surgical suite and eliminated the  $\epsilon$ -caprolactone catalyst carrier used previously.<sup>12</sup> An NCO:OH index of 120 yielded similar volumes of each phase for potential delivery of an nHA-PTKUR glue through a 1:1 double barrel syringe. The short fiber shape of the NS nHA compared to the spherical shape of nHA used previously (19.5 m<sup>2</sup>/g, 100 nm) led to an increase in nHA surface area of 38.5 m<sup>2</sup>/g.<sup>19</sup> This smaller grain size is anticipated to enhance cellular attachment and new bone formation, and the larger surface area of reactive OH groups to enhance reactivity and interfacial bonding of the OH groups of nHA with the NCO reactive groups on LTI.<sup>19,28,36-40</sup>

Enhanced interfacial bonding was anticipated to increase mechanical properties of the nHA-PUR and allow for the addition of porosity without sacrificing bone-like strength.<sup>36</sup> Previously, a hybrid polymer composed of nHA-LTI and polycaprolactone triol (MW=300 g/mol) demonstrated mechanical properties sufficient for weight-bearing applications.<sup>19,25</sup> The mechanical properties for the nHA-PTKUR material were a factor lower since a diol is anticipated to exhibit a lower crosslink density than the triol. In another study discussed in Chapter 3, PTKUR blended with 60 wt% ungrafted nHA

demonstrated a maximum modulus of 1300 MPa and yield strength of 90 MPa after 1 week cure in ambient conditions.<sup>12</sup> PTKUR without nHA and 55 wt% CaP had a modulus of 940 MPa and yield strength of 40 MPa after 1 week. The significantly higher mechanical properties are attributed to higher nHA volume (compared to 45 wt% in the current study) and a higher wt% CaP (compared to 45 wt% in the current study). Additionally, nHA-PTKUR nanocomposite materials were left in ambient temperatures only 24 hours prior to leaching. The mechanical properties of the nHA-PTKUR nanocomposites are comparable to the mechanical properties reported 24 hours post-cure in the previous study in Chapter 3. Furthermore, nHA-PTKUR nanocomposites (including the glue and CaP materials) were immersed in water for five days prior to mechanical testing for consistency between the sucrose containing materials and non-sucrose containing nHA-PTKURs. Given that the nHA-PTKUR exhibited 4 wt% mass loss after 10 days in hydrolytic conditions, slight degradation of the nHA-PTKUR could be responsible for lower mechanical properties after a five-day leach period. All groups demonstrated mechanical properties exceeding those of trabecular bone (compressive strength: 5-10 MPa, modulus: 50-400 MPa).<sup>41</sup> Subjecting the nHA-PTKUR to a physiologically relevant environment and cure time (ie. cure time to match recovery time prior to weight-bearing) may provide better insight to the potential for weight-bearing applications (weight-bearing strength = 70-90 MPa).<sup>42</sup>

nHA-PTKUR alone (“glue”), and putties containing 45 wt% CaP particles, 35 wt% CaP and 10 wt% sucrose, or 45 wt% sucrose were implanted in femoral condyle cylindrical defects bilaterally in rabbits. The nHA-PTKUR materials exhibited extensive cellular infiltration and osteogenesis at 4 and 12 months. All groups demonstrated a combination of intramembranous and endochondral bone formation. As discussed in Chapter 2,

intramembranous bone formation describes the direct differentiation of MSCs to osteoblasts and the subsequent deposition of bone.<sup>43,44</sup> During endochondral bone formation, MSCs proceed down the chondrogenic pathway and the cartilaginous callus is remodeled to bone.<sup>43,45</sup> Stevenel's Blue staining revealed the presence of irregularly shaped nodules embedded within the nHA-PTKUR. Safranin O/Fast Green staining methods were adapted for ground sections to verify these nodules were cartilaginous in nature and revealed mineralization of some of the nodules was ongoing. Dennis, et al. promote tissue engineering strategies that harness endochondral ossification, suggesting that following the principles of developmental skeletogenesis may enhance bone regeneration.<sup>46</sup>

A PUR/allograft biocomposite in a critical size rabbit calvaria exhibited both intramembranous and endochondral bone formation; however, chondrogenesis was prevalent in large voids away from the implanted material, so the PUR did not likely influence this mechanism.<sup>4</sup> The combination of mechanisms demonstrated in the present study is hypothesized to be a result of the minimal porosity of the nHA-PTKUR and the concentration of nHA embedded in the PUR structure.<sup>19</sup> Chondrogenesis thrives in hypoxic conditions anticipated where porosity is low, and direct osteogenesis is more likely to occur in oxygenated environments.<sup>46,47</sup> Interestingly, literature also points to the development of hypoxic zones caused by the mineralization process and suggests that hypoxic conditions may favor osteocytogenesis.<sup>48</sup> These findings and the current work suggest the impact of oxygen content on bone graft remodeling mechanisms.

Stevenel's Blue staining also revealed differential staining of the nHA-PTKUR (**Figure 6.7B**). This was most evident in the minimally porous glue specimen where the polymer stained darker blue at the perimeter and lighter towards the core of the implant.

The darker blue was higher towards the core of the implant for the material groups that incorporated porogen. Dark blue staining was evident in the glue implanted in the tibial defect, especially along the plane of host-bone after four months and a majority of the graft was stained dark blue after 12 months. Previous investigations of polypropylene meshes showed a similar phenomenon and the authors proved preferential histological stain uptake in microcracks within the material formed as a result of degradation.<sup>49</sup> Given the patterns of dark blue staining of the four groups included in the present work, alteration in the nHA-PTKUR are likely the cause of the enhanced staining. Un-implanted materials exposed to the simulated oxidative environment described previously for degradation studies and a neat control will be processed for histology and stained with Stevenel's Blue to investigate this hypothesis.

Defect length measured from 2D  $\mu$ CT reconstructions taken from the center of the defect indicated material incorporation and new bone formation at 4, 12, and 18 months (**Figure 6.4A**). Some material was forced out of the defect space and into the marrow space proximal to the condyles during implantation causing large variation in defect width measurements. Therefore, only defect length provided a reliable parameter of remodeling. The AOI for histomorphometry was chosen to be similar to the VOI used in  $\mu$ CT analysis. The regions for histomorphometry were slightly larger than for  $\mu$ CT analysis but normalizing to the size of the AOI (ie. bone percent) should allow for comparison. Histomorphometry demonstrated a higher percent bone for all regions compared to  $\mu$ CT. nHA-PUR polymers require stringent  $\mu$ CT thresholding given the mineral content of the polymer (and CaP), so a smaller scan voxel size may minimize the discrepancy between the two modes of measurement. Furthermore, the VOI for  $\mu$ CT included the proximal



volume where graft may have overflowed into the marrow space during implantation. This added graft material outside of the defined defect space will lead to a lower percent bone than if the defect space was appropriately surrounded by trabecular bone.

## 6.6 Conclusion

This work describes the formulation of an injectable, settable, and cell-degradable nHA-PTKUR BVF that incorporated up to 25 vol% nHA. The addition of CaP particles and/or sucrose improved handling properties for a moldable putty and sucrose leaching induced porosity without sacrificing bone-like mechanical properties. Both the nHA-PTKUR glue and the putties demonstrated controlled remodeling via a unique combination of intramembranous and endochondral bone formation at 4 and 12 months when implanted in the femoral condyles of rabbits. Furthermore, the remodeling rate can be altered for the desired application by adjusting the CaP:sucrose ratio. These findings show that the addition of nHA to a PTKUR enhances bone cell activity. Furthermore, implantation of four variations of nHA-PTKUR bone grafts in two preclinical models demonstrates the potential of nHA-PTKUR as injectable and moldable, tissue engineering bone grafts that can be tuned for the desired implantation methods and remodeling demands of various applications.

## References

1. Adhikari R, Gunatillake PA, Griffiths I, Tatai L, Wickramaratna M, Houshyar S, Moore T, Mayadunne RT, Field J, McGee M and others. Biodegradable injectable polyurethanes: synthesis and evaluation for orthopaedic applications. *Biomaterials* 2008;29(28):3762-3770.
2. Adolph EJ, Guo R, Pollins AC, Zienkiewicz K, Cardwell N, Davidson JM, Guelcher SA, Nanney LB. Injected biodegradable polyurethane scaffolds support tissue infiltration and delay wound contraction in a porcine excisional model. *Journal of Biomedical Materials Research Part B: Applied Biomaterials* 2015.
3. Bonzani IC, Adhikari R, Houshyar S, Mayadunne R, Gunatillake P, Stevens MM. Synthesis of two-component injectable polyurethanes for bone tissue engineering. *Biomaterials* 2007;28(3):423-433.
4. Dumas JE, BrownBaer PB, Prieto EM, Guda T, Hale RG, Wenke JC, Guelcher SA. Injectable reactive biocomposites for bone healing in critical-size rabbit calvarial defects. *Biomedical Materials* 2012;7(2):024112.
5. Dumas JE, Davis T, Holt GE, Yoshii T, Perrien DS, Nyman JS, Boyce T, Guelcher SA. Synthesis, characterization, and remodeling of weight-bearing allograft bone/polyurethane composites in the rabbit. *Acta Biomaterialia* 2010;6(7):2394-2406.
6. Guelcher SA, Patel V, Gallagher KM, Connolly S, Didier JE, Doctor JS, Hollinger JO. Synthesis and In Vitro Biocompatibility of Injectable Polyurethane Foam Scaffolds. *Tissue Engineering* 2006;12(5):1247-59.
7. Guelcher SA, Srinivasan A, Dumas JE, Didier JE, McBride S, Hollinger JO. Synthesis, mechanical properties, biocompatibility, and biodegradation of polyurethane networks from lysine polyisocyanates. *Biomaterials* 2008;29(12):1762-1775.
8. Hafeman AE, Zienkiewicz KJ, Zachman AL, Sung H-J, Nanney LB, Davidson JM, Guelcher SA. Characterization of the degradation mechanisms of lysine-derived aliphatic poly(ester urethane) scaffolds. *Biomaterials* 2011;32(2):419-429.
9. Nagata M, Oi A, Sakai W, Tsutsumi N. Synthesis and properties of biodegradable network poly (ether-urethane) s from L-lysine triisocyanate and poly (alkylene glycol) s. *Journal of Applied Polymer Science* 2012;126(S2).
10. Storey RF, Wiggins JS, Puckett A. Hydrolyzable poly (ester-urethane) networks from l-lysine diisocyanate and d, l-lactide/ $\epsilon$ -caprolactone homo-and copolyester triols. *Journal of Polymer Science Part A: Polymer Chemistry* 1994;32(12):2345-2363.
11. Dumas JE, Prieto EM, Zienkiewicz KJ, Guda T, Wenke JC, Bible J, Holt GE, Guelcher SA. Balancing the Rates of New Bone Formation and Polymer Degradation Enhances Healing of Weight-Bearing Allograft/Polyurethane Composites in Rabbit Femoral Defects. *Tissue Engineering Part A* 2014;20(1-2):115-129.
12. McEnery MA, Lu S, Gupta MK, Zienkiewicz KJ, Wenke JC, Kalpakci KN, Shimko DA, Duvall CL, Guelcher SA. Oxidatively degradable poly (thioketal urethane)/ceramic composite bone cements with bone-like strength. *RSC advances* 2016;6(111):109414-109424.
13. Cisneros-Pineda OG, Herrera Kao W, Loría-Bastarrachea MI, Veranes-Pantoja Y,

- Cauich-Rodríguez JV, Cervantes-Uc JM. Towards optimization of the silanization process of hydroxyapatite for its use in bone cement formulations. *Materials Science and Engineering: C* 2014;40(0):157-163.
14. Guda T, Walker JA, Pollot BE, Appleford MR, Oh S, Ong JL, Wenke JC. In vivo performance of bilayer hydroxyapatite scaffolds for bone tissue regeneration in the rabbit radius. *Journal of Materials Science: Materials in Medicine* 2011;22(3):647-656.
  15. Guda T, Walker JA, Singleton BM, Hernandez JW, Son J-S, Kim S-G, Oh DS, Appleford MR, Ong JL, Wenke JC. Guided bone regeneration in long-bone defects with a structural hydroxyapatite graft and collagen membrane. *Tissue Engineering Part A* 2012;19(17-18):1879-1888.
  16. Lee JH, Hwang CJ, Song BW, Koo KH, Chang BS, Lee CK. A prospective consecutive study of instrumented posterolateral lumbar fusion using synthetic hydroxyapatite (Bongros®-HA) as a bone graft extender. *Journal of Biomedical Materials Research Part A* 2009;90(3):804-810.
  17. Lovati AB, Lopa S, Recordati C, Talò G, Turrisi C, Bottagisio M, Losa M, Scanziani E, Moretti M. In Vivo Bone Formation Within Engineered Hydroxyapatite Scaffolds in a Sheep Model. *Calcified Tissue International* 2016:1-15.
  18. Clarke B. Normal bone anatomy and physiology. *Clinical journal of the American Society of Nephrology* 2008;3(Supplement 3):S131-S139.
  19. Lu S, McGough M, Rogers B, Wenke J, Shimko D, Guelcher S. Resorbable nanocomposites with bone-like strength and enhanced cellular activity. *Journal of Materials Chemistry B* 2017;5(22):4198-4206.
  20. Mi HY, Palumbo S, Jing X, Turng LS, Li WJ, Peng XF. Thermoplastic polyurethane/hydroxyapatite electrospun scaffolds for bone tissue engineering: effects of polymer properties and particle size. *Journal of Biomedical Materials Research Part B: Applied Biomaterials* 2014;102(7):1434-1444.
  21. Mi H-Y, Jing X, Salick MR, Cordie TM, Peng X-F, Turng L-S. Morphology, mechanical properties, and mineralization of rigid thermoplastic polyurethane/hydroxyapatite scaffolds for bone tissue applications: effects of fabrication approaches and hydroxyapatite size. *Journal of Materials Science* 2014;49(5):2324-2337.
  22. Tetteh G, Khan AS, Delaine-Smith RM, Reilly GC, Rehman IU. Electrospun polyurethane/hydroxyapatite bioactive Scaffolds for bone tissue engineering: The role of solvent and hydroxyapatite particles. *Journal of the Mechanical Behavior of Biomedical Materials* 2014;39(0):95-110.
  23. Yang W, Both SK, Zuo Y, Birgani ZT, Habibovic P, Li Y, Jansen JA, Yang F. Biological evaluation of porous aliphatic polyurethane/hydroxyapatite composite scaffolds for bone tissue engineering. *Journal of Biomedical Materials Research Part A* 2014.
  24. Cetina-Diaz SM, Chan-Chan LH, Vargas-Coronado RF, Cervantes-Uc JM, Quintana-Owen P, Paakinaho K, Kellomaki M, Di Silvio L, Deb S, Cauich-Rodríguez JV. Physicochemical characterization of segmented polyurethanes prepared with glutamine or ascorbic acid as chain extenders and their hydroxyapatite composites. *Journal of Materials Chemistry B* 2014;2(14):1966-

- 1976.
25. Lu S, McGough MA, Shiels SM, Zienkiewicz KJ, Merkel AR, Vanderburgh JP, Nyman JS, Sterling JA, Tennent DJ, Wenke JC. Settable polymer/ceramic composite bone grafts stabilize weight-bearing tibial plateau slot defects and integrate with host bone in an ovine model. *Biomaterials* 2018.
  26. Xie R, Hu J, Ng F, Tan L, Qin T, Zhang M, Guo X. High performance shape memory foams with isocyanate-modified hydroxyapatite nanoparticles for minimally invasive bone regeneration. *Ceramics International*.
  27. Martin JR, Gupta MK, Page JM, Yu F, Davidson JM, Guelcher SA, Duvall CL. A porous tissue engineering scaffold selectively degraded by cell-generated reactive oxygen species. *Biomaterials* 2014;35(12):3766-3776.
  28. Webster TJ, Ergun C, Doremus RH, Siegel RW, Bizios R. Enhanced functions of osteoblasts on nanophase ceramics. *Biomaterials* 2000;21(17):1803-1810.
  29. MacMillan AK, Lamberti FV, Moulton JN, Geilich BM, Webster TJ. Similar healthy osteoclast and osteoblast activity on nanocrystalline hydroxyapatite and nanoparticles of tri-calcium phosphate compared to natural bone. *International journal of nanomedicine* 2014;9:5627.
  30. Standard I. 9277, "Determination of the Specific Surface Area of Solids by Gas Adsorption Using the BET Method,". International Organization for Standardization, Geneva, Switzerland 1995.
  31. Harmata AJ, Ward CL, Zienkiewicz KJ, Wenke JC, Guelcher SA. Investigating the effects of surface-initiated polymerization of  $\epsilon$ -caprolactone to bioactive glass particles on the mechanical properties of settable polymer/ceramic composites. *Journal of Materials Research* 2014;29(20):2398-2407.
  32. International A. Standard test method for isocyanate groups in urethane materials or prepolymers. ASTM International; 2010.
  33. Christenson EM, Anderson JM, Hiltner A. Oxidative mechanisms of poly(carbonate urethane) and poly(ether urethane) biodegradation: In vivo and in vitro correlations. *Journal of Biomedical Materials Research Part A* 2004;70A(2):245-255.
  34. Harmata AJ, Uppuganti S, Granke M, Guelcher SA, Nyman JS. Compressive fatigue and fracture toughness behavior of injectable, settable bone cements. *Journal of the mechanical behavior of biomedical materials* 2015;51:345-355.
  35. International A. ASTM F451-16, Standard specification for acrylic bone cement. West Conshohocken, PA; 2016.
  36. KICKELBICK G. Concepts for the incorporation of inorganic building blocks into organic polymers on a nanoscale. *Progress in Polymer Science* 2003;28(1):83-114.
  37. Laurencin CT, Kumbar SG, Nukavarapu SP. Nanotechnology and orthopedics: a personal perspective. *Wiley Interdisciplinary Reviews: Nanomedicine and Nanobiotechnology* 2009;1(1):6-10.
  38. Liu Q, de Wijn JR, de Groot K, van Blitterswijk CA. Surface modification of nano-apatite by grafting organic polymer. *Biomaterials* 1998;19(11):1067-1072.
  39. Ngiam M, Liao S, Patil AJ, Cheng Z, Chan CK, Ramakrishna S. The fabrication of nano-hydroxyapatite on PLGA and PLGA/collagen nanofibrous composite scaffolds and their effects in osteoblastic behavior for bone tissue engineering. *Bone* 2009;45(1):4-16.

40. Sun F, Zhou H, Lee J. Various preparation methods of highly porous hydroxyapatite/polymer nanoscale biocomposites for bone regeneration. *Acta Biomaterialia* 2011;7(11):3813-3828.
41. Fernando S, McEnery M, Guelcher S. Polyurethanes for bone tissue engineering. *Advances in Polyurethane Biomaterials* 2016:481.
42. Kühn K-D. Bone cements: up-to-date comparison of physical and chemical properties of commercial materials: Springer 2000.
43. Gilbert S. Osteogenesis: the development of bones. *Developmental biology* 2000;6.
44. Stricker S, Mundlos S. Chapter seven - FGF and ROR2 Receptor Tyrosine Kinase Signaling in Human Skeletal Development. In: Birchmeier C, editor. *Current Topics in Developmental Biology*: Academic Press; 2011. p 179-206.
45. Akter F, Ibanez J. Chapter 8 - Bone and Cartilage Tissue Engineering. *Tissue Engineering Made Easy*: Academic Press; 2016. p 77-97.
46. Dennis SC, Berkland CJ, Bonewald LF, Detamore MS. Endochondral Ossification for Enhancing Bone Regeneration: Converging Native Extracellular Matrix Biomaterials and Developmental Engineering In Vivo. *Tissue Engineering Part B: Reviews* 2014.
47. Bornes TD, Jomha NM, Mulet-Sierra A, Adesida AB. Hypoxic culture of bone marrow-derived mesenchymal stromal stem cells differentially enhances in vitro chondrogenesis within cell-seeded collagen and hyaluronic acid porous scaffolds. *Stem cell research & therapy* 2015;6(1):84.
48. Chen X, Wang L, Zhao K, Wang H. Osteocytogenesis: Roles of Physicochemical Factors, Collagen Cleavage and Exogenous Molecules. *Tissue Engineering Part B: Reviews* 2018.
49. Iakovlev VV, Guelcher SA, Bendavid R. Degradation of polypropylene in vivo: a microscopic analysis of meshes explanted from patients. *Journal of Biomedical Materials Research Part B: Applied Biomaterials* 2015;105(2):237-248.

## CHAPTER 7

### VII. SUMMARY AND CONCLUSIONS

The high incidence of bone defects and injuries that require intervention is anticipated to continue to rise steeply.<sup>1</sup> Natural bone grafts such as autograft (AG) have been predominately used in the past; however, patient morbidity and increased peri- and post-operative costs of AG procedures advocates the use of synthetic, tissue engineering bone grafts that regenerate the patients' natural tissue.<sup>2</sup> The benefits associated with synthetic bone grafts over natural graft options have led to a drastic increase in bone tissue engineering research and advancement and a market growth rate of 15% per year.<sup>1,3</sup> In this work, a hydrolytically stable poly(thioketal urethane) (PTKUR) tissue engineering bone graft that degrades in response to reactive oxygen species (ROS) was synthesized and bone graft remodeling investigated in multiple translational *in vivo* models for various applications. The results of the studies detailed herein demonstrate the advantages of a tissue engineering bone graft that degrades directly in response to patient biology with the goal of matching the rates of material resorption and osteogenesis.

Synthesis of a novel, low molecular weight hydroxyl functional thioketal (TK) diol was critical in the development of a lysine-based PTKUR. Synthesis and characterization of the TK diol was described in detail in Chapter 3. Methods used previously by our group were then adapted to use the diol and lysine triisocyanate (LTI) prepolymer to fabricate a PTKUR. Bench testing in simulated oxidative conditions verified the material degraded rapidly in oxidative environments but exhibited no mass loss in hydrolytic conditions. The low molecular weight of the TK diol yielded PTKUR composites with final moduli exceeding 1000 MPa when blended with MASTERGRAFT (MG) calcium phosphate microparticles and yield strengths around 900 MPa when blended with nanocrystalline

hydroxyapatite (nHA) particles. Implantation in a rabbit femoral condyle plug defect revealed osteoclast-mediated resorption of the cements at 6 and 12 weeks demonstrating a cell-degradable bone graft was achieved.

Given the cell-mediated resorption mechanism of PTKUR, demonstrated in Chapter 3, the material was considered an attractive option for implementation as an autograft (AG) extender. AG was anticipated to enhance infiltration of cells into the defect, thereby initiating oxidative degradation of PTKUR. Chapter 4 demonstrates that by manipulating the PTKUR fabrication technique, moldable PTKUR AG extenders with 69 vol% AG (31% PTKUR) that cure *in situ* were achieved. This AG volume was decreased further by the addition of CaP particles (44 vol% AG, 17% CaP, 39% PTKUR). Once cured, PTKUR AG extenders exhibited compression resistant mechanical properties. *In vivo* studies in a preliminary rat model and a biologically and mechanically stringent spine model demonstrated the PTKUR AG extender supported cellular infiltration and osteogenesis.

In Chapter 5, the PTKUR AG extender formulation was refined to increase the maximum AG content (78 vol% AG, 22 vol% PTKUR) and improve handling properties based on surgeon feedback. This development decreased the tack free time (TFT) by 8 minutes and compression resistant mechanical properties were maintained. This PTKUR AG extender was implanted in a stringent 20 mm defect in the rabbit radius to investigate cellular infiltration and graft remodeling. The PTKUR AG extender demonstrated bone growth from the defect interfaces and cellular infiltration was evident at 12 weeks. Fluorochrome injections were included in the study protocol to investigate mineralization activity at various time points. Positive fluorochrome binding within the defect at 4 and 8 weeks suggested implanted AG may have acted as nucleation sites for mineralization.

Furthermore,  $\mu$ CT and histology show more consistent remodeling of the PTKUR AG extender than the AG control. Together, Chapter 4 and 5 advocate the use of PTKUR as a settable, compression resistant AG extender.

The cell-mediated resorption mechanism of PTKUR represents an important initial step toward the development of resorbable bone cements for weight-bearing applications. In Chapter 6, the osteogenic and mechanical benefits of nanocrystalline hydroxyapatite (nHA) are exploited in a nHA-PTKUR in which LTI-grafted nHA is dispersed in the LTI prepolymer phase and PCL-grafted nHA in the TK phase. This nHA-PTKUR polymer maintained the hydrolytic stability of PTKURs and achieved a modulus and strength of 350 MPa and 50 MPa, respectively. The addition of up to 45 wt% sucrose porogen was hypothesized to accelerate initial integration with the host bone to maximize weight-bearing potential. Furthermore, up to 45 wt% CaP microparticles was incorporated with nHA-PTKUR to investigate the effects of slowly-degrading, mechanically robust, and osteoconductive CaP. The addition of 45 wt% CaP did not affect the modulus and sucrose containing materials maintained a modulus around 200 MPa. Composites demonstrated lower strengths and yield strain than the nHA-PTKUR alone; however, these mechanical properties were similar for all nHA-PTKUR composite groups. nHA-PTKUR and nHA-PTKUR composites of sucrose, CaP, or a combination of sucrose and CaP were implanted in rabbit femoral condyle plug defects for up to 18 months. The small sample size did not allow for significant conclusions to be drawn based on the material group; however, all groups exhibited a unique combination of endochondral and intramembranous bone formation with new calcified bone within the defects as early as 4 months. Chapter 6 presents a critical step toward the development of a PTKUR bone graft with potential in



weight-bearing applications.

## References

1. Amini AR, Laurencin CT, Nukavarapu SP. Bone Tissue Engineering: Recent Advances and Challenges. *Critical reviews in biomedical engineering* 2012;40(5):363-408.
2. Glassman SD, Carreon LY, Campbell MJ, Johnson JR, Puno RM, Djurasovic M, Dimar JR. The perioperative cost of Infuse bone graft in posterolateral lumbar spine fusion. *The Spine Journal* 2008;8(3):443-448.
3. Bohner M. Resorbable biomaterials as bone graft substitutes. *Materials Today* 2010;13(1):24-30.

## CHAPTER 8

### VIII. FUTURE DIRECTIONS

Future work will build on the conclusions of this dissertation to further investigate the remodeling mechanisms and discover the maximum potential for PTKUR in bone grafting applications. This chapter will focus first on future directions to optimize a cell-degradable PTKUR autograft (AG) extender based on the current approach outlined in Chapters 4 and 5. Suggestions for alternative approaches will also be discussed briefly. Then, work towards the addition of porosity to a nanocrystalline hydroxyapatite-polyurethane (nHA-PUR) hybrid composite will be presented and preliminary results of implantation in a weight-bearing tibial plateau defect model in sheep discussed. Future studies on the hybrid material are then proposed.

#### 8.1 PTKUR Autograft Extender

##### *Enhancements to Current Approach*

In the studies outlined in Chapters 4 and 5, *in vivo* investigation of a PTKUR AG extender was taken out 8 and 12 weeks in the rabbit spine and radius, respectively. In both cases,  $\mu$ CT and histological analysis indicated implanted AG in control animals was completely resorbed or remodeled by the final time point. The slower resorption rate of the PTKUR AG extender maintained implanted AG at the defect site up to sacrifice. We hypothesize that by maintaining the defect space, the AG extender will allow for improved bone quality once the AG extender is completely remodeled. Given the cell-mediated resorption mechanism of PTKUR described in Chapter 3 and the results presented in

Chapters 4 and 5, osteogenesis should continue as cells infiltrate the graft and break down the polymer leading to complete bridging with bone of similar quality to the host bone it replaced.<sup>1</sup> Assuming the PTKUR AG extender is remodeled at a similar rate to new bone formation, defect stability should be maintained.

To test this hypothesis: (1) studies should be carried out to time points exceeding complete resorption of the PTKUR and (2) post-harvest mechanical studies should be included to justify the longer time points by evaluating bone quality. An *in vitro* study to test the effects of AG location (ie. surface AG versus embedded AG) may further explain the different remodeling mechanism of the AG extender compared to the AG control. The addition of an *in vitro* study to assess temporal cellular activity and cytokine release surrounding implanted AG will further justify the longer time points. As discussed in Chapter 6, nHA-PTKUR persisted up to 18 months *in vivo*. However, the LTI-PEG/TK formulation used for the AG extender should resorb faster than ceramic/polymer hybrid nHA-PTKUR given the hydrophilic properties of LTI-PEG prepolymer.<sup>2</sup> Incorporating fast-resorbing AG rather than ceramic CaP particles will also accelerate remodeling.<sup>3,4</sup> Finally, we hypothesize that once cells have infiltrated the AG extender, the cell-material surface contact area will be increased leading to an accelerated remodeling rate. A long-term *in vivo* study to test material resorption rate would be beneficial; however, cellular activity varies by animal and model.<sup>5-7</sup> I suggest repeating the rabbit radius study presented in Chapter 5 with a final time point of 24 weeks and including mechanical analysis of the radius-ulna complex as an outcome measure.<sup>8</sup>

## *Alternative Approaches to Accelerate Cellular Infiltration and PTKUR AG Extender*

### *Remodeling*

Aim II demonstrates the feasibility of a PTKUR AG extender to provide mechanical integrity, minimize the AG needed for osteoinductivity, and maximize the applications for which AG can be used. Future work is needed to find the absolute minimum AG content necessary to maintain osteoinductivity and to optimize the graft for accelerated bone regeneration. Variation of AG content and the addition of a variety of CaPs (MG,  $\beta$ -TCP, HA, bioactive glass, etc.) may be investigated. Furthermore, a hydroxyapatite scaffold with a collagen wrap increased the volume of new bone in a radius defect compared to the hydroxyapatite scaffold alone.<sup>9</sup> Guan, et al. demonstrated a PUR/collagen scaffold synthesized via phase separation increased cell attachment *in vitro* and others have shown the surface addition of collagen enhances biological activity and adds an additional tool to adjust mechanical properties.<sup>10,11</sup> Bulk addition of collagen to a settable PTKUR AG extender may accelerate cellular infiltration and remodeling. This work may involve the development of an *in vitro* model to simulate AG implants and minimize the *in vivo* studies necessary to test the library of materials.

## 8.2 nHA-PUR Hybrid Nanocomposite

### *Accelerated Remodeling of a Mechanically Robust nHA-PUR for Weight-Bearing*

#### *Applications*

#### **Background and introduction adapted with permission from:**

##### **The Royal Society of Chemistry:**

Lu, S, **McGough, MAP**, Rogers, BR, Wenke, JC, Shimko, DA, Guelcher, SA. "Resorbable nanocomposites with bone-like strength and enhanced cellular activity." *Journal of Materials Chemistry B*, 2017, **5**(22): 4198-4206.<sup>18</sup>

Lu, S, **McGough, MA**, Shiels, SM, Zienkiewicz, KJ, Merkel, AR, Vanderburgh, JP, Nyman, JS, Sterling, JA, Tennent, DJ, Wenke, JC, Guelcher, SA. "Settable polymer/ceramic composite bone grafts stabilize weight-bearing tibial plateau slot defects and integrate with host bone in an ovine model." *Biomaterials*, 2018, accepted.<sup>19</sup>

*Background and introduction.* Bone cements for treatment of fractures at weight-bearing sites are subjected to dynamic physiological loading from daily activities.<sup>12</sup> An ideal biomaterial for fracture repair near an articulating joint sets rapidly after implantation, stabilizes the fracture with minimal rigid implants, stimulates osteogenic differentiation of endogenous cells, and remodels at a rate that maintains osseous integrity. Nanocrystalline hydroxyapatite (nHA) enhances osteogenic differentiation, new bone formation, and osteoclast differentiation activity compared to amorphous or micron-scale crystalline hydroxyapatite.<sup>13-17</sup> However, the brittle mechanical properties of nHA precludes its use in treatment of weight-bearing bone defects. Previously, we developed a settable nHA-poly(urethane) (nHA-PUR) nanocomposites synthesized from lysine triisocyanate (LTI) grafted nHA/LTI prepolymer, and poly(caprolactone) triol that is easily injected using a double-barrel syringe, exhibits mechanical properties exceeding those of conventional bone cements, enhances mineralization, and undergoes osteoclast-mediated degradation *in*

*vitro*.<sup>18</sup> In a follow-up *in vivo* study, we proved the potential for lysine-based, hybrid, nHA-PUR/ceramic composites in a weight-bearing defect in sheep.<sup>19</sup> However, prolonged infiltration rates and biomaterial/host bone mechanical mismatch *in vivo* are limitations of current formulations.<sup>19</sup> The goal of this preliminary work was to introduce the porosity necessary for accelerated infiltration and peripheral remodeling while maintaining the strength and compression resistance necessary for weight-bearing applications. Quasi-static mechanical testing and fatigue studies were used to determine the maximum amount of porogen that can be incorporated in a nHA-PUR without sacrificing weight-bearing potential. We investigated two PUR formulations, nHA-PCLUR and a faster degrading nHA-PEUR, with equivalent amounts of the desired ratio of CaP and a porogen (sucrose) in the rigorous tibial plateau defect model in sheep. The material was also tested in non-weight-bearing femoral plug defects to compare healing and remodeling in the different environments. CT and  $\mu$ CT were used to study the patterns of nHA-PUR remodeling and resorption in weight-bearing and non-weight-bearing defects over 16 weeks in this large animal model. Combining these results, with those presented in Chapter 6 will lead to a nHA-PTKUR bone graft with weight-bearing potential.

*Experimental.* nHA-PCLUR and nHA-PEUR were synthesized by reacting polycaprolactone triol (300 g/mol) or poly( $\epsilon$ -caprolactone-*co*-glycolide-*co*-DL-lactide) triol (300 g/mol)<sup>20</sup> with nHA-LTI quasi-prepolymer (65 wt% nHA) at an index of 140.<sup>19</sup> The triols were blended with a mixture of CaP and sucrose porogen prior to reacting with the prepolymer so that CaP and sucrose were homogeneously dispersed throughout the cured PUR composites. A sucrose sweep was performed on nHA-PCLUR composites to investigate the effects of sucrose loading. The total solids (CaP + sucrose) was maintained

at 55 wt% composite for mechanical testing and the sucrose content varied from 0 – 55 wt% composite to identify a lead candidate solids ratio for use in a weight-bearing bone graft (**Table 8.1**). Materials for mechanical testing were loaded into 6 mm cylindrical tubes, and cured under a weight (0.96 kg) for 24 hours to ensure cohesion throughout cure. Sucrose was leached from specimens for five days in water at 37°C prior to further characterization. After the five-day leach, samples were dried completely at room temperature. Scanning electron microscopy (Zeiss Merlin SEM) was used to visualize the resulting morphology of the leached composites. Leached samples were cut to a height of 12 mm and the edges made completely flat using a Buehler IsoMet Low Speed Saw (Lake Bluff, IL). Samples were rehydrated for 24 hours in water at 37°C immediately prior to all mechanical testing. To determine the bulk properties of the materials, cylindrical specimens were placed between flat platens and compressed at a rate of 25 mm/min (MTS 858 Bionix Servohydraulic Test System, Eden Prairie, MN) until failure. The engineering stress and strain were used to calculate bulk modulus, yield strength, and yield stress.

Specimens for fatigue testing were cyclically loaded to 5 MPa to determine the upper limits of porosity that maintain weight-bearing potential. Fatigue testing was performed on nHA-PCLUR composites of increasing sucrose content until premature failure occurred consistently. Compressive fatigue testing was performed following methods adapted from work previously published by our lab.<sup>19,21</sup> Leached and rehydrated cylindrical specimens were wrapped in wet gauze, and placed between flat platens for testing. The MTS was equipped with an extensometer (634.31F-24) attached to the upper and lower platens with o-rings and a constant drip system to maintain hydration and a constant specimen temperature near 37°C. The first specimen of each group was tuned to



ensure the desired stress was approached throughout testing and the tuning parameters were maintained for the entire group. Samples were compressed to 5 MPa at a frequency of 5 Hz until the specimen reached runout ( $10^6$  cycles) or a strain value greater than 3.5%. Failure was described as either a 3% increase in strain or a 1% creep deformation when the minimum strain of the cycle was compared to that of the first recorded cycle. Force and strain values were recorded at an acquisition rate of 200 Hz every 500<sup>th</sup> cycle. The lead candidate sucrose/CaP ratio with maximum sucrose content that achieved runout in fatigue testing was fabricated using the nHA-PEUR formulation and the mechanical properties verified prior to performing an *in vivo* study in sheep.

Bilateral weight-bearing tibial plateau defects and non-weight-bearing medial and lateral femoral condyle drill hole defects were created in the hind-limbs of 6 sheep (**Figure 8.1**, n=4/group).<sup>19,22</sup>

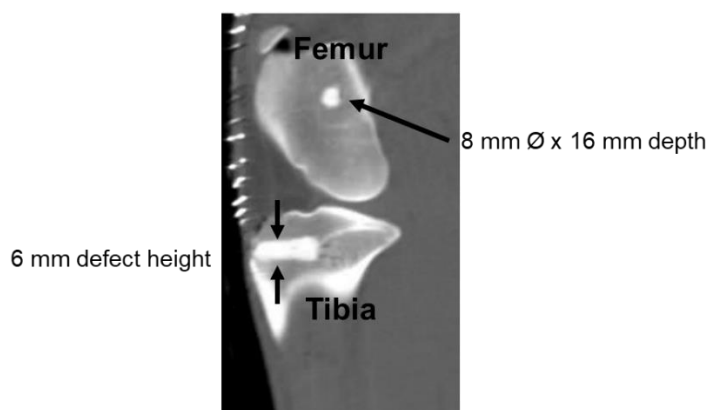


**Figure 8.1.** Sagittal CT image demonstrating positioning and dimensions of the tibial plateau and femoral condyle defects.

A single, mid-line incision was created in each leg to access both defect sites. A small, rectangular surgical guide ensured precision and consistency in the creation of the tibial plateau defect. The guide was affixed to the medial side of the tibia with the back edge of the guide approximately 2.5 mm from the back of the tibia and the top 3 mm from the top

of the tibial shelf using k-wires. Placement of the guide was verified using a C-arm x-ray imaging device. The guide was removed and the k-wire used to guide a surgical drill across the width of the tibia (medial to lateral). The wires were then removed and a piezoelectric system used to clear the remainder of the defect. The result was a tibial plateau defect (6 mm height) that ranged across the entire medial-to-lateral width of the tibia and approximately half the anterior-to-posterior depth leaving a thin shelf above the defect. A k-wire was drilled across the medial-to-lateral width of the femur to demarcate the center of the femoral condyle defects to ensure the two defects were aligned. The k-wires were used to guide a surgical drill with a diameter of 8 mm to create cylindrical defects approximately 16 mm in length. After both the medial and lateral defects were created, the k-wire was removed.

Once all of the defects were created, they were filled with: nHA-PCLUR composite, nHA-PEUR composite, or a clinical control, Norian (calcium phosphate bone cement). Both PUR groups contained 45 wt% CaP and 10 wt% sucrose particles and each animal had the same material implanted in all defects, bilaterally. The PURs were fabricated as described above and hand molded to fill the defects. A small plastic plunger and surgical elevator were used to ensure the defects were completely filled.

Animals were euthanized 16 weeks post-operatively. Defect regions of the tibia and femur were harvested and fixed in 10% formalin immediately following a final, 16-week CT scan.  $\mu$ CT images were acquired at a voxel size of 24.2  $\mu$ m (Scanco  $\mu$ CT 50) to assess bone remodeling qualitatively. One animal from each experimental group (n=2/group) was euthanized early, 1-week post-implantation, due to tibial shelf fractures. The tibias and femurs were harvested immediately and stored in formalin until processed. The nHA in the

prepolymer enabled visualization of the grafts using  $\mu$ CT. The defects from specimens harvested early were scanned as described previously and BV/TV analysis utilized to quantify the porosity of the remaining nHA-PUR graft. Porosity was defined for a 2 mm x 2 mm cube selected from the center of the defect. The material was recovered from the tibial defects for mechanical analysis. A cubic sample averaging 6-8 mm<sup>3</sup> was cut from each specimen of harvested material using a low speed saw and quasi-static mechanical testing performed according to the procedure described above.

*Preliminary results and discussion.* A sucrose sweep was performed to identify the maximum sucrose loading (and resulting porosity) the material could withstand without sacrificing weight-bearing potential. SEM images showed increasing porosity with increasing sucrose content as expected (**Figure 8.2**). The pore walls exhibited in SEM are generally thin for the 45 and 55 wt% sucrose and are hypothesized to degrade more rapidly than bulk polymer *in vivo*.

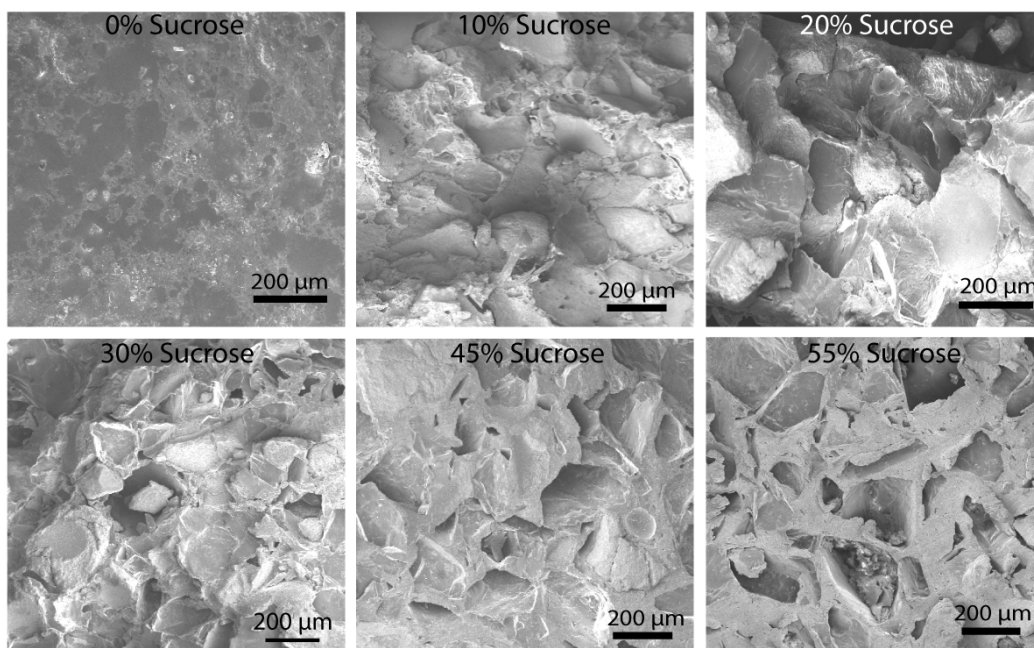


**Figure 8.2.** SEM images indicate the porosity of nHA-PEUR that resulted after performing a sucrose sweep from 0-55 wt% sucrose.

Stress-strain curves reveal the transition from a plastic-like composite with 0-20 wt% sucrose to a more elastic material with 45 and 55 wt% sucrose (**Figure 8.3 A**). Materials with 30 wt% sucrose exhibited both plastic and elastic characteristics with a plateau around 10 MPa at 20% strain. Modulus, yield strength, and yield strain of composites leached for 5 days are shown in **Figure 8.3 B-D**. The modulus of a composite with no sucrose is significantly higher than any composites incorporating sucrose (3X higher) and the modulus decreases with increasing sucrose content. The yield strength decreased with increasing sucrose content while the yield strain increased, as anticipated. 55 wt% sucrose materials without CaP did not exhibit a yield point and thus, were not included in the analysis of yield strength and yield stress. These data corroborate conclusions drawn from stress-strain curves (**Figure 8.3 A**) that porogen concentration can alter the mechanical properties of PURs to exhibit a range of mechanical characteristics from plastic to foam-like without altering the PUR chemistry.

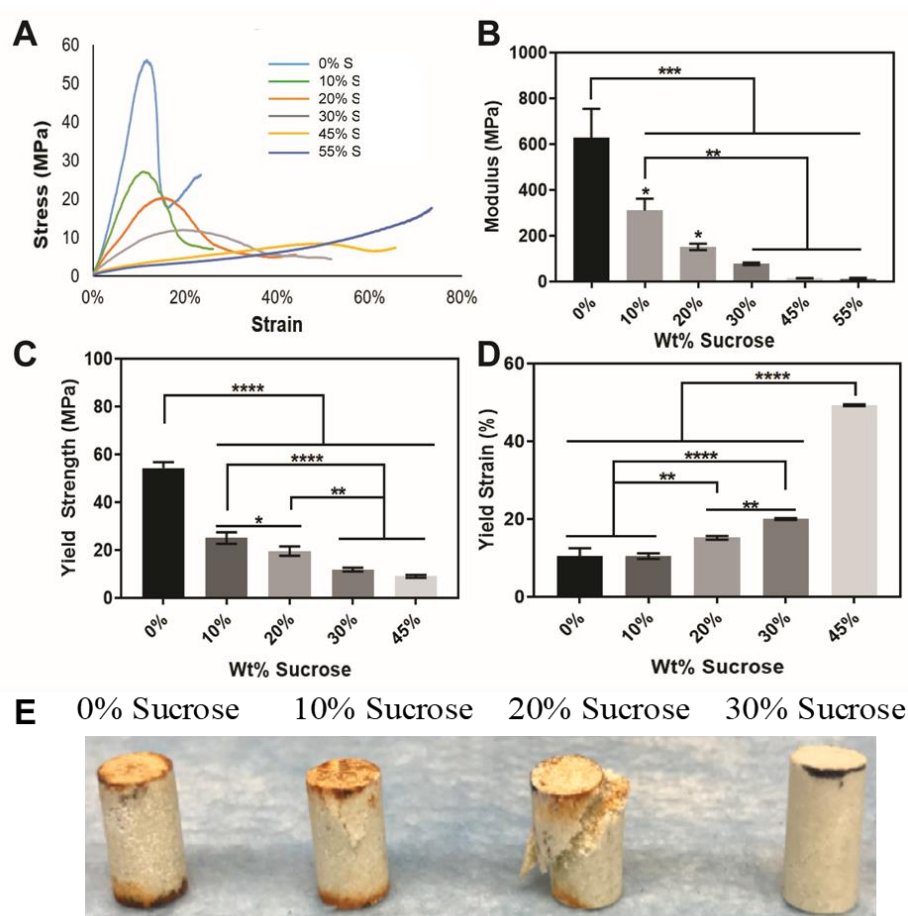


**Figure 8.3.** Compressive mechanical properties resulting from sucrose sweep. (A) Representative stress-strain curves show a transition from plastic-like (0-20 wt% sucrose) to foam-like (45-55 wt% sucrose) mechanical properties. (B) Modulus and (C) yield strength decrease and (D) yield strain increases with increasing sucrose content, as anticipated by increased porosity. (E) Photographs of fatigue test specimens indicate a maximum of 10 wt% sucrose can be incorporated without losing weight-bearing potential. (\*:  $P \leq 0.05$ , \*\*:  $P \leq 0.01$ , \*\*\*:  $P \leq 0.001$ , \*\*\*\*:  $P \leq 0.0001$ )

From static compressive data, we predicted up to 30 wt% sucrose composites may be able to withstand 5 MPa cyclic loading. Higher porosity, foam-like grafts (45 and 55 wt% sucrose) are anticipated to exhibit 20 - 40% strain from 5 MPa loading (based on static data) and do not have a suitable modulus for weight-bearing applications. As presented in **Table 8.1**, 10 wt% sucrose (45 wt% CaP) composites generally reached runout based on the definitions of creep strain and strain increase. One specimen failed

early based on creep strain but achieved runout in terms of strain. Given that all of the other nHA-PCLUR specimens nHA-PEUR specimens reached runout, 10 wt% sucrose was considered the maximum sucrose content that could be incorporated without sacrificing weight-bearing potential. **Figure 8.3 E** shows representative samples after dynamic fatigue testing. 0 and 10% sucrose samples remain intact while 20 wt% sucrose failed and 30 wt% sucrose samples appear to have compressed and recovered in a sponge-like manner.

**Table 8.1.** Sucrose sweep. Sucrose/CaP ratios and post-leach mechanical properties. Fatigue life is reported as average number of cycles until failure (number of specimen to runout/total number of specimens).

Sucrose (%)	CaP (%)	Static Compressive Properties			Compressive Fatigue Life (5 MPa)	
		Modulus (MPa)	Ultimate Yield Strength (MPa)	Yield Strain (%)	1% Creep Deformation	≥ 3% Strain
<b>nHA-PCLUR Composite</b>						
0	55	629 ± 126	54.3 ± 2.48	10.4 ± 2.10	> 1,000,000 (3/3)	> 1,000,000 (3/3)
10	45	311 ± 51.3	25.1 ± 2.40	10.5 ± 0.739	973,000 (2/3)	> 1,000,000 (3/3)
20	35	152 ± 13.8	19.6 ± 1.95	15.2 ± 0.456	74,000 (0/3)	250,000 (0/3)
30	25	77.4 ± 5.31	11.8 ± 0.799	20.0 ± 0.251	--	--
45	10	14.3 ± 0.966	9.05 ± 0.550	49.3 ± 0.222	--	--
55	0	12.6 ± 3.78	--	--	--	--
<b>nHA-PEUR Composite</b>						
10	45	264 ± 16.7	22.3 ± 0.741	10.4 ± 0.492	> 1,000,000 (3/3)	> 1,000,000 (3/3)

Based on the results of mechanical analysis, nHA-PCLUR and nHA-PEUR composites containing 10 wt% sucrose and 45 wt% CaP were implanted in weight-bearing tibial plateau defects and non-weight-bearing femoral plug defects bilaterally in sheep. Two of the four experimental animals were sacrificed after 9-10 days due to tibial shelf fracture in one limb (**Figure 8.4**).

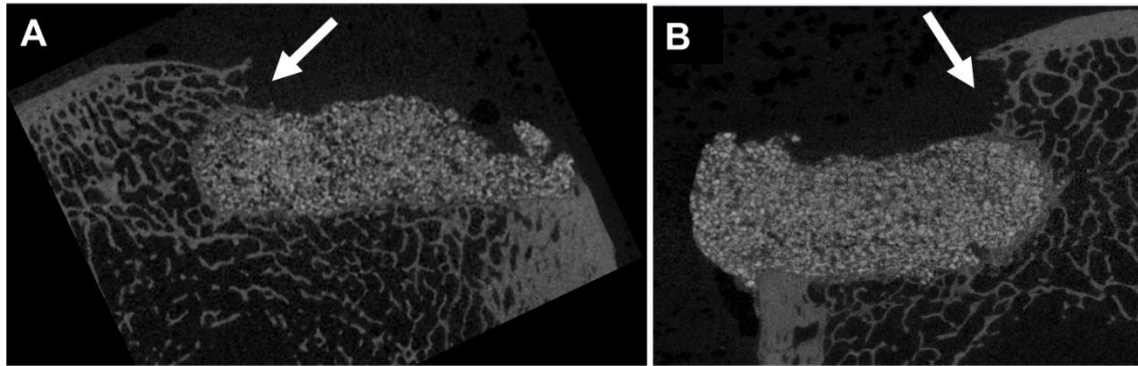


**Figure 8.4.**  $\mu$ CT images indicating tibial shelf fracture in sheep implanted with (A) nHA-PCLUR composite and (B) the nHA-PEUR composite materials. (arrows indicate location of host bone fracture)

BV/TV  $\mu$ CT analysis was used to determine the porosity of the materials *ex vivo* and static compression testing alluded to the mechanical properties of the materials post-implantation. The mechanical testing was performed 3 weeks post-harvest, so the time in formalin may have altered the mechanical properties slightly. BV/TV analysis indicated an average porosity around 12 wt% for both materials which was likely induced by sucrose leaching (**Table 8.2**).

**Table 8.2.** Porosity and mechanical properties of 10 wt% sucrose/45 wt% CaP materials explanted prior to the 16-week time point.

	nHA-PCLUR		nHA-PEUR		Average*	StDev*
	Left	Right*	Left	Right		
<b>Tibia Defect Porosity (%)</b>	16.03	10.6-21.4	11.71	9.47	12.4%	3.3%
<b>Modulus (MPa)</b>	117	77.8	125	105	115.7	10.1

\*Outlier not included

One tibia from the nHA-PCLUR group had large variation in porosity and was not included in analysis. This variation was likely due to filling issues in which the material was not tightly packed in the defect prior to cure. The moduli of explanted nHA-PURs was

116 ± 10 MPa for both groups. This value is 150 – 200 MPa lower than the values calculated for specimens not implanted (**Table 8.1**). The decrease in modulus could have been caused by a filling issue in which the material was not packed as tightly as for bench testing. *In vivo* conditions may have affected material properties by inducing premature breakdown; however, this is unlikely given the short 9-10 day time period and since the other samples in the nHA-PUR groups were carried out for 16 weeks. Future studies should assess the mechanical properties of materials explanted at 16 weeks to compare the moduli of the early specimens with the 16-week specimens. These samples would likely contain ingrown bone which should be taken into account during analysis.

A larger sample size is necessary to draw affirmative conclusions based on  $\mu$ CT analysis.  $\mu$ CT of specimens from the small sample of animals that survived 16 weeks show a disruption of the host bone (**Figure 8.5**). As demonstrated by 2D sagittal reconstructions, both tibiae from the nHA-PCLUR group do not have a continuous tibial shelf and a slight resorption gap is evident in one specimen. One of the two tibiae from the nHA-PEUR group demonstrated slight degradation of the tibial shelf and both exhibited a large resorption gap surrounding the perimeter of the defect. Small gaps at the graft/host bone interface are evident in half of the experimental femoral defects (**Figure 8.6A-B**). These gaps are localized and do not occur for the entire perimeter of the defect as in the tibiae indicating a filling defect may have occurred at the time of surgery. Although the sample size is small, it is probable that nHA-PEUR resorbs too quickly for use in a weight-bearing defect considering the large resorption gaps. The Norian control was well integrated with the host-bone surrounding the tibial defects, but three out of four limbs from the Norian control group displayed tibial shelf fractures (**Figure 8.5**). The control was also well



integrated with the host-bone surrounding the femoral defects (**Figure 8.6C**); however, two femoral condyle defects demonstrated incomplete fill. Histological analysis will allow for visualization of bone ingrowth into the composite bone grafts and confirm the cellular activity within resorption gaps and gaps caused by filling defects.

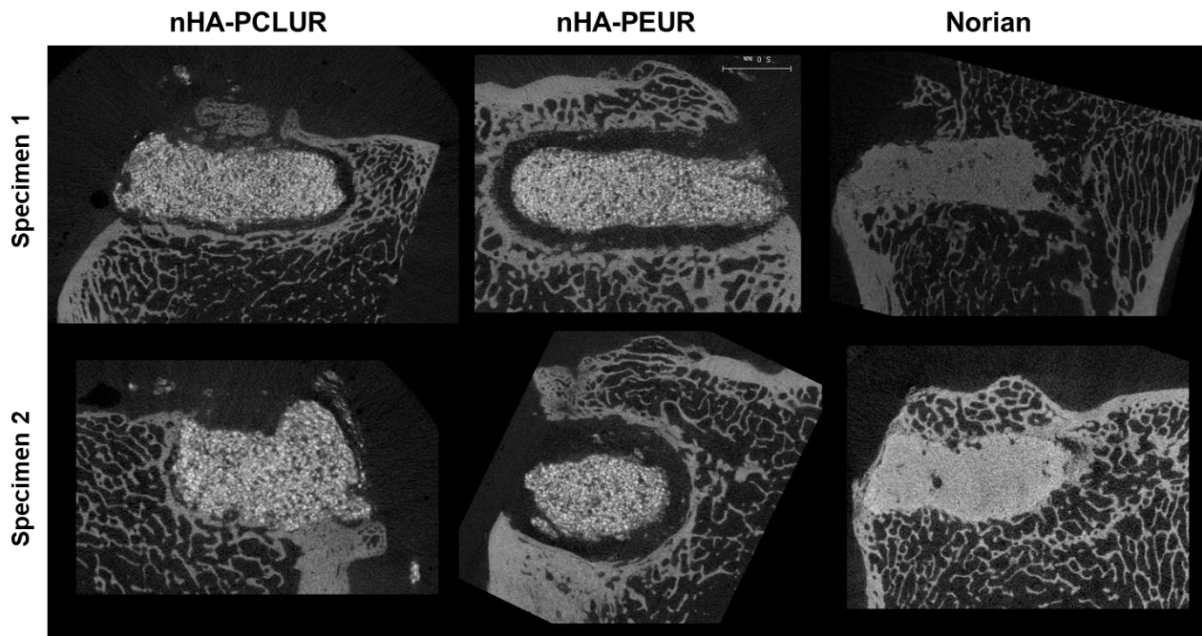


**Figure 8.5.**  $\mu$ CT images of tibial plateau defects 16 weeks post-implantation show interruption of host bone at the defect site in all groups and a resorption gap in 1 nHA-PCLUR specimen and both nHA-PEUR specimens.

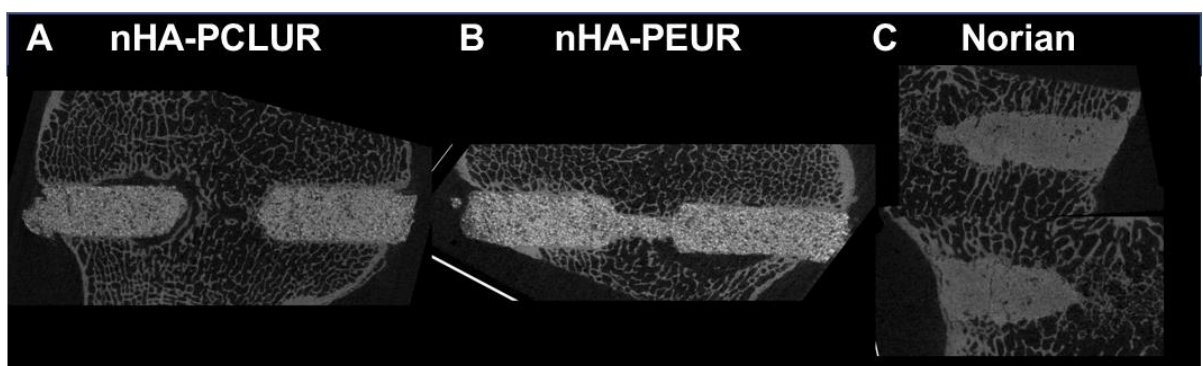


**Figure 8.6.**  $\mu$ CT images of femoral plug defects 16 weeks post-implantation for one femur specimen from the (A) nHA-PCLUR, (B) nHA-PEUR, and (C) Norian clinical control groups.

*Conclusion and suggestions for future work.* The work described herein demonstrates the feasibility of a nHA-PCLUR composite containing 10 wt% sucrose for use in weight-bearing applications and alludes to the use of quasi-static and dynamic mechanical testing to predict material performance *in vivo*. Further model development may lower the incidence of premature failure seen in the current study.  $\mu$ CT analysis of materials implanted *ex vivo* in saw bones may help to more accurately quantify working time, material packing, and homogeneity to eliminate inconsistencies in porosity. In the current study, sheep were kept from weight-bearing for three days. Increasing this time to 5-7 days may allow for greater infiltration prior to weight-bearing which would potentially improve failure rate.

A follow-up study should be done to increase the sample size of the nHA-PCLUR and Norian groups for statistical significance. Furthermore, we hypothesize that a PTKUR formulated with a tri-functional TK triol will lead to a stronger, more highly crosslinked oxidatively degradable PTKUR that would tolerate greater porosity without compromising weight-bearing potential. To this end, we have identified a molecule that may lead to the synthesis of a trifunctional TK. The proposed reaction scheme is illustrated in **Figure 8.7**.

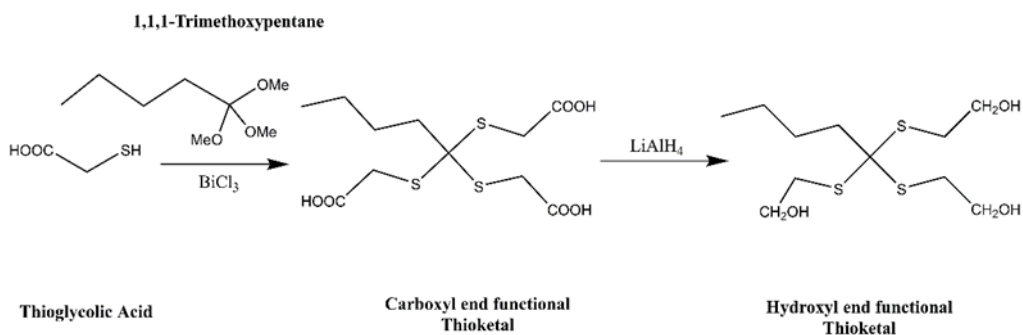


**Figure 8.7.** Synthesis of a thiokeetal triol.

Starting with 1,1,1-trimethoxypentane and following the two-step synthesis route described in Chapter 1 is predicted to yield a trifunctional thioketal with a similar equivalent weight to that of the diol. This triol would provide another variable that could be altered based on the minimum porosity needed for infiltration. Blending the TK diol and triol could result in a library of mechanical properties for weight-bearing and non-weight-bearing applications. I would suggest eliminating the nHA-PEUR group in future studies given the consistent resorption gaps in two specimens and inclusion of a nHA-PTKUR material.

#### *Condition-Based Remodeling Mechanisms of an nHA-PUR Bone Void Filler*

Histological analysis reported in Chapter 6 indicated a combination of endochondral and intramembranous ossification in the remodeling of a PTKUR bone void filler. Based on the environment surrounding each of these events, we hypothesize endochondral bone formation may occur where there is less porosity, and thus hypoxic conditions, and intramembranous bone formation on pore interfaces where there is immediate access to oxygen (**Figure 8.8**).<sup>23</sup>

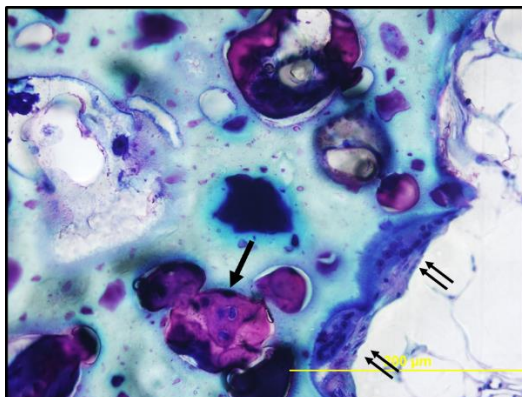


**Figure 8.8.** Representative histology figures from study presented in Chapter 6 indicating environment surrounding endochondral bone formation (single arrow) versus that surrounding intramembranous bone formation (double arrow).

The osteoconductivity of the scaffolds (ie. incorporation of nano-hydroxyapatite +/- CaP particles) may also play a role. An *in vitro* study to test this hypothesis would provide insight into the rate and mechanism of remodeling of various PUR materials. Mesenchymal stem cells (MSCs) are capable of differentiating into cartilage, bone, muscle, tendon, ligament, and fat.<sup>24,25</sup> Our lab previously described a method to encapsulate MC3T3 osteoblast precursor cells in PURs using alginate beads.<sup>26</sup> Adapting this method to MSCs would broaden the differentiation potential and allow for investigation of cellular activity in various environments.

Future studies should investigate differentiation of encapsulated MSCs (via alginate beads) in a library of PURs. Gas foaming, 3D printing, and composite formulations can all be used to alter the porosity of the PURs of interest.<sup>27-30</sup> Various PUR formulations could also be used to investigate the effects of the thioketal diol, triol, and the incorporation of nHA. MSCs encapsulated in alginate beads could then be added to the various formulation to result in PURs with encapsulated progenitor cells. Histological analysis methods described previously (Sanderson's Rapid Bone Stain/van Gieson, Safranin O, TRAP, IHC, etc.) would describe the spatiotemporal mechanisms of bone formation and graft remodeling in the specific material conditions. Based on the results in Chapter 6, one could anticipate more endochondral ossification in less porous PURs and intramembranous ossification in highly porous PURs. Based on these results, future PUR formulations could be designed to more closely meet the cellular demands of specific applications.

## References

1. Khan SN, Cammisa FP, Sandhu HS, Diwan AD, Girardi FP, Lane JM. The Biology of Bone Grafting. *Journal of the American Academy of Orthopaedic Surgeons* 2005;13(1):77-86.
2. Nagata M, Oi A, Sakai W, Tsutsumi N. Synthesis and properties of biodegradable network poly (ether-urethane) s from L-lysine triisocyanate and poly (alkylene glycol) s. *Journal of Applied Polymer Science* 2012;126(S2).
3. Boyce T, Lee S, Kaes D, Belaney R, Shimp L, Knaack D. Cellular penetration and bone formation depends upon allograft bone fraction in a load bearing composite implant. *Trans Soc Biomater* 2005;133.
4. Dumas JE, Davis T, Holt GE, Yoshii T, Perrien DS, Nyman JS, Boyce T, Guelcher SA. Synthesis, characterization, and remodeling of weight-bearing allograft bone/polyurethane composites in the rabbit. *Acta Biomaterialia* 2010;6(7):2394-2406.
5. Bagi CM, Berryman E, Moalli MR. Comparative bone anatomy of commonly used laboratory animals: implications for drug discovery. *Comparative medicine* 2011;61(1):76-85.
6. Muschler GF, Raut VP, Patterson TE, Wenke JC, Hollinger JO. The design and use of animal models for translational research in bone tissue engineering and regenerative medicine. *Tissue Engineering Part B: Reviews* 2010;16(1):123-145.
7. Pearce A, Richards R, Milz S, Schneider E, Pearce S. Animal models for implant biomaterial research in bone: a review. *Eur Cell Mater* 2007;13(1):1-10.
8. Wheeler DL, Stokes KE, Park HM, Hollinger JO. Evaluation of particulate Bioglass® in a rabbit radius osteotomy model. *Journal of Biomedical Materials Research* 1997;35(2):249-254.
9. Guda T, Walker JA, Singleton BM, Hernandez JW, Son J-S, Kim S-G, Oh DS, Appleford MR, Ong JL, Wenke JC. Guided bone regeneration in long-bone defects with a structural hydroxyapatite graft and collagen membrane. *Tissue Engineering Part A* 2012;19(17-18):1879-1888.
10. Guan J, Stankus JJ, Wagner WR. Development of composite porous scaffolds based on collagen and biodegradable poly (ester urethane) urea. *Cell transplantation* 2006;15(1):17-27.
11. Zuber M, Zia F, Zia KM, Tabasum S, Salman M, Sultan N. Collagen based polyurethanes—A review of recent advances and perspective. *International Journal of Biological Macromolecules* 2015;80:366-374.
12. Ramakrishna S, Mayer J, Wintermantel E, Leong KW. Biomedical applications of polymer-composite materials: a review. *Composites Science and Technology* 2001;61(9):1189-1224.
13. Laurencin CT, Kumbar SG, Nukavarapu SP. Nanotechnology and orthopedics: a personal perspective. *Wiley Interdisciplinary Reviews: Nanomedicine and Nanobiotechnology* 2009;1(1):6-10.
14. Ngiam M, Liao S, Patil AJ, Cheng Z, Chan CK, Ramakrishna S. The fabrication of nano-hydroxyapatite on PLGA and PLGA/collagen nanofibrous composite scaffolds and their effects in osteoblastic behavior for bone tissue engineering. *Bone* 2009;45(1):4-16.
15. Sato M, Webster TJ. Nanobiotechnology: implications for the future of

- nanotechnology in orthopedic applications. *Expert review of medical devices* 2004;1(1):105-114.
16. Sun F, Zhou H, Lee J. Various preparation methods of highly porous hydroxyapatite/polymer nanoscale biocomposites for bone regeneration. *Acta Biomaterialia* 2011;7(11):3813-3828.
  17. Webster TJ, Ergun C, Doremus RH, Siegel RW, Bizios R. Enhanced functions of osteoblasts on nanophase ceramics. *Biomaterials* 2000;21(17):1803-1810.
  18. Lu S, McGough M, Rogers B, Wenke J, Shimko D, Guelcher S. Resorbable nanocomposites with bone-like strength and enhanced cellular activity. *Journal of Materials Chemistry B* 2017;5(22):4198-4206.
  19. Lu S, McGough MA, Shiels SM, Zienkiewicz KJ, Merkel AR, Vanderburgh JP, Nyman JS, Sterling JA, Tennent DJ, Wenke JC. Settable polymer/ceramic composite bone grafts stabilize weight-bearing tibial plateau slot defects and integrate with host bone in an ovine model. *Biomaterials* 2018.
  20. Guelcher SA, Srinivasan A, Dumas JE, Didier JE, McBride S, Hollinger JO. Synthesis, mechanical properties, biocompatibility, and biodegradation of polyurethane networks from lysine polyisocyanates. *Biomaterials* 2008;29(12):1762-1775.
  21. Harmata AJ, Uppuganti S, Granke M, Guelcher SA, Nyman JS. Compressive fatigue and fracture toughness behavior of injectable, settable bone cements. *Journal of the mechanical behavior of biomedical materials* 2015;51:345-355.
  22. Gisepp A, Wieling R, Bohner M, Matter S, Schneider E, Rahn B. Resorption patterns of calcium-phosphate cements in bone. *Journal of Biomedical Materials Research Part A* 2003;66(3):532-540.
  23. Bornes TD, Jomha NM, Mulet-Sierra A, Adesida AB. Hypoxic culture of bone marrow-derived mesenchymal stromal stem cells differentially enhances in vitro chondrogenesis within cell-seeded collagen and hyaluronic acid porous scaffolds. *Stem cell research & therapy* 2015;6(1):84.
  24. Oreffo ROC, Cooper, C., Mason, C., Clements, M. Mesenchymal stem cells: Lineage, plasticity, and skeletal therapeutic potential. *Stem Cell Reviews* 2005;1(2):169-178.
  25. Pittenger MF, Mackay AM, Beck SC, Jaiswal RK, Douglas R, Mosca JD, Moorman MA, Simonetti DW, Craig S, Marshak DR. Multilineage potential of adult human mesenchymal stem cells. *science* 1999;284(5411):143-147.
  26. Guo R, Ward CL, Davidson JM, Duvall CL, Wenke JC, Guelcher SA. A transient cell-shielding method for viable MSC delivery within hydrophobic scaffolds polymerized in situ. *Biomaterials* 2015;54:21-33.
  27. Guo R, Lu S, Page JM, Merkel AR, Basu S, Sterling JA, Guelcher SA. Fabrication of 3D scaffolds with precisely controlled substrate modulus and pore size by templated-fused deposition modeling to direct osteogenic differentiation. *Advanced healthcare materials* 2015;4(12):1826-1832.
  28. Hafeman AE, Zienkiewicz KJ, Zachman AL, Sung H-J, Nanney LB, Davidson JM, Guelcher SA. Characterization of the degradation mechanisms of lysine-derived aliphatic poly(ester urethane) scaffolds. *Biomaterials* 2011;32(2):419-429.
  29. Prieto EM, Talley AD, Gould NR, Zienkiewicz KJ, Drapeau SJ, Kalpakci KN, Guelcher SA. Effects of particle size and porosity on in vivo remodeling of settable

- allograft bone/polymer composites. *Journal of Biomedical Materials Research Part B: Applied Biomaterials* 2015;103(8):1641-1651.
30. Guelcher S, Srinivasan A, Hafeman A, Gallagher K, Doctor J, Khetan S, McBride S, Hollinger J. Synthesis, in vitro degradation, and mechanical properties of two-component poly (ester urethane) urea scaffolds: effects of water and polyol composition. *Tissue engineering* 2007;13(9):2321-2333.

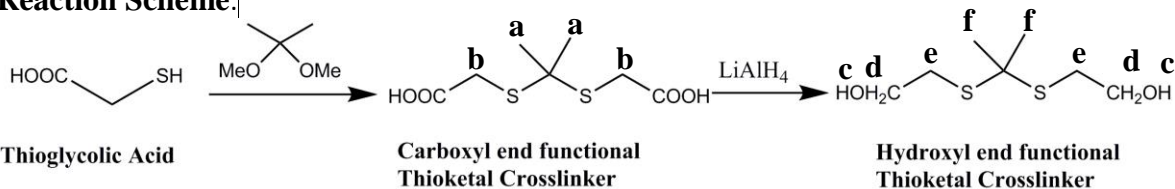
APPENDIX  
EXPERIMENTAL PROTOCOLS



---

**Guelcher Lab**  
**Thiokeetal Diol Synthesis**

---

**Reaction Scheme:****Before starting:**

- Read and understand the MSDS of the reagents listed below.
- Dry glassware in oven overnight and allow to cool before use.
- Personal protective and safety equipment required:
  - Disposable nitrile gloves
  - Hood
  - Cleanroom face mask
  - Appropriate attire according to the Chemical Hygiene Plan (shoes, labcoat, goggles, etc.)

**Reagents: (store at RT unless otherwise noted)**

- Acetonitrile (anhydrous)
- Bismuth(III) chloride (BiCl<sub>3</sub>)
- 2,2-dimethoxypropane (DMP)
- Thioglycolic acid (TGA)  
**Fatal if inhaled, wear mask when using**
- Lithium Aluminum Hydride (LiAlH<sub>4</sub>)  
**Releases flammable gases when in contact with water**
- Tetrahydrofuran (THF) (anhydrous, contains 250 ppm BHT as inhibitor)
- Diethyl ether (anhydrous)
- Sodium hydroxide (1M in water)
- Sodium sulfate
- Acetone

---

**Guelcher Lab**  
**Thioketal Diol Synthesis (cont'd)**

---

**Materials and Equipment:**

- 1 L three neck round bottom flask (RBF)
- 2 L three neck RBF
- 1 L RBF
- Egg shaped stir bar
- Glass stopcock (one-way, flow control adapter)
- Glass stopper
- Rubber septa
- Mechanical stirrer
- Stir rod and accessories
- 24 mL syringe(x2)
- 60 mL syringe
- 16-20 gauge needles (x3)
- 18-20 gauge, 12 in. needle
- 16-20 gauge cannula
- Balloon & short vacuum tubing (x2)
- Glass hose connector/adaptor
- Reflux condenser
- Addition funnel
- Erlenmeyer Flask
- Buchner flask (x2)
- Buchner funnel (x2)
- Filter paper – Whatman 1820-070  
Glass Microfiber binder free filter
- Separation funnel (2L)

**Procedure for 30 g Batch Size:**Carboxylic End Functional Thioketal Crosslinker Synthesis

1. Add BiCl<sub>3</sub> (2.15 g, 6.51 mmol, 0.01X + slight excess) to 1 L three neck RBF with football stir bar in ventilation hood.
2. Attach septum in middle neck, one-way glass stopcock on left and a rubber septa on the right neck. Grease and clip glass connections.
3. Apply vacuum through glass stopcock. Heat the RBF with heat gun under vacuum for 3-5 minutes to ensure completely dry catalyst conditions. Allow to cool to RT under vacuum.
4. Replace vacuum with N<sub>2</sub> filled balloon and open nitrogen to reaction.

---

**Guelcher Lab**  
**Thioketal Diol Synthesis (cont'd)**

---

- a. Fit balloon to end of short piece of vacuum tubing and rubber band to secure.
  - b. Close valve and remove vacuum line.
  - c. Fill balloon with N<sub>2</sub> gas and twist at top to hold gas in for transfer.
  - d. Fit vacuum line with balloon to glass stopcock, release twisted balloon and open stopcock to reaction.
5. Add 500 mL anhydrous acetonitrile to RBF using N<sub>2</sub> to push solvent through cannula into reaction vessel to dissolve BiCl<sub>3</sub>. Allow BiCl<sub>3</sub> to dissolve before moving to next step.
- a. Insert tip of cannula into Sure/Seal™ cap, keep above liquid.
  - b. Insert needle with low N<sub>2</sub> flow into Sure/Seal™ cap.
  - c. Insert other end of cannula through rubber stopper into reaction vessel.
  - d. Push cannula into acetonitrile to begin transfer.
  - e. When about ½ of 1 L bottle has been transferred, remove cannula from reaction first to maintain inert reaction conditions.
6. Add 2,2-dimethoxypropane (95.77 mL, 781.59 mmol -1.2X) to RBF using syringe with needle through rubber septa. (Can use 12” needle if difficult to reach reagent in bottle)
7. Add thioglycolic acid (46 mL, 651.32 mmol – 1X ) to RBF using syringe with needle through rubber septa. (Can use 12” needle if difficult to reach reagent in bottle)

---

**Guelcher Lab**  
**Thioketal Diol Synthesis (cont'd)**

---

8. Allow reaction to stir for 24 hours at RT, 250 rpm.
9. Filter product using a Buchner funnel.
10. Record mass of oven-dried 1 L RBF with stopper.
11. Pour product into tared RBF and rotovap acetonitrile off with water bath at 30-35°C.
12. Attach glass hose connector/adaptor and dry under high vacuum for at least 24 hours (2-3 days desirable) to yield completely dry carboxylic acid functional thioketal crosslinker as a dark red, solid (probably stuck to RBF walls). Store in refrigerator if not immediately performing hydroxyl functionalization.
13. NMR in DMSO to verify structure.
  - a.  $\delta$  1.59, s (**a**)
  - b.  $\delta$  3.32, s (**b**)

**Clean-up: Thiol reaction creates very strong odor that will be on all glassware and anything that comes into contact with TGA or product.**

1. Dispose of any solid waste in a waste bag to be left in hood until disposal (including gloves that may have come into contact with TGA or product).
2. Dispose of sharps in sharps waste container.
3. Clean long needles and cannulas:
  - a. Attach to new, clean 3 mL syringe
  - b. Pour acetone into beaker
  - c. Pull acetone through syringe and expel multiple times

---

**Guelcher Lab**  
**Thioketal Diol Synthesis (cont'd)**

---

- d. Wipe down exterior with acetone and Kimwipes
  - e. Dry in oven
4. Clean glassware:
- a. Rinse glassware with acetone or DCM into waste container.
  - b. Leave glassware in hood overnight if possible. If not, continue directly to step c.
  - c. Introduce glassware into the base bath for 24 hrs. Rinse with a lot of cold running water after removing from the base bath.
  - d. Rinse with acetone and dry in the oven.

### Hydroxyl Functionalization

1. Clear any unrelated reagents from hood and bring scale into hood.
2. Set condenser to 10-15 °C and set up 2 L three neck RBF with mechanical stirrer in the center, reflux condenser in left neck (side closest to vacuum pump, capped with one way glass stopcock), and addition funnel (capped with rubber septum) in right neck. Apply vacuum grease and clip glass connections.
3. Apply vacuum through condenser and use hot air gun on RBF for 3-5 minutes to ensure glassware assembly is thoroughly dried. Cool completely under vacuum.
4. Replace vacuum line on septum with N<sub>2</sub> filled balloon (follow procedure described above).
5. Find mass of COOH TK by weighing the capped RBF containing the product from above. Subtract mass of RBF and stopper and record mass of COOH TK.

---

**Guelcher Lab**  
**Thioketal Diol Synthesis (cont'd)**

---

6. Add ~400 mL anhydrous THF to RBF containing COOH TK using nitrogen to push solvent through cannula inserted into RBF (see step 4 above) or a large syringe. Shake/swirl to dissolve TK in solvent.
7. Use mass of COOH TK and run sheet to determine amount  $\text{LiAlH}_4$  needed.
8. Weigh  $\text{LiAlH}_4$  (2x mol COOH intermediate) **in fume hood**, close off  $\text{N}_2$  balloon and add  $\text{LiAlH}_4$  to RBF (remove addition funnel in right neck to add  $\text{LiAlH}_4$ , then replace).
  - a. Mass closed 25 g container of  $\text{LiAlH}_4$ .
  - b. Empty bottle into reactor and re-mass for mass  $\text{LiAlH}_4$ .
  - c. Weigh extra needed from open bottle of  $\text{LiAlH}_4$  using conventional methods.
  - d. Re-attach dropping funnel and re-open  $\text{N}_2$  valve.
  - e. Dispose of anything with contact to  $\text{LiAlH}_4$  in ziplock bag and place in solid waste bag in hood.
9. Place reaction set up in ice bath and turn on reactor.
10. Using large syringe with long needle, add ~350 mL diethyl ether to RBF with  $\text{LiAlH}_4$ .
11. Use cannula and nitrogen or large syringe to transfer TK solution to addition funnel (see step 4 above, may have to fill dropping funnel multiple times until all of TK solution is in reactor).

---

**Guelcher Lab**  
**Thioketal Diol Synthesis (cont'd)**

---

12. Drop TK solution to stirring RBF at 0°C until all has been added, continually replenishing the ice bath. (3.5-4 hrs.)
- \*Be very careful, at 0 °C you may still see reflux, so don't add TK solution rapidly. May result in blast or flame from hydrogen generation inside flask.\**
13. Replace water bath with oil bath. Start oil stirring slowly (will stir faster once oil is heated) and steadily heat reaction to 52°C to reflux overnight (at least 12 hours). Reflux rate should be about 1 drop/45 seconds at this temperature. Note: Increase heat slowly as it is easy to overshoot oil bath temperature.
- \*\*Ensure reaction is stirring smoothly after a couple of hours in heat with no large solids on top\**
14. Cool reaction to room temperature.
- 15. \*\*Quench LiAlH<sub>4</sub> from reaction\*\* CAUTION!!**
- Remove N<sub>2</sub> and stopcock from condenser, but leave condenser attached.
  - Add about 100 mL of wet ether to dropping funnel (can remove rubber septum at this point).
  - While stirring, slowly drop in wet ether allowing reaction to cease before dropping more.
  - Add about 75 mL water to dropping funnel and slowly add to reactor. Add more water if quenching is still evident.

---

**Guelcher Lab**  
**Thioketal Diol Synthesis (cont'd)**

---

16. Add ~300 mL 1M NaOH through dropping funnel (can have stopcock completely open) while stirring and wait for reaction to subside and product to separate slightly.
17. Using a Buchner funnel and flask, filter out solid by-product.
18. Extract product.
  - a. Pour filtered liquid into separation funnel. Shake vigorously releasing pressure 2-3 times and allow to separate until distinct layers are evident. Remove bottom layer (should see a red/brown tinted water layer on the bottom).
  - b. Add 75-100 mL of water to separation funnel to wash product. Shake vigorously releasing pressure 2-3 times and allow to separate until distinct layers are evident. Remove bottom layer (should see a red/brown – colorless clear water layer on the bottom) and capture translucent yellow organic layer in an Erlenmeyer flask.
  - c. If separation isn't evident, try:
    1. Add diethyl ether solvent.
    2. Add small amount of NaCl salt to separate rag layer.
    3. Add more water and/or NaOH to adjust pH of aqueous layer.
19. Add sodium sulfate to organic solution until sodium sulfate no longer clumps. Leave covered in refrigerator an hour-overnight for complete water removal.
20. Filter out sodium sulfate through Buchner funnel.



---

**Guelcher Lab**  
**Thioketal Diol Synthesis (cont'd)**

---

21. Tare 1 L RBF, then slowly pour solution into RBF for rotovap (use ether to rinse flask into RBF).
22. Rotovap solvent off with water bath not exceeding 40 °C.
23. Attach glass hose connector/adapter and dry under high vacuum at least 48 hours to remove organic solvents trapped in compound to yield OH functionalized TK crosslinker as a yellow/orange viscous liquid.
24. Can continue to add diethyl ether to solids from step 11 to salvage more TK from reaction. Repeat steps 11-17 if it appears compound is being removed (indicated by yellow color-change of solvent). Keep separate in case impure.
25. NMR in DMSO to verify structure.
  - a.  $\delta$  4.84, s (**c**)
  - b.  $\delta$  3.33, t (**d**)
  - c.  $\delta$  2.56, t (**e**)
  - d.  $\delta$  1.59, s (**f**)

**Clean-up: Thiol reaction creates very strong odor that will be on all glassware and anything that comes into contact with TGA or product.**

1. Dispose of any solid waste in a waste bag to be left in hood until disposal (including gloves that may have come into contact with TGA or product).
2. Dispose of sharps in sharps waste container in hood.
3. Clean glassware:

---

**Guelcher Lab**  
**Thioketal Diol Synthesis (cont'd)**

---

- a. Rinse glassware from making acid solution in sink, flushing with a lot of water to dilute.
- b. Rinse glassware in hood with water bottle into waste container labeled for reaction.
- c. Rinse again with acetone or DCM into waste container.
- d. Leave glassware in hood overnight if possible. If not, continue directly to step e.
- e. Introduce glassware into the base bath for 24 hrs. Rinse with a lot of cold running water after removing from the base bath.
- f. Rinse with acetone and dry in the oven.

---

**Guelcher Lab**  
**LTI-TK Quasi-Prepolymer**

---

**Before starting:**

- Glassware must be dried in oven, over night before use.

**Reagents:**

- Thioketal (TK) Diol
- Lysine-triisocyanate (LTI)

**Materials:**

- 100 mL round bottom flask (RBF)
- Large egg-shaped stir bar
- Rubber stopper
- Argon inlet line with needle
- Argon outlet needle (attached to line on gas bubbler if desired)
- Syringe with 16G needle and needle cap
- Syringe for product
- Syringe cap
- Plastic pipettes with tips cut off
- Oil bath
- Stir plate with thermocouple

**Procedure:**

1. Slowly heat oil bath to 45°C with a final stirring speed of 100 rpm.
2. Tare the RBF and stir bar, add appropriate amount of LTI and cap with rubber stopper. (2.5:1 molar ratio of LTI:TK produced good handling properties. *McEnergy, et al. RSC Advances, 2016.*)
3. Tare the syringe with 16G needle and needle cap for TK diol.
4. Tare syringe with needle and draw appropriate amount of TK into syringe (+ about 0.15 g excess to account for TK lost in syringe). Keep syringe upside down until use.
5. Clamp RBF in oil bath and out-gas reactor with argon for several minutes. Keep gas flowing as the reaction proceeds.

---

**Guelcher Lab****LTI-TK Quasi-Prepolymer (cont'd)**

---

6. Insert TK needle into RBF stopper and start slowly adding TK into reaction flask with LTI. (Inject slowly/dropwise for ~15 minutes).
7. When all TK has been added, leave TK syringe as is and allow the reaction to proceed for a total time of 3 hours at 45°C.
8. After reaction is complete, turn off hot plate/stirrer and argon and remove stopper from RBF.
9. Tare a syringe with cap.
10. Use plastic pipettes with tips cut off to transfer LTI-TK into back of capped syringe (remove plunger).
11. Holding syringe upside down, hold plunger in place at back of syringe and remove cap. Once material has cleared the syringe tip, carefully reinsert plunger. Purge with argon and store at 4°C.
12. Replace needle cap and weigh TK syringe. Subtract original syringe/needle/cap mass from this mass to estimate the amount of TK lost in the needle (not added to reaction). Subtract this amount from original "TK added" mass for actual TK.

**Clean-up**

1. Dispose of sharps in appropriate container.
2. Acetone and wipe rubber stopper clean.
3. Put RBF in KOH/isopropanol bath for 24 hrs.
4. Rinse with a lot of cold running water.
5. Rinse with acetone and dry in oven.

---

## Guelcher Lab

### Quasi-Static Compressive Fatigue Testing

---

#### Principle:

Find fatigue life of polyurethane composites under compression with constant, 37 °C hydration.

Adapted from: *D. Harmata, et al. J Mech Behav Biomed Matr, 2015.*

#### Before starting:

- Make cylindrical PUR specimens with height = 2X diameter.
- Soak in water/PBS at 37 °C for ~24 hours to simulate *in vivo* conditions.

#### Materials:

- Medical gauze
- Water drip system
- Constant temperature circulator
- Water reservoir with hose
- MTS load cell (12.5 kN), Nyman Lab
- MTS extensometer, Nyman Lab
- Rubber o-rings (x2)
- Cylindrical fatigue platens, Nyman Lab
- External drive

#### Procedure:

1. Turn on battery tower by pressing power button on box closest to computer.
2. Turn on computer.
  - a. Password: admin
3. Turn on MTS controller (power switch on back).
4. Turn on pump (in back closet).
  - a. Yellow valve
  - b. Parallel to pipe = on
5. Locate skinny, cylindrical platens and water reservoir (with overflow tubing) and set up according to **Figure A1**. **\*\*DO NOT ATTACH**



**Figure A1.** MTS setup for fatigue testing.

---

**Guelcher Lab****Quasi-Static Compressive Fatigue Testing (cont'd)**

---

## EXTENSOMETER AT THIS POINT\*\*

- a. Loosely attach top platen.
  - b. Place an o-ring or rubber washer (diameter close to that of platen) on bottom platen under nut. Screw in bottom platen through hole in reservoir container. Add another o-ring around base of nut.
  - c. Use pliers to hold platens parallel and tighten both.
6. To open the program:
- a. Station manager
  - b. Project 1
  - c. 858AT strain
  - d. Maddi\_Fatigue\_New
7. Once program has opened:
- a. File → Restore saved view
  - b. Interlock 1 → reset
  - c. Station Controls → 2<sup>nd</sup> button (detectors)
    - i. Load, lower limit: -0.5 kN
    - ii. Strain Limits: 5 and -3.5%
    - iii. Close and check again
8. Activate the pump.
- a. Check: Exclusive control → HPU Power: click on the 1 line, 2 lines, finally 3 lines button

---

**Guelcher Lab****Quasi-Static Compressive Fatigue Testing (cont'd)**

---

- b. Lower platen to limit (Lift frame if necessary) to ensure the platens can never touch each other during run. Lift upper platen.
  - c. Power down pump: 3 lines, 2 lines, 1line
  - d. Power up pump
9. Warm up the equipment.
- a. At the left, click on: Function Generator and select Displacement mode.
  - b. Check that the parameters are: 40mm, 10mm, 2 Hz, and control mode is set at 'displacement.'
  - c. Click on the PLAY button and let it run for 3 mins.
  - d. Click the STOP button.
  - e. Reset load (in the window: Signal Auto Offset).

10. Tune specimen (Figure A2).

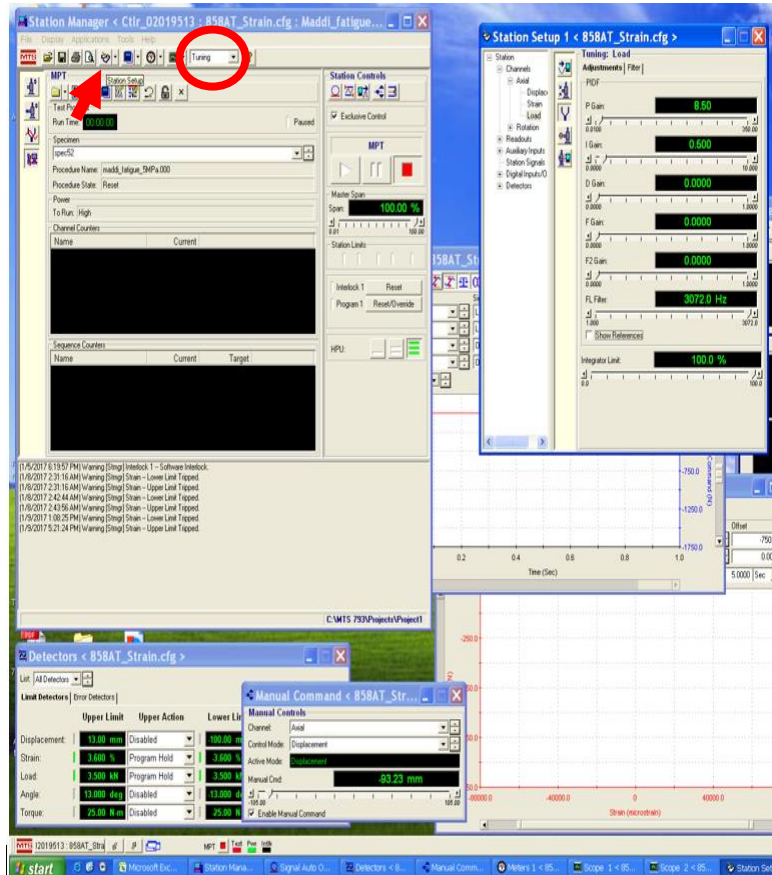


Figure A2. Tuning setup for fatigue testing.

- Select “Tuning” in the drop down at the top (Red circle), Password: Tuning
- Select “Station Setup” (Red arrow) so that the dialogue box on the right opens.
- In the Station Setup dialogue box, under Channels → Axial, select “Load” as indicated on the figure.
- Start with  $P=1$  and  $I= 0.25$  ( $D, F, F2=0$ ).



---

**Guelcher Lab****Quasi-Static Compressive Fatigue Testing (cont'd)**

---

- e. In Station Manager, select “Function Generator” icon on the right and set the Control Mode to “Load.”
- f. Set Target, Amplitude, and Frequency to match desired Force for fatigue test.

Example: If desired stress is 5 MPa (=166 N for 6 mm diameter specimen)

Target setpoint = -88 N

Amplitude = 78 N



Frequency = 5 Hz (match what test will be run at)

- g. Compensator: Choose “Null Pacing”
- h. Ensure Scope 1 is open and “Load” and “Load Command” are set to display.
- i. Place specimen between platens.
  - i. Wrap specimen in thin piece of gauze to maintain hydration.
  - ii. Ensure manual command window is set to displacement.
  - iii. Lower upper platen to about -5 N, zero force before platen touches specimen.
- j. Tune Specimen
  - i. Hit play
  - ii. Rescale Scope 1 and ensure “Load” and “Load Command” axes are the same scale

---

**Guelcher Lab****Quasi-Static Compressive Fatigue Testing (cont'd)**

---

- iii. Increase P gain and I gain in 0.25-0.5 increments until the “Load” matches the “Command Load” height (P) and is in phase (I).
  - iv. Stop button once these are in sync.
  - k. In manual command window, change to “Displacement” and lift platen back to where load is about -1 N.
11. Set up procedure for fatigue test.
- a. In “Station Manager” window, select MPT icon  on left.
  - b. Open procedure “maddi\_Fatigue\_5MPa” using the folder icon on top of the MPT window.
  - c. Select the procedure editor icon  on the top of the MPT window to open the “MPT Procedure Editor” window.
  - d. Double click each of the icons to ensure they are set as desired:
    - i. “Data acq cyclic” – In first tab, select desired “time between points” for data acquisition. Currently set to 200 Hz (0.005 sec)
    - ii. “Pre-load...” – Select desired preload conditions. Currently set to -10 N at a ramp time of 10 seconds.
    - iii. “Cyclic Loading” – In first tab, select desired frequency to run test at (Segment shape: sine, 5 Hz), max. number of cycles (Count box checked, 1,000,000 cycles).Set desired load for testing. Here, -166 N  $\cong$  5 MPa for a 6 mm

diameter specimen. Keep minimum “Absolute End Level 2” at -10 N so specimen stays between platens throughout testing.

iv. **\*\*Save any changes as a new procedure!!**

12. Once procedure is set, ensure that the “Detectors” window has Strain and Load limits set to “Program Hold” and all other detectors are set to “Disabled.” Set strain limits to produce desired data (Here, test stops at  $\pm 3.6\%$ . Set load limits to meet test needs (here,  $\pm 3.5$  kN is more than enough).

13. With the force around -1 to -2 N, **attach extensometer** to upper and lower platens using o-rings that are tight around the platens. See Figure 1.

i. Place extensometer so it is equally spaced above and below the specimen.

ii. Use crochet hook to grab o-ring and pull it around platens. Attach upper, then lower.

iii. Ensure “Strain” and “Force” outputs did not change drastically during this step.

iv. Remove pin from extensometer gently. Again, ensure no readouts changed drastically.

14. Turn on water heater and adjust the flow rate using the blue knob (\*away from specimen\*). Want water to drip very slowly, but to never stop.


---

**Guelcher Lab****Quasi-Static Compressive Fatigue Testing (cont'd)**

---

15. Move end of hose very close to specimen so that water droplets are wicked to specimen. Use micrometer to carefully position and ensure extensometer is not contacted by water.
16. Before starting test ensure:
  - a. Load and Strain are set to “Program Hold”
  - b. Desired program is loaded
  - c. Strain is zeroed
17. Zero strain in “Signal Offset” window and hit play button to start test.

**After Test is Finished**

1. Carefully remove extensometer.
  - a. Remove bottom, then top o-ring
  - b. Replace pin (may have to wiggle slightly)
2. If strain limit is tripped to stop test:
  - a. In “Detectors” window find red warning. In drop down for that limit, select “Disabled” and then change back to “Program Hold”. Should have green indicator now.
3. Select new specimen  in MPT window and name next specimen.
4. In “Manual Command” window, check “Enable Manual Command” and raise upper platen to remove specimen.
5. Use paper towels to soak up water from reservoir.
6. Add new specimen and repeat steps 10-17.

---

**Guelcher Lab****Quasi-Static Compressive Fatigue Testing (cont'd)**

---

7. If no new specimen, follow shut down procedure.

**Obtain Data**

1. My Computer → C: → MTS 793 → Projects → Project 1 → MPT → Specimens
2. Each sample should have folder in “Specimens.” Save entire folder to USB.

**MTS Shut Down**

1. Turn off water heater. Empty water and wipe down with paper towels.
2. In the “Signal Auto Offset” window, select “Clear Offset.”
3. Dry out any water remaining in reservoir.
4. Separate platens to about 40 mm and take down set up.
5. Rinse/dry off platens if necessary.
6. HPU power down: 3, 2, 1 lines.
7. Close Program (DO NOT save any changes).
8. Close valve in back closet.
9. Shut down computer.
10. After computer is off, power button on 1<sup>st</sup> battery tower.
11. Power off MTS (back switch).

**Notes:**

- Check on specimen 1-2 times a day to make sure it is being hydrated and water reservoir is not overflowing
- Use syringe to remove water from reservoir if necessary \*be sure to not touch extensometer\*

**Principle:**

Rotate 2D reconstruction and analyze bone parameters for cylindrical defects of various lengths and diameters using the μCT50.

**Rotation Procedure**

Goal: Rotate 2D reconstruction so that a circle normal to the insertion of the defect is visible in the XY plane. See **Figure A3** for desired defect orientation as viewed in each plane.

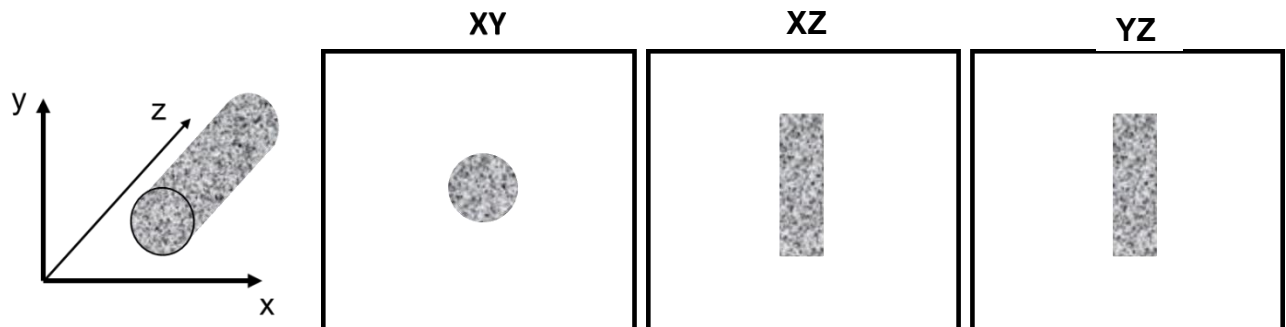


**Figure A3.** Desired defect orientation for μCT analysis.

1. Load ISQ file of interest so that defect is visible in XZ and YZ planes. (can load every 5<sup>th</sup> or 10<sup>th</sup> slice, ie. click bar of slider so that every 10<sup>th</sup> slice loads)
2. In XZ plane, use angle tool to measure rotation angle necessary to orient defect according to **Figure A3** in that plane.
3. Repeat in YZ plane.
4. Return to XY plane and contour entire defect using box or circle that ensures all of defect is included. Contour selection through entire scan.
5. Use script 28 to rotate.
  - a. Input rotation angles measured in blanks for appropriate axes and run script.

The axis of rotation will be the axis **not** included in the name of the plane in

---

**Guelcher Lab**  
**μCT Analysis of Cylindrical Defects (cont'd)**

---

which the angle measurement was made (ie. If angle measured in XZ plane, the rotation will be done about the Y axis).

- b. MISC:misc1 = x rotation (cw)
  - c. MISC:misc2 = y rotation (ccw)
  - d. MISC = z rotation (cw)
6. Open new ISQ file generated from the first rotation (“...R.ISQ”) and complete any additional rotations necessary by repeating steps 1-5. \*Note: may take over an hour to generate new ISQ file.

**Measurement Procedure**

Goal: Measure bone parameters of cylindrical defect in 4 radial sections assigned by concentric cylinders according to **Figure A4** using script #231 after completing rotations. Green circle is the diameter of the defect.

1. Determine the size of the large outer circle (blue) to be contoured for analysis.

- a. Determine the value of X in schematic using scan voxel size (voxel = μm/slice).

Ex: 5 mm defect, 17.2 μm voxel size.

$$5 \text{ mm} = 6X \therefore X = 0.833 \text{ mm}$$

$$\rightarrow 17.2 \text{ μm/slice} \therefore X = 48.4 \text{ slices}$$

$$\text{Larger circle} = 8X$$

$$\therefore \text{Larger circle} \approx 387$$

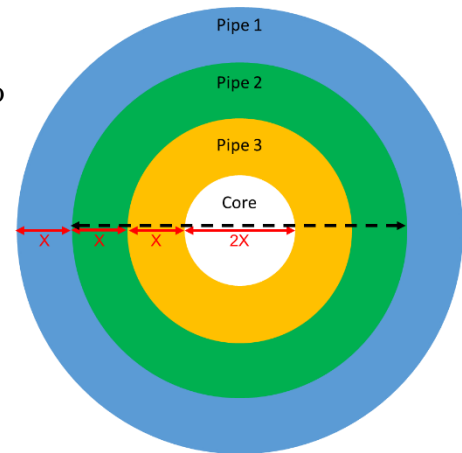


**Figure A4.** Schematic of AOI using script 231. The green circle (dotted line) is the defect diameter, the blue circle is the circle drawn during contouring. Program outputs bone parameters for colored rings.

---

**Guelcher Lab**  
**μCT Analysis of Cylindrical Defects (cont'd)**

---

2. Determine desired length of measurement. Use voxel size to convert this to number of slices.
3. On the first slice within desired length range, use circle tool to draw circle with the size determined in a. The size readout is in the bottom left box of the μCT screen (ie. WxH: 387 x 387 [p]). Use “ctrl + c” command to copy circle and location.
4. Scroll to final slice of length selection and use “insert” key or “ctrl + v” to paste same circle there.
5. Use contour range to morph the shape throughout the selection.  
  
\*Note: If defect is not straight, the circle can be moved slightly throughout the contour. Do not do this for large inconsistencies.
6. Use script #231 to run measurements.
  - a. Ensure “Default VOI” is selected to include all of the contouring.
  - b. Choose desired filtering (“Gauss Sigma” and “Gauss Support”) and thresholding.
7. Data will output to the “Data” folder on MicroCT FTP under the scan number for the sample. Download the file “...Concentric.txt” to retrieve data.  
  
\*Note: Data for “pipe 1” is the BV/TV (and BV, TV) for the volume of the blue ring, “pipe 2” is the data for the volume of green ring, etc.



---

**Guelcher Lab****Safranin O/Fast Green Staining of Ground Sections**

---

**Principle:**

Use safranin O and Fast green to stain for cartilage in ground, PMMA sections.  
*Adapted from Josh Johnson (Vanderbilt Center for Bone Biology).*

**Materials:**

- Fast Green Solution (0.2% Fast Green SF in water) – 250 mL
- Safranin O Solution (0.1% Safranin O in water) – 250 mL
- Acetic Acid (1% in water) – 1 L

**Procedure:**

1. Filter stains through filter paper and funnel into separate histology buckets.
2. Add acid to 4 separate 250 mL histology buckets.
3. Stain in Fast Green. 5 min
4. Rinse in fresh acetic acid. Dip
5. Stain in safranin O. 3 min
6. Rinse in fresh acetic acid. Dip
7. Repeat steps 3-5.
8. Blot dry with Kimwipes.

**Notes:**

1. *2 cycles sufficient for rabbit femoral plug defects (30 – 70  $\mu$ M ground sections).  
May repeat steps 3-5 until desired color balance.*
2. *May mount slides with coverslips if desired.*

**Stain Colors/Detection:**

Cartilage – red (in proportion to proteoglycan content)  
Bone – green/blue

**Clean-up:**

1. Dump acetic acid in sink and rinse bucket thoroughly ( $\leq$  1% acid).
2. If still translucent and no cloudiness, add fast green and safranin O back to original containers. Rinse buckets thoroughly in sink.

---

**Guelcher Lab**  
**Immunohistochemical Staining of Ground Sections**

---

**Principle:**

Use immunohistochemistry to detect blood vessels (CD31/PECAM, endothelial cells) and macrophages (CD68) in ground, plastic sections. Adapted from *Immunohistochemical Staining\_AM* protocol from Sterling Lab.

**Materials:**

- Humidifying staining chamber (Sterling lab)
- 4 staining buckets and 1 staining rack (Sterling lab)
- IMMEDGE hydrophobic pen (Fisher Scientific, cat. NC9545623)

**Antibodies/detectors:**

- Goat anti-Mouse IgG (H+L) Cross-Absorbed Secondary Antibody, HRP (ThermoFisher, cat. 31432)
- CD31/PECAM-1 Antibody (JC/70A) (Novus Biologicals, LLC, cat. NB600-562-0.1ml)
- Anti-CD68 antibody [KP1] (Abcam, cat. Ab955)
- ImmPACT NovaRED (Vector Labs, cat.. SK4805)
- Goat serum (Sterling lab)

**Reagents:**

- Sodium citrate ()
- Tween 20 (Sigma, P1379)
- 1X PBS
- 50% H<sub>2</sub>O<sub>2</sub> (Fisher, H341)
- Methanol
- Aqua-Mount (Thermo Scientific, 13800)

**Before starting:**

1. Prepare solutions.

- **Citrate buffer:** (10mM sodium citrate): 2.94g sodium citrate in 900 mL H<sub>2</sub>O
  - pH to 6 using NaOH/HCl
- **TPBS:** 500 μL Tween 20 in 1L 1X PBS
- **0.5% H<sub>2</sub>O<sub>2</sub>:** 2.5 mL H<sub>2</sub>O<sub>2</sub> in 247.5 mL methanol
  - \*\* For use only if using an HRP labeled secondary antibody
- **5% Goat serum:** 0.5 mL goat serum in 9.5 mL PBS

---

**Guelcher Lab**  
**Immunohistochemical Staining of Ground Sections (cont'd)**

---

**Procedure:**

1. Antigen retrieval.  
  
Preheat citrate buffer to 80°C in microwave.  
  
Transfer to histology bin. Soak at RT. 1 x 1 hr
2. PBS wash in histology bins. 3 x 3 m
3. *Step for HRP labeled secondary only. If no HRP, skip to step 5.*  
  
0.5% H<sub>2</sub>O<sub>2</sub> wash in histology bins. 1 x 10 m
4. PBS wash in histology bins 3 x 3 m
5. Shake off excess water and dry edges with Kimwipe. Draw barrier around section with hydrophobic pen.
6. Block with serum. 1 x 1 hr  
  
Arrange slides in humidifying chamber facing up. Drop 5% goat serum using pipettor  
  
or transfer pipettes.  
  
Use transfer pipette or Kimwipe (away from defect) to remove serum.
7. Incubate in primary antibodies. overnight
  - a. Dilute primary antibodies in goat serum:  
  
CD68 – 1:200 (ie 20 µL Ab in 4 mL serum)  
  
CD31 – 1:100 (ie 40 µL Ab in 4 mL serum)

---

**Guelcher Lab****Immunohistochemical Staining of Ground Sections (cont'd)**

---

b. Use pipettor or transfer pipette to drop antibody solution onto slides (around 0.75 mL/slide).

*NOTE: These antibodies cannot be used on the same slide. Must use separate slides for each marker.*

c. Use transfer pipette or Kimwipe to remove antibodies.

8. Add slides to slide holder and wash in TPBS in histology bins. 3 x 3 m

Use Kimwipe to dry area around defect.

9. Incubate in secondary antibodies. 1 x 1hr

a. Dilute secondary antibody in goat serum:

Goat anti-mouse IgG-HRP – 1:500

b. Use pipettor or transfer pipette to drop secondary antibody solution onto slides.

*NOTE: Use same secondary antibody for both primary antibodies in this procedure.*

10. Add slides to slide holder and wash in TPBS in histology bins. 3 x 3 m

Use Kimwipe to dry area around defect.

11. Detect with NovaRed Chromagen Kit 12-15m

a. Make detection solution according to instructions with kit.

b. Use transfer pipette to add detector solution to slides. Let stand 12 – 15 minutes until color begins to appear.

**c. Stop reaction with distilled H<sub>2</sub>O wash in histology bins.**

---

**Guelcher Lab****Immunohistochemical Staining of Ground Sections (cont'd)**

---

12. Optionally, mount slides with Permount Mounting solution and glass coverslips being careful to eliminate bubbles.

**Notes:**

1. *Times listed may vary depending on the sample and section thickness.*
2. *Tested for these antibodies. May be adapted for other targets.*
3. *May counterstain with hematoxylin (Harris Formula) if desired.*